UNIVERSITÀ
DI PAVIA

DEPARTMENT OF ELECTRICAL, COMPUTER AND BIOMEDICAL ENGINEERING

DOCTORAL SCHOOL IN MICROELECTRONICS
XXXVIII CYCLE

Ultrafast Lithium Niobate Modulators for Quantum Communication

---

Author:
Andrea Bernardi

Supervisor:
prof. Daniele Bajoni
Dr. Federico Andrea Sabattoli

Contents

List of abbreviations

ASE amplified spontaneous emission.

AWG arbitrary waveform generator.

BOX buried oxide.

BQP bounded-error quantum polynomial time.

BSM Bell-state measurement.

BTO barium titanate.

CAR coincidence-to-accidental ratio.

CHSH Clauser–Horne–Shimony–Holt.

CPW coplanar waveguide.

CV-QKD continuous-variable quantum key distribution.

DBR distributed Bragg reflector.

DV-QKD discrete-variable quantum key distribution.

DWDM dense wavelength-division multiplexing.

EBQKD entanglement-based quantum key distribution.

EO electro-optic.

EPR Einstein–Podolsky–Rosen.

ER extinction ratio.

FAU fiber array unit.

FCA free-carrier absorption.

FCD free-carrier dispersion.

FDE finite-difference eigenmode.

FSR free spectral range.

FWHM full width at half maximum.

FWM four-wave mixing.

G-S-G ground-signal-ground.

GBS Gaussian boson sampling.

GVD group velocity dispersion.

InP indium phosphide.

ITU International Telecommunication Union.

JSI joint spectral intensity.

JTI joint temporal intensity.

LHVM local hidden variable model.

LN lithium niobate.

LNOI lithium niobate on insulator.

MMI multi-mode interferometer.

MPW multi-project wafer.

MZI Mach–Zehnder interferometer.

MZM Mach–Zehnder modulator.

PDK process design kit.

PIC photonic integrated circuit.

PPKTP periodically poled potassium titanyl phosphate.

PPLN periodically poled lithium niobate.

PRBS pseudo-random bit sequence.

PSL post-selection loophole.

PSR polarization splitter-rotator.

PVM projection-valued measurement.

QBER quantum bit error rate.

QFT quantum Fourier transform.

QKD quantum key distribution.

QPM quasi-phase matching.

QRNG quantum random number generator.

QST quantum state tomography.

RF radio frequency.

RIE reactive-ion etching.

SFWM spontaneous four-wave mixing.

SHG second-harmonic generation.

SiN silicon nitride.

SKR secret key rate.

SNR signal-to-noise ratio.

SNSPD superconducting nanowire single-photon detector.

SOI silicon-on-insulator.

SPDC spontaneous parametric down-conversion.

SPM self-phase modulation.

SQL standard quantum limit.

TE transverse electric.

TES transition-edge sensors.

TFLN thin-film lithium niobate.

THG third-harmonic generation.

TIR total internal reflection.

TM transverse magnetic.

TPA two-photon absorption.

TPS thermo-optic phase shifter.

TWE traveling-wave electrodes.

VNA vector network analyzer.

VOA variable optical attenuator.

XPM cross-phase modulation.

Chapter 1

Introduction

Quantum systems, described by the principles of quantum mechanics, formulated in the early 20th century, exhibit unique and counterintuitive properties such as superposition and entanglement, governed by a well-defined set of postulates. In recent years, advances in technology have made it possible to actively manipulate and control quantum systems, enabling experimental access to phenomena that were once purely theoretical. As a result, a new class of quantum technologies has emerged, exploiting the properties of quantum mechanics to achieve results that would be impossible using classical methods. These developments have given rise to several promising fields, including quantum communication [1, 2], quantum computation [3, 4], and quantum metrology and sensing [5], each demonstrating remarkable advantages for specific applications.

Among the various branches of quantum technologies, quantum communication, and in particular quantum key distribution (QKD), represents one of the most advanced and commercially promising applications that are in the early stages of market development. QKD provides a solution to the vulnerabilities of classical communication systems by enabling the secure exchange of cryptographic keys guaranteed by the laws of quantum mechanics rather than computational complexity. As in classical telecommunications based on optical fiber networks, light naturally emerges as the most suitable carrier of quantum information: photons not only propagate with low loss over long distances, but also provide an ideal platform for encoding and manipulating quantum states.

Building on this foundation, numerous demonstrations of quantum communication systems have been reported [6–10]. A major recent trend, however, is the development of quantum technologies based on integrated photonic platforms, capable of generating, manipulating, and detecting single photons on a chip, an approach commonly referred to as integrated quantum photonics [11–13]. Quantum photonic chips play a pivotal role in enabling the miniaturization, stability, and scalability of quantum systems. In addition, integrated platforms offer significant advantages in terms of cost, robustness, and reproducibility, which are essential prerequisites for the large-scale deployment of quantum technologies. Several on-chip components relevant to quantum communication have already been demonstrated, including sources of nonclassical light [14, 15], quantum photonic circuits for state processing [16], and integrated single-photon detectors [17, 18].

This thesis presents the development of an integrated quantum photonic circuit based on the thin-film lithium niobate (TFLN) technological platform, designed to operate as a

reconfigurable quantum state projector. The realized quantum receiver is tailored for the manipulation of quantum states encoded in the time degree of freedom, and is specifically engineered to address an intrinsic security issue of time-bin encoding, the temporal post-selection loophole (PSL) [19]. The thesis includes the experimental demonstration of different quantum applications, including an entanglement-based quantum key distribution (EBQKD) protocol implemented using the developed integrated photonic circuit.

The first two chapters provide the theoretical background necessary to introduce and contextualize the development of the proposed device. Chapter 2 presents a review of integrated photonics, describing the main building blocks that, when combined, enable a wide range of applications. Many of these components are also incorporated into the integrated circuit developed in this work. In addition, this chapter includes a discussion of various technological platforms, highlighting their main features and typical fields of application. Chapter 3 provides an overview of quantum applications, with particular focus on systems that exploit photons as elementary qubit carriers. The chapter concludes with a detailed discussion of time-domain quantum state encoding, outlining its main features and challenges, and defining the issues that the presented device aims to address. Chapter 4 presents the design and development of the integrated quantum circuit, covering the entire process from simulations and design layout to wafer- and chip-level characterization. The chapter also includes details on the packaging of the circuit, integrating both electrical and optical connections for full operability.

In Chapter 5, the experimental demonstrations that validate the quantum nature of the system are presented, including entanglement certification and quantum state tomography (QST) of the generated time-bin entangled photon pairs, both enabled by the manipulation capabilities of the developed quantum receiver. Chapter 6 introduces two distinct implementations of an EBQKD protocol, enabled by the device's reconfigurability. The different configurations and their associated trade-offs are analyzed and discussed in detail. Finally, the main results and features of the developed system are summarized, comparing them with the current state of the art and outlining possible future improvements and applications.

Part I

Theoretical background

Chapter 2

Introduction to photonic integrated technologies

Photonics is the science and technology of generating, guiding, controlling, amplifying, and detecting light. Light possesses remarkable physical properties, such as its extremely high propagation speed, multiple controllable degrees of freedom (intensity, phase, polarization, and wavelength), the ability to propagate through diverse media with minimal perturbation, and its efficiency in transferring energy. These unique features make light an ideal carrier of both information and power, enabling a broad range of applications. As a result, photonic technologies play a central role in modern society, underpinning fields such as optical fiber telecommunications [20, 21], biomedical and environmental sensing [22, 23], solid-state lighting [24], advanced manufacturing [25], and emerging quantum technologies [26], among many others [27].

Today, many photonic applications benefit from integration and miniaturization at chip level, following a developmental trajectory reminiscent of the rapid scaling of the electronics industry that began in the 1960s. While electronics is based on the control of electrons, photonics revolves around the manipulation of photons. The rise of integrated photonics has been largely enabled by the technological maturity of materials and fabrication techniques originating from the microelectronics industry.

Beginning in the 1980s, researchers adapted CMOS-compatible silicon fabrication platforms to realize photonic components [28–30]. During this period, substantial effort was devoted to developing standardized photonic building blocks such as waveguides, modulators, couplers, and photodetectors, that could be co-integrated within a single optical chip. The rapid growth of fiber-optic communications accelerated this transition and continues to drive the demand for scalable and reliable photonic solutions to satisfy the increasing global data traffic.

As in electronics, reducing the footprint of photonic components enables the dense integration of multiple functions on a single platform [31]. Miniaturization also offers key advantages in terms of performance [32], energy efficiency [20], and reliability [31]. Moreover, the compatibility of photonic platforms with CMOS fabrication processes allows for high-volume, cost-effective, and scalable production of photonic integrated circuits (PICs). These characteristics have established integrated photonics as a cornerstone technology for next-generation optical systems.

The evolution of integrated photonics is often compared to the microelectronics as the photonic analogue of Moore's law. However, a few important distinctions exist. Unlike electronics, photonics lacks a universal building block equivalent to the transistor [33]. Furthermore, integrated photonic platforms are typically customized for specific applications, and fabrication costs remain significantly higher [34]. In contrast, electronic hardware benefits from economies of scale and a broad ecosystem of standardized components and design tools, enabling faster and more generalized technological progress. These factors have resulted in a slower scaling rate for photonics compared to electronics.

Nevertheless, this slower evolution presents valuable opportunities for innovation at both the device and system levels. In particular, although silicon photonics has achieved remarkable success, the intrinsic limitations of silicon motivate the exploration of complementary material systems. For instance, the indirect bandgap of silicon prevents efficient light emission, necessitating the use of III–V compound semiconductors such as indium phosphide (InP) to realize on-chip lasers and amplifiers. Similarly, materials such as lithium niobate (LN) and silicon nitride (SiN) provide strong electro-optic (EO) or second-order nonlinear responses, wide optical transparency windows, and low propagation losses. Together, these alternative platforms significantly extend the functionality of integrated photonic systems, enabling a broader range of advanced applications in communications, sensing, and quantum technologies [11].

Building on these developments, research efforts are now actively exploring hybrid and heterogeneous integration combining multiple material platforms such as silicon, III–V semiconductors, and LN within the same chip. These hybrid approaches aim to merge the strengths of different materials, enabling functionalities and performance levels that cannot be achieved with a single platform [35, 36]. Recent advances are expanding the scope of integrated photonics well beyond traditional telecommunication applications. Emerging areas include biosensing [37], quantum information processing [11], and optical neural networks [38], where PICs are increasingly recognized as key enabling technologies.

In this chapter, I first review the fundamental building blocks employed across various integrated photonic platforms to realize the basic functionalities. For each block, a description and its working principle are provided, since most of these components are implemented in the integrated photonic module developed during this PhD project. The second section presents an overview of the most widely adopted integrated photonic platforms, emphasizing their respective advantages, limitations, and application domains. Finally, the last section focuses on the nonlinear optical properties of materials and their applications. Particular attention is given to third-order nonlinearities in silicon and second-order nonlinearities in LN, as these represent two of the most efficient and widely exploited mechanisms in nonlinear optics. Such properties enable the realization of key building blocks for diverse applications, including those employed in the experimental demonstrations of the quantum protocols described in Chapters 5 and 6.

2.1 Fundamental building blocks

In this section, I review the fundamental building blocks considered essential for the manipulation of light, outlining their working physical principles and key characteristics within integrated photonic systems. These components are typically based on the same underlying physical principles but have been implemented in different material platforms, each exhibiting distinct performance characteristics.

Over the years, these building blocks have been continuously optimized to fulfill specific functional requirements, depending on the target application and the properties of the chosen platform. When properly combined and engineered, these photonic components enable the realization of complex integrated circuits.

2.1.1 Waveguides

A waveguide is an optical structure designed to confine and guide light along a defined path. Waveguides are fundamental components of integrated optical circuits, as they enable the routing and distribution of optical signals within a chip.

The guiding property of a waveguide relies on the principle of total internal reflection (TIR). This occurs at the interface of two dielectric media with different refractive indices when light propagates from a medium of higher refractive index n_1 into one with a lower refractive index n_2 ($n_1 > n_2$). As illustrated in Figure 2.1a, this mechanism provides confinement in the vertical dimension (x-axis). In practical devices, confinement must also occur laterally in the plane perpendicular to the propagation direction (xy-plane), which is achieved by surrounding the guiding region (core) with cladding materials of lower refractive index.

While this geometrical description provides useful intuition, it is only accurate when the waveguide dimensions are significantly larger than the optical wavelength. For integrated photonic waveguides, where feature sizes are typically comparable to the wavelength due to the high refractive index contrast between core and cladding material, a full electromagnetic analysis is required as the TIR picture alone is insufficient to accurately describe light propagation.

To rigorously analyze waveguide behavior, Maxwell's equations are applied to the system. In a lossless, source-free medium, they can be written as:

$$\begin{cases} \nabla \times \mathbf{H} = i\omega\epsilon_0 n^2 \mathbf{E}, \\ \nabla \times \mathbf{E} = -i\omega\mu_0 \mathbf{H}, \end{cases} \tag{2.1}$$

where $\mathbf{E}$ and $\mathbf{H}$ denote the electric and magnetic fields, ω is the angular frequency, ϵ_0 and μ_0 are the vacuum permittivity and permeability, and n is the refractive index. By applying boundary conditions that enforce field continuity at dielectric interfaces, and considering confinement in the transverse (x, y) plane with propagation along the z-direction, the field solutions can be expressed as:

$$\begin{cases} \mathbf{E}(x, y, z, t) = \mathbf{E}_m(x, y)\, e^{i(\omega t - \beta z)}, \\ \mathbf{H}(x, y, z, t) = \mathbf{H}_m(x, y)\, e^{i(\omega t - \beta z)}, \end{cases} \tag{2.2}$$

where $\mathbf{E}_m$ and $\mathbf{H}_m$ represent the mode field distributions, and β is the propagation constant.

The guided modes of a waveguide are generally classified as either transverse electric (TE) or transverse magnetic (TM), depending on which longitudinal field component vanishes. In TE modes, the longitudinal electric field component E_z is zero and H_z is nonzero, while for TM modes, the longitudinal magnetic component H_z vanishes, with nonzero electric component E_z. From the Maxwell's equations, it can be shown that the remaining field components are nonzero and related to E_z and H_z [39].

When the transverse dimensions of a waveguide are sufficiently large, higher-order modes can propagate alongside the fundamental one. The fundamental mode, denoted TE_{00} or TM_{00}, exhibits a single intensity maximum across the transverse cross-section, as shown in Figure 2.1b. Higher-order modes, labeled TE_{nm} or TM_{nm}, display multiple intensity maxima and nodes, where n and m correspond to the number of field nodes along the transverse dimensions of the core. For instance, Figure 2.1c illustrates the higher-order mode TE_{01} in a rib waveguide structure.

Exact analytical solutions for complex integrated geometries are generally not feasible, so numerical methods are used to solve for the optical modes. finite-difference eigenmode (FDE) solvers [40] are widely employed to compute mode profiles, effective refractive indices, and propagation constants for arbitrary waveguide structures.

The *propagation constant* β describes the mode's propagation behavior. If β is real, the mode is guided and propagates; if β is imaginary, the mode is evanescent and decays exponentially, and if β is complex, the mode is leaky and loses energy during propagation. For guided modes ($\beta \in \mathbb{R}$), β satisfies

$$n_2 \frac{\omega}{c} < \beta < n_1 \frac{\omega}{c},$$

which ensures exponential decay in the cladding and confinement within the core. The propagation constant can also be expressed as:

$$\beta = n_{\text{eff}} \frac{\omega}{c}, \tag{2.3}$$

where n_{eff} is the effective refractive index of the mode, bounded between the refractive indices of the core and cladding ($n_2 < n_{\text{eff}} < n_1$).

In general, β depends on the optical frequency and provides information about the mode's chromatic dispersion. A propagating mode at different frequencies experiences a change in β due to *waveguide dispersion*, which arises because the modal field distribution varies with wavelength. An additional contribution, known as *material dispersion*, results from the intrinsic frequency dependence of the refractive indices $n_1(\omega)$ and $n_2(\omega)$. The total dispersion can be described by expanding $\beta(\omega)$ in a Taylor series around the central frequency ω_0:

$$\beta(\omega) = \beta_0 + \beta_1(\omega - \omega_0) + \frac{1}{2}\beta_2(\omega - \omega_0)^2 + \frac{1}{6}\beta_3(\omega - \omega_0)^3 + \cdots, \tag{2.4}$$

where each coefficient β_n has a distinct physical meaning:

- β_0: the phase constant at ω_0, related to the **phase velocity** $v_p = \omega_0/\beta_0$;

- β_1: the inverse of the **group velocity**, $v_g = 1/\beta_1$, describing pulse envelope propagation;
- β_2: the **group velocity dispersion (GVD)** parameter, responsible for pulse broadening and chirping;
- β_3: the **third-order dispersion** term, relevant for ultrashort or broadband optical pulses.

Another important waveguide parameter is the *propagation loss*, which can be expressed through the imaginary part of the refractive index:

$$n = n_{\text{eff}} + i n_{\text{im}}, \tag{2.5}$$

where n_{im} accounts for optical losses. These losses are typically expressed per unit length through the attenuation coefficient

$$\alpha = n_{\text{im}} \frac{\omega}{c}.$$

Substituting this expression into Eq. (2.2) yields an exponentially decaying field intensity along the propagation direction z:

$$\begin{cases} E(z) = E(0)\, e^{-\alpha z}, \\ H(z) = H(0)\, e^{-\alpha z}. \end{cases} \tag{2.6}$$

Losses cause exponential attenuation of the optical power along the propagation direction and originate from several mechanisms. One contribution arises from *material absorption*, when the waveguide material is not fully transparent at the operating wavelength or contains fabrication-induced defects and impurities. A second, and often dominant, contribution in integrated waveguides is *sidewall scattering*, caused by surface roughness at the core–cladding interface due to imperfections in the fabrication process.

In summary, waveguide design involves balancing multiple factors to optimize performance for a given application. Increasing the waveguide cross-section enhances mode confinement and reduces scattering loss for the fundamental mode, but it also increases the probability of supporting higher-order modes. Since single-mode operation is generally preferred to avoid mode-dependent distortion and coupling inefficiency, the geometry is typically chosen so that only the fundamental mode is supported at the operating wavelength. Even under single-mode conditions, the design must also account for chromatic dispersion management and fabrication tolerances, which together determine the final performance of the integrated optical system.

2.1.2 Input and output couplers

To effectively use an integrated optical circuit, it is essential to couple light into and out of the chip. This step is crucial for interfacing the PIC with external components such as lasers, detectors, or other elements involved in optical signal processing. In most cases, coupling is achieved using optical fibers, as they are well-suited for long-distance optical signal transmission due to their low propagation losses and wide availability.

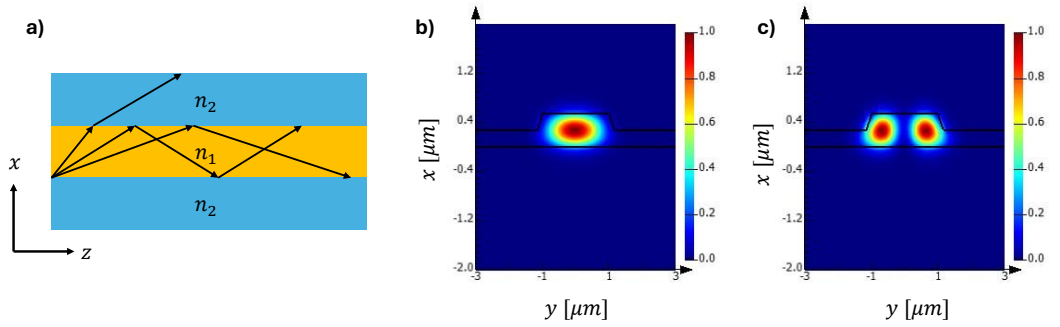

Figure 2.1: **Waveguide propagation. a)** Representation of the TIR phenomenon by ray-optics schematic in a slab waveguide, with $n_1 > n_2$. FDE simulation of the electric field intensity of propagating modes: **(b)** the TE_{00} fundamental mode and **(c)** the TE_{01} higher-order mode, supported due to the sufficiently large waveguide width.

Integrated photonic platforms generally exhibit a high refractive index contrast (e.g., Si/SiO_2: 2.04, $TFLN/SiO_2$: 0.76, Si_3N_4/SiO_2: 0.6), leading to strong optical confinement within the waveguide core. This confinement results in a small mode-field diameter, typically on the order of 1 µm, in contrast to the 10 µm mode-field diameter of standard single-mode fibers such as SMF28 [41]. While strong confinement is advantageous for compactness and enables dense integration of photonic components, it also introduces a substantial mode mismatch with optical fibers, significantly reducing coupling efficiency and increasing insertion loss.

To mitigate this issue, coupling structures are employed to gradually transform the tightly confined on-chip mode into a larger optical mode that better overlaps with the fiber mode. Several strategies have been developed for this purpose, among which the two most widely adopted are: **(i)** *edge coupling*, which typically employs inverse tapers and mode expanders to enlarge the optical mode at the chip facet, and **(ii)** *grating couplers*, which use surface-etched periodic structures to couple light vertically between the chip and the fiber. Each approach presents specific advantages and limitations depending on the application requirements, and their relative performance is discussed in the following sections.

Edge couplers Also referred to as butt-couplers, these operate by terminating the on-chip waveguide at the chip lateral facet, where the waveguide is adiabatically tapered to gradually expand the mode effective area. The objective is to enlarge the on-chip optical mode to better match the mode field diameter of an optical fiber, thereby reducing mismatch and minimizing coupling losses. In this configuration, light is injected directly into the waveguide through the polished edge of the chip, which requires careful dicing and cleaving to achieve smooth facets and reduce scattering losses due to surface roughness.

When tapering alone is insufficient to match the fiber mode, alternative external solutions can be used to reduce the mode-field diameter by focusing effect as shown in Figure 2.2. For example, lensed fibers that are terminated with a curved interface to produce a focusing effect [42], can reduce the optical spot size to typically between 2 µm and 6 µm, improving overlap with the confined waveguide mode. Alternatively, high-numerical-aperture fibers with smaller mode field diameters can be employed [43].

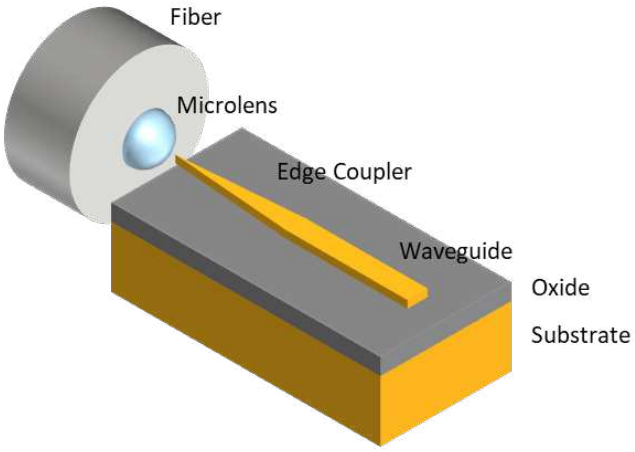

Figure 2.2: **Edge coupler.** Schematic of an inverse-taper edge coupler, where light is coupled using a microlensed fiber. Figure from ref. [50].

Edge coupling generally provides relatively low coupling losses. State-of-the-art values below 1 dB per facet have been reported for TFLN [44–47], around 0.7 dB for silicon photonics [48], and even lower for SiN platforms, where coupling losses below 0.1 dB have been demonstrated [49]. Moreover, edge couplers typically offer a broad coupling bandwidth, often exceeding 100 nm and are also less sensitive to polarization than grating couplers, making them particularly attractive for applications requiring polarization diversity.

However, edge coupling requires precise alignment between the fiber and the chip facet, as well as high-quality facet preparation often involving polishing and, in some cases, the use of anti-reflective coatings to suppress back reflections, which can be detrimental in specific applications. These requirements can complicate packaging and increase fabrication costs.

Grating couplers Grating couplers operate on the principle of diffraction from a periodic structure formed by alternating sections of high-index guiding material and lower-index cladding. With appropriate design, they can achieve efficient vertical coupling of light into and out of the waveguide at a well-defined angle with respect to the chip plane. The main design parameters include the grating period, the duty cycle (also known as the fill factor, i.e., the ratio between etched and unetched regions), and the etch depth, as shown in Figure 2.3a and in the zoomed view in Figure 2.3b. Physically, each grating period acts as a small scattering source that radiates light into free space. When the grating period is properly engineered, the scattered waves from each period interfere constructively at a specific angle, defined by the phase-matching condition.

A major advantage of grating couplers is their ability to couple light through the top surface of the chip, enabling wafer-level optical testing. This is particularly useful during fabrication, as it allows in-line wafer characterization without requiring chip dicing. It also facilitates coupling to multiple neighboring devices or to multiple structures on the same chip.

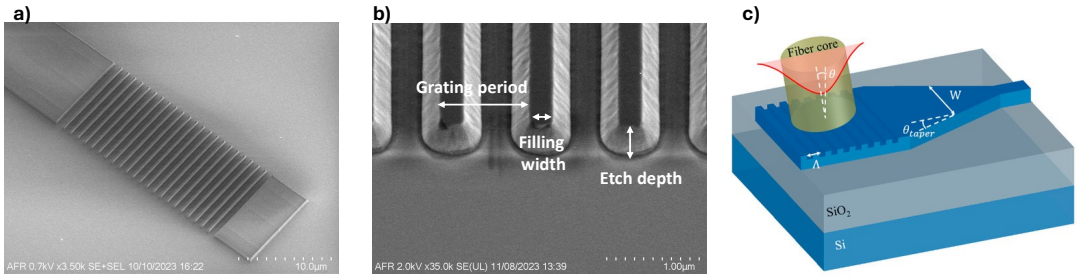

Figure 2.3: **Grating coupler. a)** and **b)** Scanning electron microscope image of a TFLN surface grating coupler showing key design parameters: period, duty cycle, and etch depth. **c)** Schematic of the coupling mechanism between an optical fiber and the grating coupler. Figure from ref. [51].

However, due to their diffraction-based nature, grating couplers exhibit strong wavelength dependence. At a fixed incident angle, the coupling bandwidth is typically limited to a few tens of nanometers. This narrow bandwidth arises directly from the phase-matching condition required for efficient diffraction-based coupling. Moreover, grating couplers generally exhibit higher coupling losses compared to edge-coupling techniques, mainly due to mode mismatch between the fiber and the emitted grating mode, penetration of light into the substrate, and back reflections from both the fiber and the grating interfaces [51]. In addition, practical implementations must account for fabrication constraints. For example, in TFLN platforms, limitations such as non-vertical sidewalls and minimum feature sizes imposed by the etching process (as shown in Figure 2.3b) can restrict design flexibility and impact coupler performance.

Despite these limitations, significant progress continues to be made. Recent demonstrations on silicon photonics have reported insertion losses as low as 0.34 dB with 1-dB bandwidths exceeding 20 nm [52], and several works have achieved sub-1 dB coupling losses [53–56]. Similarly, for TFLN, coupling losses below 1 dB with 1-dB bandwidths around 45 nm have been demonstrated [57].

2.1.3 Phase modulators

Phase modulation of light is a fundamental functionality in integrated photonic platforms, enabling a wide range of applications. Therefore, the availability of efficient and tunable phase modulators is of primary importance. Practical examples include coherent and incoherent optical communication protocols, frequency comb generation, stabilization of resonant structures such as ring resonators, and phase control in various types of interferometers, such as Mach–Zehnder interferometers (MZIs), discussed in the following section.

The variation of the optical phase can be induced by modifying the refractive index of the material where the light propagates, therefore inducing a variation of the effective refractive index (n_{eff}, defined in Eq. 2.3) experienced by the propagating mode in the integrated waveguide. This index change can be achieved by exploiting different physical mechanisms depending on the material platform. Some of the most relevant mechanisms are described below.

thermo-optic phase shifters (TPSs). In TPSs, the refractive index variation is induced by a local change in the waveguide temperature. This is typically achieved by placing a thin metal layer (e.g., Ti, TiN, or Au) in close proximity to the waveguide. When a current flows through the metal, resistive heating occurs via the Joule effect, locally increasing the waveguide temperature. The dissipated thermal power follows Ohm's law as $P = VI$. A key design trade-off exists in the heater–waveguide spacing: placing the heater closer improves modulation efficiency but increases propagation losses due to metal-induced absorption, whereas larger separations reduce heating efficiency.

A drawback of this approach is its relatively low modulation speed, since thermal processes are inherently slow. Typical modulation bandwidths do not exceed the tens of kilohertz range. Additionally, when multiple waveguide heaters are placed in close proximity, thermal crosstalk can occur [58, 59], where heat from one TPS diffuses into neighboring regions, unintentionally altering the operating point of nearby photonic components. Despite these limitations, TPSs remain widely used for setting and stabilizing static operating points in integrated devices, owing to their simplicity, CMOS compatibility, and compact design.

The efficiency of the thermo-optic effect is quantified by the *thermo-optic coefficient*, which relates the refractive index variation to the temperature change. Typical values at a wavelength of 1550 nm are:

- Silicon: $1.8 \times 10^{-4}\ \mathrm{K}^{-1}$ [60];
- SiN: $2.45 \times 10^{-5}\ \mathrm{K}^{-1}$ [61];
- LN: $3.95 \times 10^{-5}\ \mathrm{K}^{-1}$ [62].

EO phase modulators. In EO modulators, a phase shift is induced by an externally applied electric field that modifies the refractive index via the linear EO (Pockels) effect. This effect occurs only in crystalline non-centrosymmetric materials (i.e., materials that lack inversion symmetry) such as LN, barium titanate ($BaTiO_3$), and III–V semiconductors such as InP and aluminum gallium arsenide (AlGaAs), but is absent in centrosymmetric materials like silicon (Si). The refractive index change is proportional to the applied electric field:

$$\Delta n \propto r\mathbf{E}, \tag{2.7}$$

where r is the EO coefficient and $\mathbf{E}$ is the applied electric field. A detailed physical description of the Pockels effect is provided in Section 2.3.1.

The EO modulators based on the Pockels effect can, in principle, achieve extremely high modulation speeds, as the refractive index change follows the electric field nearly instantaneously. Two key figures of merit characterize their performance: the *3-dB modulation bandwidth*, defined as the frequency at which the modulation response drops to 50% of its maximum value, and the *half-wave voltage* V_π, the voltage required to induce a phase shift of π radians.

Recent advances have focused on optimizing electrode and circuit designs to maximize electric field overlap with the optical mode. TFLN modulators, in particular, have demonstrated modulation frequencies exceeding 100 GHz, with V_π values in the range of 1–3 V, depending on device geometry [63]. Thanks to their combination of large bandwidth, low drive voltage, and low optical loss, EO modulators are widely used in classical optical communication systems for high-speed data transmission at hundreds of gigabits per second. They are also increasingly relevant for quantum applications, where fast and low-noise phase control is critical.

p–n and p–i–n junction modulators. Another approach for phase modulation in integrated photonics is based on altering the effective refractive index via *free-carrier injection* or *depletion*. This mechanism is particularly important in silicon photonics, where the lack of the Pockels effect necessitates alternative high-speed modulation strategies. In this approach, compatible with standard CMOS fabrication, a p–n or p–i–n junction is integrated along the waveguide core. By applying a forward or reverse bias across the junction, carriers are injected or depleted in the guiding region, thereby changing the carrier concentration and the effective refractive index through the *plasma dispersion* effect.

However, this method introduces intrinsic trade-offs. Carrier injection increases free-carrier absorption (FCA), leading to additional optical losses [29]. To improve modulation efficiency, larger depletion regions and optimized junction geometries have been proposed [64, 65]. These designs, however, often trade lower drive voltages for increased capacitance, which limits the achievable modulation bandwidth.

Despite these challenges, state-of-the-art silicon p–i–n modulators have demonstrated modulation bandwidths in the tens of GHz range, with optimized designs achieving sub-volt V_π values [66]. This makes them a practical and scalable solution for integrated photonics, particularly in platforms where the Pockels effect is absent.

2.1.4 Mach–Zehnder interferometer

The MZI is one of the most widely used devices in photonic applications for controlling the intensity of an optical signal. Its operation relies on the principle of interference between two optical paths, enabling modulation of the output power by adjusting the relative phase difference between the arms.

As illustrated in Figure 2.4a, the MZI consists of an input optical beam splitter, typically implemented in integrated photonic platforms as a directional coupler or a multi-mode interferometer (MMI) coupler, which divides the incoming optical signal into two paths (arms). One or both arms contain a phase modulation section, and the paths are then recombined in a second coupler characterized by 2 input and 2 output ports (2×2 coupler), where interference occurs. The relative phase shift between the two arms, ϕ_1 and ϕ_2, can be introduced using any of the techniques described in the previous section such as thermo-optic, EO, or free-carrier-based modulation depending on the material platform and desired performance. Assuming symmetric interferometric paths and a balanced 2×2 coupler, the

output powers at the two output ports are given by:

$$P_{\text{OUT, bar}} = P_{\text{IN,1}} \sin^2\left(\frac{\Delta\phi}{2}\right) + P_{\text{IN,2}} \cos^2\left(\frac{\Delta\phi}{2}\right), \tag{2.8}$$

$$P_{\text{OUT, cross}} = P_{\text{IN,1}} \cos^2\left(\frac{\Delta\phi}{2}\right) + P_{\text{IN,2}} \sin^2\left(\frac{\Delta\phi}{2}\right), \tag{2.9}$$

where $P_{\text{IN,1}}$ and $P_{\text{IN,2}}$ are the optical input powers, and $\Delta\phi = \phi_1 - \phi_2$ is the differential phase shift between the two arms. By varying $\Delta\phi$, the output intensity can be tuned between a minimum (destructive interference) and a maximum (constructive interference), allowing precise control of the transmitted optical power. The two output ports exhibit complementary transmission as a function of $\Delta\phi$.

The performance of an MZI modulator can be characterized using several key figures of merit. One of the most important is the *extinction ratio (ER)*, which quantifies the modulator's ability to suppress the optical signal. It is typically expressed in decibels (dB) as the ratio between the maximum and minimum output powers:

$$\text{ER (dB)} = 10 \log_{10}\left(\frac{P_{\text{max}}}{P_{\text{min}}}\right).$$

In an ideal case, the MZI would exhibit an infinite ER ($P_{\text{min}} \to 0$), corresponding to complete destructive interference. In practice, however, the ER is finite due to imperfections such as unequal propagation losses between the two interferometer arms, unbalanced splitting ratios in the 2×2 couplers, or any fabrication-induced asymmetries. These imperfections prevent perfect destructive interference, thereby reducing the achievable ER and limiting performance in applications that require high contrast between optical states.

As an example, Figure 2.4b reports the measured output power of an MZI as a function of the applied thermal power for the integrated optical circuit developed in this work and described in Chapter 4. In this case, the recorded *ER* is about 20 dB, likely limited by the unbalanced optical path lengths of the two interferometric arms, which differ by approximately 1.3 cm.

Since an MZI modulator necessarily incorporates at least one phase modulator, other figures of merit are the *half-wave voltage* V_π and the *3-dB EO bandwidth*. These parameters are determined by the underlying modulation mechanism and the material platform, as discussed in the previous section, and they influence both the modulation speed and the efficiency of the MZI.

2.2 Technological platforms for integrated photonics

Beyond silicon photonics, research in integrated photonic platforms has expanded to a wide variety of material systems. The motivation behind this diversification is to overcome the intrinsic limitations of silicon and to meet the distinct performance requirements of various applications. Silicon suffers from several fundamental drawbacks: it is not suitable for light detection in the telecommunication band (its absorption range extends from approximately 200 nm to 1100 nm); it cannot efficiently emit light at any wavelength due to its indirect

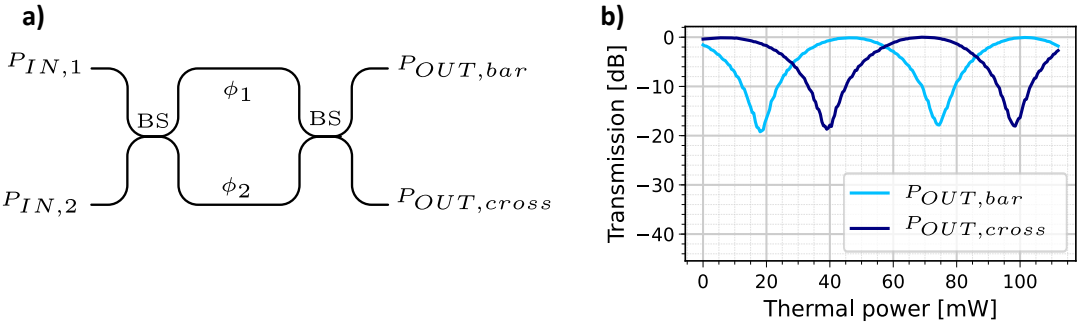

Figure 2.4: **Mach–Zehnder interferometer (MZI). a)** Schematic representation of an integrated MZI consisting of two 2×2 couplers and phase modulation sections in each arm. **b)** Measured output power as a function of the applied thermal power for a TFLN-based MZI device. The observed ER of approximately 20 dB is limited by the unbalanced arm lengths of about 1.3 cm.

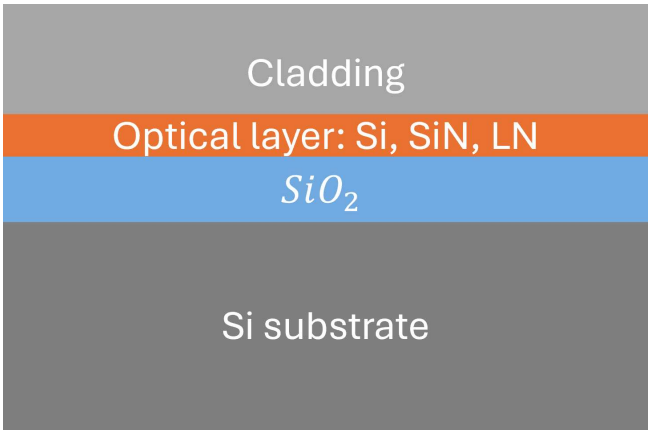

Figure 2.5: **Schematic of integrated photonic wafer structures.** Standard wafer structure typically involved in different technological platforms, such as SOI, SiN, and TFLN wafers.

bandgap; it lacks second-order optical nonlinearity because of its centrosymmetric crystal structure, and when its third-order nonlinearity is exploited, nonlinear absorption processes such as two-photon absorption (TPA) introduce additional losses and limit performance.

Silicon photonics, also known as silicon-on-insulator (SOI), is based on a multilayer stack comprising a thin crystalline silicon device layer, a buried oxide (BOX) layer of silicon dioxide, and a thick silicon substrate. Optical waveguides and components are patterned within the silicon device layer. In alternative material platforms, including those discussed below, the silicon device layer is replaced by a different optical material, while the underlying silicon substrate and BOX are often retained, as shown schematically in Figure 2.5. In most cases, a top cladding layer of silicon dioxide is also deposited to protect the optical layer.

In the following, some of the most widely adopted photonic integration platforms are compared: SOI, SiN, InP, and TFLN. Their main features, advantages, and limitations are discussed, highlighting their relevance for integrated photonics. Finally, Table 2.1 summarizes the main features and performance metrics of the described different platforms.

2.2.1 Silicon-on-Insulator

Silicon photonics rapidly gained importance thanks to its compatibility with CMOS fabrication processes. During the 2000s, it experienced significant acceleration, primarily driven by the growing demand for high-bandwidth optical communication. Today, silicon photonics represents the most mature and robust photonic platform, supported by a well-established ecosystem covering design, fabrication, and packaging. The availability of multi-project wafers (MPWs) services enables even small research groups without in-house cleanroom facilities to access advanced silicon photonic technologies at reduced cost. These services rely on verified process design kits (PDKs) that include standardized components and ensure reliable fabrication [67].

The optical properties of silicon components are primarily determined by the high refractive index contrast between silicon and silicon dioxide ($\Delta n \approx 2.04$), which allows for strong light confinement and highly compact devices. Typical propagation losses are in the range of 1–2 dB/cm, mainly caused by sidewall scattering, although the exact values depend strongly on fabrication quality and waveguide geometry. Silicon is transparent over the wavelength range from approximately 1.1 µm to 4 µm, covering the main telecommunication bands and part of the near-infrared spectrum.

Silicon photonics supports a wide variety of passive components, including waveguides, MMIs, grating couplers, and edge couplers. For active devices, silicon enables TPSs and p–i–n modulators based on the plasma dispersion effect. However, due to its indirect bandgap, silicon cannot provide light emission or optical amplification. To overcome this limitation, several approaches have been proposed, the most successful being the heterogeneous integration of silicon with III–V semiconductors [68].

Beyond linear applications, silicon is also widely exploited for its third-order optical nonlinearity ($\chi^{(3)}$, see Section 2.3.2). With proper engineering of dispersion and phase-matching conditions, silicon waveguides enable efficient nonlinear processes such as four-wave mixing (FWM), self-phase modulation (SPM), and third-harmonic generation (THG). The strong optical confinement achievable in integrated waveguides further enhances the efficiency of these effects. Such nonlinear capabilities allows for various applications, including wavelength conversion [69], entangled photon-pair generation [70], nonlinear microscopy [71], and soliton generation [72].

However, these nonlinear processes are fundamentally limited by optical absorption mechanisms in silicon. The most significant is *TPA* [73], in which two photons are simultaneously absorbed, exciting an electron from the valence band to the conduction band. This effect is particularly detrimental at telecommunication wavelengths (around 1.55 µm), where the combined energy of two photons exceeds the silicon bandgap. The generated free carriers induce both FCA [74] and free-carrier dispersion (FCD), which introduce additional losses and degrade the efficiency of nonlinear processes.

Finally, photodetectors operating at telecommunication wavelengths in the O (1310 nm) and C (1550 nm) bands can be monolithically integrated on silicon chips through CMOS-compatible epitaxial growth of germanium on silicon. These devices, typically realized as reverse-biased p–i–n junctions, provide broadband response (up to tens of GHz) and represent a reliable and cost-effective solution for optical receivers within the silicon photonics

platform [67].

2.2.2 Silicon nitride (SiN)

SiN has emerged as a complementary material to silicon in integrated photonics, offering key advantages such as ultra-low propagation loss, negligible TPA at telecommunication wavelengths, and a broad transparency window. Compared to silicon, SiN exhibits a lower refractive index contrast with a silicon dioxide cladding ($\Delta n \sim 0.6$). Although this results in larger device footprints, it provides important benefits, including improved fabrication tolerance, enhanced phase stability against imperfections, and reduced scattering losses from sidewall roughness [75]. As a result, SiN waveguides have demonstrated state-of-the-art propagation losses below 0.1 dB/cm [76].

These properties make SiN particularly well suited for applications requiring long optical paths, such as delay lines, large-scale interferometers, and high-Q resonators. Its wide bandgap suppresses TPA at telecom wavelengths, enabling high optical power handling, while the broad transparency window—from the visible (400 nm) to the mid-infrared (approximately 4 µm)—supports a wide range of applications. These include biochemical sensing [77], LiDAR systems [78], precision metrology [79], and nonlinear photonics, such as frequency comb generation [80] and optical parametric oscillation [81].

SiN is fabricated using CMOS-compatible processes and is often co-integrated with silicon on the same wafer. In such heterogeneous platforms, silicon is typically employed for compact active components (e.g., modulators and detectors), while SiN provides ultra-low-loss routing, long optical delays, and large-scale interferometric circuits [67].

2.2.3 Indium phosphide (InP)

In contrast to the other material platforms described in this Thesis, InP belongs to the family of III–V compound semiconductors. These materials play a fundamental role in photonics because, as it is a direct-bandgap semiconductors, it enable for direct light emission and optical amplification, functionalities that are not possible in Si, SiN, or TFLN.

InP has a direct bandgap of approximately 1.35 eV, corresponding to an emission wavelength of about 923 nm, and thus it remains transparent at longer wavelengths [82]. However, when InP is combined with quaternary alloys such as InGaAsP, the bandgap can be engineered to match the emission wavelengths required for the telecommunication windows around 1.3 µm and 1.55 µm [83]. By tailoring the composition and spatial distribution of these alloys, quantum wells or quantum dots can be formed, enabling further tuning of the electronic band structure and, consequently, of the emission wavelength. Using this approach, III–V heterostructures can emit across a broad spectral range from 0.9 μm up to about 2 μm [84]. Optical gain and lasing are achieved in InP photonic circuits by integrating wavelength-selective optical resonators, typically distributed Bragg reflector (DBR) [85] and distributed-feedback gratings [86].

Waveguides are formed by exploiting the refractive-index contrast between the different III–V alloys, as the refractive index is inversely related to the bandgap energy of the material. Typical waveguide structures use InP as the cladding, and InGaAsP as the core guiding

region [84], which having a lower bandgap, exhibits a higher refractive index. Propagation losses as low as 0.8 dB/cm have been reported [87]. Although this material system enables both passive and active components, they cannot rely on the same layer composition: active devices require a bandgap close to the operating wavelength to provide efficient optical gain under electrical pumping, while passive devices require a larger bandgap to ensure transparency and low propagation loss. The coexistence of these functionalities is enabled by multiple epitaxial growth and selective etching steps, which define the active and passive regions of the photonic circuit in different layers [88].

Fast phase modulation can be achieved in InP by exploiting the Pockels effect. Modulators employing travelling-wave electrodes can achieve bandwidths exceeding tens of GHz, with typical figures of merit $V_\pi L \approx 0.7\ \mathrm{V} \cdot \mathrm{cm}$ and bandwidth-length products around 16 GHz · cm [89, 90]. InP supports both second-order ($\chi^{(2)}$) and third-order ($\chi^{(3)}$) nonlinear effects. The second-order nonlinearity originates from its non-centrosymmetric crystal structure, enabling processes such as second-harmonic generation (SHG) and spontaneous parametric down-conversion (SPDC) [91]. InP also exhibits significant third-order nonlinearity characterized with $n_2 \approx 1.9 \times 10^{-17}\ \mathrm{m}^2/\mathrm{W}$ [92], enabling Kerr-based effects such as FWM and SPM [93]. Despite these capabilities, the dominant nonlinear loss mechanism is TPA, which can increase optical loss and degrade the performance of nonlinear process.

Since III–V materials are not naturally compatible with CMOS fabrication processes, modern photonic integration increasingly employs hybrid and heterogeneous integration techniques. These approaches combine the efficient light-generation and amplification capabilities of III–V materials with the low-loss routing and scalability of other platforms, such as Si and SiN [94].

2.2.4 Thin-film lithium niobate TFLN

LN ($LiNbO_3$, LN), first synthesized in 1949 [95], is one of the most versatile and widely used materials in photonics. It exhibits a broad transparency window from 350 nm to 5 µm covering the visible to the mid-infrared spectrum, and has a relatively high refractive index ($n \approx 2.2$ at 1550 nm).

LN is non-centrosymmetric and possesses excellent nonlinear properties. It exhibits large second-order nonlinear coefficients, enabling efficient $\chi^{(2)}$ processes such as Pockels effect modulation, SHG, and parametric down-conversion. In addition, LN features a third-order nonlinear coefficient ($n_2 \approx 1.8 \times 10^{-19}\ \mathrm{m}^2/\mathrm{W}$), comparable to SiN ($n_2 \approx 2.5 \times 10^{-19}\ \mathrm{m}^2/\mathrm{W}$) and approximately 20 times smaller than that of silicon ($n_2 \approx 4.5 \times 10^{-18}\ \mathrm{m}^2/\mathrm{W}$) [96], as outlined in Table 2.1. Due to its wide indirect bandgap, LN does not provide light emission or photodetection and is therefore mainly employed for passive and nonlinear optical functionalities.

Bulk LN. Initially, LN was used in bulk crystal form for second-order nonlinear optics [97], EO modulation [98], and acousto-optic beam deflection [99]. It remains an important material for high-power optical systems operating in free space, where its large optical aperture and high damage threshold are advantageous.

Early integrated LN. One of the LN key properties is its large linear EO (Pockels) coefficient ($r_{33} \approx 30$ pm/V), which enables high-speed and broad bandwidth modulation. In the 1990s, integrated waveguides were fabricated by titanium indiffusion [100], leading to the first integrated EO modulators [101].

Although these devices were produced using microfabrication processes, the weak refractive index contrast between the core and the cladding limited light confinement. Consequently, these devices required large footprints, with bending radii on the order of centimeters that are much larger than those achievable in other integrated photonics technologies.

Thin-film lithium niobate (TFLN). A major advancement came with the development of thin-film lithium niobate on insulator (LNOI) [102]. In this platform, a thin LN layer is bonded onto a SiO_2 substrate, and waveguides are defined by direct etching of the LN film. The resulting higher refractive index contrast compared to bulk or diffused LN waveguides allows for strong mode confinement, enhanced overlap between optical and electrical fields, and significantly reduced device dimensions. This enables modulators with lower driving voltages (V_π) and higher bandwidths [63, 103]. One of the main technological challenges remains LN etching, as sidewall roughness contributes to scattering losses. Nevertheless, state-of-the-art devices achieve propagation losses as low as $0.02\,\mathrm{dB\,cm^{-1}}$ [104].

Another unique feature of LN is its ferroelectric nature. Indeed, the orientation of ferroelectric domains can be engineered and inverted by applying a strong electric field, creating a spatially periodic modulation of the sign of the nonlinear susceptibility $\chi^{(2)}$ along the propagation direction of the waveguide. The domain inversion can be designed such that the phase of the generated second-harmonic field is effectively reset by π at each poling period, thereby compensating for the phase mismatch between the interacting waves and allowing the nonlinear signal to build up constructively along the propagation length. This technique is known as quasi-phase matching (QPM), and greatly enhances conversion efficiency for SHG, optical parametric oscillation, and frequency conversion. periodically poled lithium niobate (PPLN) has long been used in bulk form, but since 2016, periodic poling has also been demonstrated in TFLN [105–107], enabling highly efficient on-chip nonlinear devices. The strong optical confinement in TFLN waveguides significantly enhances optical intensities, further improving nonlinear conversion efficiency.

The combination of a wide transparency window, strong EO response, high nonlinear coefficient, and the capability to implement periodic poling in thin-film form makes LN one of the leading platforms for next-generation integrated photonics. Its applications span high-speed EO modulators, phase and amplitude modulators, second-harmonic and frequency converters, frequency combs, quantum light sources, and precision metrology.

2.3 Optical nonlinearities

This section introduces the theoretical background necessary to understand the physical effects exploited by a few key optical components used in the experimental demonstrations of quantum applications presented in the following chapters. I focus on third-order nonlinear

Property	SOI	SiN	InP	TFLN
Refractive index	~ 3.48	~ 2.0	~ 3.17	~ 2.2
Transparency window	$1.1 - 4\,\mu m$	$0.4 - 4\,\mu m$	$0.9 - 2\,\mu m$	$0.35 - 5\,\mu m$
Propagation loss	$1 - 2\,dB/cm$	$< 0.1\,dB/cm$	$\sim 0.8\,dB/cm$	$0.02 - 0.1\,dB/cm$
Second-order nonlinearity $\chi^{(2)}$ (larger Pockels coefficient)	No	No	$r_{41} \approx 1.2\,pm/V$	$r_{33} \approx 30\,pm/V$
Third-order nonlinearity (Nonlinear Index n_2)	$4.5 \times 10^{-18}\ m^2/W$	$2.5 \times 10^{-19}\ m^2/W$	$1.9 \times 10^{-17}\ m^2/W$	$1.8 \times 10^{-19}\ m^2/W$
TPA and FCA	Yes	No	Yes	No
Light emission / amplifications	No	No	Yes	No
Photodetection	$200 - 1100\,nm$	No	$400 - 920\,nm$	No
CMOS compatibility	Yes	Yes	No	No

Table 2.1: **Comparison of key properties of different integrated photonic platforms.** The reported information summarizes the main features discussed in the section 2.2. Representative values are given at 1550 nm wavelength.

processes in silicon integrated waveguides employed for the generation of entangled photon pairs, and on second-order nonlinearities in LN, which are used for ultrafast optical phase modulation. Before addressing these specific effects, the general concepts of nonlinear optics are introduced.

Nonlinear optics studies light–matter interactions in which the response of a medium depends nonlinearly on the intensity of the applied electromagnetic field. Under typical illumination conditions with incoherent or low-intensity light sources, nonlinear effects are negligible. However, the invention of the laser in 1960 provided intense and coherent light sources [108], enabling the systematic exploration and technological exploitation of nonlinear optical phenomena.

When light propagates through a material, its interaction can be described by the induced dipole moment per unit volume, given by the polarization vector $\mathbf{P}$. In the simplest case, the polarization depends linearly on the electric field $\mathbf{E}$:

$$\mathbf{P} = \varepsilon_0 \chi^{(1)} \mathbf{E}, \tag{2.10}$$

where ε_0 is the vacuum permittivity and $\chi^{(1)}$ is the linear susceptibility. This approximation holds for weak fields. For stronger fields, however, higher-order terms must be included for an accurate description of light–matter interactions. The polarization can thus be expanded as a power series in $\mathbf{E}$:

$$\mathbf{P} = \varepsilon_0 \left(\chi^{(1)} \mathbf{E} + \chi^{(2)} \mathbf{E}^2 + \chi^{(3)} \mathbf{E}^3 + \cdots \right), \tag{2.11}$$

where $\chi^{(n)}$ is the n^{th}-order nonlinear susceptibility, described by a tensor of rank $n+1$. These higher-order terms are responsible for the wide variety of nonlinear optical effects observed in different materials, although contributions beyond third order are typically negligible

due to their weak magnitude. Nonlinearities associated with $\chi^{(2)}$ give rise to second-order effects, which scale quadratically with the electric field amplitude and occur only in non-centrosymmetric crystals. While nonlinearities associated with $\chi^{(3)}$ give rise to third-order effects, which can occur in both centrosymmetric and non-centrosymmetric media, making them relevant for platforms such as silicon photonics.

2.3.1 Second-order nonlinearities in lithium niobate

LN has been widely exploited for decades thanks to its exceptional second-order nonlinear properties. Its second-order susceptibility tensor contains relatively large coefficients [109], making LN one of the most efficient materials for EO and nonlinear optical processes such as SHG and SPDC [110]. Among these effects, one of the most technologically important is the modulation of the optical field phase induced by an external electric field, with a frequency (ω_{RF}) at least 10^{-3} lower than the optical one (ω_0). This phenomenon, known as the EO effect, arises from the Pockels effect, whereby the applied electric field alters the effective refractive index experienced by the propagating optical mode.

Formally, this can be described by expanding the polarization vector to include second-order terms. Considering only the i-th component of the polarization, it can be expressed as:

$$P_i(\omega_0) = \varepsilon_0 \chi^{(1)}_{ij} E_j(\omega_0) + \varepsilon_0 \chi^{(2)}_{ijk} E_j(\omega_0) E_k(\omega_{RF}) + \cdots, \tag{2.12}$$

where $\chi^{(1)}_{ij}$ and $\chi^{(2)}_{ijk}$ are the linear and second-order susceptibility tensor coefficients, respectively. If $E_k(\omega_{RF})$ corresponds to a radio frequency (RF) field with $\omega_{RF} \ll \omega_0$, the second-order term acts as a perturbation to the linear optical response, yielding:

$$P_i(\omega_0) = \varepsilon_0 \left[\chi^{(1)}_{ij} + \chi^{(2)}_{ijk} E_k(\omega_{RF}) \right] E_j(\omega_0). \tag{2.13}$$

Hence, the applied electric field alters the material's linear permittivity, which can be written as:

$$\varepsilon^{\text{eff}}_{ij} = \varepsilon_{ij} + \Delta\varepsilon_{ij}, \tag{2.14}$$

where the unperturbed permittivity and its change due to the applied field are given by:

$$\varepsilon_{ij} = 1 + \chi^{(1)}_{ij}, \qquad \Delta\varepsilon_{ij} = \chi^{(2)}_{ijk} E_k(0).$$

Historically, the modulation is described in terms of the *impermeability tensor* $\eta_{ij} = (\varepsilon^{-1})_{ij}$ [111]. In this formalism, the change in impermeability due to the applied field is expressed as:

$$\Delta\eta_{ij} = r_{ijk} E_k(\omega_{RF}), \tag{2.15}$$

where r_{ijk} is the linear EO (Pockels) tensor. The relationship between r_{ijk} and the second-order susceptibility is:

$$\Delta\eta_{ij} = \Delta\left(\frac{1}{\varepsilon_{ij}}\right) = -\frac{\Delta\varepsilon_{ij}}{\varepsilon^2_{ij}} = -\frac{\chi^{(2)}_{ijk} E_k(\omega_{RF})}{\varepsilon^2_{ij}}. \tag{2.16}$$

Since the dielectric permittivity tensor ε_{ij} is real and symmetric, it can be diagonalized by choosing suitable principal axes:

$$\varepsilon_{ij} = \varepsilon_i \, \delta_{ij},$$

where ε_i are the principal permittivities and δ_{ij} is the Kronecker delta. Due to the symmetry properties of ε_{ij}, the EO tensor r_{ijk} is symmetric in its first two indices. For practical use, the third-rank tensor r_{ijk} is often expressed in contracted notation as a two-dimensional matrix r_{ij}.

Overall, the change in refractive index due to the applied electric field can be obtained from the impermeability tensor:

$$\Delta\left(\frac{1}{\varepsilon_i}\right) = \Delta\left(\frac{1}{n_i^2}\right) = -2\frac{\Delta n_i}{n_i^3} = r_{ij} E_j(\omega_{RF}). \tag{2.17}$$

From this, the induced refractive index change is given by:

$$\Delta n_i = -\frac{1}{2} n_i^3 \, r_{ij} \, E_j(\omega_{RF}). \tag{2.18}$$

This relationship forms the basis for EO modulators, particularly in TFLN, as discussed in Chapter 4. It directly links the applied electric field to the change in refractive index.

In the telecom band, lithium niobate exhibits relatively large EO coefficients ($r_{33} \approx 31\,\mathrm{pm\,V^{-1}}$), enabling highly efficient modulators. In integrated photonics, careful electrode design allows operation up to hundreds of GHz. The intrinsic bandwidth of the Pockels effect itself is much higher and is not the limiting factor; rather, the main constraint lies in efficiently delivering the high-frequency electrical signals across the optical waveguide.

In recent years, there has been growing interest in materials exhibiting even higher EO performance than TFLN. A notable example is barium titanate (BTO), which possesses one of the largest EO coefficients known ($r_{42} \approx 923\,\mathrm{pm\,V^{-1}}$). Such high values make BTO highly promising for both high-speed modulation and second-order nonlinear processes. Current research is focused on developing wafer-scale growth of crystalline BTO on silicon substrates, paving the way toward scalable and high-performance hybrid photonic platforms [112].

2.3.2 Third-order nonlinearities in Silicon

Silicon, in the crystallographic configuration used in SOI wafers for integrated photonics, is a centrosymmetric material. As a result, its second-order susceptibility is null ($\chi^{(2)} = 0$). However, silicon exhibits a relatively large third-order susceptibility $\chi^{(3)}$, more than two orders of magnitude higher than that of silica glass [113], the material used in standard telecommunication optical fibers. This strong $\chi^{(3)}$ response enables a wide range of third-order nonlinear effects in silicon waveguides and resonant structures, including SPM, cross-phase modulation (XPM), FWM, and third-harmonic generation (THG).

The nonlinear polarization of the medium for the i-th field component can be written as

$$P_i = \varepsilon_0 \chi_{ij}^{(1)} E_j + \varepsilon_0 \chi_{ijkl}^{(3)} E_j E_k E_l + \cdots, \tag{2.19}$$

where the second term corresponds to the third-order nonlinear processes. In general, three frequency components $\omega_1, \omega_2, \omega_3$ can interact to generate a fourth component ω_4, subject to energy conservation:

$$\omega_4 = \pm\omega_1 \pm \omega_2 \pm \omega_3, \tag{2.20}$$

and momentum conservation (phase matching):

$$k_4 = \pm k_1 \pm k_2 \pm k_3, \tag{2.21}$$

where k_i are the propagation constants of the interacting electromagnetic waves. Because the guided modes in silicon waveguides experience chromatic dispersion, and because the interacting optical frequencies may be widely separated, satisfying the phase-matching condition is generally nontrivial. As a result, the waveguide geometry must be carefully engineered to enable efficient nonlinear interactions.

For simplicity, consider an optical field composed of three frequency components with the same polarization, which can be expressed in scalar form as

$$E(t) = E_1 e^{-i\omega_1 t} + E_2 e^{-i\omega_2 t} + E_3 e^{-i\omega_3 t} + \text{c.c.}$$

Substituting this expression into Eq. (2.19), the resulting third-order nonlinear polarization contains multiple terms, each of which can be associated with a specific nonlinear effect:

$$\begin{aligned}
P^{(3)}(t) = {} & 3\,\varepsilon_0\chi^{(3)}|E_1|^2 E_1\, e^{-i\omega_1 t} + \text{c.c.} && \text{(SPM)} \\
& + 6\,\varepsilon_0\chi^{(3)}|E_2|^2 E_1\, e^{-i\omega_1 t} + \text{c.c.} && \text{(XPM)} \\
& + \varepsilon_0\chi^{(3)} E_1^3\, e^{-i3\omega_1 t} + \text{c.c.} && \text{(THG)} \\
& + 3\,\varepsilon_0\chi^{(3)} E_1 E_2 E_3\, e^{-i(\omega_1+\omega_2+\omega_3)t} + \text{c.c.} && \text{(Sum-frequency)} \\
& + 3\,\varepsilon_0\chi^{(3)} E_1 E_2 E_3^*\, e^{-i(\omega_1+\omega_2-\omega_3)t} + \text{c.c.} && \text{(FWM).}
\end{aligned} \tag{2.22}$$

Among these effects, FWM is of particular relevance for quantum optics, as it enables the generation of entangled photon pairs in the telecommunication band, which is essential for quantum communication applications.

FWM, in its spontaneous form spontaneous four-wave mixing (SFWM), the degenerate-pump configuration requires only a single pump field injected into the waveguide. In this case, two pump photons at frequency ω_P are annihilated, and a signal–idler photon pair is created at frequencies symmetrically detuned from the pump to satisfy energy conservation:

$$2\hbar\omega_P = \hbar\omega_S + \hbar\omega_I. \tag{2.23}$$

This process is illustrated schematically in Figure 2.6. In practice, efficient generation in the telecom band is achieved through dispersion engineering of the waveguide, since the pump, signal, and idler wavelengths are spectrally close. In this work, SFWM is exploited to generate time-bin entangled photon pairs, as presented in Chapter 5 and later used in the QKD demonstrations of Chapter 6.

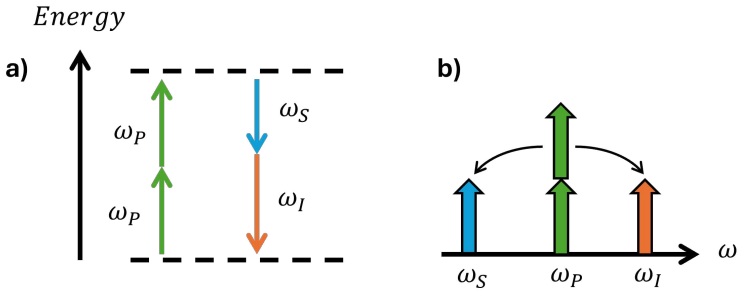

Figure 2.6: **Spontaneous four-wave mixing (SFWM)** Schematic representation of the SFWM process. **a)** Energy-level diagram showing how two pump photons at frequency ω_P are annihilated to generate a signal–idler photon pair at frequencies ω_S and ω_I, symmetrically detuned from the pump. **b)** Corresponding spectral representation illustrating the symmetric detuning of the signal and idler around the pump frequency.

The spontaneous nature of SFWM arises from vacuum fluctuations, which provide the initial seed for the creation of signal–idler photon pairs in the presence of the strong pump field. When phase matching is satisfied, this leads to efficient generation of quantum-correlated photons directly on chip. A quantum mechanical description of SFWM involves both the linear and nonlinear parts of the Hamiltonian:

$$H_L = \int dk\, \hbar\omega_k\, a_k^\dagger a_k, \tag{2.24}$$

$$H_{\mathrm{NL}} = -\int dk_1\, dk_2\, dk_3\, dk_4\, S(k_1,k_2,k_3,k_4)\, a_{k_1}^\dagger a_{k_2}^\dagger a_{k_3} a_{k_4} + \mathrm{H.c.}, \tag{2.25}$$

where $a_i^\dagger$ and a_i are the photon creation and annihilation operators, and $S(k_1,k_2,k_3,k_4)$ is the nonlinear coupling coefficient, which depends on the effective mode area and the phase-matching conditions. As described in Ref. [114], for the case of a degenerate two-photon pump, the generated signal and idler power scales as

$$P_{S,I} = \frac{\hbar\omega_P}{\mathcal{T}}\,(\gamma P_P L)^2, \tag{2.26}$$

where P_P is the pump power, L is the waveguide length, and γ is the nonlinear parameter:

$$\gamma = \frac{2\chi^{(3)}\omega_P}{n^2\epsilon_0 c^2 A_{\mathrm{eff}}}, \tag{2.27}$$

with A_{eff} the effective modal area. The factor $\mathcal{T}$ accounts for dispersion and the effective phase-matching bandwidth:

$$\mathcal{T} \approx \frac{3}{2}\sqrt{2\pi|\beta_2(\omega_P)|L}, \tag{2.28}$$

where $\beta_2(\omega_P)$ is the group-velocity dispersion at the pump frequency.

Overall, the advantages of integrated waveguides can be understood in terms of the nonlinear parameter γ. Even when the available optical pump power is limited, the strong optical confinement achievable in integrated platforms, especially in silicon due to its high refractive index contrast, leads to very small effective mode areas. This confinement results in high optical intensities and therefore large effective nonlinear interactions, enabling efficient photon-pair generation in compact on-chip devices.

Chapter 3

Introduction to quantum photonic technologies

This chapter provides an overview of quantum photonic technologies, spanning from the underlying theoretical principles to their practical implementation challenges. It begins with a review of the key concepts of quantum mechanics that form the basis of modern quantum technologies. Particular emphasis is placed on the description of quantum states, their unique properties, and the concept of entanglement, which represents one of the most powerful resources for quantum information processing. In this context, different approaches for encoding quantum information into photonic states are introduced. Photons are presented as natural carriers of quantum information, owing to their robustness, weak interaction with the environment, and suitability for long-distance transmission.

Building on these foundations, the chapter outlines the main applications of quantum technologies, including quantum computation, communication, and sensing, with a particular focus on their photonic implementations. Then, the fundamental properties of entanglement are described, highlighting how they can be exploited in quantum communication systems. Such properties enable protocols and functionalities that cannot be achieved using classical approaches.

Finally, the chapter presents a detailed analysis of quantum telecommunication systems based on temporal encoding of photons. Both the theoretical framework and the intrinsic limitations of current approaches are analyzed. This discussion establishes the foundation for the research presented in this PhD work, which aims to overcome these limitations.

3.1 The Qubit

Classical information processing relies on the manipulation of bits, the fundamental units of information, which can assume one of two possible values, conventionally denoted as 0 and 1. In the framework of quantum technologies, the analogue of the classical bit is the quantum bit, or *qubit*. Like a bit, a qubit is also defined on a two-level system with logical states $|0\rangle$ and $|1\rangle$. However, the essential difference is that a qubit is not restricted to being in one of these states, but can exist in a coherent superposition of both.

Formally, a qubit $|\psi\rangle$ is described by a vector in a two-dimensional Hilbert space spanned by the computational basis $\{|0\rangle, |1\rangle\}$:

$$|\psi\rangle = \alpha |0\rangle + \beta |1\rangle ,$$

where $\alpha, \beta \in \mathbb{C}$ are complex coefficients. The squared amplitudes $|\alpha|^2$ and $|\beta|^2$ represent the probabilities of measuring the system in state $|0\rangle$ or $|1\rangle$, respectively. A state of this form is referred to as a *pure state*, and the normalization condition $|\alpha|^2 + |\beta|^2 = 1$ ensures that the total probability of obtaining either outcome is unity.

More generally, a quantum system may not be in a well-defined pure state, but rather in a statistical mixture of several possible states, each occurring with a certain probability p_i. Such states are described by a *density matrix* ρ, which generalizes the notion of a quantum state. Mixed states are represented as convex combinations of pure states:

$$\rho = \sum_i p_i \ |\psi_i\rangle \langle\psi_i| ,$$

where $\sum_i p_i = 1$ and p_i denotes the probability that the system is in the state $|\psi_i\rangle$. Pure states are a special case, corresponding to density matrices of the form $\rho = |\psi\rangle \langle\psi|$.

Beyond the computational basis $\{|0\rangle, |1\rangle\}$, it is often convenient to work in alternative orthonormal bases. One example is the *diagonal basis*, composed of $\{|+\rangle, |-\rangle\}$, defined as

$$|+\rangle = \tfrac{1}{\sqrt{2}}(|0\rangle + |1\rangle), \qquad |-\rangle = \tfrac{1}{\sqrt{2}}(|0\rangle - |1\rangle).$$

Another example is the *circular (rotational) basis*, composed of $\{|R\rangle, |L\rangle\}$, given by

$$|R\rangle = \tfrac{1}{\sqrt{2}}(|0\rangle + i\,|1\rangle), \qquad |L\rangle = \tfrac{1}{\sqrt{2}}(|0\rangle - i\,|1\rangle).$$

A geometric representation of a qubit is provided by the *Bloch sphere*. Any pure qubit state can be expressed as

$$|\psi\rangle = \cos\left(\tfrac{\theta}{2}\right) |0\rangle + e^{i\phi} \sin\left(\tfrac{\theta}{2}\right) |1\rangle ,$$

with spherical coordinates $\theta \in [0, \pi]$ and $\phi \in [0, 2\pi]$. On the Bloch sphere, shown in Figure 3.1, θ determines the relative weight of $|0\rangle$ and $|1\rangle$ (latitude), while ϕ specifies their relative phase (longitude). The north and south poles correspond to the computational states $|0\rangle$ and $|1\rangle$, whereas states on the equator represent equal-weight superpositions differing only by the relative phase.

A qubit can be physically realized in various two-level quantum systems. In photonics, qubits can be encoded using several degrees of freedom of photons, such as polarization, time, frequency, or spatial modes, as described in Section 3.2. This versatility represents a major advantage compared to other physical implementation platforms. Alternative realizations include spin states of electrons or nuclei in a magnetic field, as well as electronic states of atoms or ions [115].

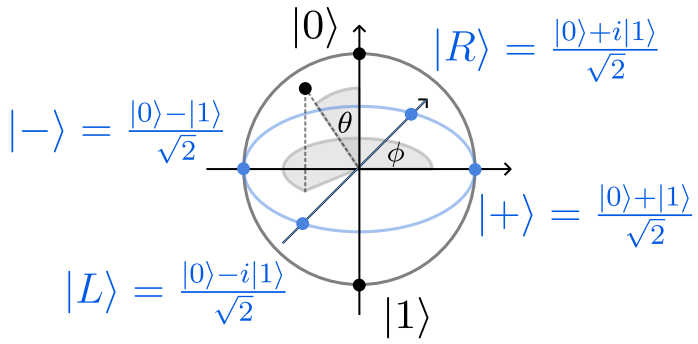

Figure 3.1: **Bloch sphere.** Graphical representation of a single qubit's quantum state. Points on the surface of the sphere correspond to a pure state in a two-dimensional Hilbert space, while points inside represent mixed states.

3.1.1 Multiple Qubits and Entanglement

When multiple qubits are combined into a composite quantum system, the overall state is described within the tensor product of the individual Hilbert spaces of each qubit. Thus, for an n-qubit system, the most general pure state can be written as

$$|\psi\rangle = \sum_{i=0}^{2^n-1} \alpha_i \, |i\rangle \,, \tag{3.1}$$

where $\{|i\rangle\}$ denotes the computational basis of the 2^n-dimensional Hilbert space, and the complex coefficients α_i satisfy the normalization condition $\sum_i |\alpha_i|^2 = 1$.

This highlights a fundamental difference between classical and quantum information. A classical register of n bits can store only one of the 2^n possible configurations at any given time. In contrast, an n-qubit quantum register can exist in a coherent superposition of all 2^n basis states simultaneously, with complex amplitudes $\{\alpha_i\}$. Before measurement, the quantum system is therefore described by a continuum of possible states, and a measurement collapses the superposition to one of the basis states with probability $|\alpha_i|^2$ [115].

A quantum composite state is said to be *separable* if it can be written as the tensor product of the states of its subsystems:

$$|\psi\rangle = |\psi_A\rangle \otimes |\psi_B\rangle \,, \qquad |\psi_A\rangle \in \mathcal{H}_A, \; |\psi_B\rangle \in \mathcal{H}_B. \tag{3.2}$$

In this case, the two subsystems are independent, and measurements performed on one have no influence on the other. Conversely, when a state cannot be written in this form—i.e., it is not expressible as a tensor product of subsystem states—it is said to be *entangled*. Entangled states exhibit correlations between measurement outcomes that cannot be reproduced by any classical statistical model, a feature famously highlighted by the Einstein–Podolsky–Rosen (EPR) paradox [116]. Such nonclassical correlations constitute one of the most powerful and counterintuitive resources of quantum mechanics.

A particularly important illustration of entanglement arises in the case of two qubits. Among all possible two-qubit states, a fundamental role is played by the *Bell states*, which

form a complete orthonormal basis of maximally entangled states:

$$\left|\Phi^+\right\rangle = \frac{1}{\sqrt{2}}\left(|00\rangle + |11\rangle\right), \qquad \left|\Phi^-\right\rangle = \frac{1}{\sqrt{2}}\left(|00\rangle - |11\rangle\right),$$
$$\left|\Psi^+\right\rangle = \frac{1}{\sqrt{2}}\left(|01\rangle + |10\rangle\right), \qquad \left|\Psi^-\right\rangle = \frac{1}{\sqrt{2}}\left(|01\rangle - |10\rangle\right). \tag{3.3}$$

These states cannot be expressed as tensor products of single-qubit states and therefore represent genuine quantum entanglement. They also demonstrate non-classical correlations: a measurement performed on one qubit instantaneously determines the corresponding outcome for the other, independently of their spatial separation.

Entanglement is a key resource enabling a wide range of quantum technologies [117]. The fundamental principles underlying its use in quantum information processing are introduced in the following Section 3.4.

3.2 Qubit encoding using photons

In principle, a qubit can be encoded in any two-level quantum system, such as the spin of an electron, the excitation of an atom, or similar degrees of freedom [115]. The choice of encoding depends on the specific requirements of the quantum application, including the coherence time of the quantum state, environmental stability, implementation complexity, scalability to multiple qubits, and available methods for state manipulation.

In the case of light, the wave-particle duality of photons allows them to exhibit particle-like behavior, formalized through the quantization of the electromagnetic field [118]. The energy of the field is carried in discrete quanta called photons, with each photon representing a single quantum of the electromagnetic field. Photons can therefore serve as carriers of quantum information. Photons are particularly advantageous for quantum technologies, as they can propagate over long distances at the speed of light with low loss and minimal interaction with the environment. Their energy is significantly larger than the thermal noise scale $k_B T$, allowing room-temperature operation and making them naturally robust against noise and decoherence. In addition, photonic systems offer compatibility with existing optical network infrastructures, extremely low decoherence, and the possibility of high-speed transmission [14, 119]. These features make photons ideal carriers for the practical implementation of quantum protocols.

In this section, I provide an overview of the main degrees of freedom of light that can be exploited to encode qubits and transmit quantum information. These include temporal, polarization, spatial, and frequency encodings.

3.2.1 Temporal encoding

The temporal encoding of entangled states was first demonstrated by Franson in 1989 [120]. He proposed a scheme that exploits the intrinsic temporal uncertainty in the emission time of photon pairs generated by a nonlinear optical source as schematically shown in Figure 3.2a. Because the exact emission time of each pair is indeterminate, sending the two photons

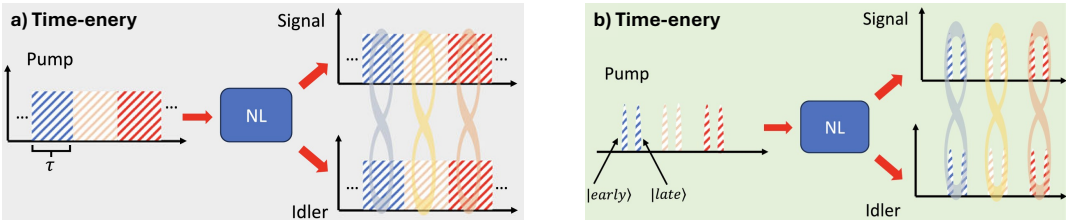

Figure 3.2: **Temporal encoding. a)** Time-energy entanglement representation in which photon pairs are generated with a large emission time uncertainty (illustrated by the colored boxes), much longer than their individual coherence time (represented by a single colored box). **b)** Time-bin entanglement representation in which only one of the two pump pulses generates an entangled photon pair, producing a superposition of emission in the early and late time-bins. Figures from Ref. [128].

through spatially separated, unbalanced interferometers allows their wavefunctions to form superpositions in the temporal domain, thereby realizing *time-energy entanglement*.

A later variation, introduced in 1999 by Gisin *et al.*, is known as *time-bin entanglement* [121]. In this scheme, the long temporal uncertainty of the source is replaced by a well-defined probabilistic emission in one of two discrete time slots, or *bins*, denoted $|early\rangle$ or $|0\rangle$ and $|late\rangle$ of $|1\rangle$ as schematically shown in Figure 3.2b. The photon pair is thus created in a coherent superposition of these two bins, forming the entangled state:

$$|\psi\rangle = \frac{1}{\sqrt{2}}\left(|00\rangle + |11\rangle\right). \tag{3.4}$$

In both approaches, temporal-state analysis is performed using unbalanced interferometers. The temporal delay is chosen to be shorter than the coherence time of the source in the case of time-energy entanglement, or equal to the time-bin separation in the case of time-bin encoding. A more detailed discussion of the behavior, features, and experimental implementation of time-energy and time-bin encoding is presented in Section 3.5.

The manipulation and decoding of temporal states is straightforward and can be achieved by varying the relative phase between the two interferometer arms using phase modulators. Temporal encoding is particularly suited for quantum communication over existing fiber-optic networks, as it is inherently robust against environmental perturbations. In contrast to polarization encoding, which is susceptible to polarization-mode dispersion in optical fibers, temporal encoding offers superior stability over long distances, making it ideal for QKD implementations [122, 123]. Moreover, time-bin entanglement supports advanced functionalities such as high-dimensional quantum encoding [124] and hyperentanglement across multiple degrees of freedom [125, 126]. Additionally, pulsed pumping in time-bin schemes provides a natural means for temporal synchronization among users, establishing a shared timing reference between communicating parties [127]. At the detection stage, single-photon detectors must be capable of resolving events separated by the interferometer delay, introducing a trade-off between repetition rate and timing resolution.

3.2.2 Polarization encoding

The direction of a light wave's electric field vector is defined by its polarization, which always lies in a plane perpendicular to the direction of propagation. Within this plane, two orthogonal directions can be chosen to define a basis of polarization states. In the quantum regime, where light is described in terms of photons, these two orthogonal states form a natural two-level system suitable for qubit encoding.

Historically, these two orthogonal polarization states are chosen as horizontal and vertical, denoted by $|H\rangle$ and $|V\rangle$, forming the *computational basis*. A single-photon polarization qubit can then be expressed as

$$|\psi\rangle = \alpha\,|H\rangle + \beta\,|V\rangle \tag{3.5}$$

Beyond the computational basis, other commonly used polarization bases are directly derived from different orientations of the electric field. The *diagonal basis*, $\{|D\rangle, |A\rangle\}$, corresponding to linear polarization at $+45^\circ$ and -45°:

$$|D\rangle = \tfrac{1}{\sqrt{2}}(|H\rangle + |V\rangle), \qquad |A\rangle = \tfrac{1}{\sqrt{2}}(|H\rangle - |V\rangle),$$

and the *circular basis*, $\{|R\rangle, |L\rangle\}$, corresponding to right- and left-handed circular polarization:

$$|R\rangle = \tfrac{1}{\sqrt{2}}(|H\rangle + i\,|V\rangle), \qquad |L\rangle = \tfrac{1}{\sqrt{2}}(|H\rangle - i\,|V\rangle).$$

Polarization encoding is widely used in quantum communication for several reasons. The polarization of photons is easy to manipulate and analyze using standard optical elements such as half-wave plates, quarter-wave plates, and polarization beam splitters. These components allow precise control of the quantum state with minimal effort, are inexpensive, and readily available. Polarization-entangled photon pairs are typically generated using nonlinear crystals with birefringence, exploiting type-II phase-matching in second-order nonlinear processes [129], which is shown in Figure 3.3. Polarization qubits are also robust against environmental perturbations, which has enabled their extensive use in free-space quantum links and QKD demonstrations [130, 131].

However, in optical fiber systems, polarization states are affected by random rotations due to fiber birefringence, which originates from manufacturing imperfections and external stresses [39]. Compensation strategies are therefore required to reliably recover the transmitted qubits [132]. A further limitation of polarization encoding is that it is inherently restricted to a two-dimensional Hilbert space. In contrast, other photonic degrees of freedom, such as temporal, frequency, or spatial modes, can support higher-dimensional quantum states, which can offer performance advantages in advanced quantum communication protocols [133].

3.2.3 Spatial mode encoding

Spatial mode (or path) encoding is realized by preparing a photon in a superposition of at least two distinct spatial modes, which can be labeled as $|0\rangle$ and $|1\rangle$. Entangled states in

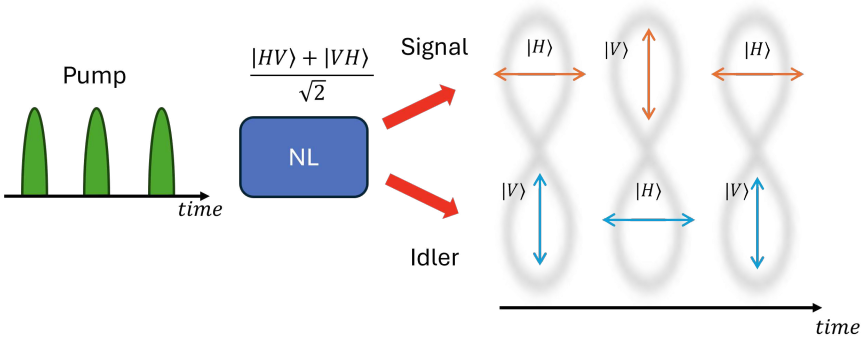

Figure 3.3: **Polarization encoding.** Schematic representation of polarization entanglement produced by a nonlinear (NL) medium pumped by a sequence of optical pulses. The generated photon pairs are in superpositions of horizontal ($|H\rangle$) and vertical ($|V\rangle$) polarization states, resulting in the creation of polarization-entangled photon pairs.

the spatial domain can be generated by coherently pumping multiple nonlinear sources in parallel, as depicted in Figure 3.4 for the case of two optical sources. Similarly to the temporal domain, the operating regime must satisfy the condition that, with high probability, only a single source emits a photon pair at a given time. In this case, the generated state is a coherent superposition of the possible emission paths, and can be expressed as:

$$|\psi\rangle = \frac{1}{\sqrt{2}} \left(|0_S 0_I\rangle + |1_S 1_I\rangle \right), \tag{3.6}$$

where $|0_S 0_I\rangle$ corresponds to the signal and idler photons being generated in the first source, while $|1_S 1_I\rangle$ corresponds to their generation in the second source. Superposition states and relative phase control can then be implemented using beam splitters and tunable phase shifters, which allow precise manipulation of the relative phase between the paths [134].

In bulk optical setups, this can be achieved by physically separating the optical paths, in combination with polarization encoding (e.g., using type-I and II phase matching in nonlinear crystals [135]). Maintaining coherent superpositions in such systems requires precise phase stability among the spatial modes, making bulk implementations highly sensitive to environmental fluctuations.

Integrated photonic platforms have recently enabled more robust and scalable spatial-mode encoding. By guiding photons through different on-chip waveguides, these platforms support high-dimensional encodings and improved scalability of quantum states [136, 137]. Moreover, the compactness of integrated circuits significantly reduces phase fluctuations among the paths, providing enhanced stability compared to bulk optical setups. Quantum gates have been successfully implemented in this framework [134, 138]. Spatial encoding has also been employed to demonstrate quantum advantage in boson-sampling experiments, where interference among large numbers of spatial modes performs computations that are exponentially hard for classical computers [139, 140].

Overall, spatial encoding naturally supports scaling to multiple modes and photons, enabling high-dimensional interference networks that are essential for advanced photonic quantum simulators and quantum computation protocols.

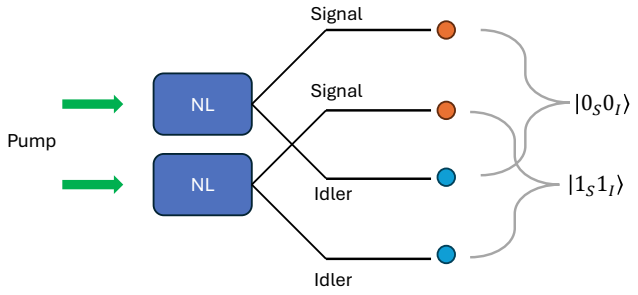

Figure 3.4: **Spatial encoding.** Example of spatial-mode encoding and the generation of spatially entangled states using two nonlinear sources (NL) and path superposition. Entanglement in the spatial degree of freedom arises from the condition that only one of the nonlinear sources emits a photon pair, leading to a coherent superposition of the possible spatial paths.

3.2.4 Frequency-bin encoding

A photon can encode quantum information in its frequency degree of freedom, an approach commonly referred to as *frequency-bin encoding*. In this scheme, different frequency modes correspond to distinct quantum states, such as $\omega_0 \rightarrow |0\rangle$, $\omega_1 \rightarrow |1\rangle$, etc., each characterized by a spectral bandwidth determined by the generation process. To ensure well-defined and distinguishable states, the frequency bins must be sufficiently separated to minimize spectral overlap.

A key advantage of frequency-bin encoding is its natural scalability: the dimensionality of the Hilbert space can be increased by adding more frequency bins, enabling high-dimensional quantum information processing [141, 142]. In this work, the focus is on the discrete-variable regime of frequency-bin encoding; however, it is worth noting that frequency encoding can also be implemented in the continuous-variable regime, where quadrature measurements of the spectral field are exploited.

Frequency-bin entangled quantum states, are typically generated through nonlinear optical processes [143]. The two main mechanisms are second-order ($\chi^{(2)}$) SPDC and third-order ($\chi^{(3)}$) SFWM. In both cases, a coherent pump generates photon pairs in correlated frequency modes, and spectral filtering is used to define the relevant frequency bins, as depicted in Figure 3.5 for a two-bin encoding scheme. Referring to the figure, the generated state can be expressed as

$$|\psi\rangle = \frac{1}{\sqrt{2}} \left(|0_{\omega_{S1}} 0_{\omega_{I1}}\rangle + |1_{\omega_{S2}} 1_{\omega_{I2}}\rangle \right), \tag{3.7}$$

where the two terms correspond to photon-pair generation in distinct signal–idler frequency modes.

After generation, photons must be manipulated to implement quantum protocols or gate operations. A common approach is via spatial separation: spectral filtering isolates the frequency bins, and phase modulation can be applied individually [144, 145]. This can be realized using free-space elements, such as prisms or gratings, or fiber-based components in the telecom C-band.

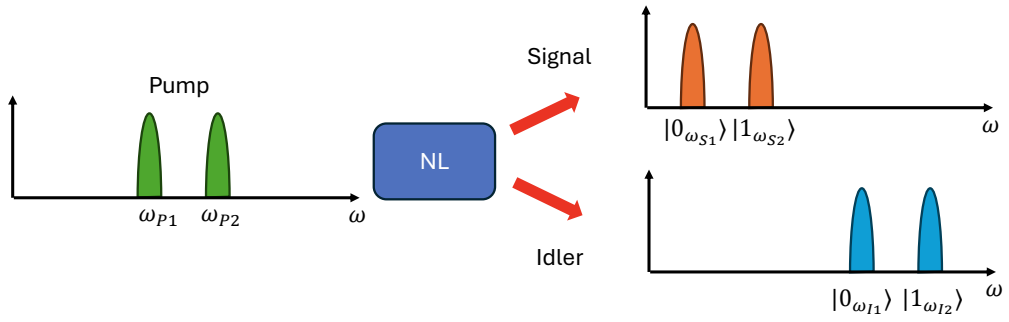

Figure 3.5: **Frequency encoding.** Generation of frequency-encoded qubits by pumping a nonlinear source (NL) with two different pump frequencies. In the regime where only a single pump pulse generates a photon pair, the output state forms a coherent superposition of the two possible frequency bins. Energy conservation imposes the relations $\omega_{P1,2} = \omega_{S1,2} + \omega_{I1,2}$ or, $2\omega_{P1,2} = \omega_{S1,2} + \omega_{I1,2}$, depending on the nonlinear interaction.

To enable quantum interference between frequency bins the frequency modes must overlap coherently. Practical solutions include EO modulators, which shift photon frequencies via phase modulation [146]. EO modulators typically allow frequency shifts up to ~ 100 GHz, which may be insufficient for integrated platforms with large free spectral range (FSR) or widely spaced frequency bins. An alternative approach uses nonlinear interactions ($\chi^{(2)}$ [147] or $\chi^{(3)}$ [148]) assisted by auxiliary pump fields to achieve frequency-bin mixing, enabling coherent interference and implementing quantum gate operations.

Direct temporal resolution of the beating between frequency modes is not practical, as even state-of-the-art single-photon detectors cannot resolve the fast timescales corresponding to typical bin separations ($1/\Delta\omega$). As a result, direct measurement of beating between frequency bins is challenging and generally limited to closely spaced bins [149]. A straightforward solution is to use dense wavelength-division multiplexing (DWDM) filters, which, similar to the manipulation step, spatially separate each frequency bin and route it to individual detectors. Another method is frequency-to-time mapping, where dispersive elements or chirped Bragg gratings convert frequency differences into time delays [150]. This enables discrimination of frequency bins using a single time-resolving detector and is relatively simple to implement, even when scaling to higher-dimensional frequency encodings.

3.3 Quantum applications

In this section, I provide an overview of the main domains in which quantum phenomena are exploited to achieve functionalities beyond classical limits. The discussion focuses on the three primary fields of quantum technology: quantum computation, quantum communication, and quantum sensing.

3.3.1 Computing

As in the classical domain, quantum computation takes input states representing information and produces output states according to a well-defined sequence of operations that implement a function. The essential difference, however, lies in the nature of the computation itself. Classical computation is deterministic and can be described by a mechanical model such as a Turing machine. Quantum computation, in contrast, is governed by the postulates of quantum mechanics, and its outcomes are generally probabilistic. Computation proceeds through a sequence of quantum operations, or *quantum gates*, which are unitary transformations acting on the qubits. Quantum algorithms can therefore be built from finite sets of such gates, directly analogous to the use of logic gates in classical computation. As in the classical domain, where universal sets of gates (e.g., NAND or NOR) allow any Boolean function to be implemented, quantum computation also admits universal sets of gates. A standard example is the set composed of the Hadamard gate, the phase gate, and the CNOT gate [115].

Another fundamental distinction from classical computation is the exploitation of quantum superposition. During computation, a quantum system can exist in a superposition of all possible computational basis states, and unitary operations act simultaneously on all components of this superposition. This effect, referred to as "quantum parallelism" [151], enables quantum algorithms to perform calculations on multiple inputs at once, providing a computational advantage over classical approaches.

Although information is encoded in a superposition of states, it cannot be accessed directly as in classical computing. At the end of a quantum algorithm, a measurement collapses the state to a single outcome, with a probability determined by the amplitudes of the superposition. Therefore, the design of a quantum algorithm must ensure that the correct result appears with high probability. This highlights a key distinction between the parallel evolution of quantum states and the practical extraction of useful information, which in some cases may require multiple repetitions of the same algorithm to achieve reliable results.

To understand the potential of quantum computation, it is useful to place it in the context of classical computational complexity. Classically, the class *P* contains problems that can be solved *efficiently* (in polynomial time) by a deterministic Turing machine. The class *NP* includes problems for which a candidate solution can be verified *efficiently* by a deterministic Turing machine, although finding a solution may not be *efficient* in general. In contrast to polynomial-time solvability, the best known algorithms for solving NP problems may require exponential time. The class of *NP*-complete problems consists of those problems in *NP* to which every other problem in *NP* can be reduced in polynomial time. Many computationally hard problems, such as the traveling salesman problem, belong to *NP*, and no efficient classical algorithms are known to solve all *NP*-complete problems. In the quantum setting, the class bounded-error quantum polynomial time (BQP) contains problems that can be solved efficiently by a quantum computer with a probability of success greater than $2/3$. The exact relationship between *BQP* and *NP* is currently unknown: it is believed that *BQP* is not large enough to include all *NP*-complete problems, meaning quantum computers are unlikely to efficiently solve every problem in *NP*. However, for certain specific problems, such

as factoring integers or simulating quantum systems, quantum algorithms provide a significant advantage over the best known classical approaches, exploiting quantum interference and entanglement to achieve performance advantages [152, 153].

A landmark example is Shor's algorithm for integer factorization, which runs in polynomial time, whereas the best known classical algorithms require sub-exponential time [154]. Shor's algorithm is based on the quantum Fourier transform (QFT), a fundamental subroutine that also underlies other algorithms such as quantum phase estimation [155], used to estimate the eigenvalues of a unitary operator. Another well-known example is Grover's algorithm for unstructured search [156], which provides a quadratic speedup compared to the best possible classical approaches. Simon's algorithm [157] is another notable case: it efficiently solves a problem that inspired the later development of Shor's factoring algorithm, and more generally, it demonstrates the potential of quantum algorithms to outperform classical ones for certain structured problems.

Despite advances in quantum algorithms, technological limitations such as noise, decoherence, and scalability challenges currently restrict their implementation to relatively small problem sizes. Scaling up the number of qubits remains difficult across all platforms, as each qubit must be individually controlled and made to interact reliably while maintaining high coherence and high-fidelity gate operations. Unwanted interactions with the environment cause decoherence, and even small gate imperfections accumulate over long sequences, corrupting the encoded quantum information. To address these issues, quantum error-correction codes and fault-tolerant protocols have been developed [158], exploiting entanglement to protect quantum states. However, these methods introduce significant overhead, making practical large-scale implementation highly demanding.

Quantum computers can be realized on a variety of physical platforms, each exploiting controllable quantum systems with long coherence times and precise manipulation. Photonic systems are one of the promising platforms for quantum computing [159]. Quantum information can be processed using linear and nonlinear optical elements, while single photon resolution detectors enable measurements with high precision. Significant milestone demonstrations of quantum computational advantage with photons have been achieved through Gaussian boson sampling (GBS), which is a classically hard problem. In particular, the experiments reported in [140, 160] demonstrated large scale GBS with, respectively, 50 and 144 indistinguishable single-photon modes, surpassing the capabilities of classical simulation on conventional computers.

Another notable demonstration was carried out by Xanadu in [161], which introduced *Borealis*, the first reconfigurable photonic quantum processor capable of performing time-multiplexed GBS across 216 optical modes. This platform demonstrated quantum advantage in 2022 and represented a major step forward compared with earlier boson-sampling implementations, which lacked reconfigurability of the interferometer. More recently, significant progress has been made toward fully integrated photonic quantum computers. A demonstration reported in [49] by PsiQuantum proposed a manufacturable integrated platform that could potentially combine the generation, manipulation, and detection of photonic qubits on a single chip. In addition, the work [159] by Xanadu introduced *Aurora*, an

integrated photonic architecture that demonstrates all key building blocks required for universality and fault tolerance. Such developments highlight the crucial role of integration for achieving large-scale, low-loss, and highly stable photonic quantum processors, enabling the feasibility of scalable photonic platforms for quantum computation.

Overall, integrated photonic technologies provide a pathway to scalable quantum computation by enabling precise control over multiple photons with high stability and reproducibility. As fabrication techniques continue to advance, photonic architectures may become one of the leading candidates for fault-tolerant and large-scale quantum computing.

3.3.2 Sensing and Metrology

Every measurement is affected by a certain amount of uncertainty. In many practical scenarios, this uncertainty is dominated by device imperfections or technical noise sources. Even when these effects are minimized through improved engineering, measurement precision is ultimately constrained by the standard quantum limit (SQL), which bounds the achievable sensitivity to a statistical scaling of $1/\sqrt{N}$, where N is the number of independent measurements. In optical interferometry, for example, the SQL arises from Poissonian fluctuations in photon number—commonly referred to as shot noise—with N corresponding to the number of detected photons.

Quantum sensing and metrology exploit coherent superpositions of quantum states to detect and measure physical quantities with sensitivities surpassing the SQL. Resources such as entanglement and squeezing enhance measurement precision beyond the bounds achievable by classical approaches [5]. When quantum correlations are fully utilized, the ultimate precision scales as $1/N$, known as the *Heisenberg limit* [162]. Although reaching this limit in practice is challenging due to losses and decoherence, even partial quantum enhancement can provide significant improvements over classical measurement strategies. Some of the most important applications where quantum sensing and metrology have demonstrated significant advantages include gravitational-wave detection [163], biological imaging [164], and atomic clocks [165].

3.3.3 Communication

Quantum communication can be defined as "the art of transferring a quantum state from one place to another" [1]. One of its most prominent applications is QKD, which enables distant parties to securely exchange cryptographic keys [1].

Classical cryptographic protocols ensure secure communication by encrypting messages with a secret key known by the legitimate parties. These protocols fall into two categories. The first category is *asymmetric cryptography*, in which a public key is used by any sender to encrypt a message, while a private key, known only to the intended recipient, is used to decrypt it. Both keys are generated by the receiver. The second category is *symmetric cryptography*, which relies on a secret key shared exclusively between the two parties and used for both encryption and decryption. In this case, security is based entirely on the secrecy of the shared key. The security of most classical schemes depends on assumptions about

computational complexity: without the secret key, an adversary is not expected to have sufficient computational power to solve the underlying hard mathematical problem required to decrypt the information. For example, one of the most widely used cryptographic schemes is RSA [166], which is an asymmetric protocol. Its security relies on the computational difficulty of factoring large integers, a task that is computationally hard for classical computers and not solvable in polynomial time. However, such protocols could be compromised by future advances in computational power, particularly through quantum computers capable of running Shor's algorithm [154].

In contrast, quantum communication can provide security based on the fundamental laws of quantum mechanics. QKD allows two parties (historically referred to as Alice and Bob) to establish a shared secret key such that any unwanted third-party attempts to obtain information (historically referred to as Eve) can be detected (Eavesdropping). A key principle underlying this is the *no-cloning theorem* [167], which states that it is impossible to create an exact copy of an unknown quantum state. Moreover, any measurement on a quantum system necessarily disturbs its state. As a result, any interception of the quantum states introduces detectable disturbances, enabling intrinsically secure cryptographic schemes based on the laws of quantum mechanics [168].

The first QKD protocol was proposed by Bennett and Brassard in 1984 [169] and is referred to as BB84. The first experimental demonstrations of BB84 were reported in 1989 [170], confirming the feasibility of secure quantum key exchange. In the following paragraph, the BB84 protocol is described in detail, outlining the steps required to effectively implement it. This protocol belonging to the class of prepare-and-measure schemes, does not rely on shared entangled states but it is the precursor of the entanglement-based version, proposed by Bennett, Brassard, and Mermin in 1992 (BBM92) [171], which is presented in Section 3.4.2 and demonstrated experimentally in the final Chapter 6.

BB84 The two users Alice and Bob, aim to establish a shared secret key. Here the protocol is explained using the polarization degree of freedom, although any two-level photonic encoding can be used. The protocol employs four quantum states forming two mutually unbiased bases. For example, the computational (rectilinear) basis $\{|H\rangle, |V\rangle\}$ and the diagonal basis $\{|D\rangle, |A\rangle\}$, where

$$|D\rangle = \tfrac{1}{\sqrt{2}}(|H\rangle + |V\rangle), \qquad |A\rangle = \tfrac{1}{\sqrt{2}}(|H\rangle - |V\rangle).$$

These bases are mutually unbiased because any pair of states from different bases has equal overlap, i.e. $|\langle D|H\rangle|^2 = 1/2$. A conventional bit assignment can be used, for instance, $0 \to \{|V\rangle, |D\rangle\}$ and $1 \to \{|H\rangle, |A\rangle\}$.

- Alice sends individual photons to Bob, choosing randomly among the four states, as schematized in the first row of Figure 3.6.
- Bob measures each qubit in a randomly chosen basis among the two predefined ones (rectilinear or diagonal). The random choices made by Alice and Bob must be independent (second row of Figure 3.6).

- When Alice and Bob choose the same basis, their results are perfectly correlated; otherwise, the outcomes are completely uncorrelated. At this point, each party holds a sequence of bits known as the *raw key*, which intrinsically contains about 25% errors due to the random and independent basis choices (third row of Figure 3.6).
- Alice and Bob publicly announces the basis used for each measurement, without revealing the measurement outcomes. All events corresponding to different basis choices are discarded. This step, known as *sifting*, removes approximately half of the raw key and produces the *sifted key*, as shown in the last two rows of Figure 3.6.
- From the sifted key, Alice and Bob publicly compare a small random subset of their bits to estimate the quantum bit error rate (QBER). This step is known as *parameter estimation*. If the QBER exceeds a certain threshold (25%) indicates the possible presence of an eavesdropper (as described below), and the protocol is aborted and restarted from the beginning. If the QBER is below the threshold, the remaining errors can be attributed to technical imperfections, a noisy transmission channel, or even partial information stealing by Eve.
- At this stage, Alice and Bob share the sifted key, but their keys may not be identical because of residual errors. They therefore perform classical *error correction*, using partial information of the sifted key.
- After error correction, Alice and Bob share the same key, but Eve may still possess partial information. Thus, finally *privacy amplification* techniques are applied to distill a shorter but fully secure secret key. This method was first proposed in [172] and ensures that any information potentially held by Eve is eliminated.

In the following, the *intercept–resend* eavesdropping strategy is analysed to illustrate how the BB84 protocol detects unwanted third-party interference [168]. In this attack, Eve intercepts each photon sent by Alice, measures it in a randomly chosen basis (just as Bob), and then resends to Bob a new photon prepared in the state corresponding to her measurement result. Due to the no-cloning theorem, Eve cannot create a perfect copy of the qubit and measure it later, and therefore must perform the measurement directly on the intercepted photon.

Since Eve chooses her measurement basis at random, in about half of the cases she uses the correct basis, the one compatible with Alice's prepared state. In these cases, she resends the correct state to Bob, and her presence remains undetected. However, in the other half of the cases, Eve uses the wrong basis. Because she has no information about Alice's random choice, the state she resends has only a $1/2$ overlap with the correct one. This highlights the importance of using quantum random number generators (QRNGs) in practical implementations to guarantee true randomness. As a result, when Alice and Bob use the same basis, these incorrect-basis events introduce errors in their correlations. Altogether, the intercept–resend attack gives Eve information about 50% of the sifted-key bits in the case she measures in the correct basis, while Alice and Bob observe an error rate of about 25% in their sifted key. Such a QBER value is easily detectable during the parameter-estimation step of the protocol.

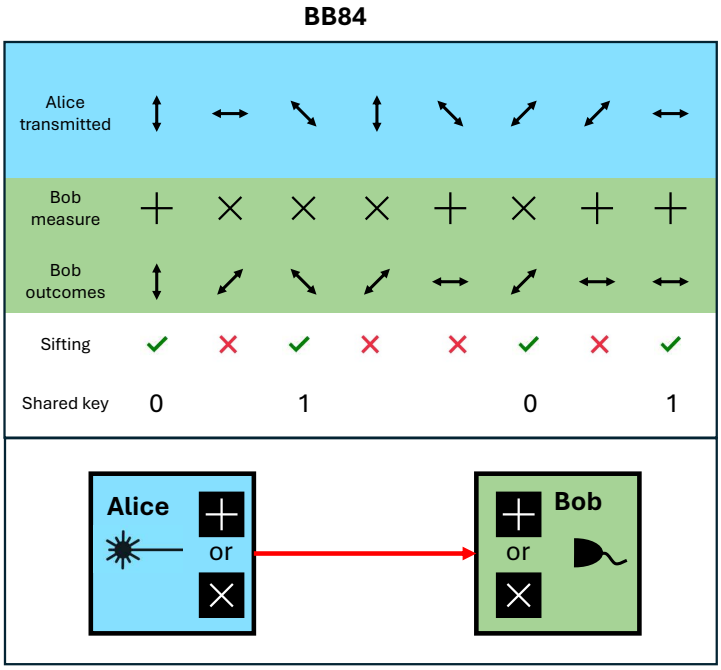

Figure 3.6: **BB84 protocol.** Schematic steps representation of the BB84 QKD protocol based on polarization photon encoding. Once the sifted key is obtained, parameter estimation, error correction, and privacy amplification steps are performed to distill a secure secret key.

If Eve applies this strategy only to a fraction of the exchanged photons, for example 10%, the QBER will scale proportionally to 2.5%, while Eve gains partial information of about 5% of the sifted key. Even if such a small error does not exceed the abort threshold, *privacy amplification* ensures that Alice and Bob can still distill a secure secret key by shortening it appropriately to remove any information Eve might possess.

Photons are the most suitable candidate for quantum communication applications, as they offer relevant advantages for the transmission of quantum states. Firstly, photon transmission can leverage the existing global fibre-optic network on which modern telecommunication systems are based. In the telecom bands, photons can propagate at the speed of light with inherently low transmission losses, enabling communication over long distances. In terms of hardware, many optical components can be inherited from traditional telecom applications, at relatively low cost and with wide availability. Photons can also be used for free-space quantum communication applications, especially for Earth-to-satellite communication. In this case, different wavelengths can be used beyond the standard telecommunications fibre-optic band ($\sim 1.3\,\mu m$ and $\sim 1.55\,\mu m$). For instance, $\sim$800 nm is often chosen to reduce beam divergence in satellite-based demonstrations [173]. In addition, photons offer different degrees of freedom on which a quantum state can be encoded, such as polarization, time, space and frequency, as described in Section 3.2.

Quantum communication protocols has moved beyond the proof-of-concept stage, with numerous experimental demonstrations and companies now offering commercial QKD systems. Companies such as ID Quantique, ThinkQuantum, Toshiba, LuxQuanta, and others,

sell modules for secure key distribution via fibre and free-space links demonstrating that QKD technology is becoming practical and commercially viable [174]. Currently, several operational quantum networks link multiple nodes, but the development of standardized hardware and universally adopted protocols remains an open challenge [175, 176].

Research is currently focused on improving system performance, such as increasing the secret key rate (SKR) over long distances, and on developing scalable hardware implementations. In terms of technological development, integrated photonic components play an important role, providing reliable, compact, and scalable solutions for photon sources, manipulation, and single-photon detection [11].

Additional research directions include the extension of communication ranges using quantum repeaters [177, 178], as well as the development of multi-user quantum networks that go beyond the original point-to-point schemes between Alice and Bob. This is often based on the adoption of classical telecom concepts such as DWDM that allow multiple users to share the same link while maintaining secure connections [179–182]. Overall, these efforts aim to create scalable and high-performance quantum communication networks.

A recent alternative approach that enables experimentally high SKRs is continuous-variable quantum key distribution (CV-QKD). The presented BB84 protocol belongs to the class of discrete-variable quantum key distribution (DV-QKD), where quantum information is encoded in discrete degrees of freedom. In contrast, in CV-QKD the key information is encoded in the continuous quadrature amplitudes of the quantized electromagnetic field, rather than in discrete quantum states [183].

CV-QKD was originally proposed using squeezed states [184], but most practical implementations employ coherent states, as they can be readily generated using standard attenuated laser sources [185]. One of the main advantages of CV-QKD is that it relies on homodyne or heterodyne detection techniques, similar to those used in classical optical telecommunications, enabling the use of high-bandwidth detectors and potentially higher SKRs [186]. Indeed, recent demonstrations have reported SKRs on the order of tens of Mbps over metropolitan-scale fibre links [187].

It represents a promising complementary approach to DV-QKD and benefits from strong compatibility with integrated photonic and telecom technologies. The use of continuous-variable quantum information carriers, instead of qubits, constitutes a powerful alternative not only for QKD but more broadly for quantum information processing [183].

3.4 Entanglement as a quantum resource

Entanglement was introduced earlier in this chapter as a special case of multi-qubit states. In this section, I discuss why entanglement is a central resource in quantum technologies, outlining its main properties and the advantages it provides across different applications.

Entanglement is one of the most fundamental and non-classical features of quantum mechanics. Formally, a bipartite quantum state ρ_{AB} is said to be *separable* if it can be expressed as a convex combination of product states:

$$\rho_{AB} = \sum_i p_i \rho_A^{(i)} \otimes \rho_B^{(i)}, \tag{3.8}$$

where p_i are probabilities, and $\rho_A^{(i)}$ and $\rho_B^{(i)}$ are local density matrices of subsystems A and B, respectively. If a state cannot be written in this form, it is *entangled*.

Although this is a negative definition, it emphasizes that entanglement represents correlations that cannot be reduced to classical statistical mixtures of individual subsystems, but instead reveal intrinsic quantum connections between them. One of the most striking consequences of entanglement is the existence of correlations between measurements on spatially separated particles that cannot be explained classically. In 1935, Einstein–Podolsky–Rosen (EPR) [116] argued that such correlations implied that quantum mechanics must be incomplete, proposing that additional "hidden variables" could predetermine measurement outcomes.

In 1964, John Bell formalized this intuition by introducing the framework of *local hidden variable models (LHVMs)*, where hidden variables govern the behavior of quantum systems in a deterministic way. Bell derived a set of constraints, now known as the *Bell inequalities* [188], which any local hidden variable theory must satisfy. Subsequent experiments [189] demonstrated violations of these inequalities, confirming that entangled states exhibit correlations that cannot be reproduced by any classical local model, thus establishing entanglement as an inherently non-classical phenomenon.

There exist several methods to experimentally certify and quantify the presence of entanglement in a quantum state [190]. One of the most widely used forms is the Clauser–Horne–Shimony–Holt (CHSH) inequality [191], proposed in 1969 and inspired by Bell's original work. It manifests in the measured outcomes of entangled states, which exhibit particular statistical behavior that cannot be generated by classical correlations. Consider a correlation experiment between two spatially separated subsystems A and B sharing an entangled state, where the measurement outcomes of the first system depend on the variables a_1 and a_2, and similarly for B, which depend on the variables b_1 and b_2. Then the LHVM imposes that the statistical measurement outcomes must satisfy the following inequality:

$$|S| = \|E(a_1, b_1) + E(a_1, b_2) + E(a_2, b_1) - E(a_2, b_2)\| \leq 2 \tag{3.9}$$

where $E(a_i, b_j)$ denotes the expectation value of the correlation experiment as a function of the variables a_i, b_j. Thus, to demonstrate the presence of entanglement, it is necessary to show a Bell parameter $S > 2$. The maximum value achievable for a two-dimensional quantum system, as predicted by quantum mechanics, is bounded by $S < 2\sqrt{2}$ [192].

While violations of Bell inequalities (such as CHSH) are a strong method to demonstrate entanglement, they are not the only way to certify it. Indeed, for instance an *entanglement witness* is an observable W such that, for any non entagled state separable state ρ_{sep},

$$\text{Tr}[W \rho_{\text{sep}}] \geq 0. \tag{3.10}$$

If, for a given quantum state ρ,

$$\text{Tr}[W \rho] < 0, \tag{3.11}$$

then the state ρ is guaranteed to be entangled [193, 194]. It is important to note that a negative expectation value of an entanglement witness is a sufficient condition for entanglement, but

not a necessary one. This means that some entangled states might not be detected by a particular witness, but whenever the witness indicates entanglement, it is a rigorous certification. Entanglement witnesses are particularly useful in experiments with high-dimensional or multi-partite systems, where full state tomography is complicated.

3.4.1 Generation of entangled states

Entangled states can be generated using a variety of methods and physical implementations. In the field of optical applications, the most widely adopted approaches for generating entangled photons exploit the nonlinear optical properties of materials, specifically second- and third-order nonlinear processes.

Second-order processes. The second-order process that is most commonly employed is SPDC. In this process, one pump photon is absorbed and two lower-energy photons are emitted. Due to the conservation of energy and momentum, the two emitted photons carry an average of half the energy of the pump photon.

SPDC has been efficiently demonstrated in bulk nonlinear crystals such as PPLN [195–198] and periodically poled potassium titanyl phosphate (PPKTP) [141, 199]. More recently, SPDC has also been implemented in integrated TFLN platforms [200, 201], although achieving reliable periodic poling on-chip remains a technological challenge. Other materials of interest include potassium niobate (PPKN) and related periodically poled structures.

These platforms provide high generation efficiency and wavelength tunability, with emission properties determined by phase-matching conditions and by engineering the poling period. An important practical advantage is that the pump wavelength is far from that of the emitted entangled photons, facilitating residual pump filtering and improving photon-pair collection efficiency. However, in integrated implementations, this becomes more challenging, as proper phase matching and dispersion engineering must be simultaneously achieved for optical modes propagating at significantly different frequencies.

Third-order processes. The third-order process relies on SFWM, where two pump photons are absorbed and a correlated pair of signal and idler photons is emitted symmetrically around the pump frequency because of the energy conservation. This process has been extensively demonstrated in integrated photonic platforms, including silicon, SiN, and other material systems [202, 203].

Generally integrated waveguide platforms provide great versatility for dispersion engineering, enabling precise phase-matching control and enhanced nonlinear interaction efficiency. The strong optical confinement achievable in these structures further increases the effective intensity of the interacting fields, significantly boosting photon-pair generation rates. Additional enhancement can be achieved with resonant structures such as micro-ring resonators, which offer both resonant field buildup and compact on-chip integration. Notably, the discrete FSR of micro-ring resonators naturally defines well-separated frequency modes, making them particularly suitable for frequency-bin entanglement [142]. Moreover, integrated photonic devices enable not only efficient photon-pair generation but also on-chip

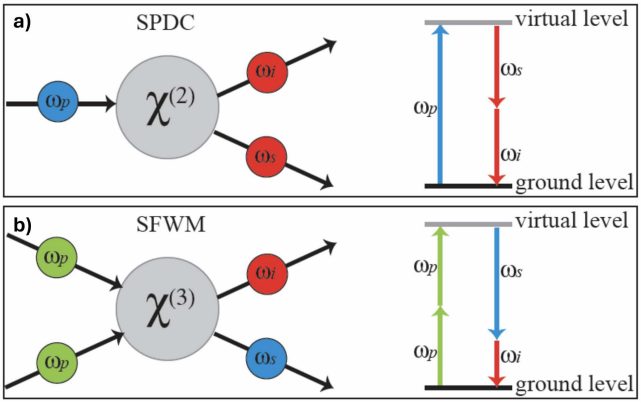

Figure 3.7: **Entanglement generation.** The diagrams illustrate nonlinear optical processes for generating entangled photons in materials with **(a)** second-order ($\chi^{(2)}$) and **(b)** third-order ($\chi^{(3)}$) nonlinearity. Figure from Ref. [205].

manipulation and filtering of the generated photons, paving the way toward compact, scalable, and programmable quantum photonic sources [204].

Generation condition A characteristic of photon-pair sources based on nonlinear optical materials is their non-deterministic nature. The probability of generating zero, one, or multiple photon pairs depends on the pump power. For entanglement-based quantum applications involving two qubits and relying on SPDC or SFWM processes, the regime of interest is the single-pair generation regime, which is achieved at relatively low pump powers. Operating in this regime, however, also increases the likelihood of generating no pairs at all. Conversely, increasing the pump power enhances the single-pair generation probability but simultaneously raises the occurrence of multi-pair events, which introduce noise and degrade the entanglement visibility and fidelity.

The output of a SPDC or SFWM source can be described as a two-mode squeezed vacuum state [206, 207]:

$$|\psi\rangle = \sqrt{1-\lambda} \sum_{n=0}^{\infty} \lambda^{\frac{n}{2}} |n\rangle_s |n\rangle_i , \tag{3.12}$$

where $n_{s,i}$ are the photon numbers in the signal and idler modes, and $\lambda = \tanh^2 r$. Here, r is the squeezing parameter, which depends on the nonlinear interaction strength and the pump amplitude ($r_{SPDC} \propto \sqrt{P_{pump}}$ and $r_{SFWM} \propto P_{pump}$).

The probability of generating n photon pairs follows a geometric distribution

$$P(n) = |\langle\psi|n\rangle_s |n\rangle_i|^2 = (1-\lambda)\lambda^n, \tag{3.13}$$

The mean photon-pair number is given by

$$\mu = \frac{\lambda}{1-\lambda} \simeq \sinh^2 r, \tag{3.14}$$

which scales with the pump power. In the low-gain regime ($\mu \ll 1$), the dominant terms are:

$$P(0) \approx 1 - \mu, \qquad P(1) \approx \mu, \qquad P(2) \approx \mu^2,$$

showing that multi-pair events increase quadratically with μ, while the single-pair rate increases linearly. This quadratic scaling of unwanted multi-pair events is a fundamental limitation of probabilistic sources, independent of whether the generation process relies on second-order (SPDC) or third-order (SFWM) nonlinearities.

The quality of photon-pair sources is commonly characterized by the *coincidence-to-accidental ratio (CAR)*, defined as the ratio between the number of coincidence events arising from single-pair generation, and the number of accidental coincidences, which originate from multi-pair emissions, detector dark counts, or any background noise. A high CAR indicates a low noise contribution and thus a higher purity and visibility of the generated quantum state, both of which are essential for reliable quantum communication. In the ideal case, neglecting detector dark counts and other technical noise sources, the CAR scales inversely with the mean pair number, approximately as:

$$CAR \approx \frac{P(1)}{P(2)} = \frac{1}{\mu}$$

This relationship highlights the intrinsic trade-off between pair-generation rate and source quality: increasing the pump power enhances brightness but simultaneously degrades the CAR due to the quadratic growth of multi-pair events.

Deterministic sources Due to the mentioned limitations of probabilistic sources of SPDC and SFWM, which face scalability challenges, there has been significant interest in the development of deterministic optical sources. These include single atoms [208] and quantum dots [209, 210], which can emit entangled photon pairs on demand. Single atoms trapped in optical cavities or tweezer arrays can be coherently driven to emit photons in well-defined temporal modes, often with the possibility of entangling successive photons or generating polarization- or time-bin entangled pairs. Quantum dots, on the other hand, are semiconductor nanostructures that can be engineered to produce pairs of entangled photons via biexciton-exciton cascades, with emission wavelengths tunable through strain, electric fields, or cavity coupling. Both platforms enable deterministic photon generation with high purity and indistinguishability.

Compared to probabilistic sources, deterministic ones offer potentially much higher generation rates, particularly in the pulsed regime of quantum applications. In such systems, the operational clock rate sets the timescale, and since probabilistic sources generate entangled pairs only with a certain probability per pulse, their overall rate scales linearly with this probability. Deterministic emitters overcome this limitation by providing entangled pairs at every clock cycle.

However, most deterministic sources have so far been developed for the generation of

single-qubit state photons, and the engineering required for realizing true on-demand entangled photon sources remains more challenging [209, 211]. Moreover, these solutions typically rely on complex material systems and highly controlled environments, often requiring cryogenic temperatures to ensure stable and reliable operation [212].

3.4.2 Entanglement in quantum communication

Entanglement plays a central role in quantum communication, particularly in the domain of QKD. In general QKD protocols can be divided into two categories: *prepare-and-measure* schemes and *entanglement-based* schemes. The first category does not rely on entanglement for its operation; the earliest example is the BB84 protocol, described in the previous section. In contrast, entanglement-based protocols exploit the quantum correlations shared by entangled photon pairs to distribute keys securely and to detect the presence of an eavesdropper. The entanglement-based analogue of BB84, is BBM92, introduced by Bennett, Brassard, and Mermin in 1992 [171]. In the experimental work presented in Chapter 6, I focus on the implementation of the entanglement-based BBM92 protocol. In the following, I provide a description of it, highlighting its connection to the BB84 protocol.

Over the years, various QKD protocols have been developed [171, 213–215], each offering different advantages such as higher key rates, improved robustness against losses, increased security against specific attacks, or reduced experimental requirements.

BBM92 The BBM92 protocol is similar to the BB84 protocol. It also involves two users, Alice and Bob, but in this case a central entangled-photon source distributes one photon of the entangled pair to Alice and to Bob, as schematically shown in Figure 3.8. Still considering the polarization degree of freedom, the source generates a maximally entangled Bell state, such as

$$\left|\Phi^{+}\right\rangle = \frac{1}{\sqrt{2}}\left(|HH\rangle + |VV\rangle\right),$$

although the protocol can be implemented with any two-level quantum system. For each received photon, Alice and Bob independently and randomly choose a measurement basis from two predetermined mutually unbiased bases. For example, they may select between the rectilinear basis $\{|H\rangle, |V\rangle\}$ and the diagonal basis $\{|D\rangle, |A\rangle\}$. Each user records both the chosen basis and the corresponding measurement outcome, as illustrated in the blue and green shaded rows of Figure 3.8.

Only the events where both users selected the same basis are retained, since these measurements are expected to exhibit perfect correlations due to the entanglement of the shared state. Measurements performed in different, mutually unbiased bases produce completely uncorrelated outcomes.

From this point onward, the protocol proceeds in the same way as BB84 previously described. After collecting a sufficiently large dataset, Alice and Bob publicly announce the basis used for each detection event, without revealing the outcomes, thereby performing the *sifting* step. They then carry out *parameter estimation* by publicly comparing a small random subset of their correlated results to estimate the QBER. If the QBER is higher than 25%, the

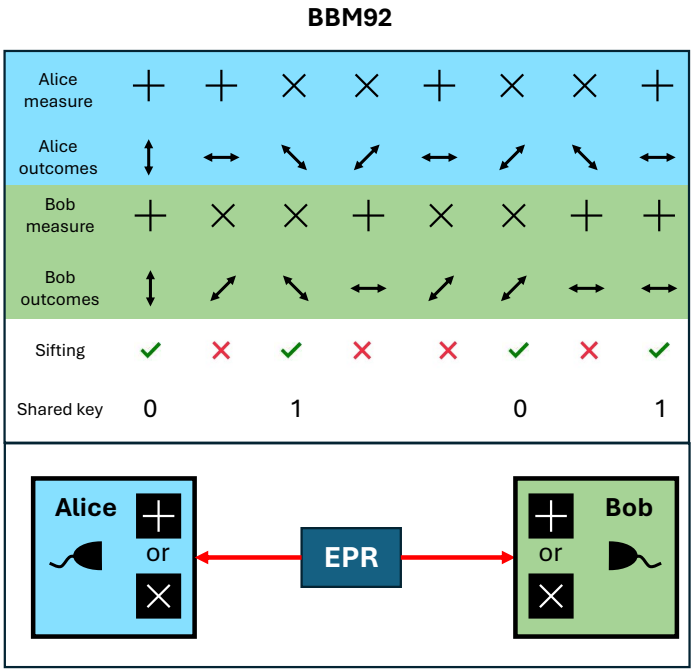

Figure 3.8: **BBM92 protocol.** Schematic steps representation of the BBM92 QKD protocol based on polarization photon encoding. Once the sifted key is obtained, parameter estimation, error correction, and privacy amplification steps are performed to distill a secure secret key. EPR: entangled photon source.

protocol is aborted. If the QBER is below the threshold, they proceed with classical *error correction* to reconcile their sifted keys, and finally apply *privacy amplification* to distill a secure secret key, as shown in the last row of Figure 3.8.

As in the BB84 protocol, according to the no-cloning theorem it is impossible for Eve to create a perfect copy of an unknown quantum state without disturbing it. Consequently, any attempt to intercept and measure the transmitted qubits modify the quantum correlations, producing detectable errors in the measurement statistics. This ensures that eavesdropping can always be identified.

The enhanced security offered by entanglement-based protocols such as BBM92, compared to prepare-and-measure schemes like BB84, arises from the nonlocal correlations of entangled states. Unlike BB84, where Alice actively prepares and sends quantum states to Bob, BBM92 relies on pre-shared entangled photon pairs. This configuration enables the direct verification of quantum correlations—typically through the violation of a Bell inequality such as CHSH—which provides a stronger and more fundamental security guarantee. In this way, even if the entangled-photon source is untrusted or located outside Alice and Bob's secure domains, the observed violation of a Bell inequality certifies the presence of genuine quantum correlations [168].

Although this approach offers stronger theoretical security guarantees, it comes at the cost of increased experimental complexity, as entanglement generation typically require more advanced hardware.

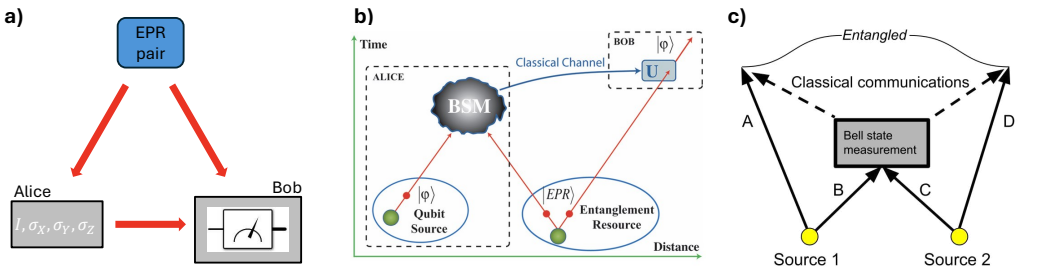

Figure 3.9: **Entanglement-based applications.** Schematic representation of entanglement-based applications other than QKD, which have no classical analogue: **a)** Superdense coding, **b)** Quantum teleportation, BSM: Bell state measurement, Figure from Ref. [1], and **c)** Entanglement swapping, Figure from Ref. [222].

Other applications of entanglement Entanglement enables powerful applications in which its correlations are exploited to perform quantum communication tasks that are impossible to achieve with classical methods. The most notable and important of these protocols, other than QKD, are described briefly here:

Quantum dense coding: (or *superdense coding*) This protocol allows two users, to exchange 2 bits of classical information by transmitting only 1 qubit, provided they share an entangled pair, as schematcally shown in Figure 3.9a. Classically, transmitting 2 bits would require sending 2 bits; entanglement thus reduces the quantum communication cost. The scheme relies on Alice applying one of four possible quantum operations to her qubit: the identity operator ($\mathbb{I}$) or one of the three Pauli gates (X, Y, and Z). She then sends this qubit to Bob, who performs a joint Bell-state measurement (BSM) on both qubits. From this joint measurement, Bob can unambiguously retrieve the 2 bits of classical information. This protocol was first demonstrated experimentally in 1996 [216].

Quantum teleportation: This protocol allows Alice to transfer an unknown quantum state to Bob using a shared entangled pair and classical communication. Importantly, the quantum state is transferred, not copied, thus complying with the no-cloning theorem. The involved steps, represented in Figure 3.9b, require that Alice performs BSM on the two quantum state and by a classical channel the outcomes information is transferred to Bob. Based on the two classical bits received, Bob applies a specific unitary correction operation (one of four possible Pauli operations to his qubit. After this correction, Bob's qubit is transformed into the original unknown state. The concept was first introduced in 1993 by Bennett et al. [217] and experimentally demonstrated in 1997 [218].

Entanglement swapping: Consider four parties, where A and B share a maximally entangled pair (Source 1), and C and D share another maximally entangled pair (Source 2) as shown in Figure 3.9c. If B and C perform a joint BSM on their two qubits, the entanglement is "swapped" [219]. Consequently, A and D end up sharing a maximally entangled state, even though they never interacted directly. This principle is crucial in quantum communication, particularly for EBQKD protocol, because it enables the construction of quantum repeaters [220, 221]. Quantum repeaters allow entanglement to be distributed over long distances, thereby overcoming the limitations of direct photon transmission imposed by loss in prepare-and-measure schemes like BB84.

3.5 Quantum communication with temporal encoding

This section introduces the fundamental principles and recent developments of quantum communication schemes based on temporal encoding, providing the necessary background for the research presented in this thesis. The discussion begins with an overview of the main temporal encoding methods and their variants, emphasizing their respective advantages and practical limitations. This framework serves to clarify the technological and security challenges associated with temporal encoding, particularly those that arise in real-world implementations.

3.5.1 Time-energy entanglement

The temporal encoding of entangled states was first proposed by Franson in 1989 [120]. This scheme exploits the intrinsic randomness in the emission times of photon pairs generated by a nonlinear medium, giving rise to a encoding referred as *time-energy entanglement*. The original proposal, schematically illustrated in Figure 3.10, considered an atom excited by a laser into a long-lived upper state with lifetime τ_1. After the emission of the first photon (γ_1), the atom occupies an intermediate energy level with a much shorter lifetime $\tau_2 \ll \tau_1$, and subsequently decays to the ground state by emitting a second photon (γ_2). Time-energy entanglement arises because the two photons are strongly correlated in their emission times (within τ_2) and energies, due to energy-momentum conservation, while the absolute emission time remains uncertain within the duration τ_1.

In modern quantum optics experiments, the atomic-level picture is typically replaced by optical sources based on nonlinear processes, such as SFWM or SPDC. For SFWM, two pump photons at frequency ω_p interact with the nonlinear medium to generate one signal and one idler photons at frequencies ω_s and ω_i. In this analogy, the long atomic lifetime τ_1 is effectively replaced by the coherence time of the pump laser, τ, which can be large for continuous-wave and narrowband sources. The short coherence time of the emitted photons, τ_p, corresponds to the duration over which an individual photon wavepacket is well-defined. Physically, τ_p is determined by the spectral bandwidth of the generated photons: narrower spectra yield longer photon coherence times, while broader spectra produce shorter coherence times. The condition $\tau \gg \tau_p$ ensures that the emission time of the photon pair is uncertain on the timescale of the pump coherence, while the relative timing between signal and idler photons remains well-defined.

Experimentally, these correlations can be characterized through the *joint spectral intensity (JSI)* and the *joint temporal intensity (JTI)*, as illustrated in Figure 3.11. The JSI is the two-dimensional probability distribution that quantifies correlations between the signal and idler photons in the frequency domain, while the JTI describes the joint probability of detecting the two photons at specific arrival times, thereby capturing their temporal correlations.

Entangled photon pairs generated by nonlinear processes can be described as [128]:

$$|\Psi\rangle = \int d\omega_i \, d\omega_s \, \phi(\omega_i, \omega_s) \, |\omega_i\rangle \, |\omega_s\rangle \, , \tag{3.15}$$

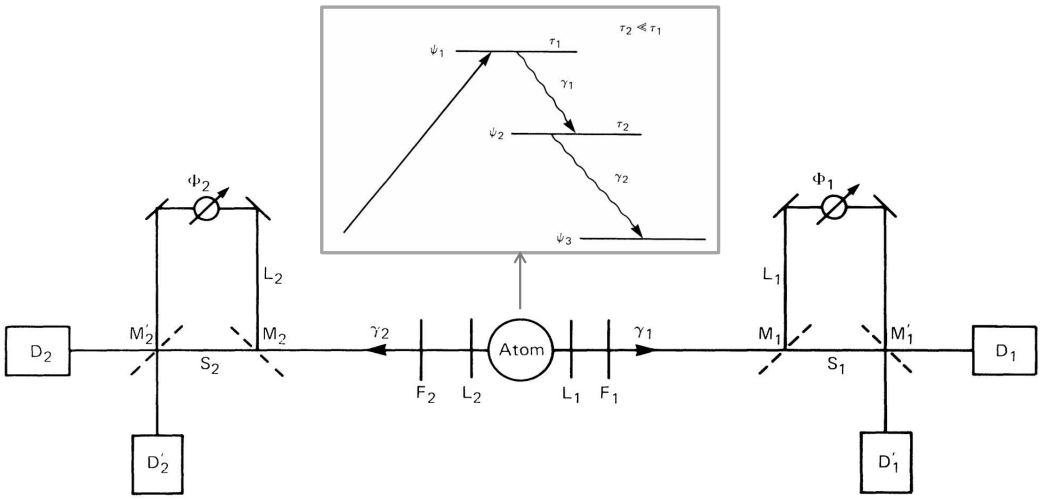

Figure 3.10: **Time-energy entanglement experimental schematic.** Original optical scheme proposed for the certification of time-energy entanglement, based on a long-lived τ_1 upper excited state and a short-lived τ_2 intermediate state that together generate photon pairs γ_1 and γ_2 correlated in both time and energy. Coincidence detection correlations are analysed by detectors D_1 and D_2 after the interferometer's path recombination. Figure from Ref. [120].

where ω_i and ω_s denote the idler and signal frequencies, and $\phi(\omega_i, \omega_s)$ is the probability amplitude for generating a photon pair at those specific frequencies (JSI). This function depends on the nonlinear process and the pump laser. In many cases, $\phi(\omega_i, \omega_s)$ can be approximated by a double-Gaussian function [128], oriented along the diagonal $(\omega_s + \omega_i)$ and anti-diagonal $(\omega_s - \omega_i)$ axes:

$$\phi(\omega_i, \omega_s) \propto e^{-\frac{\tau^2}{4\pi}(\omega_i+\omega_s-2\Omega_p)^2} e^{-(\delta_i(\omega_i-\Omega_i)-\delta_s(\omega_s-\Omega_s))^2}, \tag{3.16}$$

with Ω_p the pump frequency, $\Omega_{i,s}$ the central idler and signal frequencies (with $\Omega_i + \Omega_s = 2\Omega_p$), and $\delta_{i,s}$ parameters related to the phase-matching condition. By Fourier transforming the JSA, it is obtained the JTI:

$$F(t_i, t_s) \propto e^{-\frac{\pi}{\tau^2}\left(\frac{\delta_i t_i+\delta_s t_s}{\delta_i+\delta_s}\right)^2} e^{-\frac{(t_i-t_s)^2}{2(\delta_i+\delta_s)^2}} e^{i(t_i\Omega_i+t_s\Omega_s)}. \tag{3.17}$$

A simulated JSI and JTI using the double-Gaussian function approximation is reported in Figure 3.11. In the double-Gaussian model, the parameter τ, which corresponds to the coherence time of the pump laser, determines the width of the JSI along the diagonal direction $(\omega_i + \omega_s)$ and the width of the JTI along the diagonal direction $(t_i + t_s)$. A longer coherence time τ results in a narrower diagonal bandwidth in the JSI, and a correspondingly broader temporal distribution along $(t_i + t_s)$ in the JTI. In contrast, the anti-diagonal width is determined by the phase-matching conditions of the nonlinear medium, through the parameters δ_s and δ_i, which set the spectral region where the nonlinear process is efficient. These constraints define the bandwidth of $(\omega_s - \omega_i)$ in the JSI and manifest in the temporal domain as the width of the JTI along the $(t_s - t_i)$ direction.

As proposed by Franson in the seminal work [120], the verification of time-energy entanglement relies on an unbalanced MZI, commonly referred to as a *Franson interferometer*,

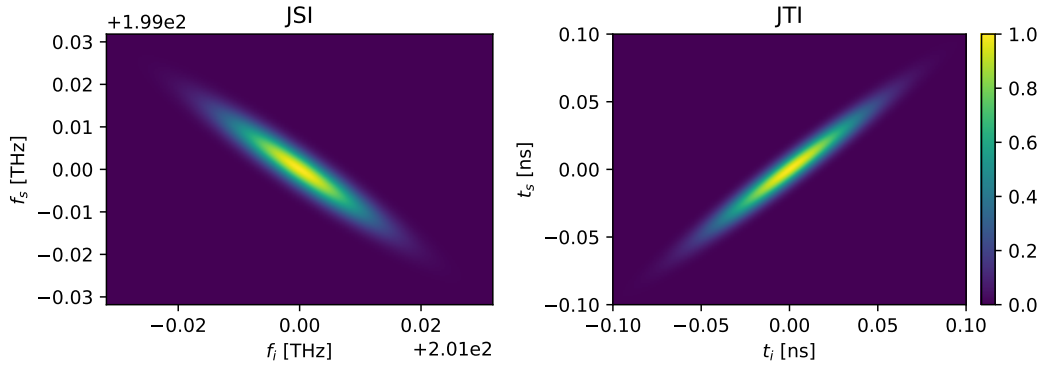

Figure 3.11: **Simulated JSI and JTI of time-energy entangled state.** Representation of the joint spectral intensity (left) and the joint temporal intensity (right). According to the double-Gaussian model in Eqs. (3.16) and (3.17), the simulation is performed assuming a pump coherence time of $\tau = 100$ ps, phase-matching parameters $\delta_{s,i} = 5$ ps, and $\delta_{s,i} = 2\tau$. The central frequencies are set to $\Omega_p = 2\pi \cdot 200$ THz for the pump, $\Omega_s = 2\pi \cdot 199$ THz for the signal, and $\Omega_i = 2\pi \cdot 201$ THz for the idler.

illustrated in Figure 3.10. Assuming two identical interferometers such that $L_1 = L_2$ and $S_1 = S_2$, the path-length difference $\Delta L = L - S$ introduces a temporal delay

$$\Delta t = \Delta L / c, \tag{3.18}$$

where c is the speed of light in the medium. This delay must satisfy the condition

$$\tau \gg \Delta t \gg \tau_p, \tag{3.19}$$

In this regime, single-photon interference is suppressed because $\tau_p \ll \Delta t$, while the long pump coherence time τ allows the two-photon wavefunction to interfere nonlocally, giving rise to time-energy entanglement correlations.

After passing through the interferometers, the two-photon state $|\Phi\rangle$ can be expressed in terms of the paths $|a_A, b_B\rangle$, where $a, b \in \{S, L\}$ denote the short (S) or long (L) arm taken by Alice's and Bob's photons, respectively. Considering all four possible path combinations, the state evolves as

$$|\Phi\rangle \;\rightarrow\; \frac{|S_A S_B\rangle + e^{i(\phi_A+\phi_B)}\,|L_A L_B\rangle + e^{i\phi_B}\,|S_A L_B\rangle + e^{i\phi_A}\,|L_A S_B\rangle}{2}, \tag{3.20}$$

where ϕ_A and ϕ_B are the phases accumulated in the long arms of Alice's and Bob's interferometers. The nonlocal interference of the entangled state between the two spatially separated interferometers is revealed through coincidence measurements through detectors D_1 and D_2 as labeled in the Figure 3.10, which record the joint detection of Alice's and Bob's photons. These coincidences depend on the specific combinations of optical paths taken by the photons, as shown in Figure 3.12a. By analyzing the coincidence detections as a function of the arrival-time difference, the resulting statistical histogram exhibits three distinct peaks, as shown in Figure 3.12b :

- **Side peaks:** Correspond to $|S_A L_B\rangle$ and $|L_A S_B\rangle$, which are temporally distinguishable due to a separation of $2\Delta t$ in detection times. These events do not exhibit interference.
- **Central peak:** Corresponds to $|S_A S_B\rangle$ and $|L_A L_B\rangle$, which are temporally indistinguishable thanks to the long pump coherence time τ. This indistinguishability allows nonlocal two-photon interference, as is described below.

The central peak events thus correspond to coherent superpositions of the two-photon wavefunction, enabled by the long pump coherence time, and give rise to nonlocal two-photon interference—a direct signature of time-energy entanglement. This can be described analytically in the following way. After the final beam splitter of each interferometer, the incoming path modes are mapped onto two output spatial modes associated with detections corresponding to the states $|0_{A,B}\rangle$ and $|1_{A,B}\rangle$. Using the balanced beam-splitter transformation:

$$|S_{A,B}\rangle \;\rightarrow\; \tfrac{1}{\sqrt{2}}\left(|0_{A,B}\rangle + i\,|1_{A,B}\rangle\right), \tag{3.21}$$

$$|L_{A,B}\rangle \;\rightarrow\; \tfrac{1}{\sqrt{2}}\left(|0_{A,B}\rangle - i\,|1_{A,B}\rangle\right), \tag{3.22}$$

and restricting the analysis to the central peak events that shows the non local interfernece (i.e., post-selecting indistinguishable detection events), the two-photon state becomes

$$|\Phi_{PS}\rangle = \frac{|S_A S_B\rangle + e^{i(\phi_A+\phi_B)}\,|L_A L_B\rangle}{2}, \;\rightarrow\; \frac{1}{2\sqrt{2}}\Big[(1+e^{i(\phi_A+\phi_B)})\,|0_A 0_B\rangle + i(1-e^{i(\phi_A+\phi_B)})\,|0_A 1_B\rangle + i(1-e^{i(\phi_A+\phi_B)})\,|1_A 0_B\rangle - (1+e^{i(\phi_A+\phi_B)})\,|1_A 1_B\rangle\Big]. \tag{3.23}$$

The coincidence probabilities can be calculated from this last expression. For instance, the probability of detecting both photons in the $|0_A 0_B\rangle$ output is

$$P(0_A 0_B) \;=\; \left|\,\langle 0_A 0_B|\,\Phi_{\mathrm{PS}}\rangle\right|^2 \;=\; \tfrac{1}{8}\left|1+e^{i(\phi_A+\phi_B)}\right|^2 \;=\; \tfrac{1}{4}\left[1+\cos(\phi_A+\phi_B)\right]. \tag{3.24}$$

By varying the relative phases ϕ_A and ϕ_B, interference fringes appear in the coincidence rates, even if Alice and Bob are spatially separated. For a test of the CHSH inequality (Eq. (3.9)), specific phase settings are chosen to maximize the violation of local realism. A common choice is $\phi_A \in \{0, \pi/2\}$ and $\phi_B \in \{-\pi/4, \pi/4\}$, which corresponds to the four measurement settings used to compute the correlation parameter S, where $E = P(0_A 0_B) + P(1_A 1_B) - P(0_A 1_B) - P(1_A 0_B)$. With these settings, the coincidence probabilities exhibit maximal nonlocal correlations, and the measured value of S can approach the quantum bound of $2\sqrt{2}$, providing an experimental demonstration of time-energy entanglement.

3.5.2 Time-bin entanglement

In 1999, Gisin *et al.* proposed a variation of Franson's time-energy scheme, initially referred to as *pulsed time-energy* entanglement and later known as *time-bin* entanglement [121]. In this scheme, shown in Figure 3.13, the generation mechanism of the entangled state is modified, while the analysing interferometer remains the same as in the Franson configuration (an

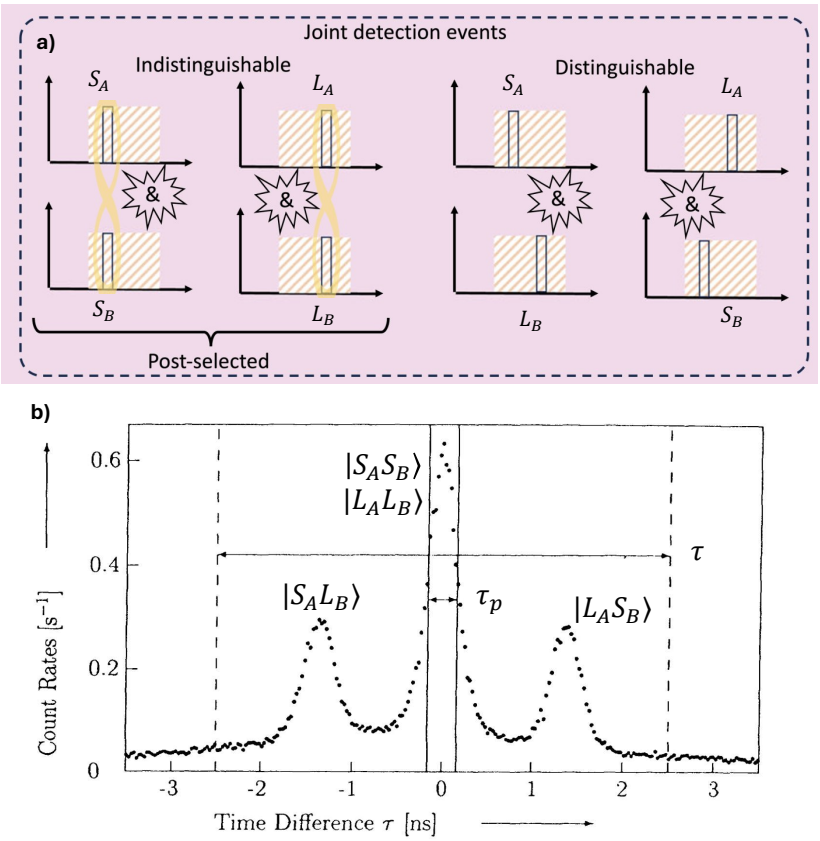

Figure 3.12: **Time-energy entanglement measurement correlation.** **a)** Possible measurement correlation events: temporally indistinguishable events give rise to nonlocal two-photon interference between the two users, while distinguishable events do not exhibit correlations. These effects are revealed by analyzing coincidence detections between D_1 and D_2 of Figure 3.10. Figure from Ref. [128]. **b)** Measured coincidence histogram as a function of the arrival-time difference between Alice and Bob, showing three distinct peaks: two side peaks corresponding to distinguishable events ($|S_A L_B\rangle$ and $|L_A S_B\rangle$) and a central peak corresponding to indistinguishable events ($|S_A S_B\rangle$ and $|L_A L_B\rangle$) that give rise to nonlocal two-photon interference. Figure from Ref. [223].

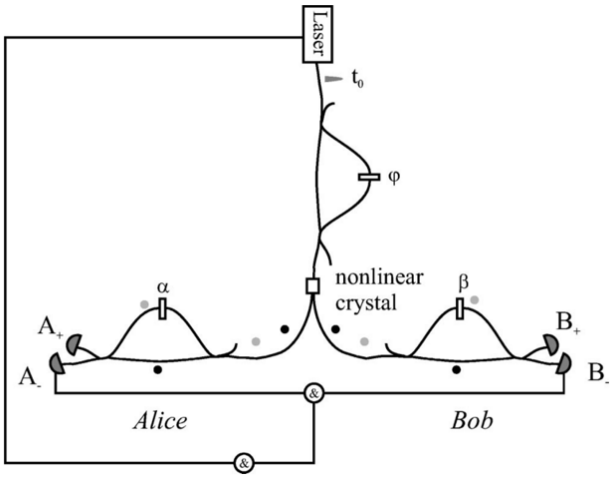

Figure 3.13: **Time-bin entanglement experimental schematic.** Optical scheme for the generation and verification of time-bin entanglement. Figure from Ref. [224].

unbalanced interferometer). The photon-pair source is no longer pumped continuously but by two coherent optical pulses separated by a fixed delay Δt. Under suitable pump-power conditions, a photon pair can be generated either in the first time-bin, denoted $|early\rangle$, or in the second time-bin, denoted $|late\rangle$. Moreover, the pump coherence time τ_p is much shorter than the bin separation, i.e., $\Delta t \gg \tau_p$. This condition ensures that the two time-bin modes do not overlap temporally, yielding a well-defined separation between early and late bins. An illustration of the expected JTI of the generated state is shown in Figure 3.14a.

The resulting quantum state is a coherent superposition of the two possible emission times of a photon pair:

$$|\Phi\rangle = \frac{1}{\sqrt{2}}\left(|early\rangle_A |early\rangle_B + e^{i\phi_p} |late\rangle_A |late\rangle_B\right), \tag{3.25}$$

where ϕ_p denotes the relative phase between the two time-bins, directly set by the relative phase of the pump pulses. For compact notation, we may write

$$|\Phi\rangle = \frac{1}{\sqrt{2}}\left(|early\rangle_{AB} + e^{i\phi_p} |late\rangle_{AB}\right). \tag{3.26}$$

When these photons are sent into the unbalanced interferometers of Alice and Bob, each photon can take either the short ($|S_{A,B}\rangle$) or long ($|L_{A,B}\rangle$) path, as in the time-energy case. It is important that the interferometer delay $\Delta L/c$ matches the temporal separation Δt. Considering the two input time-bins $|early\rangle_{AB}$ and $|late\rangle_{AB}$ with the two interferometer paths $|S_{A,B}\rangle$ and $|L_{A,B}\rangle$ leads to eight possible coincidence events. An illustrative representation of the evolution of the JTI through the unbalanced interferometers is shown in Figure 3.14b. By analysing the coincidence detections as a function of the arrival-time difference between the two users—i.e., integrating statistical events along the $t_A + t_B$ axis—three coincidence peaks are observed, as shown in Figure 3.14c:

- **Side peaks:** $|early\rangle_{AB}|S_AL_B\rangle$, $|early\rangle_{AB}|L_AS_B\rangle$, $|late\rangle_{AB}|S_AL_B\rangle$, and $|late\rangle_{AB}|L_AS_B\rangle$, which are distinguishable in time since their detection times differ by $\pm\Delta t$.
- **Central peak:** $|early\rangle_{AB}|L_AL_B\rangle$ and $|late\rangle_{AB}|S_AS_B\rangle$, which are temporally indistinguishable. Additionally, $|early\rangle_{AB}|S_AS_B\rangle$ and $|late\rangle_{AB}|L_AL_B\rangle$ are indistinguishable when analysing the coincidence histogram versus $t_A - t_B$, but they can be discriminated when using synchronization with the pump laser emission time, as shown in Figure 3.14b (outer diagonal cases).

Thus, the wavefunction components that overlap temporally at the central peak are $|early\rangle_{AB}|L_AL_B\rangle$ and $|late\rangle_{AB}|S_AS_B\rangle$. As in the time-energy case, this indistinguishability leads to nonlocal interference. Restricting to the post-selected central events, the quantum state evolves as

$$|\Phi_{PS}\rangle \;\rightarrow\; \frac{e^{i\phi_p}|late\rangle_{AB}|S_AS_B\rangle + e^{i(\phi_A+\phi_B)}|early\rangle_{AB}|L_AL_B\rangle}{\sqrt{2}}. \tag{3.27}$$

After mapping the time-bin modes to the detection outputs via the balanced beam-splitter transformation (Eq. 3.22), it is obtained:

$$\begin{aligned}|\Phi_{PS}\rangle \;\rightarrow\; \frac{e^{i\phi_p}}{2\sqrt{2}}\Big[&(1+e^{i(\phi_A+\phi_B-\phi_p)})|0_A0_B\rangle + i(1-e^{i(\phi_A+\phi_B-\phi_p)})|0_A1_B\rangle \\ &+i(1-e^{i(\phi_A+\phi_B-\phi_p)})|1_A0_B\rangle - (1+e^{i(\phi_A+\phi_B-\phi_p)})|1_A1_B\rangle\Big].\end{aligned} \tag{3.28}$$

The nonlocal interference is analysed using the coincidence probability for a specific detector pair. For example, the coincidence probability for the pair $P(0_A, 0_B)$ is:

$$P(0_A0_B) \;=\; \left|\langle 0_A0_B|\,\Phi_{PS}\rangle\right|^2 \;=\; \tfrac{1}{8}\left|1+e^{i(\phi_A+\phi_B-\phi_p)}\right|^2 \;=\; \tfrac{1}{4}\left[1+\cos(\phi_A+\phi_B-\phi_p)\right]. \tag{3.29}$$

Note that this probability is not normalized, as only one detection outcome is considered and varies with the phase sum $\phi_A + \phi_B - \phi_p$. Considering the full distribution, including all four detector outcomes, the probability is normalized to unity.

Time-bin encoding offers important advantages over time-energy entanglement for quantum communication applications. In time-energy schemes, the photon-pair emission time is uncertain within the long coherence window of the pump laser (τ), requiring detectors to remain continuously active. This continuous operation increases accidental coincidences and dark-count noise. In contrast, time-bin entanglement defines two well-separated temporal modes, allowing detectors to be gated only at the expected arrival times of the early and late bins [128]. This gating capability significantly reduces background noise, improves the signal-to-noise ratio (SNR), and extends the achievable transmission distance. Furthermore, unlike time-energy schemes, time-bin encoding does not require a pump laser with a long coherence time τ. Finally, pulsed pumping naturally provides both a timing reference and a repetition clock, making time-bin entanglement highly compatible with existing telecommunication infrastructures [225].

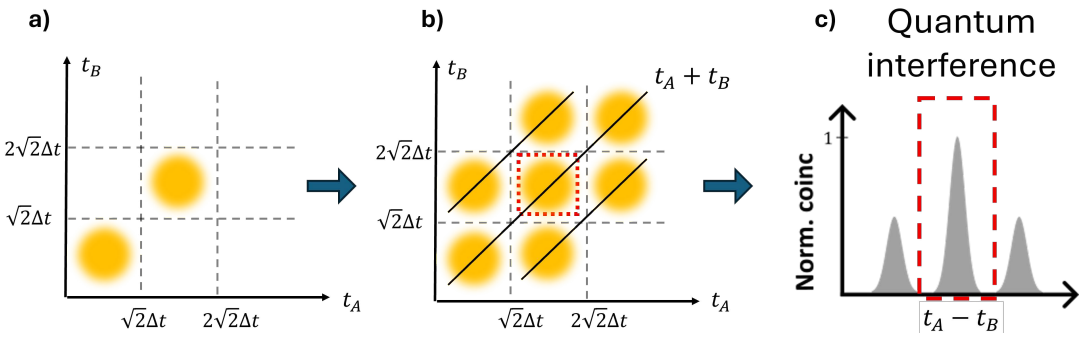

Figure 3.14: **Time-bin JTI.** Representation of the JTI distribution for time-bin entangled photons: **(a)** before the analyser interferometer, **(b)** after propagation through the unbalanced analyser interferometer, **(c)** resulting three-peak coincidence pattern obtained by integrating the JTI along the diagonal axis ($t_A + t_B$ = const.).

3.5.3 Loopholes

The experimental correlation features observed in both time-energy and time-bin configurations enable the demonstration of non-local interference patterns, i.e., correlations between distant measurements.

In ideal conditions, with a perfectly balanced entangled state and an ideal interferometer, these correlations ((3.24) and (3.29)) can exhibit a maximum interference pattern with coincidences probability ranging from 0 to 1. A main figure of merit to evaluate the entanglement quality and the analyzing interferometer stage is the visibility of the expected sinusoidal function. The visibility V for the coincidence probability function $P(\phi_A, \phi_B)$ is defined as:

$$V = \frac{\max[P(\phi_A, \phi_B)] - \min[P(\phi_A, \phi_B)]}{\max[P(\phi_A, \phi_B)] + \min[P(\phi_A, \phi_B)]} \tag{3.30}$$

Such a visibility, when it exceeds the Bell inequality bound of $1/\sqrt{2}$ ($\sim 70.7\%$), effectively rules out LHVMs [226].

In real experiments, however, the observed nonlocal correlations are inevitably affected by imperfections and technical limitations, which can allow alternative LHVMs to reproduce similar statistical results. For this reason, most experimental demonstrations of Bell inequality violations rely on a set of auxiliary assumptions. If these assumptions are not strictly satisfied, LHVMs may still account for the observed correlations, leaving open what are known as *loopholes*. These loopholes represent potential weaknesses in the experimental verification of entanglement.

In time-energy and time-bin entanglement experiments, three main loopholes are typically considered:

Locality loophole. This loophole arises if the choice of measurement settings or the detection events at Alice's and Bob's stations are not space-like separated, which would in principle allow classical communication between the parties within the light cone. It was first closed in 1998 by using a quantum random number generator to select measurement settings at stations separated by 400 m [227].

Detection loophole. This loophole is due to the fact that low detection efficiencies can allow selective sampling of detection events, enabling LHVMs to mimic quantum correlations. To achieve the maximum violation of the CHSH inequality, the minimum detection efficiency required is 83% [228]. For many years this threshold could not be reached, as efficient detectors and low-loss components were not available. More recently, significant progress in detection efficiency has enabled the closure of the detection loophole through the use of highly efficient superconducting transition-edge sensors (TES) [229, 230]. Nevertheless, in photonic implementations, closing this loophole remains challenging because optical components used for photon manipulation and interferometry still introduce significant losses.

Temporal (post-selection) loophole. While the two loopholes described above are also relevant for other degrees of freedom of entanglement implementation, the *temporal PSL* is specific to time-energy and time-bin encoding schemes. As described in the previous sections, only events in the central time binning contribute to the nonlocal interference. In particular, these are the $|S_A S_B\rangle$ and $|LL\rangle$ contributions for time-energy entanglement, and the $|early\rangle_{AB}|L_A L_B\rangle$ and $|late\rangle_{AB}|S_A S_B\rangle$ contributions for time-bin entanglement, while the side peaks are discarded. The discarded events—corresponding to $|S_A L_B\rangle$ and $|L_A S_B\rangle$ for time-energy entanglement, and to the other six contributions in the time-bin case—imply that selective post-processing has been performed. This leaves room for LHVMs to reproduce the observed correlations [19].

Different strategies have been proposed to address this issue.

Polarization beam splitter. One approach is to exploit an additional degree of freedom—most commonly polarization—so that, by means of a polarization beam splitter, the path taken in the unbalanced interferometer can be deterministically selected [231]. While it is effective for closing the loophole, this method is not directly optimized for information encoding in scalable quantum communication, where hyperentanglement or multiplexing are desired.

There have also been alternative proposals, often labeled as *genuine*, in the sense that only a single degree of freedom, the temporal one, is exploited.

Hug interferometer. Another approach is the so called "hug interferometer", in which the interferometers of Alice and Bob are compenetrated [232], as shown in Figure 3.15. In this configuration, the events that would normally be discarded ($|S_A L_B\rangle$ and $|L_A S_B\rangle$) lead to coincident detections on the same user's side and are thus naturally filtered out. Conversely, when one photon is detected by each user, the geometry of the setup ensures temporal superposition of $|S_A S_B\rangle$ and $|L_A L_B\rangle$ (or equivalently $|early\rangle_{AB}|L_A L_B\rangle$ and $|late\rangle_{AB}|S_A S_B\rangle$), giving rise to the desired quantum nonlocal interference. This method has also been demonstrated on an integrated SiN platform [233]. However, its practical implementation is challenged by the stringent requirement of maintaining relative phase stability, particularly when the two users are widely separated and the transmission links must be actively stabilized. Additionally, the compenetrated interferometer structure can limit the security of QKD implementations, as an eavesdropper could, in principle, act on the analyzer interferometer. Finally, the hug interferometer reduces the maximum achievable key rate because non-interfering events are discarded spatially, whereas methods such as *polarization beam splitter*

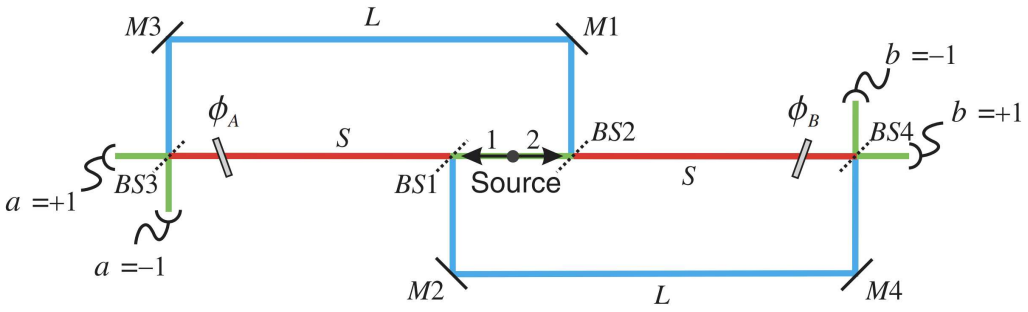

Figure 3.15: **"Hug" interferometer.** Interferometer scheme enabling the elimination of temporal post-selection in time-energy and time-bin Bell experiments. Distinguishable events are removed when both entangled photons arrive at the same side of the setup and do not contribute to the coincidence detection between the two users. Figure from Ref. [232].

or *switching* schemes can exploit all events injected into the analyzer for quantum statistical measurements.

Switching. As originally proposed in the first work introducing time-bin encoding [121], the temporal PSL can be eliminated by inserting an optical switch, synchronized with the pump source, before the unbalanced analysing interferometer, as shown in Figure 3.16. The optical switch allows to selectively routes photons into the two paths according to the applied modulation phase ϕ_M. Specifically, the modulation is configured such that, at the expected arrival time of the $|early\rangle_{AB}$ bin (dark shaded photons in the Figure 3.16), the photon is routed toward the long path $|L\rangle$, while at the arrival time of the $|late\rangle_{AB}$ bin (light shaded photons in the Figure 3.16), the switch directs the photon toward the short path $|S\rangle$. In this way, temporal PSL is intrinsically avoided as all detection events correspond to indistinguishable path combinations ($|early\rangle_{AB}|L_AL_B\rangle$ and $|late\rangle_{AB}|S_AS_B\rangle$), leading to nonlocal interference without discarding any events.

Unlike the previously mentioned methods that can be applied to both time-energy and time-bin schemes, this switching approach is specific to time-bin encoding. The first experimental implementation of this method was demonstrated in 2018 using bulk and fiber-based components to certify entanglement [234]. Notably, it has also been realized in an integrated form within the scope of this PhD project and will be described in detail in the next chapter.

Overall, these loophole-closure techniques are not essential for demonstrating entanglement certification in principle, but are directly relevant for guaranteeing the intrinsic security of quantum applications such as QKD, where an eavesdropper could exploit to hack the system, as has been demonstrated in the time-energy scenario [235].

To date, no experimental demonstration with time-energy or time-bin entanglement has simultaneously closed both the detection, locality and temporal PSLs, leaving a fully loophole-free test still open in this domain.

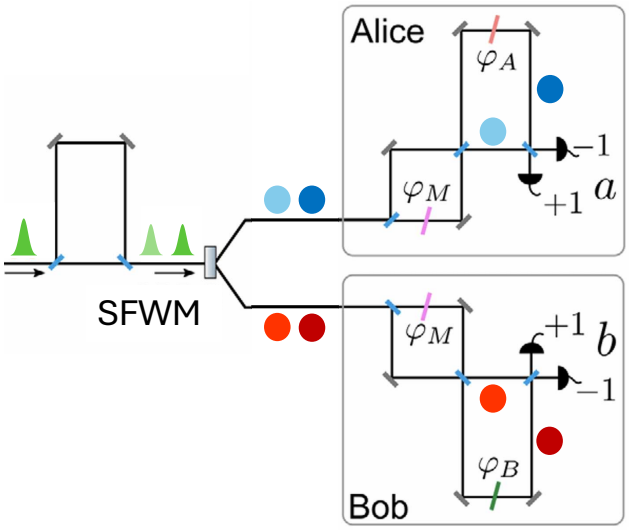

Figure 3.16: **Switching scheme.** Generic setup of a time-bin Bell experiment enabling the elimination of temporal post-selection through the use of an optical switch. The blue (red) pulses correspond to the signal (idler) photons in the early (late) time-bin, indicated by the dark (light) shaded regions. By appropriately driving the phase ϕ_M, the two time-bins are deterministically routed and coherently overlapped at the output of the final interferometer, thereby removing the need for temporal PSL. Figure from Ref. [234].

Summary

In this first part of the thesis, the main theoretical background and concepts relevant to the second part have been introduced. Some of these concepts are directly involved in the work presented later, while others provide an overview of the main alternative approaches in the field that are not explicitly used but are important for contextualizing the research.

In the second part of the thesis, the focus shifts to the specific implementation developed during the PhD. In particular, I will use the TFLN technology platform to create a PIC tailored for manipulating time-bin encoded quantum states. The research goal is to overcome the limitations imposed by temporal post-selection by implementing a switching scheme combined with platform engineering, making use of the technology's intrinsically high EO performance and low propagation losses.

Part II

Results

Chapter 4

Thin-Film Lithium Niobate Receiver for Quantum Communication

In this chapter, it is presented a custom-designed device developed to overcome key security and efficiency limitations affecting quantum communication protocols based on time-bin encoding.

As discussed in the previous chapter, both time-bin and time-energy encoding schemes suffer from the PSL, which compromises the **security** of quantum protocols such as QKD [235]. Moreover, when using stand-alone unbalanced interferometers as measurement setups (Figure 3.10 and Figure 3.13), the overall **detection efficiency** is inherently reduced for both time-energy and time-bin encodings. In particular, only 50% (time-energy) and 25% (time-bin) of photon detection events contribute to nonlocal measurement correlations, while the remaining 50% and 75% are discarded because the corresponding photons do not temporally overlap within the interferometric measurement window as shown in Figure 3.12b. Another major limitation arises from the **timing resolution** required by single-photon detection systems. In implementations that rely on temporal post-selection, detectors must resolve the fine separation between the early and late bins, posing a significant experimental limitation[179, 236], or alternatively, forces the use of larger separations, thereby limiting the overall transmission clock rate.

These issues are addressed in this work by adopting the *switching* scheme originally proposed in the seminal time-bin encoding paper by Brendel *et al.* [121]. The switching approach offers several advantages. By enabling deterministic interference between the two time-bin components, it eliminates the need for temporal post-selection, thereby closing the associated security loophole and maximizes the detection efficiency as no events are discarded. Additionally, it relaxes the timing requirements of the detection system: in a synchronized quantum link where time-bin states are transmitted periodically at a fixed repetition rate, detectors only need to register one event per clock cycle, rather than resolve the sub-nanosecond separation between the two bins.

The first experimental proof-of-principle demonstration of this concept was reported in 2018 by Vedovato *et al.* [234], whose setup is schematically illustrated in Figure 3.16. In their

experiment, entanglement was verified by scanning the interferometric phase and observing a violation of Bell's inequality. However, that implementation relied on fiber-based components with relatively large temporal separations between time-bins (~ 3 ns), which limited scalability and hindered full photonic integration. To address these limitations, the device developed in this work implements the switching scheme integrated with an unbalanced interferometer for time-bin state manipulation, realized on the TFLN photonic platform.

At the time of this work's conceptualisation (2022), the state-of-the-art performance of the TFLN platform was characterized by EO modulation bandwidths exceeding 100 GHz [237–241]. Furthermore, TFLN modulators achieved remarkable modulation efficiencies, with $V_\pi L$ products reaching approximately 1.7 V·cm [242–244]. Simultaneously, significant advancements in fabrication processes enabled low propagation losses below 0.1 dB/cm [104, 245, 246], alongside improved coupling efficiencies for fiber interfacing with loss < 1 dB per facet [57, 247].

These properties are particularly attractive for implementing the switching scheme, which requires high-speed modulation to manipulate closely spaced time-bin states. This capability also enables the realisation of a wide-bandwidth time-bin projector, which is suitable for fast and arbitrary quantum state operations, as will be discussed later in this chapter. Meanwhile, low propagation loss allows for the realisation of interferometers incorporating delayed paths and featuring high interference performance. Furthermore, integration on a photonic chip offers several advantages, including compactness, reproducibility, enhanced phase stability, and intrinsic alignment-free operation; key factors for future deployable quantum systems.

The device presented here was fabricated by Advanced Fiber Resources (AFR) Milan, a company specializing in high-performance LN modulators for telecom applications. This industrial maturity establishes TFLN as a prime candidate for integrated quantum photonic technologies in the next generation of quantum communication systems [248]. The following sections describe the design, modeling, fabrication, and characterization of the TFLN receiver.

4.1 Device architecture and design strategy

In this section, the **key performance requirements** that determine the main design parameters are described, and they are summarized in Table 4.1. The design process follows a series of trade-offs between optical performance, modulation speed, and detection capabilities. In the second part of this section, the overall device architecture and its detailed implementation are presented in accordance with outlined specifications.

The central design parameter is the target delay of the unbalanced MZI, which directly determines the time-bin separation. Increasing this separation requires a longer integrated delay line, which introduces higher unbalanced propagation losses between the two interferometer arms. For the TFLN platform used here, previous characterizations indicate a propagation loss of approximately 0.2 dB/cm, corresponding to about 0.26 dB for every 100 ps of delay. This attenuation degrades the maximum achievable interference visibility as the delay increases, an effect modeled and numerically quantified in Section 5.3.

Physical constraints	**Target / Constraint**	**Impact on design**
SNSPD resolution	55 ps jitter	Unbalanced MZI delay line
Optical propagation loss:	0.2 dB/cm	Quantum interference/visibility
MZM: optical loss	Trade-off with V_π and bandwidth	MZM design
MZM: bandwidth	< 100 GHz	MZM design
MZM: driving voltage (V_π)	< 5 V (CMOS compatible)	MZM design
Clock rate	Time-bin separation	Unbalanced MZI delay line
Pulse duration (FWHM)	< 1/5 time-bin separation	Unbalanced MZI delay line

Table 4.1: Main design parameters and their influence on the device architecture.

The choice of time-bin separation also determines the required modulation speed of the Mach–Zehnder modulator (MZM). To correctly switch between maximum and minimum transmission states, the device must operate at a frequency equal to the inverse of twice the time-bin separation. While a shorter delay line is desirable to maintain high interference visibility, the minimum achievable separation is ultimately limited by the EO modulation bandwidth of the MZM. In this respect, the TFLN platform provides sufficient bandwidth (exceeding 100 GHz [63]) to support separations in the tens-of-picoseconds range.

Furthermore, the optical pulse duration must be short enough to prevent temporal overlap between adjacent bins and ensure their orthogonality in the computational basis. For Gaussian-shaped pulses, the time-bin separation should be at least a few times the pulse width to preserve orthogonality (5 standard deviations for 1.24% overlap). While the TFLN platform features optical components operating in the C+L telecom bands, the performance of the overall system is limited by the optical bandwidth of the external components, including the nonlinear source, fibre-based components, filters, and the pulsed laser source. In addition, maintaining a limited optical bandwidth (e.g., ∼100 GHz, corresponding to ∼0.8 nm or ∼5 ps full width at half maximum (FWHM) for Fourier-limited pulses) is desirable to ensure compatibility with standard DWDM telecommunication systems.

Finally, the dominant constraint in this implementation arises from the detection system. The employed superconducting nanowire single-photon detectors (SNSPDs) exhibit a timing jitter of approximately 55 ps, setting a lower bound on the achievable time-bin separation. It is indeed essential that detection events from consecutive clock cycles remain distinguishable, and that the early and late time-bins can be reliably resolved in some of the experimentally implemented quantum applications.

Considering these constraints, two device versions were designed with time-bin separations of 100 ps and 50 ps, These correspond to switching rates of 5 GHz and 10 GHz, respectively. These values are well within the capabilities of the TFLN platform. The 50 ps and 100 ps separations enable the use of optical pulses with durations of a few tens of picoseconds, corresponding to optical bandwidths on the order of hundreds of GHz, while

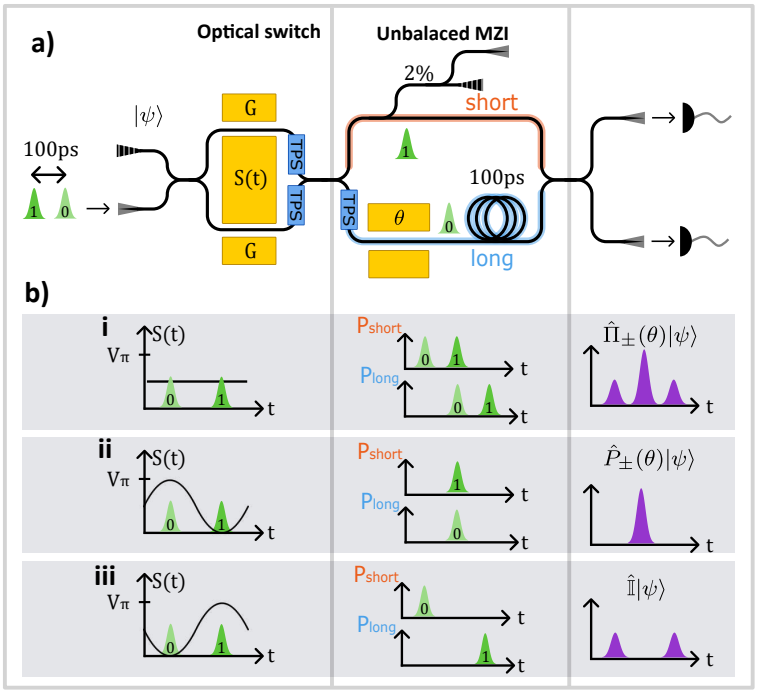

Figure 4.1: **Conceptual schematic.** **a)** Schematic of the integrated optical circuit. **b)** The evolution of the input photon state is illustrated for the three possible working conditions: (i) the first stage MZM is biased at quadrature with no RF modulation on the optical switch; (ii) the MZM is driven such that early (late) time-bin photons are routed into the longer (shorter) path of the unbalanced MZI; (iii) the RF modulation is inverted, routing early (late) photons into the shorter (longer) path.

remaining compatible with standard telecom channel allocations.

Overall this design strategy ensures an optimal balance between modulation speed, quantum interference performance, and detection constraints. In particular, the adoption of short time-bin separations—among the smallest reported for quantum time-bin encoding (see Table 6.1)—enables potential operation at repetition rates in the GHz regime.

A **conceptual schematic** of the device is shown in Figure 4.1a. The circuit is composed of two main functional stages arranged in a cascaded configuration. The **first stage** consists of a balanced MZM that operates as a reconfigurable optical switch. By appropriately driving the MZM, the optical transmission at one output port can be switched between its maximum and minimum values, while the complementary behavior appears at the second port. This function is implemented using long and broad modulation bandwidth EO phase modulators embedded in each arm of the interferometer and configured in a push-pull scheme [249]. In this configuration, equal but opposite phase shifts are applied to the two arms, maximizing modulation efficiency. Finally, two TPSs, one per arm, are included to control the bias point and ensure stable operation.

The **second stage** is an unbalanced MZI with a propagation delay of 100 ps. The relative phase shift between the two arms, and hence the working point of the interferometer, can be tuned using either thermal or EO phase modulators integrated on the longer arm. This stage enables interference between temporally separated components, allowing analysis of entangled time-bin states. The two interferometric stages are interconnected through 2×2

MMIs designed to operate as 50:50 beam splitters. The output ports of the unbalanced MZI are coupled to edge couplers for optical interfacing. In packaged devices, edge couplers provide access through standard optical fiber connectors.

In addition to the main components essential for implementing a PSL-free time-bin projector, a few **auxiliary optical structures** were integrated to facilitate device control and testing. At the input of the optical switch, the first MMI has two input ports: one connected to an edge coupler for quantum signal injection, and the second to a grating coupler for vertical access, enabling in-line monitoring during wafer-level testing. A second monitoring structure is included in the shorter arm of the unbalanced MMI. It consists of a 2% tap coupler followed by a 1×2 MMI that divides the signal between two outputs, one routed to an edge coupler and the other to a grating coupler. This configuration allows real-time monitoring of the optical switch operating point during operation. The second grating coupler also provides vertical access for wafer-level testing of the optical switch.

The overall layout of the fabricated chip is shown in Figure 4.2. Given the available die area of 14.4 mm $\times$ 3 mm, the optical layout was optimized to maximize spatial efficiency. The longer dimension of the chip is primarily used to accommodate the MZM, whose electrode length typically extends from the sub-centimeter to centimeter scale, and to implement the delay lines. Along the transverse direction, three different design variants are integrated on the same die (hereafter referred to as the n^{th} config.) to explore different modulation configurations, while maintaining compactness.

Two distinct delay lengths have been implemented for the unbalanced MZI: 100 ps and 50 ps. The 1^{st} and 2^{nd} configurations provide a 100 ps delay, while the 3^{rd} configuration features a 50 ps path-length delay. All designs include a TPS on the longer arm for static phase tuning. Among the 1^{st} and 2^{nd} configurations, the difference is that the 1^{st} configuration also integrates a high-speed EO phase modulator in the longer arm of the unbalanced MZI. The absence of a configuration that combine the EO phase modulator with a 50 ps delay is dictated by the intrinsic length of the delay line itself. The length of the integrated delay waveguide of approximately 0.7 mm is insufficient to accommodate the electrodes, particularly when accounting for waveguide routing constraints such as bends and minimum curvature radii. The chip layout was designed to be integrated into a standard metallic package, ensuring stable electrical and optical interfacing through conventional RF and fibre connectors. Further details on the packaging design and assembly are discussed in Section 4.5.2.

The following sections of this chapter describe the device development, as far as possible, in chronological order, from the initial design of the MZM to fabrication and final packaging. An exception is made for the "Quantum visibility modeling" which is presented in Section 5.3 as it depends also on the specific experimental setup in addition to the intrinsic device features. These steps are summarized in the workflow diagram shown in Figure 4.3. The initial phase consists of defining the target specifications, as outlined at the beginning of this section. These requirements, combined with the constraints imposed by the available die area, guide the design of the optical switch based on the MZM, which is described in Section 4.3. Subsequently, all the design considerations, including device specifications and packaging constraints, lead to the definition of the full chip layout, which has been presented

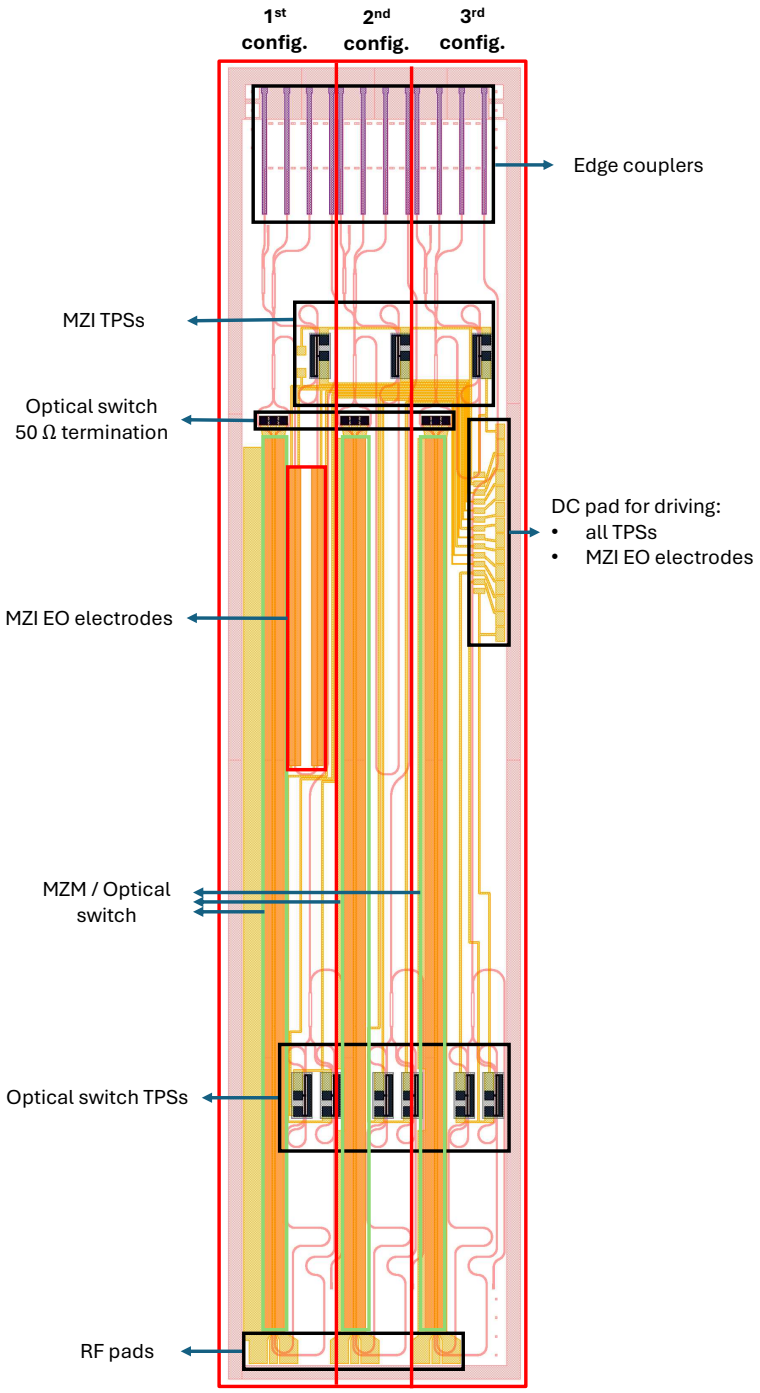

Figure 4.2: **Chip design.** Layout of the die developed for the TFLN receiver, showing the three implemented design variants with different unbalanced-MZI delays and phase-modulation configurations. The 1^{st} config. features a 100 ps delay with both EO and TPS modulators; the 2^{nd} config. also implements a 100 ps delay but includes only a TPS modulator; the 3^{rd} config. employs a 50 ps unbalanced MZI with a single TPS modulator. The available die dimension is 14.4 mm × 3 mm.

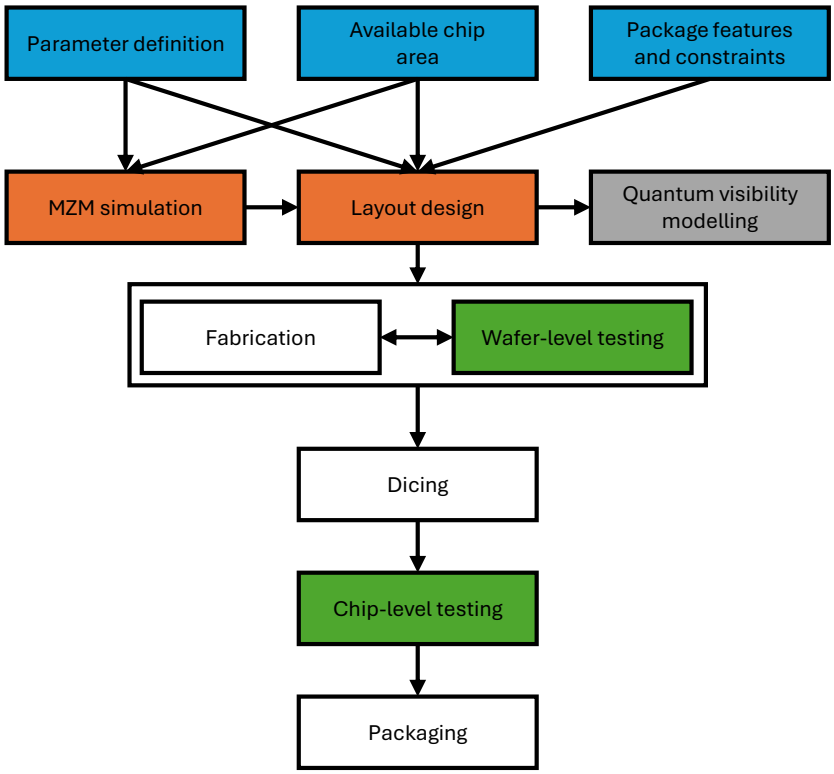

Figure 4.3: **Development workflow of the TFLN receiver.** Schematic representation of the procedural phases involved in the realization of the device.

in the second part of this section to provide an overview of the design choices. Once the design is finalized, the fabrication process begins. During fabrication, intermediate wafer-level characterizations are performed at key steps to monitor the process and ensure device performance. At the end of fabrication, the chips are diced, and 16 integrated optical chips from the first available wafer are tested, each including the three configuration variants. Based on these measurements, a subset of devices is selected for packaging and subsequent use in the quantum demonstrations.

4.2 Operating principles

The device is designed to operate on a generic single qubit served in its input

$$|\psi\rangle = \alpha\,|0\rangle + \beta\,|1\rangle\,e^{i\theta}$$

where α and β are the probability amplitudes, and θ is the relative phase between the two time-bins. Here, $|0\rangle$ and $|1\rangle$ correspond to the photon states in the early and late time-bins, respectively, separated by 100 ps (50 ps, according to the config.), as set by the path imbalance of the unbalanced MZI. By applying different modulation signals to the optical switch and

controlling the phase of the unbalanced MZI, the device can function as an arbitrary time-bin projector. Three distinct operating configurations have been identified and employed for experimental demonstrations, although other operating regimes can also be defined.

In the first configuration (*mode 1*), illustrated in Figure 4.1.i, the balanced MZM is biased at the quadrature point, acting as a 50:50 beam splitter. In this passive configuration, the device behaves like a standard time-energy or time-bin interferometer analyzer, equivalently consisting of only the unbalanced interferometer. When a generic optical field encoding the time-bin state $|\psi\rangle$ is injected, photons are randomly routed through either the short or long arm of the unbalanced interferometer. Those traveling through the longer arm experience the 100 ps (50 ps) delay, resulting in a three-peak detection pattern in the arrival-time histogram after recombination. Interference arises only in the central peak, where the early and late time-bins overlap temporally. More rigorously, this configuration implements the projection-valued measurement (PVM)

$$\hat{\Pi}_{\pm}(\theta) = \tfrac{1}{4}\hat{\mathbb{I}} + \tfrac{1}{2}\hat{P}_{\pm}(\theta), \tag{4.1}$$

where $\hat{\mathbb{I}} = |0\rangle\langle 0| + |1\rangle\langle 1|$ is the identity operator representing the non-interfering contributions from distinguishable events—namely, early (late) photons propagating through the short (long) arm, which correspond to the outer peaks in the detection histogram. While

$$\hat{P}_{\pm}(\theta) = \tfrac{1}{2}\big(\,|0\rangle \pm e^{i\theta}\,|1\rangle\,\big)\big(\,\langle 0| \pm e^{-i\theta}\,\langle 1|\,\big) \tag{4.2}$$

describes the temporally indistinguishable interferometric contribution associated with the central peak. The signs $\pm$ account for the dependence on the two output ports of the unbalanced MZI stage, which exhibit a relative phase shift of π.

The distinctive functionality of the device emerges when the MZM operates as a high-speed optical switch (*mode 2*), where photons in the early (late) time-bin are deterministically routed into the longer (shorter) arm of the unbalanced interferometer, as shown in Figure 4.1.ii. To deterministically route photons between two time-bins separated by 100 ps (50 ps), the MZM must be modulated between its maximum and minimum transmission within that interval, corresponding to a modulation frequency of 5 GHz (10 GHz). In this configuration, photons from the two time-bin slots are temporally overlapped at the output of the second interferometer, leading to a single interference peak in the detection pattern, where all photons contribute coherently. The implemented PVM corresponds to $\hat{P}_{\pm}(\theta)$ as defined in Eq. (4.2). By varying the phase θ in the longer arm of the unbalanced MZI—either via the TPS or the EO modulator—it is possible to project the time-bin state onto any equatorial state of the Bloch sphere (Figure 3.1), without requiring temporal post-selection. The phase control can be achieved with high precision and stability over long timescales (tens of hours) using the TPS, and at GHz speeds using the EO phase modulator.

A third operating condition (*mode 3*) is achieved when the modulation signal applied to the optical switch at 5 GHz (10 GHz) is phase-shifted by 180°, thereby reversing the photon routing, as illustrated in Figure 4.1.iii. In this configuration, measurement in the computational basis is performed by post-selecting detection events in the early or late time-bin,

maximizing the detection efficiency. Here, the PVM reduces to $\hat{\mathbb{I}}/2$, corresponding to projection of the qubit onto the poles of the Bloch sphere (Figure 3.1). The effective time-bin separation at the output doubles from 100 ps (50 ps) to 200 ps (100 ps), as the late (early) pulse propagates through the longer (shorter) interferometer path. This increased temporal separation relaxes the constraints on detector timing resolution, enhancing compatibility with detectors exhibiting moderate timing jitter.

Comparing *mode 1* and *mode 2*, there is a fundamental difference in the achievable interference visibility when all detected events are considered, i.e., without temporal post-selection. For a balanced time-bin encoded pure state $|\psi\rangle = (|0\rangle + |1\rangle)/\sqrt{2}$ at the device input, the maximum interference visibility at the output ports can be computed by applying the PVM associated with each *mode*. Thus, for *mode 1* we obtain:

$$\langle\psi|\,\hat{\Pi}_{\pm}(\theta)\,|\psi\rangle = \frac{1}{4} + \frac{1}{4}\left[1 \pm \cos(\theta)\right] \tag{4.3}$$

while for *mode 2*, employing active switching, we have:

$$\langle\psi|\,\hat{P}_{\pm}(\theta)\,|\psi\rangle = \frac{1}{2}\left[1 \pm \cos(\theta)\right] \tag{4.4}$$

Using the visibility V, defined in Eq. (3.30) as the figure of merit when varying the phase parameter θ, it follows that the achievable visibility contrast increases from a maximum of 50% in *mode 1* to 100% in *mode 2*, due to the active optical switching.

This distinction becomes even more significant when dealing with time-bin entangled photon pairs. Consider a maximally entangled Φ-type Bell state:

$$\left|\Phi^{+}\right\rangle = \frac{|00\rangle + |11\rangle}{\sqrt{2}} \tag{4.5}$$

where each photon of the pair is sent to a separate device, as in the schematic of Figure 3.13, both operating in *mode 1*. In this case, the overall PVM applied by the system corresponds to the tensor product of the two individual PVMs. For *mode 1*, the joint coincidence probability, dependent on both applied phases θ_A and θ_B, is:

$$C_{mode1}(\theta_A, \theta_B) = \left\langle\Phi^{+}\right|\hat{\Pi}_{\pm}(\theta_A) \otimes \hat{\Pi}_{\pm}(\theta_B)\left|\Phi^{+}\right\rangle = \frac{1}{4} \pm \frac{1}{16}\cos(\theta_A + \theta_B), \tag{4.6}$$

where the $\pm$ depends on which output port statistics are considered. As discussed in Section 3.5, applying temporal post-selection allows achieving 100% visibility by considering only the temporally overlapping bins. Conversely, if no temporal post-selection is applied, the resulting two-photon interference visibility is limited to

$$V = \frac{\max(C_{mode1}(\theta_A, \theta_B)) - \min(C_{mode1}(\theta_A, \theta_B))}{\max(C_{mode1}(\theta_A, \theta_B)) + \min(C_{mode1}(\theta_A, \theta_B))} = \frac{5-3}{5+3} = 25\%.$$

Since this visibility lies below the threshold of $1/\sqrt{2} \simeq 70.7\%$, the Bell-CHSH inequalities cannot be violated [250]. In this regime, temporal post-selection is required to recover quantum correlations, thereby introducing a PSL that undermines loophole-free nonlocality tests

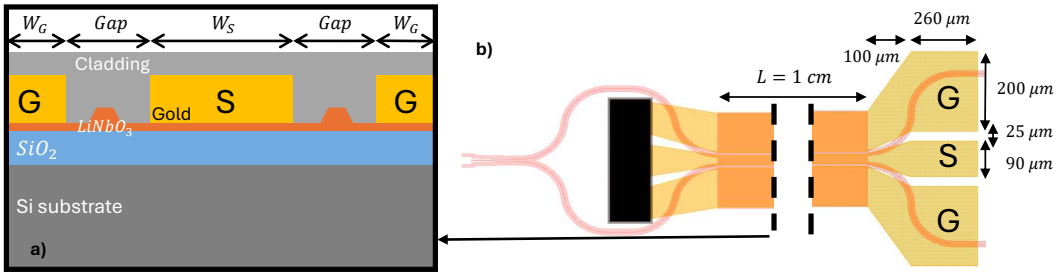

Figure 4.4: **MZM cross section. a)** Schematic cross section of the fabricated MZM, showing the main structural layers and the electrode geometry. The tunable geometrical parameters W_S, W_G, and *Gap* are indicated. **b)** Top-view layout of the coplanar waveguide (CPW) electrode structure in a ground-signal-ground (G-S-G) configuration.

and can compromise security in EBQKD systems [235]. Furthermore, even when temporal post-selection is applied, only 25% of the coincidence events contribute to quantum interference, thereby limiting the achievable SKR and requiring detectors with high temporal resolution for closely spaced time-bins.

In contrast, when both devices operate in *mode 2*, the time-bin components are deterministically overlapped, enabling maximum quantum interference. The corresponding measurement statistics are described by

$$C_{mode2}(\theta_A, \theta_B) = \left\langle \Phi^+ \right| \hat{P}_{\pm}(\theta_A) \otimes \hat{P}_{\pm}(\theta_B) \left| \Phi^+ \right\rangle = \frac{1}{4} \pm \frac{1}{4} \cos(\theta_A + \theta_B). \tag{4.7}$$

This configuration closes the PSL, produces a single interference peak in the time-resolved coincidence histogram, and achieves up to 100% visibility while increasing throughput by eliminating discarded events. It is important to note that the correlations for a single pair of output ports are normalized to $1/2$, since varying the $\pm$ indices accounts for the four possible combinations of the interferometer outputs.

As a result, this configuration enables entanglement certification without temporal post-selection and supports secure QKD with a fourfold increase in SKR across all mutually unbiased bases (X, Y, and Z), thanks to the reconfigurability and versatility of the developed device across both slow and high-speed operational regimes.

4.3 Optical switch design and simulation

The core element of the switching stage is a MZM, chosen for its ability to achieve high-speed optical modulation through the intrinsically broadband EO response of LN. The MZM functions as a controllable interferometer: the input optical signal is split into two arms, each undergoing phase modulation via the EO effect in a push-pull configuration. After recombination, the resulting interference depends on the relative phase difference between the two arms, producing an intensity-modulated output signal (see Section 2.1.4).

By driving the MZM between its two extreme transmission states (maximum and minimum), the device enables deterministic routing of photons between output ports, thereby implementing a high-speed optical switch. Phase modulation in the LN waveguides is

achieved by applying an electric field across the interferometer arms, exploiting the Pockels effect to modulate the refractive index, as discussed in Section 2.3.1. LN is particularly advantageous for this application due to its large EO coefficient, low optical loss, and broadband response, which together enable efficient and high-speed modulation in integrated photonic platforms.

The following section outlines the design and optimization of the MZM structure, emphasizing the trade-offs between optical, electrical, and fabrication constraints that determine high-speed modulation performance.

The optical switch was designed under both technological and performance constraints to ensure efficient modulation. Figure 4.4a illustrates a schematic cross section of the fabricated MZM, where the main geometrical parameters are indicated. Since the chip was fabricated on a shared wafer using the Advanced Fiber Resources Milan foundry process, the vertical stack parameters—including oxide and cladding thicknesses, waveguide height and etch depth, and metal layer thickness were fixed by the process flow. These parameter values are not explicitly reported here due to confidentiality agreements with the foundry. By contrast, the optimisation work carried out in this thesis focused on the in-plane geometrical parameters: the widths of the signal and ground electrodes (W_S and W_G), the electrode separation (Gap), and the electrode length (L), all of whose data are reported and have been tailored to meet the required electrical and optical performance.

In the following sections the engineering of the electrode geometry to ensure optimal operation in the gigahertz frequency regime is presented. Indeed, at such frequencies in TFLN technology, the electrodes behave as a traveling-wave transmission line rather than a lumped-element circuit. This is because the RF and optical fields co-propagate along the modulator when the RF wavelength becomes comparable to the electrode length (approximately 2 cm at 5 GHz in vacuum). To achieve efficient EO modulation, different design criteria have to be simultaneously considered:

- **Impedance matching:** The characteristic impedance of the RF line and the termination load should both match the 50 Ω source impedance to maximize power transfer and minimize reflections.
- **Velocity matching:** The RF phase velocity should be matched to the optical group velocity in the waveguide to maximize modulation bandwidth.
- **Field overlap optimization:** The spatial overlap between the RF and optical modes have to be maximized within the LN region to minimize the half-wave voltage (V_π).
- **Insertion loss minimization:** The electrodes must be positioned close enough to ensure strong modulation efficiency, while avoiding excessive optical absorption caused by the nearby metal layers.

A push-pull configuration was adopted, using a coplanar waveguide (CPW) electrode layout in a ground-signal-ground (G-S-G) geometry, as shown in Figure 4.4. In this arrangement, the ground electrodes are placed on the outer sides, while the central electrode carries the RF signal. The resulting electric fields in the two interferometer arms are equal in magnitude and opposite in direction, inducing symmetric but opposite refractive index variations.

4.3.1 Electrode geometry and cross-section modeling

As an initial step in designing the traveling-wave electrodes (TWE) for MZM, a parametric sweep was performed to identify electrode geometries that ensure optimal RF performance according ot the optical mode properties. This involved varying the in-plane geometrical features, specifically the signal electrode width W_S and the electrode Gap between the signal and ground lines, while fixing the ground electrode width at $W_G = 100\,\mu m$. This choice is justified because W_G has a negligible influence on the RF properties when it is significantly larger than W_S [251].

The propagation features of the optical mode are retrieved with the simulation software *Ansys Lumerical MODE 2020* [40]. The employed cross section structure involved the full oxide BOX layer thickness (refractive index from [252]), the LN waveguide with a rib geometry (refractive index from [253]), and the upper cladding layer. The FDE solver area is $10 \times 6\,\mu m$ with a 10 nm square mesh size. The simulated results yield an optical group index of $n_g = 2.35$ for the entire C+L band, which served as the target value for RF velocity matching. The optical field distribution, illustrated in Figure 4.6c, corresponds to the fundamental TE mode supported by the TFLN waveguide, designed for operation in the C+L telecommunication bands.

Similarly, the RF electromagnetic mode analysis was performed to extract the transmission line parameters of the TWE. In this case, the *Ansys CST 2023* solver [254] was used. The cross-sectional geometry of the TWE was defined with the appropriate material properties and dimensions. Importantly, the dielectric properties were defined at RF frequencies, where LN exhibits higher permittivity values ($\epsilon_{O,LN} = 43$ and $\epsilon_{E,LN} = 28$) compared to its optical refractive indices. The electrical conductivity of the gold electrodes was set to $\sigma = 4.56 \times 10^7\,S\,m^{-1}$, while the silicon substrate conductivity was set to $\sigma = 1 \times 10^{-2}\,S\,m^{-1}$, according to the used technology platform. The structure was excited using a wave port with dimensions of $200 \times 160\,\mu m$. A non-uniform mesh was employed, ranging from 80 nm to 50 µm square edge size, with the higher resolution in the electrode gap region where the optical waveguide is located. This allows accurate evaluation of the EO overlap integral, discussed in the following section. The electromagnetic field distribution was simulated at a frequency of 5 GHz, corresponding to the target modulation frequency for the 100 ps time-bin separation (2^{nd} and 3^{rd} config.).

Figures 4.5a and b show the simulated results for the transmission-line characteristic impedance (Z) and the microwave effective index (n_m) as functions of the signal electrode width (W_S) and the electrode Gap. From these results, an intrinsic trade-off between these parameters can be observed: a $50\,\Omega$ impedance can be achieved either by increasing the gap between the electrodes or by reducing W_S, whereas the RF effective index remains nearly constant with gap and slightly increases with wider signal electrodes. In summary, both Z and n_m should ideally be increased to reach their respective target values; however, achieving this requires opposite parameter adjustments. From the simulated parameter range and considering this trade-off, it follows that increasing the gap improves impedance matching and slightly raises the RF effective index. However, as discussed in the next subsection, this improvement comes at the cost of a significant increase in V_π, since a larger gap reduces

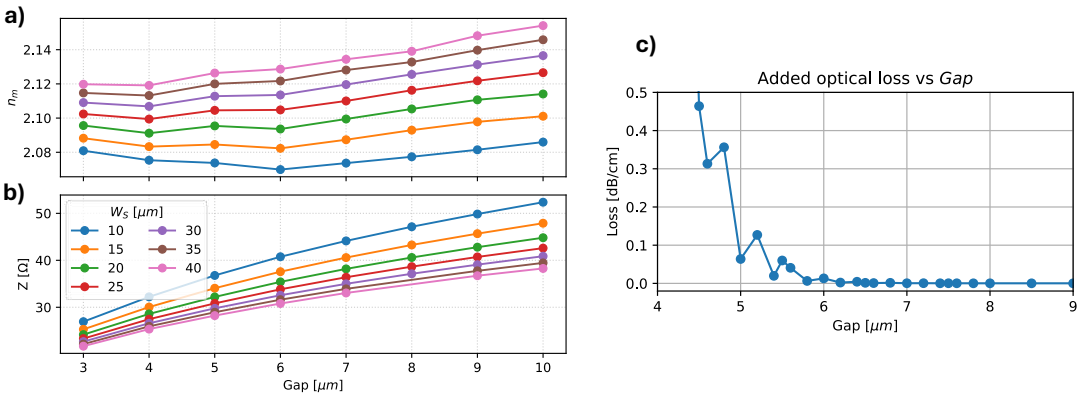

Figure 4.5: **RF and optical cross-section simulations. a)** Microwave effective index (n_m) and **(b)** simulated characteristic impedance (Z) as functions of the signal electrode width (W_S) and electrode Gap. **c)** Simulated optical propagation loss due to metal absorption as a function of the electrode separation (Gap). Narrower gaps enhance modulation efficiency but increase optical losses through stronger evanescent field coupling to the metal electrodes.

the electric-field overlap with the optical mode and consequently decreases the modulation efficiency.

Overall, within this parameter range, perfect impedance and velocity matching cannot be achieved simultaneously. Nevertheless, the resulting mismatch remains acceptable for the target operating frequency and intended application.

Finally, optical propagation losses were evaluated to quantify absorption caused by the overlap between the optical evanescent field and the metallic electrodes. To perform this estimation, simulations were carried out using the *Ansys Lumerical MODE 2020* solver, based on the same model employed for the optical mode analysis, but including the gold electrodes. Their absorptive properties were taken into account through the complex refractive index, specifically by considering the non-zero imaginary part, according to [252]. As shown in Figure 4.5c, the simulated losses rise steeply for narrow electrode gaps because of field-metal coupling. These values account only for excess losses due to metal absorption and exclude other contributions such as sidewall scattering or intrinsic material attenuation.

4.3.2 Electro-optic overlap integral

The modulation efficiency of the transmission-line geometry was evaluated through the calculation of the half-wave voltage-length product ($V_\pi L$), a key figure of merit that quantifies the voltage required to induce a π phase shift over a given modulator length.

The effective refractive index variation induced by the RF field in the LN waveguide is expressed by Eq. (2.18) in Section 2.3.1:

$$\Delta n_e = -\frac{n_e^3 r_{33} E_{\mathrm{RF}}}{2}, \tag{4.8}$$

where n_e is the extraordinary refractive index of LN, r_{33} is the EO tensor coefficient, and E_{RF} is the applied RF electric field along the extraordinary axis. LN exhibits strong birefringence, with its largest EO tensor component $r_{33} \approx 30.8\,\mathrm{pm\,V^{-1}}$ corresponding to the extraordinary

optical axis. For this reason, the electrode configuration was designed to generate an electric field as closely aligned as possible with this axis, thereby maximizing modulation efficiency.

Because the RF electric field is non-uniform across the rib waveguide and the optical mode partially extends into the cladding, the effective refractive index variation experienced by the optical mode is reduced by a factor Γ ($0 < \Gamma < 1$), known as the *overlap integral*. The simulated RF and optical field intensity distributions, extracted from the mode simulations described in the previous section, for the optimized MZM cross-section are shown in Figure 4.6a-c. These highlight the spatial confinement of the optical mode within the LN core and the corresponding RF field distribution in the electrode region. The optical waveguide is symmetrically positioned between the signal and ground electrodes to ensure optimal overlap between the optical and microwave fields. The RF field map reveals how the discontinuity of the dielectric permittivity across material interfaces imposes continuity of the displacement field $\mathbf{D} = \varepsilon\mathbf{E}$. As a result, the electric-field amplitude inside the LN region (Figure 4.6b) is significantly weaker than in the surrounding cladding, owing to the higher dielectric constant of LN ($\varepsilon_{E,LN} \approx 28$) compared to the cladding material ($\varepsilon_{clad} \approx 3.7$) at GHz frequencies.

The effective refractive index change can therefore be expressed as [243]:

$$\Delta n_{\text{eff}} = -\frac{n_e^3 r_{33} E_{\text{RF}} \Gamma}{2}. \tag{4.9}$$

The overlap integral Γ quantifies the spatial overlap between the RF and optical fields within the LN region and is defined as:

$$\Gamma = \frac{Gap}{V_{\text{RF}}} \frac{\iint_{\text{LN}} E_{\text{RF}}(x,y)\,|E_{\text{opt}}(x,y)|^2\,dx\,dy}{\iint_{\text{all}} |E_{\text{opt}}(x,y)|^2\,dx\,dy}. \tag{4.10}$$

where V_{RF} is the applied RF voltage, $E_{\text{RF}}(x,y)$ is the RF electric field distribution, and $E_{\text{opt}}(x,y)$ is the optical mode profile. The numerator integrates over the LN region, where the EO coefficient r_{33} is nonzero while the denominator normalizes the optical mode. The factor Gap/V_{RF} normalizes the RF field contribution, ensuring that Γ is a dimensionless quantity bounded between 0 and 1.

The phase shift induced in one arm of the MZM is given by:

$$\Delta\phi = \frac{2\pi}{\lambda}\Delta n_{\text{eff}} L = -\frac{\pi n_e^3 r_{33}\Gamma}{\lambda} E_{\text{RF}} L. \tag{4.11}$$

Assuming a uniform RF field ($E_{\text{RF}} \approx V_{\text{RF}}/Gap$), a reasonable approximation once the overlap factor Γ is included, the single-arm phase shift becomes:

$$\Delta\phi_{\text{arm}} = -\frac{\pi n_e^3 r_{33}\Gamma}{\lambda}\frac{V_{\text{RF}} L}{Gap}. \tag{4.12}$$

In a push-pull configuration, the differential phase shift doubles:

$$\Delta\phi_{\text{pp}} = 2\Delta\phi_{\text{arm}} = -\frac{2\pi n_e^3 r_{33}\Gamma}{\lambda}\frac{V_{\text{RF}} L}{Gap}. \tag{4.13}$$

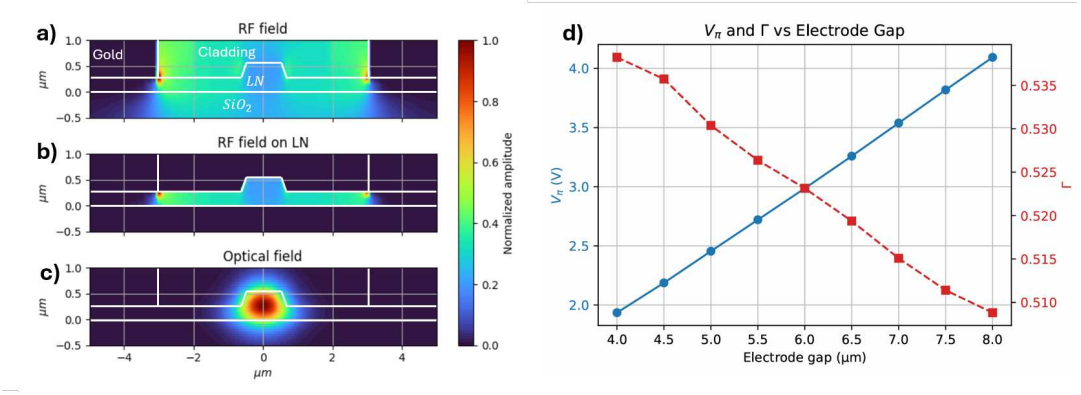

Figure 4.6: **Simulated V_π and overlap factor Γ. a-c)** Simulated distributions of the RF and optical field intensities in the MZM cross-section. **d)** Dependence of the calculated V_π (blue) and overlap integral Γ (red) on the electrode separation Gap. A larger gap improves impedance matching and optical losses but increases V_π due to reduced field overlap.

The corresponding $V_\pi L$ product is therefore:

$$V_\pi L = \frac{\lambda Gap}{2n_e^3 r_{33}\Gamma}. \tag{4.14}$$

Figure 4.6d reports the simulated dependence of both V_π and the overlap integral Γ on the Gap. As expected, V_π increases with larger Gap due to the weaker electric-field overlap with the optical mode, whereas Γ decreases correspondingly.

Considering the simulated performance parameters: impedance matching, RF effective index, modulation efficiency, and excess optical loss; the final electrode geometry was chosen to provide a balanced trade-off among all these factors. The optimized design features a central signal width of $W_S = 25\,\mu m$, a $Gap = 6\,\mu m$, and a ground width of $W_G = 100\,\mu m$. Numerical simulations yielded an overlap factor of $\Gamma = 0.52$, corresponding to a predicted $V_\pi L \approx 3\ V \cdot cm$ at $\lambda = 1550$ nm. This estimate assumes ideal impedance-matched conditions, while the simulated characteristic impedance of approximately $35\,\Omega$ introduces partial reflections at the MZM input, reducing the effective RF voltage across the electrodes, as estimated in the following Section.

Nevertheless, the simulation results confirm that the selected geometry enables efficient EO modulation suitable for high-speed, low-voltage operation on the TFLN platform. The predicted performance meets the design goals, especially the target V_π below 5 V, and demonstrates potential compatibility with CMOS-level electronic drivers [255].

4.3.3 RF performance and scattering parameter analysis

After defining the optimized transverse geometry of the RF electrodes, the frequency-dependent characteristics of the TWEs was analyzed using full 3D electromagnetic simulations. The main outcomes of this analysis are the simulated scattering parameters (S-parameters), which describe the transmission and reflection behavior of the RF signal along the modulator electrodes. By combining the simulated electrical scattering parameters with an analytical model, presented in the following, it is possible to retrieve the frequency-dependent EO

modulation performance. As a starting point, the total length of the MZM modulation section was set to 1 cm, taking into account both the available chip length (14.4 cm) and the target half-wave voltage of $V_\pi \approx 3\,\mathrm{V}$.

The electromagnetic simulations were performed using *Ansys CST 2023* [254]. In this case, the 3D geometry was defined starting from the cross-sectional model used for the RF mode simulations. The structure was extended to the electrode length of 1 cm, and the same material properties were adopted as in the previous RF mode simulations, with the addition of a second wave port at the end of the transmission line. Figure 4.7 reports the simulated electrical scattering parameters (S_{11} and S_{21}) for the selected electrode design, showing a 3 dB electrical bandwidth of 13.8 GHz. Also in this case RF propagation losses were accounted for by considering the finite electrical conductivity of gold ($\sigma = 4.56 \times 10^7\,\mathrm{S\,m^{-1}}$) and the silicon substrate ($\sigma = 1 \times 10^{-2}\,\mathrm{S\,m^{-1}}$). Dielectric losses in the LN layer and in the cladding were not included in the model, as they are negligible over the considered GHz frequency range [256]. Surface roughness effects were also neglected, since they become relevant only when the root-mean-square roughness is comparable to the skin depth $\delta = \sqrt{\frac{2}{\omega\mu_0\mu\sigma}}$ [257]. In the present case, for the gold electrodes—which exhibit the highest electrical conductivity in the simulated system and therefore the smallest skin depth—the skin depth at the operating frequency of 5 GHz is approximately 1 µm, which is significantly larger than the roughness of the fabricated material interfaces. Therefore, its impact can be safely neglected.

Based on the extracted RF parameters, the corresponding EO modulation response as a function of frequency can be estimated analytically following the model proposed in [258]. Precisely, the EO modulation response is defined as the logarithmic ratio between the voltage amplitude detected at the photodetector ($V_{\mathrm{out}}(f)$) that measures the optical output power modulation, and the amplitude of the applied RF driving signal ($V_{\mathrm{in}}(f)$). Under the assumptions of small-signal modulation and quadrature biasing of the modulator, the optical output power varies linearly with the applied RF signal:

$$M(f) = 20\log_{10}\left\{\frac{V_{\mathrm{out}}(f)}{V_{\mathrm{in}}(f)}\right\} = 20\log_{10}\left\{\frac{1}{V_{\mathrm{in}}(f)}\frac{1}{L}\int_0^L V_{\mathrm{in}(f)}e^{-(\alpha(f)+ib(f))l}\,dl\right\}. \tag{4.15}$$

Here, L is the electrode length, and $\alpha(f)$ is the RF attenuation coefficient, extracted from the magnitude of the simulated S_{21} parameter as a function of frequency. The term $b(f) = (n_m - n_g)\frac{2\pi f}{c}$ accounts for the phase mismatch between the microwave and optical waves, where $n_m = 2.105$ and $n_g = 2.35$ denote the microwave effective index and the optical group index, respectively.

The physical meaning of this formulation is that the effective phase modulation of the optical signal—that is directly proportional to the modulation voltage because of Pockels effect—arises from the superposition of infinitesimal EO contributions ($\propto V_{\mathrm{in}}e^{-(\alpha+ib)l}$) along the propagation direction. These contributions are weighted by the local RF voltage amplitude, which decays along the electrode length and is accounted by the parameter α, and by the relative RF phase experienced by the optical wave, which is accounted by the parameter

b. Following [243], the previous expression can be rewritten in the following form:

$$M(f) = 20\log_{10}\left\{ e^{-\frac{\alpha L}{2}} \left[\frac{\sinh^2\left(\frac{\alpha L}{2}\right) + \sin^2\left(\frac{bL}{2}\right)}{\left(\frac{\alpha L}{2}\right)^2 + \left(\frac{bL}{2}\right)^2} \right]^{1/2} \right\}. \tag{4.16}$$

Thus, the simulated EO modulation bandwidth is reported in Figure 4.7 , for the simualted α and b values, and with the selected $L = 1\,\text{cm}$. It exhibits a 3 dB bandwidth of approximately 30 GHz, while the purely electrical response at this frequency is reduced by about 5 dB. This behavior is a characteristic feature of traveling-wave modulators, for which the EO bandwidth can exceed the purely electrical (EE) bandwidth in the absence of, or in the presence of only small, velocity mismatch. This occurs because the electrical bandwidth is determined solely by the RF voltage amplitude at the end of the transmission line, while the EO response results from the cumulative contribution of all infinitesimal modulation segments along the electrode length. In the ideal case of perfect velocity matching, the 3 dB EO bandwidth corresponds to 6.41 dB the EE bandwidth. In the present case, the residual velocity mismatch is expected to reduce this enhancement by approximately 1.41 dB.

In general, as indicated by Equation (4.16), increasing the MZM length leads to a reduction of the EO bandwidth due to two main effects. First, higher RF attenuation along the electrodes reduces the delivered electrical signal, with losses scaling as αL, where α depends primarily on the electrode cross-section geometry. Second, velocity mismatch between the microwave and optical waves further limits the bandwidth, with the corresponding term scaling as bL. At the same time, the modulator length directly influences the half-wave voltage V_π, which decreases approximately as $1/L$. Therefore, the electrode length represents a trade-off parameter between high-speed operation and low driving voltage requirements.

The MZM requires electrical connection to the RF lines of the package through wire-bonding techniques in order to effectively feed the modulation signal. To enable reliable wire bonding, the electrodes must be wider than the 25 µm signal electrode used in the traveling-wave section. For this reason, the on-chip transmission line includes widened metal contact pads connected to the TWE through tapered transition sections, as illustrated in Figure 4.4b. To guarantee sufficient space for reliable bonding, the width of the central signal electrode in the pad region was chosen to be 90 µm. From a geometrical standpoint, the pads and the tapered transition are realized by depositing the metal layer above the cladding layer, while the electrical contact with the underlying RF transmission line of the MZM is maintained on the edge taper side towards the MZM electrodes. The RF pad design followed a procedure similar to that adopted for the TWEs. First, a 2D RF modal simulation was performed to define the pad cross-section geometry. Subsequently, full 3D electromagnetic simulations were carried out to extract the frequency-dependent scattering parameters of the pads and tapered transition. In this case, optimization of the EO modulation efficiency was not required, as the pad region does not overlap with the optical waveguides. Therefore, the design was driven primarily by RF impedance matching considerations and geometrical constraints related to wire bonding. As shown in Figure 4.4b, the final pad geometry features a signal electrode width of 90 µm, ground electrodes with a width of 200 µm, and a gap of 25 µm

between signal and ground electrodes. Compared to the TWEs, the increased ratio between signal width and gap results in a characteristic impedance of about 50 Ω to interface with standard external RF instrumentation and components. The pad length is 200 µm, followed by a tapered transition region of 100 µm that connects the pad geometry to the narrower TWEs. The overall structure of pad and tapper ensures a flat frequency response over the operating frequency range up to 20 GHz.

Overall, the electrode design features a 50 Ω transmission line in the pad region, followed by a tapered transition to the 35 Ω TWEs. The TWEs are terminated on-chip with two 70 Ω resistors connected in parallel between the signal and ground electrodes, providing an effective termination impedance of 35 Ω, which matches the simulated characteristic impedance of the traveling-wave structure.

The residual impedance mismatch between the external 50 Ω RF components and the on-chip 35 Ω electrodes introduces a power reflection at the input of the MZM. The corresponding voltage reflection coefficient is given by:

$$\Gamma = \frac{Z_L - Z_0}{Z_L + Z_0} = \frac{35 - 50}{35 + 50} \approx -0.176. \tag{4.17}$$

The associated reflected power fraction is $|\Gamma|^2 \approx 3.1\,\%$. From this result, the power successfully delivered to the MZM electrodes can be estimated as $P_{\text{del}} = (1 - |\Gamma|^2)P_{\text{in}}$, where P_{in} is the incident RF power. Given that $P = V^2/(2Z)$, the delivered voltage amplitude V_{del} across the 35 Ω electrodes relates to the input amplitude V_{in} in the 50 Ω line as follows:

$$P_{\text{del}} = \frac{V_{\text{del}}^2}{2Z_L} = (1 - |\Gamma|^2)\frac{V_{\text{in}}^2}{2Z_0} \tag{4.18}$$

$$V_{\text{del}} = V_{\text{in}}\sqrt{(1 - |\Gamma|^2)\frac{Z_L}{Z_0}}. \tag{4.19}$$

Substituting the design values, we obtain $V_{\text{del}} \approx 0.824\,V_{\text{in}}$. This indicates that while only 3.1 % of the power is lost to reflections, the lower characteristic impedance of the electrodes results in a delivered voltage amplitude that is approximately 82 % of the input signal amplitude.

4.4 Wafer-level processing

The fabrication of the integrated photonic circuits was carried out using the TFLN process developed by Advanced Fiber Resources Milan for high-speed modulators. Rather than defining a new technological process, this work leveraged Advanced Fiber Resources's platform to integrate multiple optical components with distinct functionalities on a single chip, including high-speed EO modulators, MMIs, TPS, and fiber-to-chip coupling interfaces. This strategy enabled the realization of a more reliable and scalable photonic device tailored for quantum communication experiments.

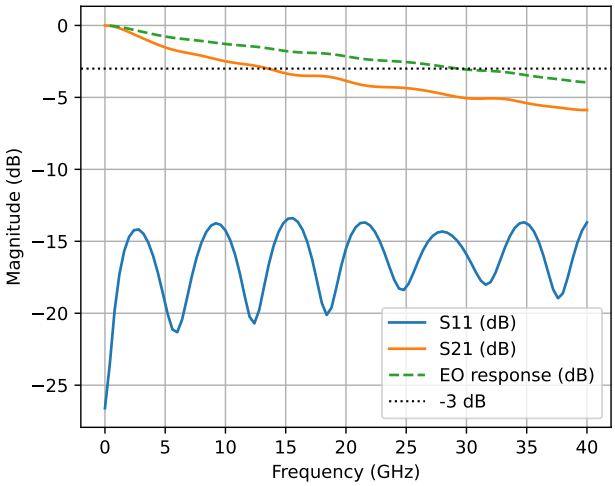

Figure 4.7: **Scattering parameters.** Simulated electrical scattering parameters (S_{11} and S_{21}) of the designed TWE structure 1 cm long, together with the corresponding theoretical EO modulation response that is derived analytically from the simulated parameters according to Eq. (4.15).

4.4.1 Fabrication

The devices were fabricated on an X-cut LNOI wafer featuring a 550 nm-thick LN device layer atop a BOX layer. Optical waveguides were defined using a rib geometry, where half of the LN layer was etched to form the guiding region. LN is etched by reactive-ion etching (RIE), which provides high anisotropy and smooth sidewalls. The areas to remain unetched were protected by a photoresist layer, whose pattern was defined by the dedicated mask layout.

After the etching step, an annealing process was carried out to reduce crystal defects and surface roughness introduced during etching [259]. This thermal treatment improves the crystalline quality of LN and decreases optical scattering losses along the waveguide.

Titanium thin films were then deposited and patterned to form resistive heaters for the TPS and to realize the terminations of the MZM TWE. By properly adjusting geometric parameters such as the width and thickness of the titanium features, the desired sheet resistance along the waveguide was achieved.

Gold layers were subsequently deposited by electroplating to form the TWEs of the MZM and the metal routing interconnections between the RF contact pads and the TPS. Gold was chosen for its high electrical conductivity and chemical stability, which ensure low-loss RF propagation and long-term device reliability.

A cladding layer was then deposited over the LN and metal structures to provide electrical insulation and mechanical protection during subsequent processing and packaging steps. This cladding ensures both optical confinement and environmental protection for the LN structures. Finally, openings were lithographically defined and etched into this dielectric layer to expose the electrical contacts and RF pads.

Cell name	Components / Configurations
Quantum receiver (QR) (Columns 2 and 4, 16 cells)	1^{st} config.: 100 ps delay, EO phase modulator in the unbalanced MZI 2^{nd} config.: 100 ps delay, TPS only in the unbalanced MZI 3^{rd} config.: 50 ps delay, TPS only in the unbalanced MZI
Test cell (TC) (Columns 2 and 4, 16 cells)	MZM with RF termination MZM without termination (open electrode) MMI test structures
Non-target designs (Columns 1, 3, and 5)	Ring resonators for optical loss characterization

Table 4.2: Distribution of cell types across the wafer layout and corresponding components.

4.4.2 Characterization

Wafer-level tests were performed to verify the quality and uniformity of the fabrication process by measuring dedicated on-chip optical test structures. The performance of these structures provides direct feedback on the effectiveness of the fabrication steps, enabling continuous monitoring and optimization of the overall technology flow. Since all processing stages are carried out directly on the wafer, these evaluations must be completed prior to the dicing stage.

During wafer-level testing, optical access to the integrated components is achieved through grating couplers, which enable vertical coupling between on-chip waveguides and external optical fibers. The wafer layout includes both individual optical components corresponding to those used in the main photonic circuit, as well as dedicated structures for process control and loss characterization. Figure 4.8 shows a schematic of the wafer layout, highlighting its division into cells. The wafer is organized into five vertical columns, each containing a stack of chips with a dedicated design. The chip developed in this work is located in the second and fourth columns, together with a dedicated test cell containing structures exclusively for characterization. These two cells are replicated eight times in each column, resulting in a total of 16 dies. These positions are labeled as "wafer field positions" or "chip IDs" and are used as references during the characterization description in the next sections.

A summary of the tested components and chip variants is reported in Table 4.2. The designed chip, labeled as QR, integrates the three configurations. The test cells (TC) include several structures for performance evaluation. Among these, the most relevant for this work are the MMI and the MZMs, which replicate the same electrode geometry used in the quantum receiver. Two MZM variants are included: one with RF termination and one without, enabling comparative analysis. Finally, the first, third, and fifth columns host auxiliary designs that are not directly related to the objectives of this work. However, they include resonant optical structures used for optical loss characterization, and their results have been considered for the evaluation of propagation losses. The results obtained from the wafer-level tests are discussed in the following paragraphs.

Propagation loss and group index Propagation loss is one of the key indicators of fabrication quality during the wafer process, as it directly reflects the optical performance of the

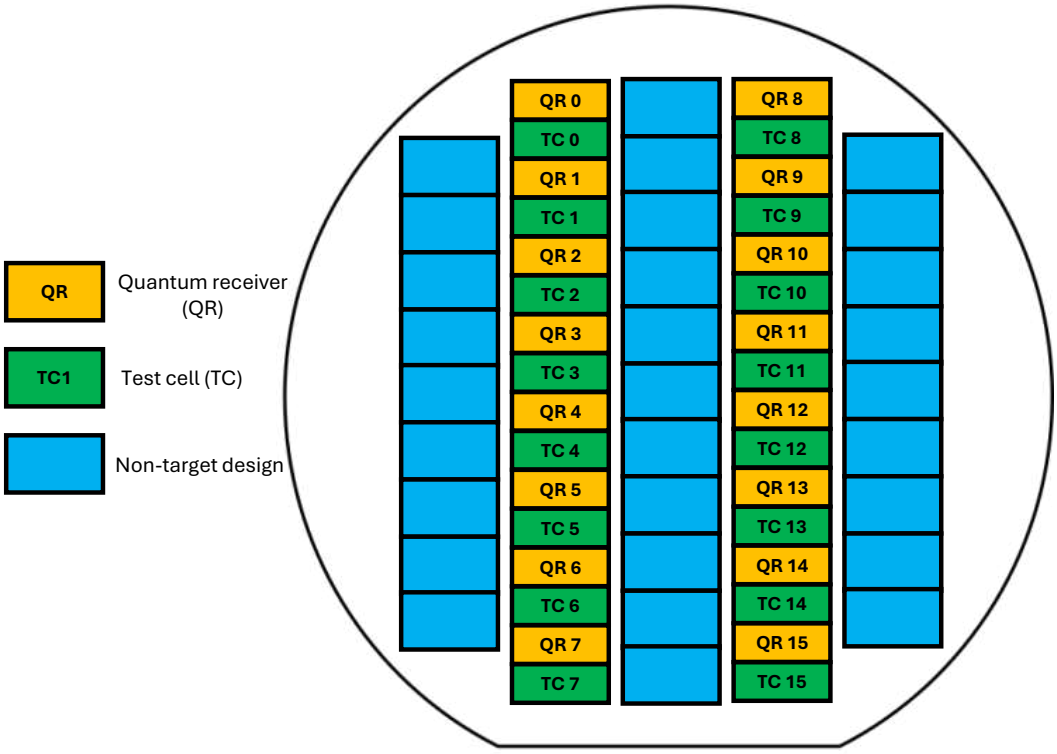

Figure 4.8: **Wafer layout.** Schematic of the position allocation of the chip designs across the 4 inch wafer, highlighting the distribution of the main photonic circuit design (QR) and the test structures (TC) used for performance evaluation and process monitoring.

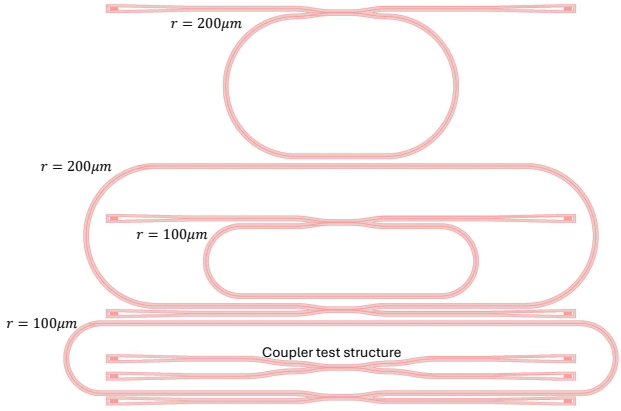

Figure 4.9: **Design of the optical ring resonator test structures.** Layout of the four racetrack-shaped resonators with different bending radii (100 µm and 200 µm) and straight section lengths, used to evaluate propagation losses and process uniformity. A directional coupler structure is also included to measure the coupling coefficient between the waveguide and the resonator.

fabricated waveguides. In TFLN waveguides, propagation losses are particularly sensitive to sidewall roughness introduced during etching, which can lead to increased scattering.

In our case, propagation losses were evaluated using dedicated optical test structures based on ring resonators, placed in the dedicated dies as indicated in Table 4.2 and Figure 4.8. By analyzing the optical transmission spectra of the resonators, it is possible to extract the waveguide propagation losses.

In particular, the optical structures in each cell include four racetrack-shaped resonators, each consisting of two semicircular bends connected by straight waveguide sections, as shown in Figure 4.9. Two designs employed smaller radii of 100 µm, while the other two used larger radii of 200 µm. For each radius value, one resonator had a longer and one a shorter straight section, allowing analysis of the dependence of propagation loss on the total straight-section length. In total, four resonators are placed in a cell, along with one coupling structure composed of a directional coupler to measure the coupling coefficient.

In this section, a brief description of the theoretical model used to analyze the ring resonator measurements is presented. A detailed derivation of the dependence of these quantities on the waveguide loss can be found, for instance, in [260]. The input optical signal was swept over a wavelength range from 1540 nm to 1560 nm, allowing the extraction of key propagation properties by analyzing the transmission response of the resonant structure around the central telecom wavelength range.

In a ring resonator, for specific wavelengths, constructive interference occurs when the optical field circulating in the ring is in phase with the injected light. Under these resonance conditions, the circulating light constructively interferes within the resonator, leading to light power enhancement within the resonant waveguide of the ring. As a result, at resonance wavelengths, the transmitted intensity at the output port is strongly reduced. A representative example of the measured transmission spectra is shown in Figure 4.10a and b. The spectral response exhibits few characteristic features that can be analyzed to retrieve the optical properties of the waveguide and the resonator. The most relevant parameters include:

- the **FSR**, defined as the wavelength spacing between two adjacent resonance dips, which is related to the optical group index;
- the **FWHM** of each resonance, corresponding to the linewidth of the transmission dip.

From these parameters, it is possible to estimate key quantities such as the waveguide propagation loss and the group index, the latter being crucial for the design of the optical switch.

The FSR of a ring resonator is related to the **group index** n_g and the resonator round-trip length L. The physical condition defining the FSR is that two consecutive resonance wavelengths correspond to constructive interference within the resonator. This implies that the phase accumulated by light after one round trip differs by 2π between two successive resonances:

$$\beta(\lambda_1)L - \beta(\lambda_2)L = 2\pi, \tag{4.20}$$

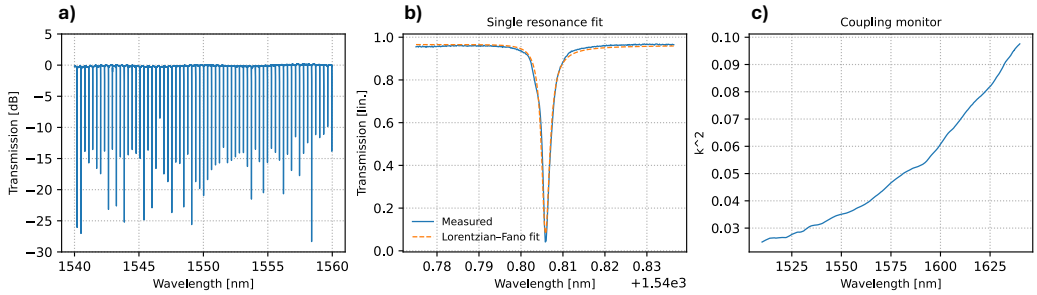

Figure 4.10: **Example of measured ring resonator transmission spectra. a)** Typical transmission spectrum from a racetrack-shaped ring resonator with a radius of 100 µm, used to extract the propagation loss and group index. The resonance dips correspond to the wavelengths fulfilling the resonance condition of the cavity. **b)** Zoomed-in view of a single resonance with the fitted Lorentzian-Fano curve [261], from which the FWHM is extracted. **c)** Broadband spectrum of the measured power coupling coefficient between the bus waveguide and the resonator, showing the wavelength-dependent coupling efficiency.

where $\beta = 2\pi n_{\text{eff}}/\lambda$ is the propagation constant. Expanding $\beta(\lambda)$ around the central wavelength λ and using the definition of the group index

$$n_g = n_{\text{eff}} - \lambda \frac{dn_{\text{eff}}}{d\lambda}, \tag{4.21}$$

one obtains

$$\text{FSR} = \Delta\lambda = \frac{\lambda^2}{n_g L}. \tag{4.22}$$

Rearranging yields the standard expression for the group index n_g, often used to extract from measured FSR values:

$$n_g = \frac{\lambda^2}{\text{FSR} \cdot L}, \tag{4.23}$$

where λ is the central (resonant) wavelength and L is the optical round-trip length of the racetrack resonator (for a racetrack geometry, $L = 2\pi R + 2L_{\text{straight}}$).

The **propagation loss** can be retrieved from the finesse F of the resonance, defined as $F = \text{FSR}/\text{FWHM}$, and from the coupling coefficient k between the bus waveguide and the resonator. The relationship between the measured quantities and the resonator parameters can be expressed as the following system:

$$F = \frac{2\pi}{\alpha L + k^2}, \tag{4.24}$$

where αL represents the round-trip loss in the resonator and k^2 is the power coupling coefficient, independently measured using the dedicated directional coupler structure (see Figure 4.10c). Thus, the losses can be retrieved as:

$$\alpha L = \frac{2\pi}{F} - k^2. \tag{4.25}$$

It is important to note that the previous formulas are strictly valid only under the assumption of uniform propagation loss throughout the resonator. In our case, this assumption does not hold due to the racetrack geometry of the resonators. Indeed, the propagation loss in the bending regions is expected to be higher because the optical mode propagates asymmetrically, with a larger portion of power overlapping the waveguide boundaries where scattering losses occur. Therefore, the total round-trip attenuation αL should be expressed as the sum of two contributions, corresponding to the straight and bending sections of the racetrack:

$$\alpha L = \alpha_s L_s + \alpha_b L_b, \tag{4.26}$$

where α_s and α_b are the propagation loss coefficients for the straight and bending sections, respectively, and L_s and L_b are their corresponding lengths.

The same consideration applies to the extraction of the group index, since the mode distribution is asymmetric in the bending sections. Therefore, the effective group index should be weighted according to the relative lengths of the straight and curved sections:

$$n_{gs} L_s + n_{gb} L_b = \frac{\lambda^2}{\mathrm{FSR}}, \tag{4.27}$$

where n_{gs} and n_{gb} are the group indices of the straight and bending sections, respectively.

By using the four different racetrack designs with varying straight-section lengths, which are known from the design layout, it is possible to independently extract the propagation loss and the group index in the straight waveguide section, while the bending contribution can be estimated or treated as a fixed offset. In Figure 4.11, the computed performance parameters of both propagation loss α_s and group index n_{gs} are reported as a function of wavelength after the LN etching step and both prior and after to the deposition of the cladding. As can be seen by comparing the data in Figure 4.11a and b, the propagation losses are higher in the early measurements due to the larger refractive index contrast at the uncovered LN-air interface. After cladding deposition, the propagation losses decrease on average from 0.26 dB/cm to 0.23 dB/cm, and the measured group index slightly reduces on average from approximately 2.3 to 2.25.

Half-Wave Voltage (V_π). The wafer layout includes dedicated test cells (TC, according to Figure 4.8 and Table 4.2) containing MZMs that replicate the same electrode geometry used in the final integrated device, enabling direct assessment of the EO modulation performance across the wafer after the electrode deposition step. Light is coupled through grating couplers, while the RF electrodes are contacted with electrical probes. Two MZM variants were implemented: one with terminated TWE (as in the optical switch) and one with an open, non-terminated electrode. For both modulators, the half-wave voltage V_π was measured at a relatively low frequency (1 MHz) by applying an RF drive with amplitude on the order of V_π and simultaneously recording the time traces of the applied RF voltage and the photodiode output (Figure 4.12a). By fitting the transfer curve with the standard sinusoidal MZM model, the estimated V_π was extracted (Figure 4.12b).

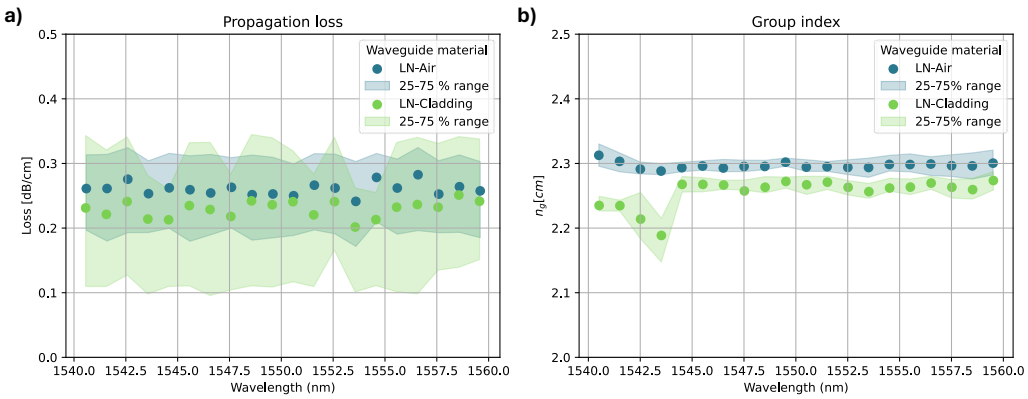

Figure 4.11: **Extracted optical parameters from ring resonator measurements.** Propagation loss **a)** and group index **b)** as functions of wavelength, obtained from wafer-level measurements of the racetrack resonators before and after cladding deposition.

The measured V_π values, mapped across the different wafer field positions, are reported in Figure 4.12c, together with the electrode load resistance for the terminated variant. Considering that the 16 field positions are distributed in a grid across the wafer and that the designed device is in close proximity to the test structures, analysing the spatial distribution of the measuredV_π values provides a direct assessment of the EO modulation performance across the wafer for the target designed chip.

The measurements were performed after the gold-electrode deposition, providing a direct assessment of the EO modulation efficiency prior to dicing and packaging. From the results, it can be observed that the measured V_π in the open configuration is lower than in the terminated case of about 0.2 V. This can be attributed to the voltage drop across the gold electrode: the small signal-electrode width W_S introduces a resistive effect that causes part of the applied voltage to drop along the electrode as the RF current flows through it. In contrast, in the open configuration the applied voltage is constant along the entire electrode length, resulting in a lower effective V_π. The measured V_π values in both configurations are higher than the simulated ones. This discrepancy can be attributed to non-ideal realization of the electrode geometry, in particular to a larger than designed electrode gap, and by over-etching of the LN in the waveguide definition. Both factors reduce the EO overlap factor Γ, thereby increasing the V_π.

Multi-Mode Interferometers The 2×2 MMIs were characterized to determine their power-splitting ratio, which ideally should be 50:50 between the two output ports, independently of the input port. Any imbalance in the splitting ratio limits the performance of the cascaded interferometric stages, particularly under destructive-interference conditions. This characterization is important in our device, since the circuit integrates two cascaded interferometers; thus, the MMI balance directly influences the achievable interference visibility.

The MMIs were evaluated by connecting multiple stages in cascade, up to a maximum of eight segments. Transmission spectra were measured for both the "through" and "cross" ports, corresponding to all-through and through-cross connections, respectively. By fitting

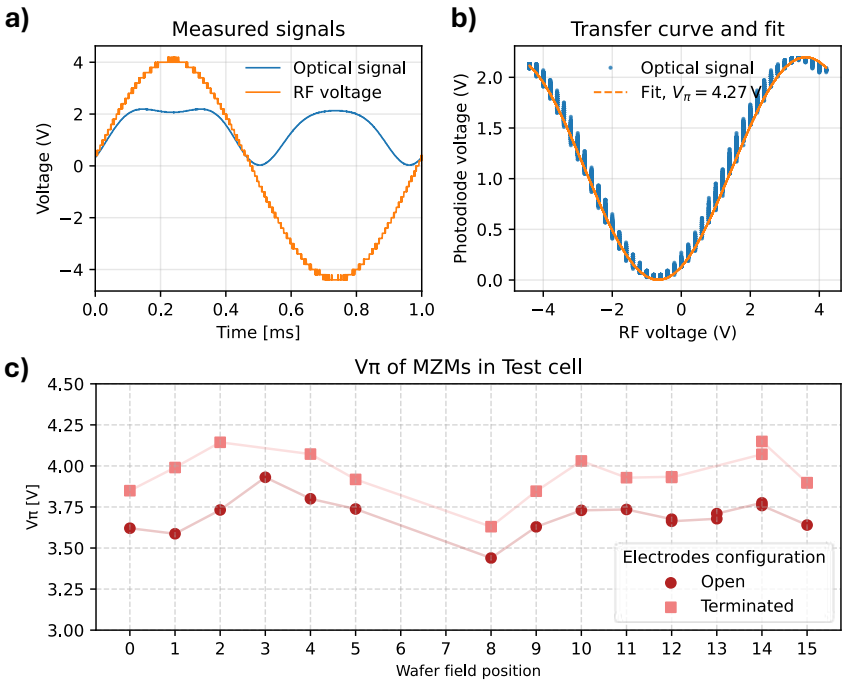

Figure 4.12: **Wafer-level V_π characterization. a)** Example of optical and electrical time-domain traces acquired from one test structure, showing the applied RF voltage and the corresponding photodiode response at 1 MHz. **b)** The associated MZM transfer curve of **(a)**, showing the photodiode output as a function of the applied RF voltage, with a sinusoidal fit used to extract V_π. **c)** Spatial distribution of the measured V_π values across the wafer for the MZM test structures.

the total insertion loss as a function of the number of cascaded segments, the average per-MMI loss was extracted for each configuration, as illustrated in Figure 4.13a. Ideally, each 2×2 MMI contributes approximately 3 dB of loss (50% power splitting per output branch).

Figure 4.13b summarizes the statistical results obtained across the multiple test structures on the wafer. The performances have been evaluated within a broad spectral region (1500-1600 nm). The measured imbalance between the two output ports is on the order of 1%. Some excess loss has been found in the region between 1500 and 1525 nm. However, the design was optimized to guarantee the desired coupling in the C+L band (1530-1625 nm). Overall, these results confirm that the MMI fabrication process achieves low excess loss and near-ideal power splitting performance, enabling high-contrast interference in the final integrated device. After wafer-level testing, the wafer was diced, yielding 16 chips, each containing the three optical circuit configurations.

4.5 Chip-level processing

The following section describes the evaluation steps and procedure used to identify the optical chips with the best performance among the 16 available that have been fabricated, so that only a limited number of them are selected for the packaging process. Among the three circuit configurations that each chip integrates, the 3^{rd} configuration, featuring 50 ps delay,

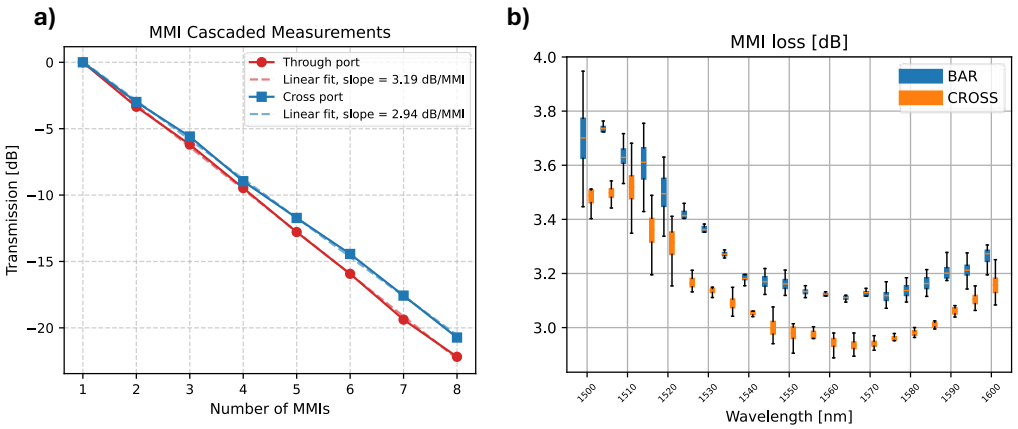

Figure 4.13: **Characterization of the 2×2 multi-mode interferometers (MMIs). a)** Example of measured transmission as a function of the number of cascaded MMI segments for both "through" and "cross" ports, used to extract the insertion loss per MMI stage. **b)** Statistical summary of MMI performance across the wafer, showing insertion loss and splitting-ratio uniformity. The results confirm low excess loss and near-50:50 splitting balance, suitable for high-visibility interferometric operation in the final device.

was not investigated. Its shorter time-bin separation imposes more stringent requirements on the data analysis, as detection system operates close to its resolution limit (55 ps jitter). For this reason, the experimental effort was focused on the 100 ps delay (1^{st} and 2^{nd}) for the demonstration of quantum applications presented in the following chapters. Nevertheless, the 50 ps design remains interesting for possible future development improvements.

4.5.1 Characterization

For each chip both configurations were evaluated using a dedicated chip-level test setup. The chip was mounted on a vacuum-assisted holder enabling fast replacement, and optical access was provided through a fiber-array unit identical to the one used in the packaged device, aligned using a 6-axis stage. Electrical signals were applied via a high-frequency RF probe connected to a voltage source.

Optical switch To evaluate the performance of the optical switch, EO modulation was applied to the electrodes. A sinusoidal signal at 100 kHz with amplitude exceeding the switching voltage was used to extract the V_π, following the same procedure used in the wafer-level characterization (see Figure 4.12a and b). In the same measurement, the ER of the modulator was obtained by recording the optical power swing over one modulation period. Both quantities were monitored at the 2% tap-port located in the short arm of the unbalanced MZI, avoiding interference contributions from the second interferometer stage. The results of the ER are reported in Figure 4.14a. The measured values show a large variability, ranging from about 10 dB to more than 30 dB. Additional analysis carried out after the chip-selection process indicates that this spread is probably caused by mode mixing inside the integrated waveguides, in particular residual coupling between the TE and TM modes, probably excited by the circular bends. The limited ER is attributed to the presence of the TM mode,

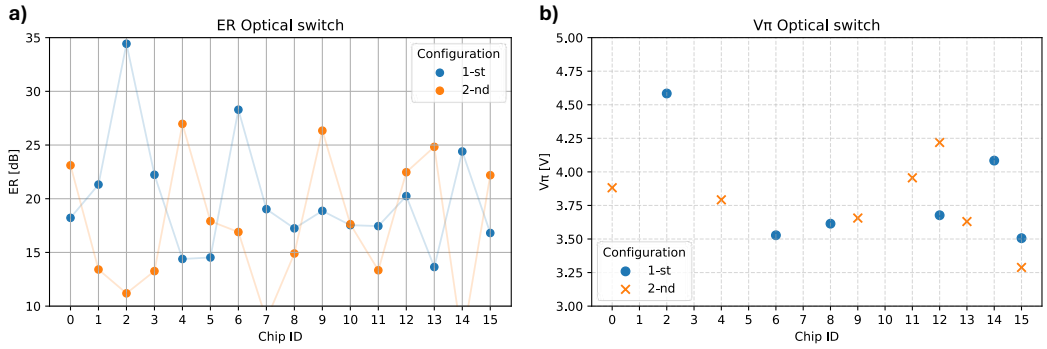

Figure 4.14: **Characterization of the optical switch. a)** Measured ER and **(b)** half-wave voltage (V_π) at 100 kHz and at $\lambda = 1550$ nm.

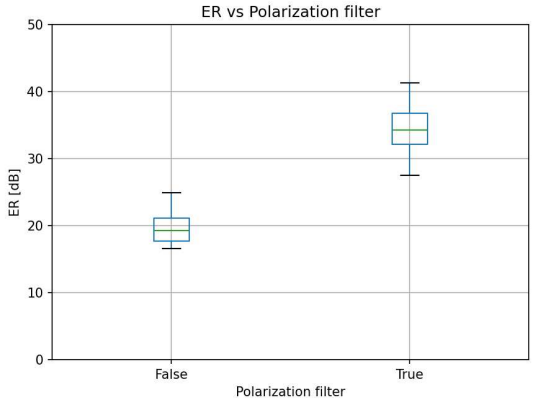

Figure 4.15: **Effect of a polarisation filter on ER.** Measured extinction-ratio difference between MZMs realized in the same wafer of the developed quantum receiver, with and without an integrated polarization filter. This suggests that additional future improvements may be achievable by integrating a polarization filter.

which produces a different and shifted interference pattern when the device is biased at minimum transmission.

A comparison between other interference structure on the same wafer, featuring identical waveguide and component geometry, shows significantly improved and more consistent ER values, as reported in Figure 4.15. This device included a polarization splitter-rotator (PSR) used a polarization filter, placed before the output coupler, effectively suppressing the residual TM component and improving the ER by approximately 15 dB. This suggests that integrating a polarization filter [262], together with the use of Euler bends to minimize mode conversion [263], would substantially improve the performance of future designs.

The measured V_π, reported in Figure 4.14b were performed on the chip and configuration that exhibited a relatively high ER. The values are comparable to those obtained at the wafer level, showing an increase of approximately 0.5 V with respect to the expected 3 V from simulations. This deviation is likely caused by fabrication tolerances, such as a larger-than-designed metal electrode gap or over-etching of LN slab. All tests were performed at a wavelength of $\lambda = 1550$ nm.

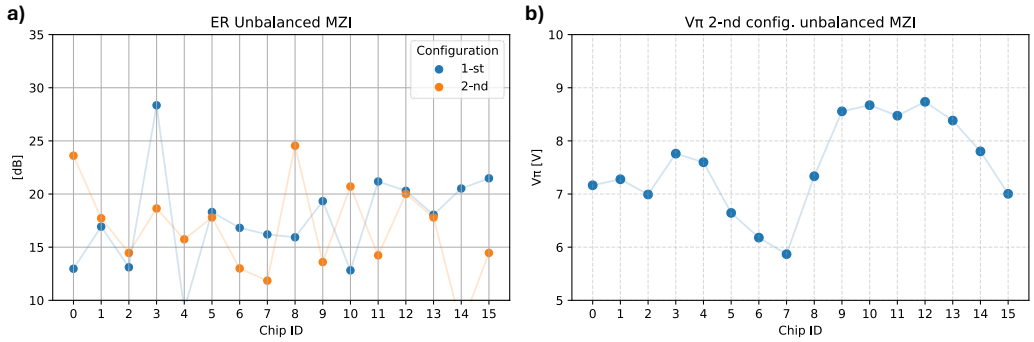

Figure 4.16: **Characterization of the unbalanced MZI. a)** Measured ER and **(b)** half-wave voltage (V_π) at $\lambda = 1550\,\text{nm}$. The slightly lower ER compared to the optical switch is attributed to differential propagation losses between the interferometer arms.

Unbalanced Mach-Zehnder interferometer The unbalanced MZI was characterized by applying a DC voltage to the TPS for the 2^{nd} configuration, and to both the metal electrodes and the TPS for the 1^{st} version, in order to determine the ER of the interferometer and the V_π of the EO modulator. The measurements were performed by monitoring the optical power at the two output ports of the MZI, while the optical switch was biased at quadrature to operate as a 50:50 beam splitter. The results, reported in Figure 4.16, show the measured V_π and ER for all tested chips at a wavelength of 1550 nm.

As in the case of the optical switch, the ER variability is likely affected by residual TM-mode excitation. Moreover, the average ER is slightly lower than that of the optical switch. This reduction is attributed to unbalanced propagation losses between the two interferometer arms, estimated to be on the order of ~ 0.2 dB for a path-length difference of 1.3 cm. For this reason, the 2% tap port is not only used to monitor the interferometer operating point, but also compensates for the excess loss in the shorter arm (approximately ~ 0.09 dB for a 2% tap). In addition, small inaccuracies in setting the bias point of the optical switch to the exact 50:50 condition can further degrade the measured ER.

Regarding the V_π, the measured values are higher than those of the optical switch, as the total electrode length is 0.66 cm and the configuration is not push-pull. Consequently, the V_π should increase by approximately a factor of 1.5×2 compared to the push-pull configuration.

Optical insertion losses were not characterized at the chip level, since manual alignment of the fiber array to the edge couplers did not provide the repeatability required for loss measurements. Instead, the optical loss performance was evaluated only after final device packaging, where precise alignment procedure is involved.

To select the chips for packaging, a performance threshold was applied based on the measured modulation efficiency and interferometric extinction. Specifically, only devices exhibiting $V_\pi < 5\,\text{V}$ and an ER $> 20\,\text{dB}$ were considered, ensuring high-quality and efficient switching operation. According to these criteria, the chips selected for packaging were:

- 1^{st} config.: IDs 6, 12, and 15
- 2^{nd} config.: IDs 4 and 9.

These devices were subsequently packaged and used for further device-level characterization, as described in the next section.

4.5.2 Packaging

The fabricated and selected chips were packaged in a metal housing, as shown in Figures 4.17a and b, with overall dimensions of 9.6×26 mm. The package provides mechanical stability, efficient thermal dissipation, and environmental protection. Due to the physical and electrical constraints of the package—which was not custom-designed for the present optical circuit—an adaptive layout strategy was adopted for packaging. In particular, the package provides 6 DC external pins and a single RF connector, allowing wire-bonded access to only one high-speed MZM at a time.

In contrast, the designed chip integrates three different configurations, which would ideally require three independent RF connectors and fourteen DC pins to fully access all electrical interfaces, as shown in the chip layout in Figure 4.2. As a result, only one of the three configurations can be electrically accessed through the package connectors, while the remaining two cannot be interfaced. In addition, not all optical interfaces are externally accessible. Each configuration includes four edge couplers spaced by 250 µm, matching the pitch of the fiber array unit (FAU). However, due to the limited die width, the spacing between edge couplers of adjacent configurations is reduced to 100 µm, as shown in Figure 4.2. This prevents simultaneous optical access to all configurations.

In the following, the packaging procedure for the 1^{st} and 2^{nd} configurations is described, as no chip from the 3^{rd} configuration was selected. Two packaged chips out of a total of five are shown in Figures 4.17a and c for the 1^{st} configuration, and in Figures 4.17b and d for the 2^{nd} configuration. Each chip was mounted inside the metal housing using a thermally conductive adhesive, ensuring both mechanical stability and efficient heat transfer to the package. To improve RF performance, the chip was positioned such that one of the lateral ground electrodes of the MZM is placed close to the metal sidewall of the package. This configuration enables short and periodic wire bonds between the 1 cm-long ground electrode and the package, thereby improving RF performance. In addition, this placement is required to properly align the on-chip RF pads with the package RF transmission line, enabling short and low-inductance wire bonds that are essential for preserving high-speed modulation performance. The high-speed driving signal for the optical switch is supplied through the G3PO RF connector, visible in Figure 4.17e. To enable the same grounding strategy adopted for the 1^{st} config., the chip corresponding to the 2^{nd} config. was additionally diced prior to assembly. This allowed the MZM electrodes to be positioned closer to the package sidewall, as illustrated in Figure 4.17c. The 6 low-frequency package pins placed laterally are wire-bonded to the on-chip electrical pads according to the specific configuration being accessed. For the 1^{st} configuration, the pin assignment from left to right, as shown in Figure 4.17a, is:

1: Unbalanced MZI ground for both TPS and EO modulator

2: Unbalanced MZI positive TPS

3: Unbalanced MZI positive EO modulator

4: Optical switch positive TPS 1

5: Optical switch positive TPS 2

6: Optical switch ground TPS 1 and 2

For the 2-nd configuration, the pin assignment is:

1: Not connected

2: Unbalanced MZI ground for TPS

3: Unbalanced MZI positive TPS

4: Optical switch ground TPS 1 and 2

5: Optical switch positive TPS 1

6: Optical switch positive TPS 2

Notice that for the 1^{st} config., the EO modulator of the unbalanced MZI is externally interfaced through the DC package pins. As discussed later in the chapter where the EO bandwidth characterization is presented, this electrical configuration limits the achievable performances, mainly due to the long wire bonds and the absence of a dedicated high-frequency connector and impedance-matched RF path.

The FAU is aligned to the optical edge couplers of the chip, which is inserted through the optical access window of the housing. The FAU fibers were subsequently spliced [264] to standard single-mode fibers (Corning SMF-28 [41] and PANDA PM1550) in order to avoid modal mismatch with the optical fibers used in the experimental setup. The FAU was aligned to maximize coupling efficiency and permanently fixed using an index-matching adhesive, thereby reducing insertion loss and suppressing back-reflections.

4.6 Module characterization

Once the devices were packaged, a series of preliminary performance evaluations were carried out to evaluate the final module performances. In particular, the EO bandwidth and the effective driving voltage required to achieve a V_π modulation at 5 GHz was characterized for the optical switch using the method described in the following sections. It is also reported the EO bandwidth of the second stage unbalanced MZI, and finally are presented the insertion loss of the module with few considerations.

4.6.1 Electro-optic bandwidth of the optical switch

To measure the EO bandwidth of the realized optical switch, a direct characterization could not be performed using the standard approach typically applied to MZM, since the optical circuit consists of two cascaded interferometers. In conventional EO bandwidth measurements, the MZM is biased at quadrature, and a small-signal RF modulation is applied. The

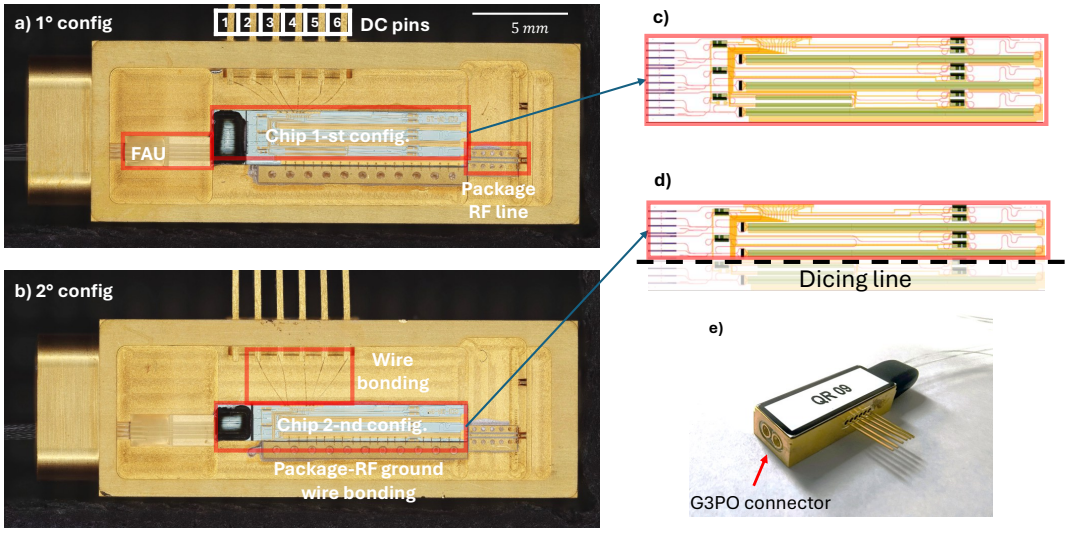

Figure 4.17: **Packaging of the integrated quantum receiver. a)** Top-view image of the fabricated integrated photonic circuit for the 1^{st} config. and **(c)** schematic of the glued chip inside the packaging. **b)** Top-view image of the 2^{nd} config., where the optical chip has been diced according to the schematic in **(d)** to allow short wire bonding to the 1 cm-long ground electrode and package. **c)** Final packaged device. FAU: fiber array unit.

variation of the optical output power as a function of the modulation frequency provides the EO response, as the quadrature point corresponds to the most linear region of the sinusoidal transfer function, particularly under small-signal excitation. This measurement is typically performed using a vector network analyzer (VNA). The VNA applies a small modulation signal while sweeping across a defined frequency range for device characterization. By monitoring the modulated optical output with a calibrated photodetector, the corresponding response at the same harmonic frequency is retrieved, allowing extraction of the EO bandwidth. In our case, this procedure was in principle possible, and an attempt was made by exploiting the 2 % tap output of the monitoring port. However, the available optical power was insufficient for the VNA photodiode to resolve the modulation response. The low optical level resulted in a noisy signal, limiting the feasibility of this method.

To overcome this, the EO bandwidth was evaluated indirectly by exploiting the cascaded configuration of the two interferometers, where the optical output power is higher, as it is limited only by the insertion loss of the module rather than a low-power monitoring port. I adopted the following approach: the first MZI was biased at its minimum transmission point, as verified by monitoring the optical power at the 2 % tap port, while the complementary output of the interferometer operates at its maximum transmission. Under these conditions, and as described in the following analytical derivation, the amplitude of the first-harmonic modulation at the final output is detectable and independent of the phase of the second stage. Notice that in this case since the input light is provided by a continuous-wave laser, the unbalance of the second stage can be neglected because the coherence length of the source is much longer than the MZI path difference. Thus, it effectively behaves as a balanced interferometer.

The analytical description of this method is provided in reference to the integrated optical

circuit schematic shown in Figure 4.18a that represent the two cascaded interferometer. Let E_{in} be the input optical field and $\phi_m(t)$ the small signal phase modulation applied by the EO modulator. The output fields at the two ports of the first MZM for a push-pull configuration are given by:

$$\begin{aligned} E'(t) &= \frac{E_{in}}{2}\left(e^{i\frac{\phi_m(t)}{2}} + e^{-i\frac{\phi_m(t)}{2}}\right), \\ E''(t) &= \frac{E_{in}}{2}\left(e^{i\frac{\phi_m(t)}{2}} - e^{-i\frac{\phi_m(t)}{2}}\right), \end{aligned} \tag{4.28}$$

where the applied modulation phase is defined as

$$\begin{aligned} \phi_m(t) &= 2\delta \sin(\omega_{RF} t) \\ &= \frac{\pi V_{RF}}{V_\pi} \sin(\omega_{RF} t) \end{aligned} \tag{4.29}$$

where δ represents the modulation index (assumed small, $\delta \ll 1$), ω_{RF} is the exciting RF angular frequency and V_{RF} is the exciting RF signal amplitude. By exploiting the Jacobi-Anger expansion [39],

$$e^{i\delta \sin(\omega_{RF} t)} = \sum_{n=-\infty}^{+\infty} J_n(\delta)\, e^{in\omega_{RF} t},$$

the optical field can be expressed as a sum of harmonic components, whose amplitudes are given by the nth-order Bessel functions of the first kind, $J_n(\delta)$. Substituting this relation into Eq. (4.28), the two output fields can be rewritten as:

$$\begin{aligned} E'(t) &= E_{in}\left[J_0(\delta) + 2\sum_{n=1}^{+\infty} J_{2n}(\delta)\cos(2n\,\omega_{RF} t)\right], \\ E''(t) &= iE_{in}\left[2\sum_{n=0}^{+\infty} J_{2n+1}(\delta)\sin((2n+1)\,\omega_{RF} t)\right]. \end{aligned} \tag{4.30}$$

Then, the output electric field at the second interferometer can then be computed by summing the two contributions $E'(t)$ and $E''(t)$, and including the phase shift of the unbalanced MZI, θ_B:

$$\begin{aligned} E'_{out}(t) &= \frac{1}{\sqrt{2}}\left(E'(t)e^{i\theta_B} + iE''(t)\right) \\ &= \frac{E_{\text{in}}}{\sqrt{2}}\left[J_0(\delta)e^{i\theta_B} + 2e^{i\theta_B}\sum_{n=1}^{+\infty} J_{2n}(\delta)\cos(2n\,\omega_{RF} t) - 2\sum_{n=0}^{+\infty} J_{2n+1}(\delta)\sin((2n+1)\,\omega_{RF} t)\right] \\ &\approx \frac{E_{\text{in}}}{\sqrt{2}}\left[J_0(\delta)e^{i\theta_B} + 2e^{i\theta_B} J_2(\delta)\cos(2\omega_{\text{RF}} t) - 2J_1(\delta)\sin(\omega_{\text{RF}} t)\right], \end{aligned} \tag{4.31}$$

where in the last step only the first terms of the Bessel expansion have been retained, as higher-order harmonics are negligible for small modulation indices ($\delta \ll 1$). Finally, the

detected optical power is given by:

$$\begin{aligned} P'_{\text{out}}(t) &\propto |E'_{out}(t)|^2 \\ &= \frac{E_{\text{in}}^2}{2}\Big[J_0(\delta)^2 + 4J_1(\delta)^2\sin^2(\omega_{\text{RF}}t) + 4J_2(\delta)^2\cos^2(2\omega_{\text{RF}}t) \\ &\quad - 4J_0(\delta)J_1(\delta)\sin(\omega_{\text{RF}}t) + 4J_0(\delta)J_2(\delta)\cos(2\omega_{\text{RF}}t) \\ &\quad - 8J_1(\delta)J_2(\delta)\sin(\omega_{\text{RF}}t)\cos(2\omega_{\text{RF}}t)\Big]. \end{aligned} \tag{4.32}$$

An analogous expression holds for the complementary port $P''_{\text{out}}(t)$.

It can be observed from Eq. (4.32) that the detected optical power contains both a DC component ($J_0(\delta)^2$) and several oscillating terms at different harmonics of the modulation frequency, all with intensity amplitude independent from θ_B. For small-signal modulation ($\delta \ll 1$), the Bessel function coefficients satisfy $J_0(\delta) > J_1(\delta) > J_2(\delta)$. Consequently, the dominant oscillating term in the output power is the first harmonic, proportional to $J_0(\delta)J_1(\delta)\sin(\omega_{\text{RF}}t)$. This term represents the primary contribution to the EO modulation response and is therefore used to determine the effective EO bandwidth of the device, which can be attributed to a frequency-dependent half-wave voltage, $V_\pi = V_\pi(f)$, according to Eq. (4.29).

As shown in Figure 4.18b, the bandwidth measurement was performed not for all the 5 packaged chips but for the three modules that were actually used for photon switching in the quantum experimental demonstrations. Specifically, those are the devices (and config.) with chip IDs 6 (1^{st}), (1^{st}), and 15 (1^{st}) that exhibited 3 dB EO modulation bandwidths of approximately 30 GHz. The figure also reports the simulated EO bandwidth, computed as described in Eq. (4.15), which closely matches the experimental results. The main difference between the simulated and measured results appears as a slight enhancement of the modulation response below approximately 5 GHz, which can be attributed to an increase in the impedance of the transmission line with frequency, leading to a reduction in the effective V_π.

4.6.2 Driving voltage at 5 GHz

An important parameter to characterize is the actual driving voltage required for the module to achieve proper photon switching operation. This value does not directly correspond to the measured V_π of the previous characterizations, since, in the experimental setup used for the demonstrations described in the next chapters, few factors may alter the effective voltage applied to the device. Indeed, the hardware setup consists of an RF signal generator providing a sinusoidal signal at 5 GHz with tunable output power. The RF signal is transmitted through a one-meter coaxial cable, which introduces frequency-dependent attenuation, followed by an adapter and a G3PO connector that delivers the signal to the module. Each of these components contributes to insertion losses before the signal reaches the modulator electrodes. Indeed the following characterization procedure allows precise determination of

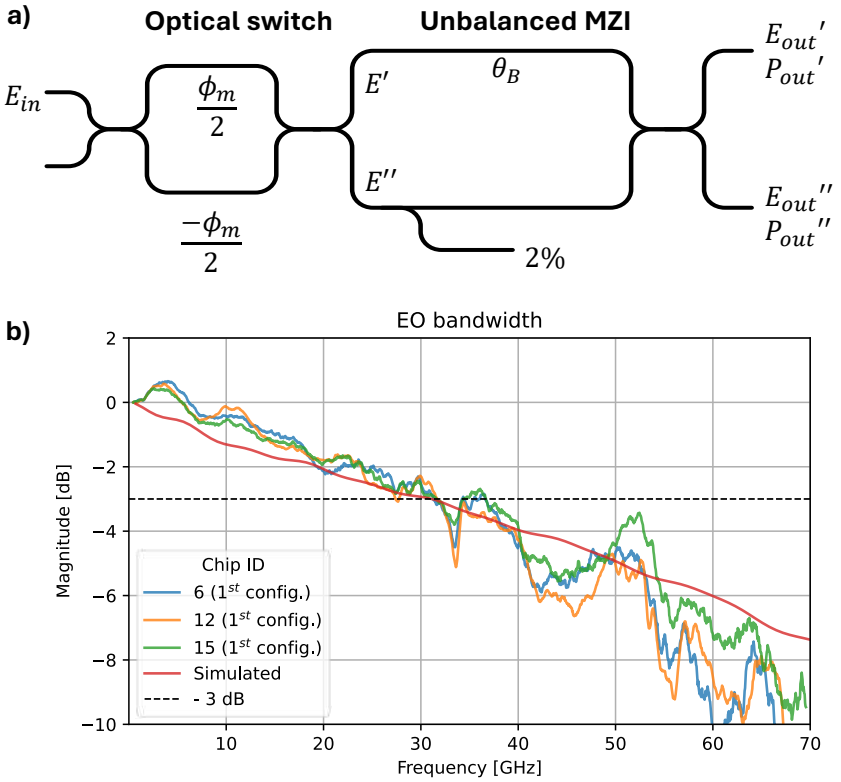

Figure 4.18: **Optical switch EO bandwidth. a)** Schematic of the device highlighting the parameters used in the analytical model for evaluating the EO bandwidth of the optical switch, including the effect of the second interferometric stage. **b)** Measured EO bandwidth of three different packaged devices, compared with the theoretical estimation obtained from simulated parameters. All three devices exhibit an EO bandwidth of approximately 30 GHz, in agreement with the simulation (Eq. (4.16)).

the RF driving power required from the instrumentation to effectively deliver a peak-to-peak V_π modulation to the optical switch.

Considering the transfer function of a MZM, the optical power at the output of the switch, monitored through the 2 % tap port, when driven with a sinusoidal signal at $\omega_{\mathrm{RF}} = 2\pi \cdot 5\,\mathrm{GHz}$ can be written as:

$$P_{\mathrm{out}}(t) = \frac{1}{2}\left[1 + \cos(\phi_{\mathrm{TPS}} + \delta \sin(\omega_{\mathrm{RF}} t))\right], \tag{4.33}$$

where the total phase term includes the contribution from the TPS, ϕ_{TPS}, and the EO modulation amplitude, δ. The output power is monitored using a low-bandwidth power meter, whose response time is much slower than the modulation frequency (5 GHz), the measured signal corresponds to the time-averaged optical power over one modulation period T:

$$\begin{aligned}\overline{P_{\mathrm{out}}(t)} &= \frac{1}{T}\int_0^T P_{\mathrm{out}}(t)\,dt \\ &= \frac{1}{2} + \frac{\cos(\phi_{\mathrm{TPS}})}{T}\int_0^T \cos(\delta \sin(\omega_{\mathrm{RF}} t))\,dt - \frac{\sin(\phi_{\mathrm{TPS}})}{T}\int_0^T \sin(\delta \sin(\omega_{\mathrm{RF}} t))\,dt.\end{aligned} \tag{4.34}$$

The last term is null due to odd sinusoidal symmetry, while the second term corresponds to the definition of the zero-order Bessel function of the first kind, $J_0(\delta)$, using its integral representation, also known as the Hansen-Bessel formula. Therefore, the time-averaged optical power is:

$$\overline{P_{\mathrm{out}}(t)} = \frac{1}{2}\left[1 + \cos(\phi_{\mathrm{TPS}})\, J_0(\delta)\right]. \tag{4.35}$$

The characterization exploits the fact that, by sweeping the parameter δ for different values of ϕ_{TPS}, the resulting curves intersect when $J_0(\delta) = 0$, corresponding to a normalized output power of 0.5. Since the first zero of the Bessel function $J_0(\delta)$ occurs at $\delta = 2.4048$, this condition allows for the precise determination of the effective V_π at 5 GHz, as:

$$2.4048 \approx \delta = \frac{\pi V_{\mathrm{RF}}}{V_\pi}, \tag{4.36}$$

where V_{RF} is retrieved from the the power delivered by the RF signal generator. The curves representing the sweep of the RF driving power of the sinusoidal signal for different values of ϕ_{TPS} are shown in Figure 4.19. These measurements correspond to the two modules used as receivers for the two users in the QKD demonstration. They respectively exhibit intersection points at 20 and 19.3 dBm, which correspond to the RF powers required to achieve the V_π modulation of 18.1 and 17.4 dBm. This calibrated voltage value was then used to implement the correct optical switching operation in the quantum experiments.

4.6.3 Electro-optic bandwidth of the unbalanced MZI

Here I report the EO bandwidth of the unbalanced MZI for the two packaged chips out of the three that implement the 1^{st} configuration. These are the devices for which fast modulation of the unbalanced MZI is exploited in the QKD experiment with active basis selection, as presented in Section 6.2.

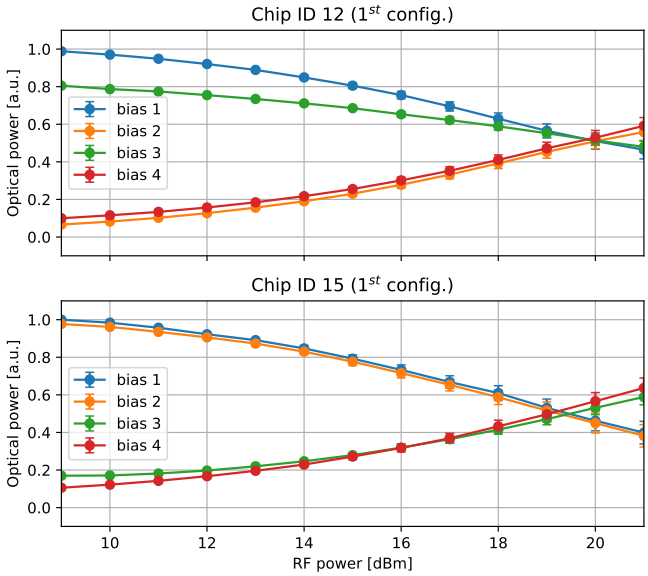

Figure 4.19: **Calibration of the effective V_π at 5 GHz.** Measured normalized optical power as a function of the applied RF driving power for different values of the thermo-optic phase ϕ_{TPS}. The intersection points of the curves correspond to the first zero of the Bessel function $J_0(\delta)$, enabling extraction of the effective V_π at 5 GHz, including all losses from the RF setup components. Results are reported for the two receiver modules used in the QKD demonstration. The measurement uncertainty is attributed to the imprecision in the delivered RF power, estimated at ± 0.1 dBm.

Unlike the optical switch, the EO bandwidth of the unbalanced MZI can be directly measured. As this modulator corresponds to the second stage of the cascaded interferometers, the measurement is performed by biasing the first MZM at quadrature, which acts as a 50:50 beam splitter, and by applying small-signal modulation to the electrode of the unbalanced MZI. By monitoring the variation of the optical output power as a function of the RF driving frequency, the EO bandwidth is extracted. The two measured bandwidths are reported in Figure 4.20. Both devices exhibit a similar behaviour: a slow roll-off up to about 100 MHz, followed by a slight increase around 500 MHz, and finally a cutoff around 1 GHz.

Compared with the optical switch, the EO bandwidth of the unbalanced MZI is significantly lower. This limitation mainly arises from two factors: (i) the unbalanced MZI is driven through the same routing technology used for the TPS, in particular via the lateral metal pins visible in Figure 4.17a and b, since the single high-speed RF connector is dedicated to the optical switch and benefits from optimized wire bonding. (ii) By design, the electrodes of the unbalanced MZI do not include a matched termination, resulting in a capacitive load and an effectively open long-cable connection that prevents optimal delivery of high-frequency signals.

To partially mitigate the second limitation and thus improve the EO bandwidth to approximately 1 GHz, a 50 Ω RF resistor was connected to the two package pins to provide a proper termination for the unbalanced MZI electrodes. By adopting this termination, the effective length of the unterminated electrode section was reduced to only a few centimeters, corresponding to the package pins, wire bonds, and on-chip routing. This significantly

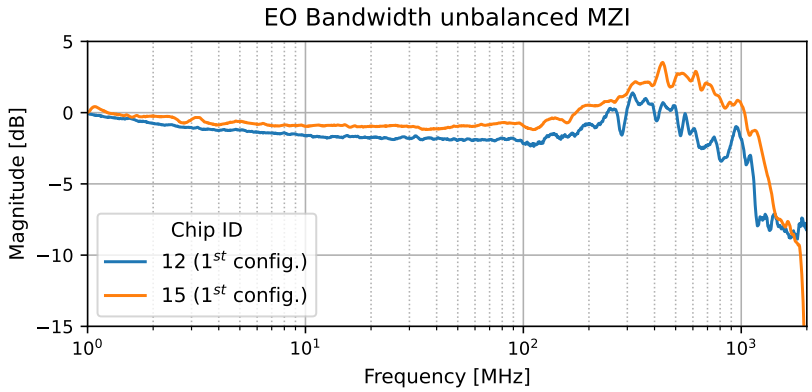

Figure 4.20: EO bandwidth of the unbalanced MZI stage for the two devices used in the QKD protocol implementation.

mitigates standing-wave effects at higher frequencies compared to the case of a much longer open-circuit connection, which would otherwise include the RF cable between the signal generator and the device, with a length on the order of tens of centimeters.

Future improvements may therefore include adopting the same features implemented for the optical switch, such as proper RF termination and an optimized high-speed connector.

4.6.4 Insertion loss

In Table 4.3 are reported the measured insertion losses of the packaged devices. The measurement is performed by injecting light into the input optical fiber of the FAU and recording the optical power at the two output fibers connected to the two outputs of the unbalanced MZI. In this way, the propagation losses correspond to the total loss of the whole system, that is, the cascade of the two interferometric stages. The average loss is 6.35 dB, with a standard deviation of 1.1 dB. The total optical loss has different contributions. The first contributions are the intrinsic propagation loss of the waveguides and the additional losses of the components such as the MMI, the TPS, and the edge-coupler structure. The expected performance regarding the device insertion loss is represented by the lower losses measured on chip ID 4. The higher and more variable losses observed in the other devices are attributed to additional contributions. In particular, these extra losses may arise from out-of-chip factors. The FAU may exhibit a slight displacement of the fibers, since it features a positioning precision of $\pm 0.5\,\mu m$, which can prevent perfect alignment with the on-chip waveguides. Moreover, the alignment procedure, comprising the placement of the index-matching glue and the final UV curing, may not have been perfectly ideal, leading to increased loss.

Summary

Finally, throughout this section the achieved results can be compared with the main performance requirements outlined in Table 4.1. In particular, high-visibility interference (ER > 20 dB) is obtained for the unbalanced interferometer, enabled by the limited propagation

Chip ID	**Output 1** [dB] ± 0.1	**Output 2** [dB] ± 0.1
4	4.5	4.8
6	7.4	7.7
9	7.8	6.8
12	5.8	6.5
15	6.1	6.1

Table 4.3: Insertion loss for each packaged chip.

loss of approximately 0.2 dB/cm. This is combined with the EO modulation capability of the MZM, which operates at the target frequency of 5 GHz with a driving voltage below 5 V. These represent the primary design constraints. In addition, another important performance metric is the overall insertion loss. Although it does not constitute a strict limitation for device operation, minimizing insertion loss is highly desirable to maximize the achievable rate. This parameter depends not only on the integrated circuit itself, but also on the entire optical system involved in the target quantum application, ultimately impacting the achievable secret key rate.

Chapter 5

Entanglement certification

The next two chapters explain how the device's functionalities are exploited to implement various quantum applications, thanks to its ability to operate as a reconfigurable time-bin state projector.

The first part of the chapter describes the practical aspects of the experimental setup and the characterization of the photon-pair source used for the measurements. It also introduces an analytical model developed to estimate the expected performance of the applications while accounting for experimental non-idealities. The second part reports the violation of the Bell inequality, providing clear evidence of the generation and manipulation of time-bin entangled states. Finally, the chapter concludes with the demonstration of another quantum application: QST.

5.1 Experimental setup

This section describes the experimental setup used for all the quantum applications discussed in this chapter and the next: entanglement certification, QST and QKD. Some minor adjustments have been made in order to implement QKD, which will be noted in the dedicated Chapter 6. The experimental setup, whose complete schematic is shown in Figure 5.1, consists of three main parts: the optical source used to generate entangled photon pairs and the two receiver stations, referred to as users Alice and Bob, that analyze the correlated photons.

Entangled photon source Time-bin entangled photon pairs are generated by pumping an integrated silicon waveguide with periodic optical pulses produced by an actively mode-locked laser (PriTel 1550nm Ultrafast Optical Clocks) operating at a repetition rate of 1 GHz. The emitted pulses exhibit approximately Gaussian spectral and temporal profile that are nearly Fourier-transform limited, with a time–bandwidth product of about 0.5. They have a spectral bandwidth of approximately 0.42 nm FWHM, corresponding to a temporal duration of about 9.2 ps, and are tuned to International Telecommunication Union (ITU) channel 33 (1550.92 nm).

The 1 GHz laser repetition rate can, in principle, be increased up to its maximum value of 5 GHz, which would result in a five-times enhancement of the quantum key generation rate. This upper limit is imposed by the 100 ps time-bin separation set by the temporal delay of

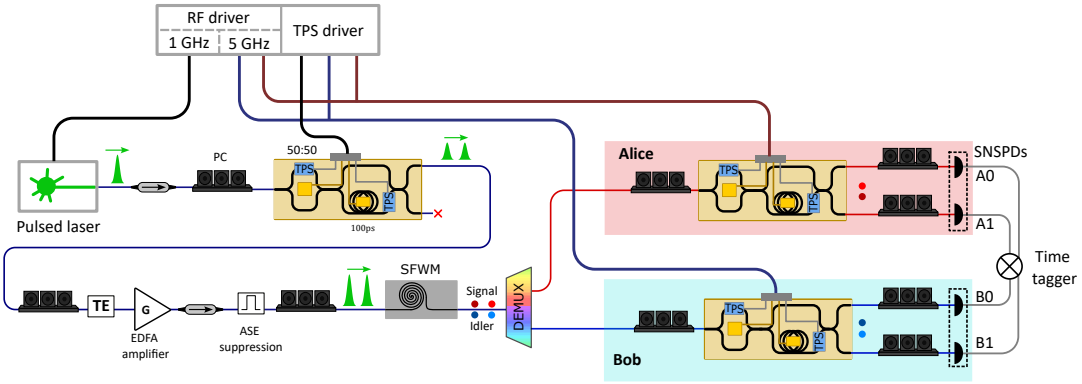

Figure 5.1: **Experimental setup.** Schematic of the experimental configuration used for the generation and analysis of time-bin entangled photon pairs. A mode-locked laser source operating at 1 GHz repetition rate provides optical pulses that are coupled into the TFLN device, properly controlled to generate twin pump pulses. These pulses are amplified and injected into the silicon photon-pair source, where SFWM occurs. The generated signal and idler photons are demultiplexed by wavelength-selective filters and directed to the two receiver stations (Alice and Bob), each composed of a TFLN device and SNSPDs. PC: polarization controller; TPS: thermal phase shifter; TE: transverse-electric polarizer filter; ASE: amplified spontaneous emission; EDFA: erbium-doped fiber amplifier; SFWM: spontaneous four-wave mixing; VOA: variable optical attenuator; SNSPD: superconducting nanowire single-photon detector; DEMUX: optical demultiplexer.

the TFLN unbalanced interferometer (1^{st} config.). However, as discussed in Sections 6.4 and 4.6.3, the rate is limited to 1 GHz repetition rate as the QKD demonstrations presented in this work were constrained by the maximum count rate of the detectors and by the bandwidth of the electrical connector driving the EO modulator of the unbalanced MZI.

The laser output passes through an optical isolator (Thorlabs IO-G-1550-APC) to suppress any potential back-reflections, and its polarization is adjusted using a fiber polarization controller to match the TE mode supported by the TFLN chip. Thus the optical pulses are injected into one of the fabricated TFLN modules (Chip ID 04), where the MZM is biased to operate as a balanced 50:50 beam splitter by adjusting the TPS. In this configuration, the device functions as an unbalanced interferometer, producing two pump pulses separated by 100 ps. By changing the MZM bias point, it is possible to control the relative amplitudes of the two pump pulses, while the phase of the unbalanced MZI determines their relative phase. With this setting the same device can act not only as a quantum receiver but also as a reconfigurable pump-pulse shaper, capable of producing arbitrary time-bin entangled states when combined with a nonlinear optical source. Moreover, using identical integrated optical circuit designs in both the source and receiver stages ensures that the temporal separation between the two pump pulses precisely matches the path imbalance of the receiver interferometers (within fabrication tolerances), enabling perfect temporal overlap of the time-bin wavefunctions.

After exiting the TFLN device, the twin pump pulses are amplified using an erbium-doped fiber amplifier (EDFA, Keopsys PEFA-SP-C), which allows precise control of the pump power. amplified spontaneous emission (ASE) noise from both the laser and the amplifier is suppressed using a cascade of DWDM optical filters (Opneti fiber based) each providing 100 GHz (0.8 nm) bandwidth centered at the pump wavelength, thereby preserving the spectral and temporal characteristics of the pump pulses. This filtering is essential because even weak residual ASE noise can overlap with the signal and idler channels, introducing

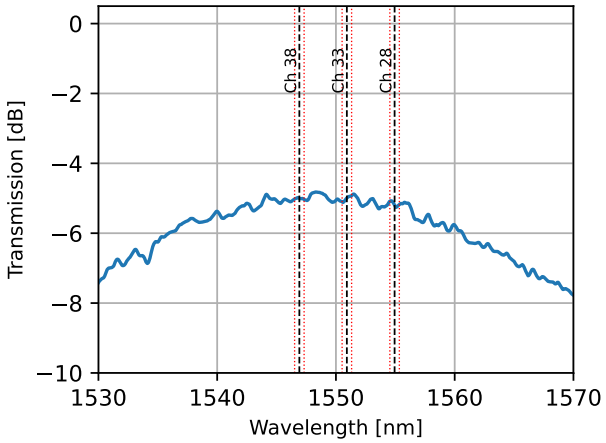

Figure 5.2: **Source transmission spectra.** Transmission spectra of the integrated silicon waveguide accessed through input and output grating couplers. The waveguide is pumped with optical pulses at ITU channel 33 (1550.92 nm) to generate entangled photon pairs via SFWM at ITU channels 28 and 38. The choice of these wavelengths minimizes the optical loss.

significant noise power.

The filtered twin pulses are then coupled into the integrated silicon waveguide, where correlated photon pairs are generated via SFWM, as described in Section 2.3.2. The pump wavelength is set to ITU channel 33 (1550.92 nm), which coincides approximately with maximum transmission of the grating couplers (see Figure 5.2) ensuring balanced extraction losses for the signal and idler photons.

Receiver stations and detection At the output of the photon-pair source, the generated signal and idler photons are spectrally separated using two bandpass DWDM filters, similar to those used for pump ASE suppression, centered at ITU channels 28 and 38 (1554.94 nm and 1546.92 nm, respectively), each with a 100 GHz (0.8 nm) bandwidth, as shown in Figure 5.2. These channels are symmetrically spaced with respect to the pump wavelength, as required by energy conservation in the SFWM process, ensuring proper collection of the signal and idler photons. The filters also suppress residual pump light and serve as demultiplexers, routing the photon pairs through optical fibers to the two receiver modules corresponding to the users *Alice* (Chip ID 12) and *Bob* (Chip ID 15). Due to the nearly rectangular spectral transmission profile of these filters (DWDM Opneti fiber based), the signal and idler photons can be approximated as spectrally rectangular, which corresponds in the temporal domain to a sinc-shaped waveform. Such a profile exhibits a time–bandwidth product of approximately 1. Since the filter bandwidth (0.8 nm) is approximately twice the spectral bandwidth of the pump pulses (0.42 nm), the coherence time of the generated photons is not significantly altered by the filtering stage and remains nearly unchanged compared to the pump pulses. More generally, if wider optical filter bandwidths are used, the coherence time of the generated photons becomes shorter than the pump pulse duration; however, they are still generated within the temporal envelope of the pump pulses. In the limit of a filter bandwidth much larger than that of the pump and a single pump pulse, this situation

tends toward the regime associated and exploited in time–energy entanglement correlations (see Section 3.5.1).

Polarization controllers are placed before each TFLN receiver chip to ensure TE-mode propagation within the integrated waveguides, thereby minimizing optical losses and maximizing EO modulation efficiency. Additional polarization controllers are located after the chips to optimize coupling for detection efficiency of the SNSPDs (Photon Spot). The employed SNSPDs feature a timing jitter of approximately 55 ps, which defines the temporal resolution for discriminating between early and late time-bin states separated by 100 ps in the computational basis. The SNSPDs support a maximum count rate of about 1.5 MHz, which ultimately limits the achievable key generation rate in the QKD configuration discussed in the next chapter. This limitation arises from the intrinsic dead time of the detectors and from latching effects, which are typical of SNSPDs at high count rates and prevent continuous operation under sustained high photon flux.

Each TFLN receiver module is connected to an external DC power supply (Rohde & Schwarz HMP4040) that controls the TPSs integrated in both the balanced MZM and the unbalanced MZI. The two packaged quantum receivers are placed on a Peltier cell, which is connected to a module controller (Vescent Slice-QT). This controller allows for precise control of the temperature of the optical chip. An RF signal generator (AnaPico APMS20G) drives the MZM with a sinusoidal signal at 5 GHz, enabling the optical switching. As detailed in Section 4.6, the applied drive voltage takes into account the insertion losses of the RF components, and therefore differs from the intrinsic V_π value of the modulator. The same RF source also provides the synchronization signal to the pulsed laser, ensuring phase-locked operation between the pulse generation and optical switching stages.

The electrical output signals from the SNSPDs are fed into a high-resolution (2 ps jitter) time-tagging module (Swabian Instruments Time Tagger X) that records single-photon detection events with picosecond precision.

This configuration enables both the verification of Bell-inequality violation and the complete QST of the generated photon pairs, thus allowing the characterization of the entangled state, as discussed in the following sections. In the configuration shown in Figure 5.1, the total optical losses from the photon-pair source to the SNSPD inputs amount to 12.2 ± 0.2dB for Alice and 10.1 ± 0.2dB for Bob.

5.2 Source characterization

The generation of time-bin entangled photon pairs was performed using the silicon waveguide source. It is a 16 mm-long silicon rib waveguide fabricated on a 300 nm-thick SOI platform developed at CEA-Leti. Access to the chip is provided via grating couplers. The total insertion loss, including input/output coupling and propagation at the pump wavelength of 1550.92 nm, was measured to be 4.8 ± 0.1dB, as shown in the transmission spectra in Figure 5.2.

Figure 5.3a shows the characterization of photon-pair generation through SFWM, performed under the same operating conditions used for the experimental demonstrations. Thus the source was pumped by twin optical pulses separated by 100 ps, at a repetition

rate of 1 GHz. The generated signal and idler photons, emitted at ITU channels 28 and 38 respectively are detected to measure the coincidence rate as a function of the pump pulse energy. The pulse energy coupled into the waveguide was estimated from the input power, taking into account the measured coupling losses and the laser repetition rate. As expected for SFWM, the detected coincidence rate exhibits a quadratic dependence on the pump pulse energy. By fitting the measured pair-generation probability per pulse (G) as a function of energy E to the model

$$G(E) = \gamma E^{\alpha}, \tag{5.1}$$

it is obtained a fitted exponent $\alpha = 1.96$, in excellent agreement with the expected quadratic dependence. The proportionality constant γ includes the overall process efficiency. During the characterization, the maximum coupled pump power was limited to below 15 dBm, corresponding to a photon-pair generation probability per pulse of more than 20%. This restriction was imposed to prevent thermal damage to the grating couplers.

The CAR, already defined in Section 2.3.2, quantifies the quality of the photon-pair source by comparing the rate of correlated photon-pair detections to that of spurious coincidences. It is defined as:

$$\mathrm{CAR} = \frac{C_E}{C_A}, \tag{5.2}$$

where C_E represents the number of effective (entangled) coincidence counts and C_A denotes the accidental coincidences within the same temporal detection window. In our measurements, accidental coincidences mainly originate from two mechanisms: (i) at high pump powers, the probabilistic nature of the SFWM process leads to a non-negligible probability of generating multiple photon pairs within a single pump pulse. When two or more pairs are emitted simultaneously, photons from different pairs may be detected within the same time window, producing accidental coincidences; (ii) at lower pump powers, the accidental rate is dominated by detector dark counts and background noise, independent of the pump power.

Before analyzing the pumping configuration with two closely spaced pulses, that represents the condition used in the experiments, the single-pulse pumping case is first described to highlight the differences. Let p denote the single-pair generation probability per pump pulse, and consequently p^2 the probability of generating two photon pairs. Considering that each photon detection event also depends on the overall detection efficiencies of the two channels, η_A and η_B, which account for coupling, transmission, and detector efficiencies, the CAR scales as:

$$\mathrm{CAR} = \frac{p\eta_A\eta_B}{p^2\eta_A\eta_B} = \frac{1}{p}. \tag{5.3}$$

In our case, since the source is pumped with two closely spaced pulses separated by 100 ps instead of a single pulse, the coincidence histogram of the detected entangled photon pairs as a function of the detection time difference (shown in Figure 5.3b) exhibits three peaks separated by the same 100 ps interval. This structure arises from accidental coincidences superimposed on the true coincidence events. To better highlight the accidental coincidence pattern, Figure 5.3c reports the coincidence histogram measured at one repetition period corresponding to uncorrelated detections, where only the accidental counts are visible. This

occurs because both pump pulses contribute to the total coincidence and accidental counts, and the overall CAR can be expressed as:

$$\mathrm{CAR} = \frac{p_1\eta_A\eta_B + p_2\eta_A\eta_B}{p_1^2\eta_A\eta_B + p_2^2\eta_A\eta_B + 2p_1p_2\eta_A\eta_B}. \tag{5.4}$$

Here, p_1 and p_2 represent the probabilities of generating a photon pair from the first and second pump pulse, respectively, while the corresponding accidental coincidences scale with p_1^2 and p_2^2. The numerator represents the total rate of true coincidences originating from both pulses, whereas the three terms in the denominator account for accidental coincidences: the first two terms correspond to multi-pair events within the same time bin, and the third term ($2p_1p_2\eta_A\eta_B$) describes cross coincidences between photons generated by different time bins. Neglecting higher-order (p^3) contributions and assuming balanced pumping conditions ($p_1 = p_2 = p/2$), the expression simplifies to:

$$\mathrm{CAR} = \frac{1}{2p}. \tag{5.5}$$

In the experiment, the effective coincidences C_E were determined as

$$C_E = C_C - C_A, \tag{5.6}$$

where C_C is the total coincidence count within the central detection window (Figure 5.3b), and C_A represents accidental coincidences obtained from time-shifted detections by integer multiples of the twin-pulse separation period (Figure 5.3c). Identical temporal integration windows were used for both quantities to ensure consistent normalization. If the side peaks can be fully temporally resolved, the cross coincidences could be excluded and the CAR would recover the single-pulse scaling of $1/p$. However, in our setup, the detector timing jitter of approximately 55 ps is comparable to the 100 ps pulse separation, leading to partial overlap between peaks. This overlap redistributes counts between true and accidental coincidences, effectively reducing the measured CAR by a factor of two compared to the ideal case. the experimental results of the CAR follows the upper bound model relation $\mathrm{CAR} \approx 1/(2p)$, as shown in Figure 5.3a, for relatively high pumping power. While the upper bound is not reached at lower pumping powers because other sources of noise, such as dark counts, limit the CAR.

5.3 Modeling experimental imperfections and system limitations

Since a few practical limitations that could intrinsically reduce the visibility of the correlated Bell curve experiment were identified during the device design phase, I developed an analytical model to quantify their impact. This model considers two main non-idealities: (i) the unbalanced propagation loss induced by the unbalanced MZI interferometer and (ii) the modulation signal applied to the MZM for photon switching.

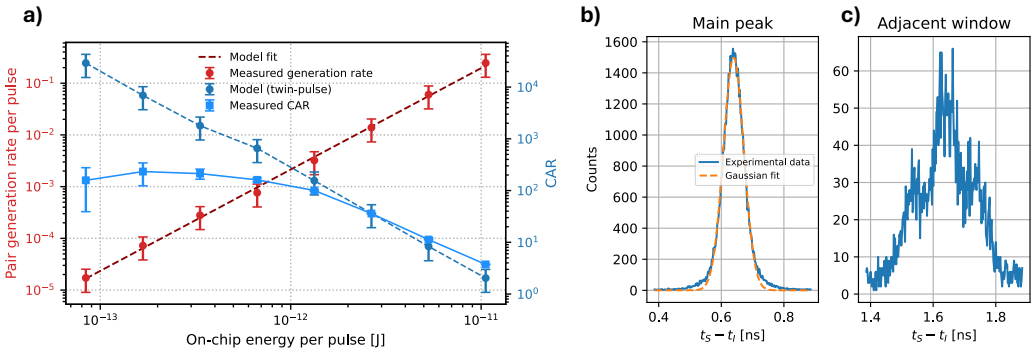

Figure 5.3: **Characterization of the silicon photon-pair source. a)** Measured photon-pair generation probability per pulse (red) and CAR (blue) as functions of the on-chip pump-pulse energy. The dashed blue line represents the model prediction for the CAR when considering multi-photon pair generation and no detector dark counts, while the dashed red line shows the exponential fit of the generation rate, yielding a coefficient of 1.96. **b)** Measured coincidence histogram as a function of the photon arrival-time difference for one representative operating point, showing that the central peak is predominantly formed by correlated (entangled) photon-pair events, with a minimal accidental background. **c)** Zoom-in of the accidental coincidence peak at one repetition period away from the central peak in **(b)**, highlighting the three partially ovelapping sub-peaks resulting from the twin-pulse excitation and the finite detector timing resolution.

The first limitation arises from the intrinsic asymmetry of the second-stage interferometer, which consists of two arms with different propagation lengths (1.31 cm, corresponding to a 100 ps delay in the LN waveguide). This asymmetry leads to unbalanced propagation losses, on the order of 0.2.5 dB, depending on the actual waveguide propagation loss. Such imbalance reduces the ability to achieve perfect destructive interference, thereby limiting the maximum attainable extinction ratio of the unbalanced interferometer.

The second limitation arises from the driving modulation of the MZM. Ideally, the modulator should be driven by a square-wave voltage with a 200 ps period, so that successive time bins separated by 100 ps experience a π phase shift between them, as illustrated schematically in Figure 5.4b. A perfect square-wave drive would yield sharp temporal transitions, ensuring that photons are deterministically routed into the desired interferometer path. In practice, however, generating such a signal would require an infinitely large electronic bandwidth, which is technically unfeasible. To relax the requirements on the driving electronics, the MZM was instead driven by a sinusoidal signal with the same peak-to-peak voltage and fundamental frequency. While this approach simplifies the driving electronics, it introduces a small non-ideality that slightly degrades the switching performance.

To account for these two effects, a simplified analytical model was developed to describe the optical circuit through the evolution of photon creation operators acting on the vacuum state. The biphoton input state can be expressed as:

$$|\Phi\rangle = \frac{1}{2}\int\!\!\int_{-\infty}^{+\infty} \left[\mu(t_A - \tau, t_B - \tau)\, e^{i\phi} + \mu(t_A, t_B)\right] a^\dagger(t_A)\, b^\dagger(t_B)\, dt_A\, dt_B\, |00\rangle\,, \tag{5.7}$$

where $\mu(t_A, t_B)$ is the single time-bin biphoton temporal wavefunction, τ is the temporal delay introduced by the unbalanced interferometer, $a^\dagger$ and $b^\dagger$ are the photon creation operators for the signal (Alice) and idler (Bob) modes, ϕ is the relative phase between the early and late

time-bin, and $|00\rangle$ represents the vacuum state of both modes. The quantities are expressed as functions of the two temporal reference frames corresponding to Alice and Bob's times, t_A and t_B.

According to the optical circuit schematic, that is shown in Figure 5.4a, both Alice's and Bob's operators evolve through a cascade of three MMIs acting as beam splitters. For Alice's interferometer, the field transformations can be expressed as:

$$\begin{cases} \hat{a}^\dagger(t_A) = \dfrac{1}{\sqrt{2}}\Big[\hat{m}_1^\dagger(t_A)\, e^{i\phi_m/2} + i\,\hat{m}_2^\dagger(t_A)\, e^{-i\phi_m/2}\Big], \\ \hat{m}_1^\dagger(t_A) = \dfrac{1}{\sqrt{2}}\Big[\hat{l}^\dagger(t_A) + i\,\hat{s}^\dagger(t_A)\Big], \\ \hat{m}_2^\dagger(t_A) = \dfrac{1}{\sqrt{2}}\Big[i\,\hat{l}^\dagger(t_A) + \hat{s}^\dagger(t_A)\Big], \\ \hat{l}^\dagger(t_A) = \dfrac{\sqrt{T_L}}{\sqrt{2}} e^{i\theta_A}\Big[\hat{d}_A'^\dagger(t_A-\tau) + i\,\hat{d}_A''^\dagger(t_A-\tau)\Big], \\ \hat{s}^\dagger(t_A) = \dfrac{\sqrt{T_S}}{\sqrt{2}}\Big[i\,\hat{d}_A'^\dagger(t_A) + \hat{d}_A''^\dagger(t_A)\Big], \end{cases} \tag{5.8}$$

where the operators $\hat{m}_1^\dagger$ and $\hat{m}_2^\dagger$ account for photons in the two arms of the optical switch, $\hat{s}^\dagger$ and $\hat{l}^\dagger$ account for photons in the shorter and longer paths in the second stage interferometers, and $\hat{d}_A'^\dagger$ represents a photon detection event for Alice. Also, ϕ_m accounts for the phase modulation of the switching stage, the coefficients T_L and T_S represent the transmission (and thus the propagation losses) of the long and short arms, respectively, and θ_A denotes the phase acquired in the longer path. Notice that the longer arm introduces a temporal delay τ in the corresponding photon detection events $\hat{d}_A'^\dagger(t_A-\tau)$.

Combining all the above relations and, for simplicity, considering only one detector ($\hat{d}'_A$), the overall interferometric transformation yields:

$$\hat{a}^\dagger(t_A) = \frac{i}{\sqrt{2}}\left[\sqrt{T_L}\,\hat{d}_A'^\dagger(t_A-\tau)\, e^{i\phi_A}\sin\!\left(\frac{\phi_m}{2}\right) + i\,\sqrt{T_S}\,\hat{d}_A'^\dagger(t_A)\,\cos\!\left(\frac{\phi_m}{2}\right)\right], \tag{5.9}$$

and an analogous expression holds for Bob's creation operator, $\hat{b}^\dagger(t_B)$.

Finally, by substituting Eq. (5.9) into Eq. (5.7), the resulting formalism enables the modeling of experimental imperfections of differential losses between the interferometer arms and non-ideal modulation waveforms, represented respectively by the transmission coefficients T_L, T_S, and the modulation function $\phi_m(t) = \frac{\pi}{2}\left[1+\sin\!\left(\frac{2\pi t}{2\tau}\right)\right]$. Using this model, numerical simulations were performed by varying the transmission coefficients and the FWHM of the Lorentzian photon wavefunction $\mu(t_A, t_B)$. The corresponding Bell-curve visibility was then estimated, as illustrated in Figure 5.4c. As shown, the use of a sinusoidal modulation leads to a slight reduction in interference visibility, which becomes more significant as the photon wave packet broadens. This occurs because a wider temporal profile increases the probability that early and late photons are incorrectly routed between the short and long interferometer paths. In our experimental conditions, where the optical pulse width is approximately 10 ps, and considering the characterized propagation loss of about 0.2 dB, the

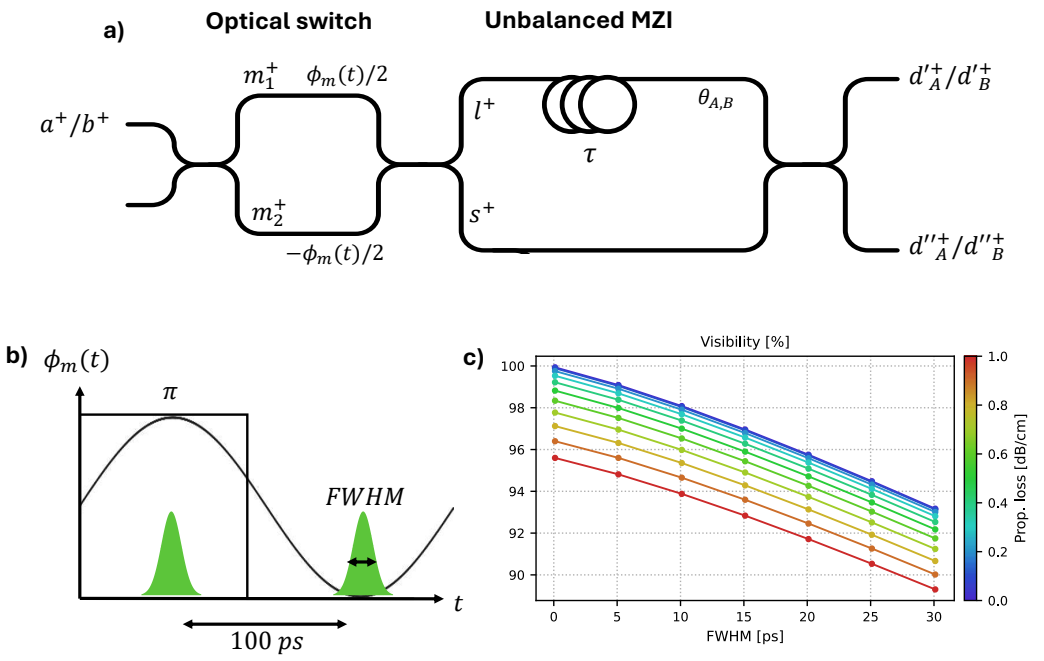

Figure 5.4: **Modelling of system non-idealities. a)** Schematic of the optical circuit showing the evolution of the photon creation operators used to model the effects of non-ideal photon switching and temporal pulse broadening. **b)** Comparison between sinusoidal and ideal square-wave driving signals applied to the MZM optical switch. **c)** Simulated nonlocal quantum interference visibility of the coincidence counts as a function of unbalanced loss between interferometer arms and time-bin wavefunction FWHM with sinusoidal switching applied.

expected maximum achievable visibility is $\sim 98\%$.

Although the analysis here focuses on the two dominant imperfections identified in our implementation, this model can be extended to include additional effects, such as different pulse shapes, arbitrary modulation waveforms, unbalanced beam splitter ratios, or imperfect synchronization between source and receivers, by incorporating the appropriate parameters into the model.

The impact of unbalanced losses could be mitigated in alternative designs by reducing the interferometer path-length difference, thereby minimizing the differential loss. However, this introduces a trade-off: a smaller time-bin separation requires faster optical switching for synchronization, as well as shorter photon pulses, which demand a broader optical bandwidth. Another possible strategy is to introduce controlled attenuation in the shorter arm to balance the interferometer [265]; although this approach preserves visibility, it increases overall insertion loss.

It is worth emphasizing that TFLN is an excellent platform for this application, offering low propagation loss and high EO bandwidth. These technological advantages enable precise photon switching and suggest that future improvements in fabrication could further reduce losses, thereby enhancing interference visibility. Finally, future implementations could exploit a pseudo-square driving waveform composed of multiple harmonics of the fundamental modulation frequency, effectively approximating a square wave while taking advantage of the device's 30 GHz EO bandwidth.

5.4 Temporal characterization

As a first experimental validation, I characterized the temporal correlations of the generated time-bin entangled photon pairs under different operating conditions of the analyzer interferometers by measuring their JTI [266], which provides a direct visualization of the unitary evolution imparted by the quantum receivers to the biphoton state under the selected operational modes. As introduced in Section 3.5, the JTI represents the two-photon coincidence probability density as a function of the arrival times of the signal (t_s) and idler (t_i) photons with respect to the laser pulse emission. It is proportional to the squared modulus of the biphoton wavefunction in the temporal domain. Experimentally, the JTI is obtained as a two-dimensional coincidence histogram of the signal and idler detection times, accumulated over a sufficiently long integration period to ensure adequate statistical accuracy.

The two spatially separated receiver modules were used to analyze the system behavior in both the passive (*mode 1*, Figure 4.1a.i) and active (*mode 2*, Figure 4.1a.ii) switching configurations. This preliminary characterization allows us to assess the quality of the optical switching and to verify the correct routing and temporal overlap of the photons before performing the Bell inequality measurements.

A quantitative comparison between measured JTIs and simulated was carried out by including nonidealities such as the finite photon temporal width and the detector timing jitter (55 ± 2 ps per SNSPD). The combined timing uncertainty broadens the coincidence distribution by approximately $\sqrt{55^2 + 55^2} \approx 77.8 \pm 0.4$ ps. In Figure 5.5a, the simulated JTIs are shown in the top row, while the corresponding experimental measurements are reported in the bottom row.

Firstly, I characterized the biphoton state generated at the output of the silicon photon-pair source, before being injected into the quantum receiver. The JTI of this state exhibits two peaks along the diagonal, corresponding to the early and late time-bin components of the entangled pair, as shown in the left column of Figure 5.5a.

When both analyzer interferometers operate in the *mode 1*, each time-bin component undergoes a unitary evolution that effectively replicates the two-lobe input pattern along both time axes, resulting in the characteristic seven-lobe interference structure. Among these, only the central lobe corresponds to temporally indistinguishable events that exhibit quantum interference, while the lateral lobes arise from distinguishable arrival-time combinations. The experimentally measured JTI (Figure 5.5a central column) reproduces the simulated pattern with high fidelity, confirming that the devices correctly implement the intended interferometric transformation.

In contrast, as shown in Figure 5.5a in the right column, when the devices operate in the *mode 2*, the RF modulation deterministically routes the two time-bin components such that they completely overlap in the central time slot along the diagonal of the JTI ($t_s = t_i$). As a result, all photon pairs interfere coherently, producing a single peak. The small residual side features in the experimental data are attributed to the finite extinction ratio of the MZM, minor bias drifts, and slight deviations of the applied RF amplitude from the ideal π-voltage. It should be noted that these features are shown on a color scale spanning four orders of magnitude, meaning their relative intensity is significantly lower than that

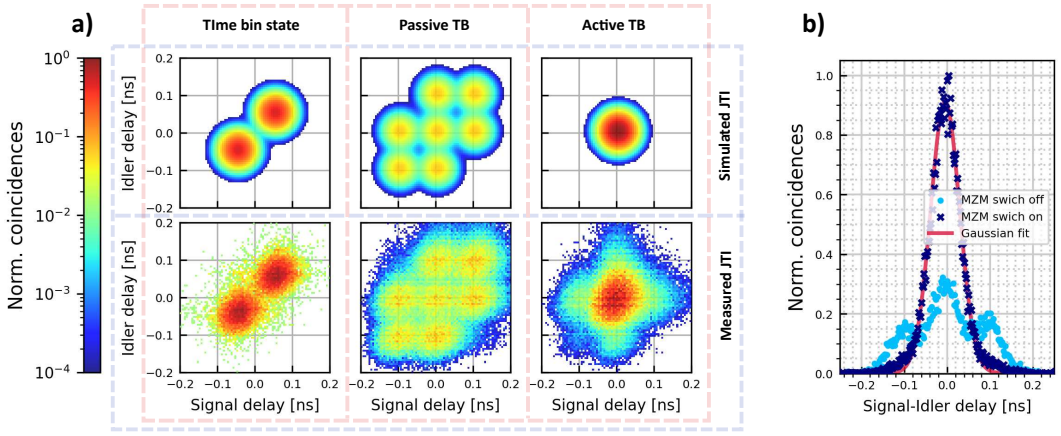

Figure 5.5: **Joint Temporal Intensity (JTI) characterization. a)** Simulated (top row) and corresponding experimental JTIs (bottom row) of the input entangled state at the device output, shown for both the passive and active switching configurations. **b)** Temporal coincidence histograms obtained by integrating the JTIs along the diagonal direction ($t_s + t_i = \text{const.}$), highlighting the characteristic three-peak structure in the passive configuration (light blue) and the single enhanced peak observed under active switching (dark blue).

of the main interference peak. The histograms for the active and passive configurations are normalized to the maximum achievable number of coincidence counts, which corresponds to the active configuration exhibiting maximum interference that is the case shown in the right column in Figure 5.5a.

To analyze the temporal coincidence profiles, the measured two-dimensional JTI maps for the *mode 1* and *mode 2* configurations were integrated along the diagonal direction ($t_s + t_i = \text{const.}$). This operation yields the coincidence rate as a function of the detection-time difference, $\Delta t = t_s - t_i$. In the passive configuration (light blue), the three peaks in Figure 5.5b correspond to the early, central, and late coincidences, arising respectively from the interferometer user path $|S_A L_B\rangle$, $|S_A S_B\rangle$ or $|L_A L_B\rangle$, and $|L_A S_B\rangle$ independently from the early and late input time-bins (see Section 3.5.1). Due to the finite timing resolution of the SNSPDs (55 ps), the three peaks partially overlap, making it difficult to apply effective post-selection when the time-bin separation is comparable to the detector resolution. Conversely, operating the device in active switching regime provides a single-peak coincidence histogram (dark blue), where all the incoming photons participate to quantum interference, therefore allowing a PSL-free violation of Bell's inequality.

5.5 Bell inequality violation

Once the temporal characterization and the functionality of the TFLN-based quantum receiver were validated, the next step was the certification of entanglement through the violation of Bell's inequality without temporal PSL. This demonstration exploits the switching capability of the developed integrated receiver and evaluates its overall performance through the measured quantum interference visibility.

Similar demonstrations of Bell inequality violation with time-bin entangled photons have been reported in the literature across different technological platforms. The work in [233]

reports a visibility of $89.2 \pm 0.7\%$ using an integrated photonic circuit based on SiN and implementing the Hug configuration [232], which effectively eliminates temporal PSL. However, this approach presents limitations for practical QKD implementations, as discussed in Section 3.5.3. The work in [234], which first experimentally demonstrated PSL-free Bell inequality violation with time-bin entangled photons by means of active switching, reports a visibility of $89 \pm 3\%$. In that case, fibre-based interferometers with long delays ($\sim$3 ns) were used, limiting scalability and integrability. More recently, in 2024 and 2025, respectively, the works [265] and [201] demonstrated integrated TFLN-based interferometers for time-bin entanglement analysis, achieving visibilities of $78.1 \pm 2.0\%$ and $99.0 \pm 0.7\%$, although both relying on temporal post-selection. In addition, in both cases the two analyzing interferometers (Alice and Bob) were implemented on the same chip, limiting their applicability to practical quantum communication scenarios.

In comparison with reported experimental demonstrations and the current state of research, no previous work has simultaneously combined an integrated implementation, closely spaced time-bin encoding, and temporal post-selection-free operation simultaneously. These features define the specific scope and novelty of the present work, which differs in key aspects from existing implementations and therefore makes direct comparison not straightforward. Nevertheless, a clear performance benchmark is provided by the requirement to violate Bell's inequality, which imposes a minimum visibility of $1/\sqrt{2}$. While this threshold represents the minimum requirement for entanglement certification, higher interference visibilities are desirable, as they directly translate into lower QBER values and therefore improved performance in QKD applications.

As a first measurement, the unbalanced interferometer phases were scanned simultaneously, i.e., under the condition $\theta_A = \theta_B$, while recording the coincidences on a single pair of detectors for both the passive and active switching configurations. In this way, the interference behavior in the two operational *mode* could be directly compared, in accordance with the theoretical predictions in Eqs. (4.6) and (4.7).

$$\begin{aligned} R_{\text{mode1}} &\propto \frac{1}{4} \pm \frac{1}{16}\cos(\theta_A + \theta_B), \\ R_{\text{mode2}} &\propto \frac{1}{4} \pm \frac{1}{4}\cos(\theta_A + \theta_B). \end{aligned} \tag{5.10}$$

The experimentally measured interference fringes are shown in Figure 5.6a. Each data point corresponds to a coincidence histogram integrated over 20 s. The active configuration, *mode 2* (blue dots) clearly exhibits a higher visibility, measured at $88.9 \pm 0.7\%$, compared to the passive configuration, *mode 1* (green dots), which reaches $23 \pm 0.6\%$. These values are fully consistent with the theoretical predictions, which set the maximum achievable visibilities at 100% and 25%, respectively. Figure 5.6b and c show the corresponding coincidence statistics as a function of the detection-time difference $\Delta t = t_A - t_B$ and of the applied phase $\theta_A + \theta_B$ (where $\theta_A = \theta_B$). The three distinct coincidence peaks characteristic of passive time-bin analysis are clearly visible. On the other hand, in the active switching configuration, only a single interference peak is produced and fully controlled through the quantum receiver phase, enabling a theoretical visibility of 100% without the need for temporal post-selection.

Finally, Figure 5.6d shows the single-photon detection rates at the output channels. As expected for time-bin entangled photons, no first-order interference is observed in the singles, since each photon is individually incoherent over the interferometer delay (10 ps coherence time versus 100 ps path imbalance). This verifies that the observed interference arises purely from two-photon correlations, a distinctive signature of entangled states.

After confirming the correct operation and PSL-free behavior, a full Franson-type Bell test was performed using all four detectors, with both Alice and Bob devices operating in the active configuration (*mode 2*). The interferometer phases were varied independently: θ_A was scanned while keeping θ_B fixed, and vice versa. The TSP were driven with powers ranging from 0 mW to 60 mW, in 1 mW steps, corresponding to phase shifts exceeding 2π radians. Each measurement point was integrated for 10 s. The measured coincidence rates for all detector combinations are reported in Figure 5.6e and f, together with sinusoidal fits used to retrieve the visibility of the interference patterns.

From the fitted curves, an average two-photon interference visibility of $(93.5 \pm 0.6)\%$ was extracted across all detector combinations, without subtracting accidental coincidences. This value is partially limited by the finite CAR of the source. Under our operating conditions, the silicon source was driven at a pair-generation probability per pulse of approximately 0.3%, corresponding to a CAR of about 100 according to the characterization shown in Figure 5.3a. Given the definition of CAR, the maximum achievable visibility in the presence of accidental events is

$$\mathcal{V}_{\max} = \frac{\mathrm{CAR}}{\mathrm{CAR}+2} \approx 98\%. \tag{5.11}$$

In addition to this CAR-limited visibility, a further $\sim$ 2% reduction is expected according with the modelled imperfections discussed earlier (including propagation loss and sinusoidal switching). The remaining few percent discrepancy can be attributed to non-ideal experimental settings, such as slight deviations in the switching voltages, thermal drifts in the biasing conditions, and small imbalance in the prepared time-bin state.

Overall, all measured visibilities exceed the classical limit of $1/\sqrt{2}$ required for violating Bell's inequality by more than 38 standard deviations. This approach allows the use of closely spaced time-bins, effectively relaxing the requirement on detector temporal resolution, which now depends on the overall repetition rate of the state rather than on the time-bin separation.

The high and consistent visibilities obtained for all detector pairs, together with the π-phase shift observed between the two independent user receivers, demonstrate the reliability, phase stability, and symmetry of the integrated devices. These results constitute direct evidence of time-bin entanglement and quantum nonlocality using fully independent integrated receivers. Although the present setup does not fulfill space-like separation conditions, the demonstrated approach is inherently PSL-free.

5.6 Quantum state tomography

Beyond entanglement certification, an important quantum application is QST, a procedure that enables the unique reconstruction of an unknown quantum state through measurements

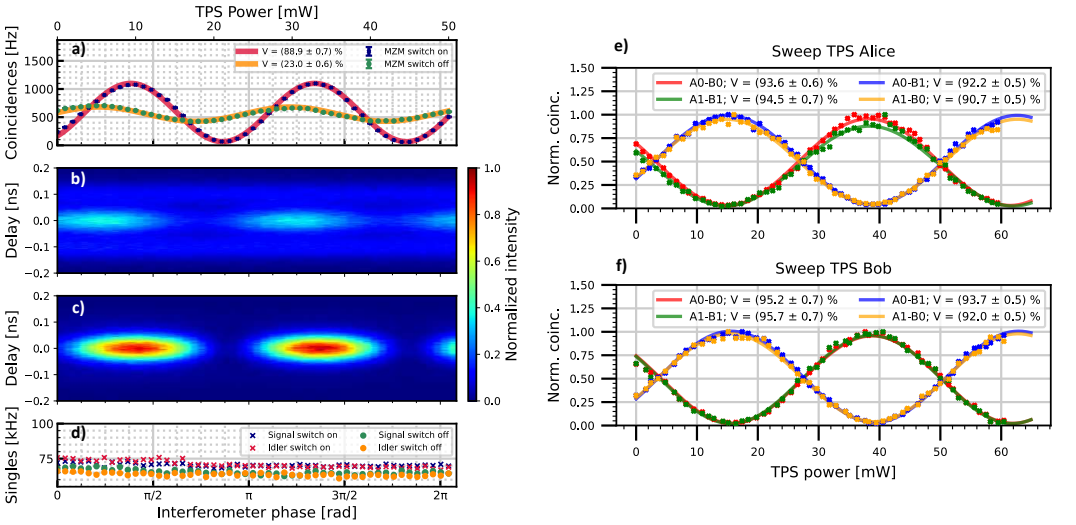

Figure 5.6: **Bell inequality violation. a)** Experimental interference fringes for the passive (green dots) and active (blue dots) switching configurations under simultaneous phase scanning ($\theta_A = \theta_B$). **b–c)** Corresponding coincidence histograms as a function of the detection-time difference Δt and the interferometer phase. **d)** Single-photon detection rates showing no first-order interference. **e–f)** Full four-detector Franson-type Bell test in active mode: coincidence rates (points) and sinusoidal fits (lines) for all detector combinations. The coincidence counts are normalized to enable direct comparison, as unbalanced losses between detectors result in different sinusoidal amplitudes. V denotes the visibility. The statistical uncertainties are smaller than the plotted markers.

performed on an ensemble of identically prepared copies. A complete QST was performed on the biphoton state generated by the integrated silicon source, by properly measuring the signal and idler photons through the arbitrary reconfigurability of the two quantum receivers, which operate as fully programmable time-bin projectors. This measurement serves a dual purpose. First, it evaluates the quality of the generated time-bin entangled state, showing that the device can operate as a programmable pump-pulse shaper, enabling the tailoring of time-bin pulse pairs with controllable relative amplitude and phase. When combined with a nonlinear optical source, this capability allows the generation of arbitrary time-bin entangled states. Second, it demonstrates the ability of the device to function as a fully reconfigurable analyzer for projecting onto arbitrary time-bin states.

The QST is performed by successively performing a series of projective measurements across three mutually unbiased bases for each qubit. This is achieved through the application of specific phase conditions to both integrated quantum receivers. Acquiring measurement outcomes for every condition over a sufficiently large ensemble of identically prepared states ensures adequate statistical precision, enabling the corresponding density matrix to be reconstructed. This provides complete information about the generated quantum state. In our case, the quantum system consists of $n = 2$ photons, each encoded in a $d = 2$-dimensional Hilbert space, thus the composite system therefore spans a space of dimension $d^n = 4$. The minimum number of projective measurements required for a complete QST is $d^{2n} = 16$ [267].

In this work, this process is facilitated by the fact that each integrated quantum receiver can simultaneously measure the two orthogonal states of a selected basis within a single

Alice			Bob		
Mode	**Phase θ_A**	**Basis**	**Mode**	**Phase θ_B**	**Basis**
mode 3	–	$Z : \{\|0\rangle, \|1\rangle\}$	*mode 3*	–	$Z : \{\|0\rangle, \|1\rangle\}$
mode 3	–	$Z : \{\|0\rangle, \|1\rangle\}$	*mode 2*	0	$X : \{\|+\rangle, \|-\rangle\}$
mode 3	–	$Z : \{\|0\rangle, \|1\rangle\}$	*mode 2*	$\pi/2$	$Y : \{\|R\rangle, \|L\rangle\}$
mode 2	0	$X : \{\|+\rangle, \|-\rangle\}$	*mode 3*	–	$Z : \{\|0\rangle, \|1\rangle\}$
mode 2	0	$X : \{\|+\rangle, \|-\rangle\}$	*mode 2*	0	$X : \{\|+\rangle, \|-\rangle\}$
mode 2	0	$X : \{\|+\rangle, \|-\rangle\}$	*mode 2*	$\pi/2$	$Y : \{\|R\rangle, \|L\rangle\}$
mode 2	$\pi/2$	$Y : \{\|R\rangle, \|L\rangle\}$	*mode 3*	–	$Z : \{\|0\rangle, \|1\rangle\}$
mode 2	$\pi/2$	$Y : \{\|R\rangle, \|L\rangle\}$	*mode 2*	0	$X : \{\|+\rangle, \|-\rangle\}$
mode 2	$\pi/2$	$Y : \{\|R\rangle, \|L\rangle\}$	*mode 2*	$\pi/2$	$Y : \{\|R\rangle, \|L\rangle\}$

Table 5.1: Summary of the nine measurement configurations used for quantum state tomography. Each configuration corresponds to a pair of measurement settings for Alice and Bob, including the operation mode (ref. to Figure 4.1b), interferometer phase, and chosen measurement basis.

configuration. To improve the accuracy of the reconstruction and mitigate statistical fluctuations, I performed an overcomplete set of 36 projective measurements. In particular, three measurement configurations were used for each device. Projections onto the equatorial bases $X = \{|+\rangle, |-\rangle\}$ and $Y = \{|R\rangle, |L\rangle\}$ were performed by operating the MZM to overlap the two time bins into a single temporal slot (*mode 2*), and by adjusting the phase of the unbalanced MZI according to Eq. (4.7), with $\theta_{A,B} = 0$ and $\pi/2$, respectively. For the computational basis $Z = \{|0\rangle, |1\rangle\}$, the projection was implemented by operating the optical switch in the reverse configuration (*mode 3*), which increases the temporal separation between the two output time bins from 100 ps to 200 ps. This configuration enables direct discrimination between the two time-bin states without interference, by associating each detection event with its corresponding arrival time. By permuting the three measurement configurations between Alice and Bob, corresponding to the Z, X, and Y bases, a total of $3 \times 3 = 9$ measurement combinations were realized. Each configuration yields the four possible joint detection outcomes between the two parties, resulting in a complete set of 36 projective measurements required for full two-qubit QST. The corresponding measurement conditions are summarized in Table 5.1.

Figure 5.7a shows the measured JTI distributions for four representative projective measurements, out of a total of nine, recorded for one of the four possible detector pairs (A0–B0). In the three projective measurements $|++\rangle\langle++|$, $|+R\rangle\langle+R|$, and $|RR\rangle\langle RR|$, a strong suppression of coincidence counts is observed in the outer time bins (i.e., when photons are detected in the early or late arrival-time windows at Alice or Bob), resulting in a well-localized overlap in the central time bin where interference occurs. According to Eq. (4.7), the first and third projectors correspond respectively to the maximum and minimum of the two-photon interference fringe, while the second corresponds to the quadrature point.

In the fourth JTI plot, the projections onto the $|00\rangle$ and $|11\rangle$ computational-basis states appear as two well-separated coincidence regions, marked by dashed lines. Although this measurement generally requires higher temporal resolution to resolve the two outcomes, the temporal separation between the peaks is doubled (200 ps), effectively relaxing the detector timing-resolution requirement by a factor of two.

For completeness, Figure 5.7c reports the normalized coincidence statistics for all projective measurements. The agreement with the ideal target distribution is generally good. The main deviations appear in the measurements performed in the Z basis, where the experimental values for the $|1\rangle$ ($|0\rangle$) are slightly lower (higher) than the expected ones. This behavior suggests that the operating conditions in *mode 3*, used to spatially separate the photons for computational-basis projections, were not perfectly optimized, resulting in a small bias between the two time-bin amplitudes.

From the full set of experimental data, the biphoton density matrix ρ was reconstructed using a maximum-likelihood estimation algorithm [268], as shown in Figure 5.7b. The quality of the reconstructed state is quantified by two standard figures of merit: the purity $\mathcal{P}$ and the fidelity $\mathcal{F}$,

$$\mathcal{P} = \mathrm{Tr}(\rho^2), \qquad \mathcal{F} = \left[\mathrm{Tr}\left(\sqrt{\sqrt{\sigma}\,\rho\,\sqrt{\sigma}}\right)\right]^2,$$

where σ is the density matrix of the target state. High values of both parameters indicate well-preserved coherence and low decoherence during state preparation and measurement. The reconstructed density matrix exhibits a purity of 93% and a fidelity of 95% with respect to the Bell state $|\Phi^+\rangle$.

A closer inspection of the real and imaginary parts reveals small deviations from the ideal form: the probability amplitude of the $|00\rangle$ component is slightly higher than that of $|11\rangle$, and the imaginary part shows a small residual phase offset relative to the ideal $|\Phi^+\rangle$ state. The former effect can be attributed to the previously discussed imprecision in the *mode 3* reverse-switching operation, or also to imperfect tailoring of the pump pulses, which may lead to an unbalanced amplitude ratio between the two time-bins. The latter deviation may arises from phase instabilities occurring at both the state-generation and detection stages. In particular, slow drifts and uncertainties in the applied phase at the bias point of the TPS of the first-stage MZM and of the second-stage MZI can introduce small residual phase errors during the acquisition. Together, these factors account for the minor imperfections observed in the reconstructed density matrix and slightly limit the achievable purity and fidelity.

Nevertheless, the reported figures of merit confirm that a high-quality entangled state was generated, fully suitable for the implementation of the entanglement-based BBM92 QKD protocol presented in the next chapter. Indeed, the security of the protocol implemented with two-dimensional quantum states requires that the QBER remains below to the 11% threshold [269]. From the measured average visibility of the quantum interference fringes, $\mathcal{V} = 93.5\%$, the corresponding QBER can be estimated as $QBER = (1 - \mathcal{V})/2 \approx 3.25\%$ [168]. This value is well below the security threshold, confirming the suitability of the generated entangled states for QKD applications.

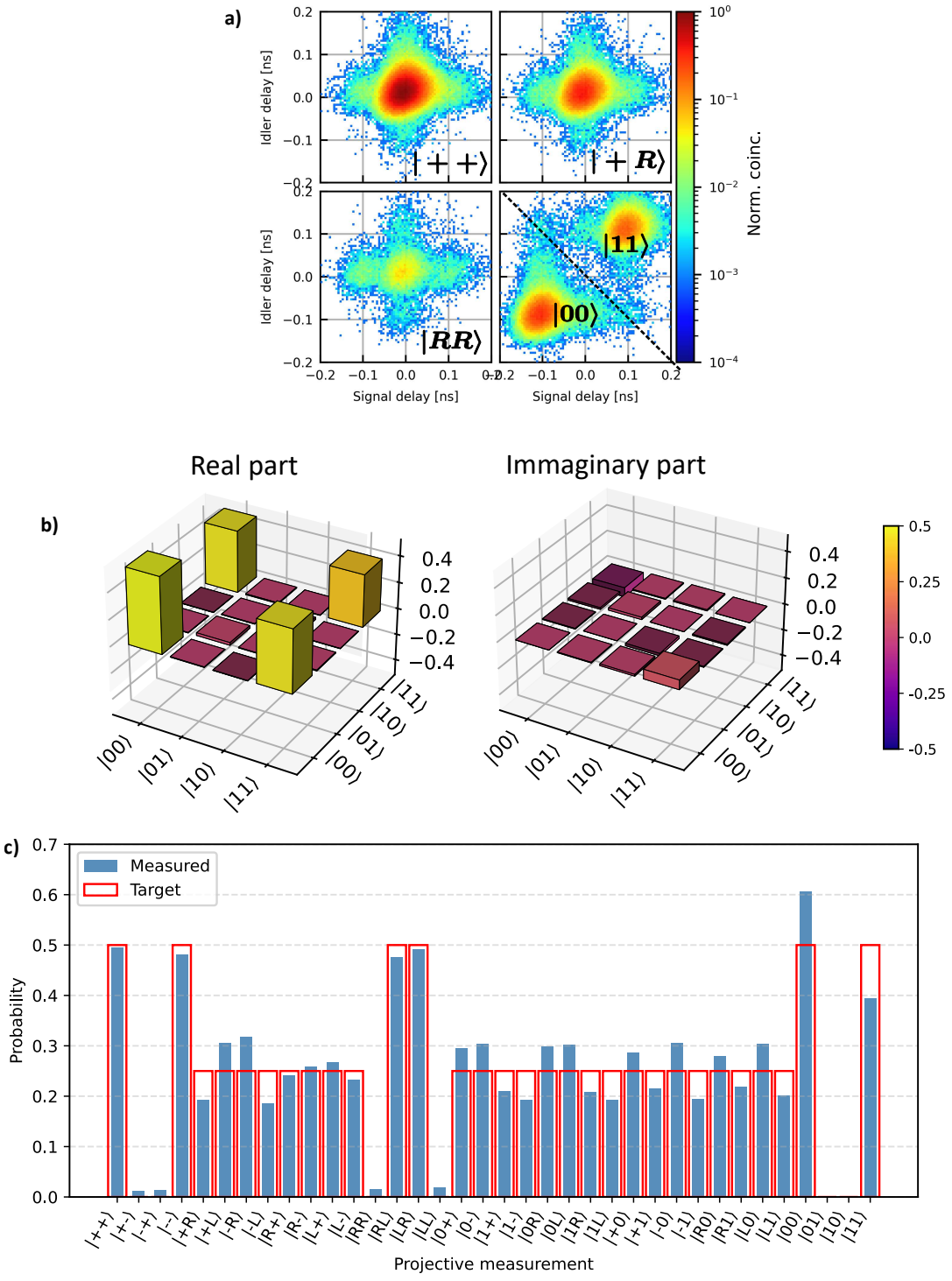

Figure 5.7: **Tomography of the entangled time-bin state. a)** JTI of the entangled time-bin state for a representative subset of the projective measurement configurations used for QST. **b)** Experimentally reconstructed density matrix of the generated quantum state, obtained via maximum-likelihood estimation. **c)** Normalized coincidence statistics for all projective measurements, compared with the ideal target distributions. The statistical uncertainties are smaller than the plotted features (the largest relative error is 0.16% among the all 36 projective measures).

Chapter 6

Quantum key distribution with time-bin encoding

In this chapter, I present the experimental demonstration of the entanglement-based BBM92 QKD protocol [171], implemented using the integrated time-bin receiver developed in this work. This experiment constitutes the first demonstration of a post-selection-free time-bin QKD system based on fast optical switching in an integrated photonic platform. The implementation is enabled by the TFLN receiver described in Chapter 4, previously validated for high-visibility time-bin interference and QST (Chapter 5).

The BBM92 protocol is operated in two configurations, made possible by the reconfigurability of the device: *passive basis selection* and *active basis selection*, which differ in the method used to choose the two mutually unbiased measurement bases. In this chapter, these two approaches are described, highlighting the trade-off between experimental constraints and achievable secure-key performance. The chapter also examines the protocol performance under varying channel loss and discusses possible improvements, including source optimization and an increase of the system clock rate.

6.1 Passive basis selection

The implementation of the entanglement-based BBM92 QKD protocol relies on the same optical setup used for the entanglement-certification and QST experiments (Figure 5.1), with only minimal modifications applied to the two receiver stations. The overall architecture is preserved: a single entangled photon-pair source is shared between the two users, and the two photons are demultiplexed and distributed to Alice and Bob.

For the passive basis selection QKD configuration, the modifications introduced at the receiver stations are illustrated in the simplified schematic of Figure 6.1. After wavelength demultiplexing, the incoming signal and idler photons pass through a passive 50:50 fiber beam splitter, which probabilistically directs each photon along one of two paths. One output is sent directly to a SNSPD, allowing time-of-arrival detection in the Z basis. The other output is injected into the integrated TFLN quantum receiver. Its two output ports are connected to two SNSPDs, which implement the interferometric projection in the X basis. In this basis, the two states are distinguished according to the output port. Each user therefore

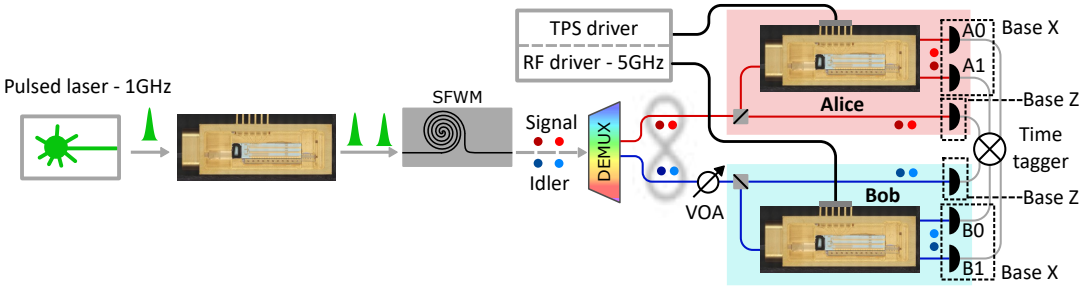

Figure 6.1: **Experimental setup for QKD with passive basis selection.** Simplified schematic of the experimental implementation of the passive basis selection QKD configuration. Compared to the detailed setup shown in Figure 5.1, a fiber-based 50:50 beam splitter is placed before the TFLN device to passively perform the basis choice: half of the photons are sent directly to an SNSPD and measured in the computational (Z) basis, while the remaining half are routed to the integrated TFLN receiver for measurement in the interferometric (X) basis. The variable optical attenuator (VOA) is used in the measurements reported in Section 6.3 to simulate a long fiber channel.

employs three SNSPDs, for a total of six detectors across Alice and Bob. Fiber polarization controllers are placed before each SNSPD to maximize detection efficiency.

The TFLN receiver operates in the switching regime (*mode 2*), where the early and late time-bin components are deterministically overlapped at the device output (Figure 4.1b.ii). This configuration implements the PVMs defined in Eq. (4.2):

$$\hat{P}_{\pm}(\theta_{A,B}) = \tfrac{1}{2}\left(|0\rangle \pm e^{i\theta} |1\rangle \right)\left(\langle 0| \pm e^{-i\theta} \langle 1| \right),$$

where the $\pm$ signs correspond to the two output ports of the device. The internal phase of the unbalanced MZI is set to $\theta_{A,B} = 0$, resulting in projective measurements in the X basis, thus projecting onto the states $|+\rangle\langle+|$ and $|-\rangle\langle-|$, without requiring temporal post-selection. In this configuration, coincidence detection events are maximized between specific detector pairs (e.g., A0–B0 and A1–B1) and minimized for the crossed detection pairs (e.g., A0–B1 and A1–B0) when the input state is the maximally entangled Bell state $|\Phi^+\rangle = \frac{|00\rangle+|11\rangle}{\sqrt{2}}$. Photons routed directly to the SNSPDs bypass the interferometric stage, and their arrival time determines whether an early ($|0\rangle$) or late ($|1\rangle$) photon is detected, corresponding to projective measurements in the Z basis.

Overall, this configuration implements the BBM92 protocol using two mutually unbiased bases, Z and X. The basis choice is intrinsically random and is determined by the passive beam splitter, which is why this scheme is referred to as *passive basis selection* QKD. The randomness of the measurement outcomes is ensured by the shared entangled state, as demonstrated in the previous chapter. These two forms of randomness are essential requirements for the correct implementation of the QKD protocol.

6.1.1 Secret key statistical analysis

To evaluate the performance of the QKD protocol, I focus on the analysis of the SKR, which represents the main figure of merit for QKD implementations. In this section, I present the statistical assumptions and analysis used to extract a reliable SKR, incorporating all steps

required in a realistic implementation: sifting, parameter estimation, error correction, and privacy amplification.

Firstly, I define the statistical quantities used in the security analysis. When distributing entangled photon pairs, I denote by $C_{|ab\rangle}$ the number of detected coincidence events between the two users when Alice and Bob project their measurements into eigenstates $|a\rangle$ and $|b\rangle$ of basis B, where $B \in \{Z, X\}$ and $a, b \in \{0, 1\}$ or $\{+, -\}$ respectively. These coincidence counts are reduced from the generation rate of the nonlinear source due to outcoupling losses, demultiplexing losses, and the receiver-side detection losses. I denote by p_B the probability that both users measure in basis B. The total coincidence detection rates in each basis are then given by

$$R_X = \frac{C_{|++\rangle} + C_{|+-\rangle} + C_{|-+\rangle} + C_{|--\rangle}}{\tau}, \tag{6.1}$$

$$R_Z = \frac{C_{|00\rangle} + C_{|01\rangle} + C_{|10\rangle} + C_{|11\rangle}}{\tau}, \tag{6.2}$$

where τ is the acquisition time required to accumulate a block of raw key.

In the passive-basis configuration, an asymmetry appears between the X and Z basis detection rates where $R_Z > R_X$. This arises because X basis detections pass through the integrated TFLN receiver, and experience approximately 6 dB of additional optical loss compared to the direct-detection Z-basis path. Experimentally, the measured optical losses were 13.3 dB (15.3 dB) and 5.9 dB (6.3 dB) for the signal (idler) photons in the X and Z basis paths, respectively. This results in maximum coincidence rates of $R_X = 959$ Hz in the X basis and $R_Z = 62$ kHz in the Z basis. Despite this asymmetry, secure QKD operation remains feasible by adopting an efficient information-reconciliation scheme [270]. Indeed, an asymmetric basis choice increases the sifting factor, which is defined as

$$q = p_X + p_Z,$$

which in our case approaches 1 because $p_Z \gg p_X$, maximizing the number of usable detection events. I therefore assign the Z basis as the *key basis*, used to generate the sifted key and the X basis as the *check basis* used for parameter estimation. This choice remains fully secure, provided that a sufficient number of measurements are collected in the less probable X basis to enable reliable parameter estimation and the detection of potential eavesdropping attempts [270].

The QBERs can be computed in each basis as:

$$Q_X = \frac{C_{|+-\rangle} + C_{|-+\rangle}}{C_{|++\rangle} + C_{|--\rangle} + C_{|+-\rangle} + C_{|-+\rangle}}, \tag{6.3}$$

$$Q_Z = \frac{C_{|01\rangle} + C_{|10\rangle}}{C_{|00\rangle} + C_{|11\rangle} + C_{|01\rangle} + C_{|10\rangle}}. \tag{6.4}$$

Here, Q_X quantifies the phase-error rate associated to X basis, while Q_Z corresponds to the bit-flip error rate affecting the Z-basis key.

In the **asymptotic regime** characterized by infinitely many measured events, the secure key rate extracted from the Z basis is [131]

$$S_Z = R_Z \left[1 - H(Q_X) - f\, H(Q_Z)\right], \tag{6.5}$$

where $H(p) = -plog_2(p) - (1-p)log_2(1-p)$ is the binary Shannon entropy, which quantifies the fraction of key used for privacy amplification, and $f = 1.06$ is the error-correction inefficiency factor, accounting for the additional bits used during the classical error-correction step.

In realistic implementations, only a finite number of signals are detected. The information obtained in the parameter estimation step therefore reflects the statistical properties of the QBER data set only with limited precision, since the estimation is performed on a finite sample. As a consequence, the observed QBER may differ from the true underlying error rate due to statistical fluctuations, and these fluctuations must be properly bounded. Typically, the deviation between the true QBER and its estimated value is upper-bounded by an uncertainty term that depends on the size of the parameter estimation sample. To bound these deviations, and thus obtain a secure lower bound on the SKR, I employ two different statistical bounds: (i) the Serfling inequality [271], applied to QKD by Tomamichel *et al.* [272], here referred to as the *Serfling bound* and (ii) a more recent method based on Chernoff inequalities [273], introduced by Mannalath *et al.* [274], here referred to as the *Chernoff bound*. These approaches enable the calculation of finite-key SKRs under more realistic constraints.

In the **finite block-size regime**, the SKR can be computed as [131, 272]

$$S_Z = R_Z \left[1 - H(Q'_X) - f\, H(Q_Z)\right] - \log\left(\frac{2}{\epsilon_{\text{cor}}\epsilon_{\text{sec}}^2}\right), \tag{6.6}$$

where ϵ_{cor} and ϵ_{sec} denote the correctness and secrecy parameters, representing the allowed probabilities of failure of the error-correction and privacy-amplification steps. Throughout this analysis, I assume $\epsilon_{\text{cor}} = 10^{-10}$ and $\epsilon_{\text{sec}} = 10^{-10}$, reasonable values according to Ref. [272, 274–277]. The term Q'_X is the upper-bounded phase-error rate, accounting for statistical fluctuations originating from the finite parameter estimation sample. Note that the source-independent nature of EBQKD implies that inefficiencies in the entangled-photon source do not affect the security analysis [277].

Using the *Serfling* bound, the fluctuation-adjusted QBER is

$$Q'_X = Q_X + \sqrt{\frac{(n_Z+1)\log(1/\epsilon_{\text{sec}})}{2n_X(n_X+n_Z)}}, \tag{6.7}$$

where n_B denotes the total number of coincidences measured in basis B:

$$\begin{aligned} n_X &= C_{|++\rangle} + C_{|--\rangle} + C_{|+-\rangle} + C_{|-+\rangle}, \\ n_Z &= C_{|00\rangle} + C_{|11\rangle} + C_{|01\rangle} + C_{|10\rangle}. \end{aligned}$$

Using instead the *Chernoff* bound, the adjusted QBER is given by

$$Q'_X = \frac{(n_Z + n_X)\,\Gamma^+_{n_X,\epsilon_{\mathrm{PE}}}(m_X/n_X) - m_X}{n_Z}, \tag{6.8}$$

where ϵ_{PE} is the parameter estimation failure probability, and

$$\Gamma^+_{n,\epsilon}(p) = \begin{cases} \gamma^+_{n,\epsilon}(p), & \text{if } p \in \left[0, \frac{1-2\kappa_{n,\epsilon}}{1+\kappa_{n,\epsilon}}\right], \\ 1+\epsilon, & \text{otherwise,} \end{cases} \tag{6.9}$$

with $\kappa_{n,\epsilon} = \frac{2}{9n}\ln(1/\epsilon)$ and

$$\gamma^+_{n,\epsilon}(x) = \frac{1}{1+4\kappa_{n,\epsilon}}\left[3\kappa_{n,\epsilon} + (1-2\kappa_{n,\epsilon})x + 3\sqrt{\kappa_{n,\epsilon}\left(\kappa_{n,\epsilon} + x - x^2\right)}\right].$$

6.1.2 Experimental results

To verify the quality and reliability of the protocol, a long-duration measurement exceeding 12 hours was performed by continuously operating the QKD setup without interruption. Under these conditions, the SKR was evaluated in both the asymptotic regime and the finite-size regime, the latter computed using the two statistical bounds for a block size of 10^6. All three SKR traces, together with the measured QBERs in the X and Z bases as a function of time, are reported in Figure 6.2a. Throughout the acquisition, the SKR exceeded 18.8 kbit/s, reaching a maximum value of 25.4 kbit/s in the finite-size regime using the *Chernoff* bound. The asymptotic-limit value is approximately 14% higher, whereas the finite-size SKR obtained using the *Serfling* bound is about 13.5% lower. Notably, the present work reports the first realizations of time-bin QKD closing the PSL, achieved at the same time with long-term operational stability, and with the highest SKR (exceeding 25 kbit/s) demonstrated so far in time-bin entanglement based systems, as summarized in Tab. 6.1.

User implementation	DoF	SKR per channel	Link length	Clock rate	Bin separation
Silica-based[278]	Time	0.14 bit/s	100 km	0.333 GHz	1 ns
Fiber-based[180]	Time	42 bit/s 29 bit/s	47 km 60.5 km	220 MHz	3 ns
Fiber-based[181]	Time	5.1 bit/s	0 km	18 MHz	3.6 ns
PIC[124]	Time	2.04 kbit/s 37 bit/s	0 km 60 km	250 MHz	64 ps
Free space[182]	Time	5.1 kbit/s	0 km	80 MHz	1 ns
Fiber-based[279]	Pol.	223 bit/s	201 km	CW	—
Fiber-based[280]	Time + Pol.	700 bit/s*	0 km	50 MHz	5 ns
Fiber-based[281]	Time-energy	7 kbit/s	50 km	CW	1.6 ns
TFLN (this work)	**Time**	**25.4 kbit/s**	0 km	**1 GHz**	**100 ps**

Table 6.1: Comparison among EBQKD demonstrations using different degrees of freedom (DoF). All implementations employ fiber-based channels, with channel losses scaling approximately as ~ 0.2 dB/km attenuation in standard single-mode fiber for the reported distances. PIC: Photonic Integrated Circuit, *: Values extracted from published plots.

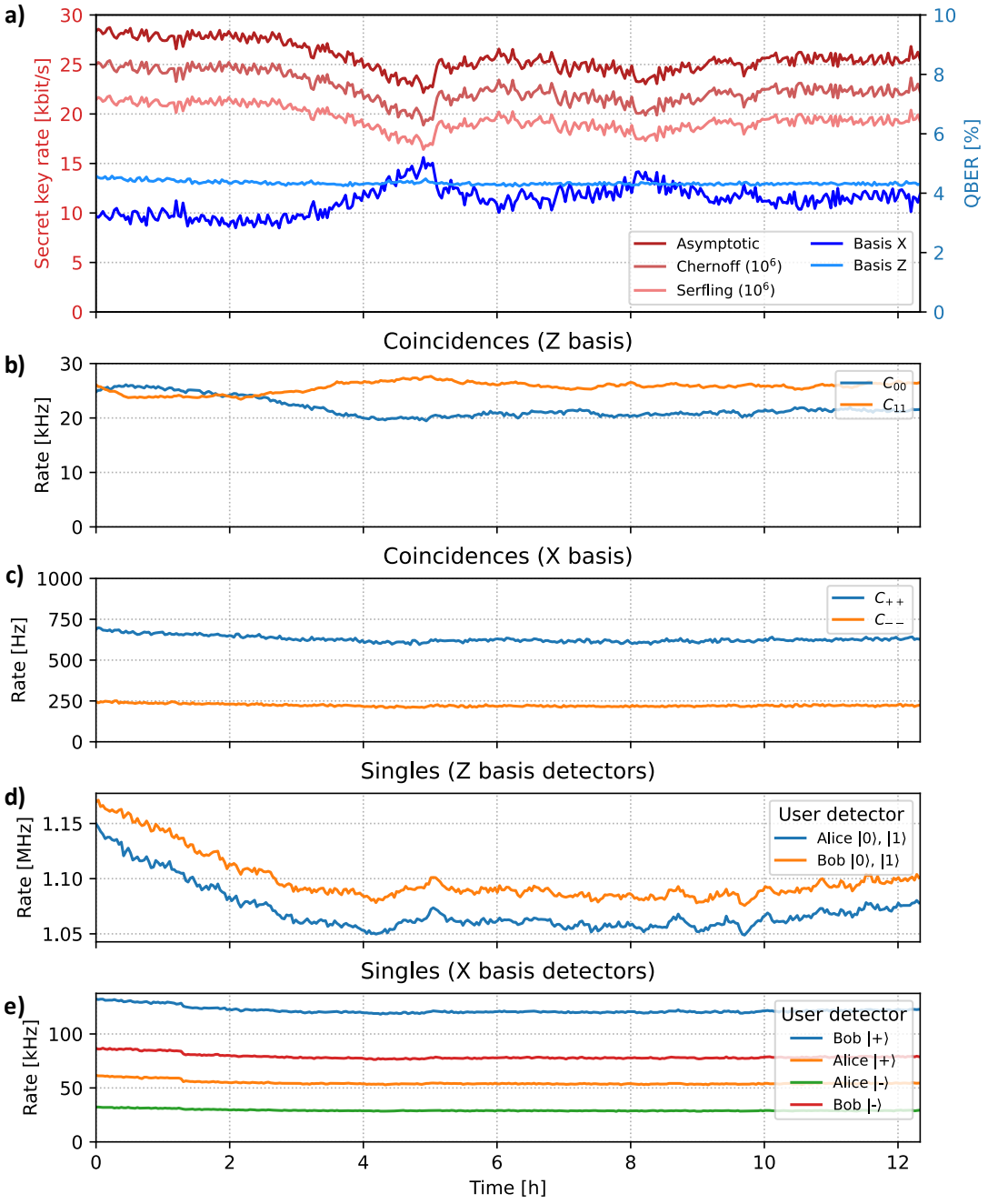

Figure 6.2: **Passive basis selection QKD.** Time evolution of the main parameters of the BB92 QKD protocol over a continuous 12-hour acquisition. **a)** SKR in the asymptotic and finite-key regimes, evaluated using Serfling and Chernoff bounds. **b)** Coincidence rate in the computational (Z) basis. **c)** Coincidence rate in the interferometric (X) basis, reduced due to the additional losses of the TFLN receiver. Time trace of the single-photon counts in the **(d)** Z basis and **(e)** X basis.

The QBER in the Z basis remains relatively stable over time, with an average value of 4.3%. This error is primarily caused by the limited temporal resolution of the SNSPDs. The time-bin separation of 100 ps is comparable to the detector timing jitter (approximately 55 ps FWHM), causing the early and late detection distributions to partially overlap. These ambiguous events lead to errors in the Z basis and they are mitigated by the optimized discarding-window strategy presented in Section 6.1.3. The QBER measured in the X basis strongly depends on the interferometric performance of the device projections. Under the source conditions used in the experiment, the pump-pulse energy of $\sim$ 2.25 pJ yields a photon-pair generation probability of $p = 1\%$ per pulse, with a measured CAR of 52 (Figure 5.3a). Additional noise contributions, such as accidental coincidences or dark counts, are negligible under these operating conditions. From the measured CAR, the expected interference visibility, using Eq. 5.11, is approximately 96.1%, corresponding to an ideal QBER of $(1 - V)/2 \approx 1.92\%$ [168]. Experimentally, an average QBER of 3.76% was recorded. This value is consistent if it is also considered the non-ideal sinusoidal switching and uncertainties in the applied DC bias and RF drive amplitude, as discussed in Section 5.3.

Overall, the long-term statistical fluctuations of the SKR are directly associated with variations in the QBER of the X basis, which, as predicted by the key-rate formulas (6.5) and (6.6). These suggest the presence of slow phase drifts either in the source interferometer used to tailor the pump-pulse pair and/or in the interferometer used in the receiver's setup. Importantly, the SKR reduction is not caused by fluctuations in the entangled-photon generation rate, as confirmed by the stability of the coincidence-count rates in the computational basis (Figure 6.2b) and in the interferometric basis (Figure 6.2c), as well as by the stability of the corresponding single-photon count rates (Figure 6.2.d and e).

From the coincidence traces, two additional features can be observed. First, as previously explained, there is an imbalance between the Z- and X-basis count rates due to the extra insertion loss of the integrated quantum receiver. Second, an imbalance appears between the coincidence counts C_{++} and C_{--} as shown in Figure 6.2c. This asymmetry probably arises from unequal losses in the two output ports of the device even if such large imbalance has not been measured form the linear device characterization (Section 4.6). Moreover, this imbalance is independent of the operating bias conditions of the two cascaded interferometers in the quantum receiver. Since the single-photon state injected into the device has a temporal coherence shorter than the imbalance of the MZI, any routing between the short and long arms performed by the optical switch (even if incorrectly directed with respect to the intended path) should still lead to an equal splitting at the final MMI. Therefore, the exact origin of this effect remains unclear.

To better illustrate the practical impact of the two statistical bounds (beyond the 12-hour temporal trace obtained at a fixed block size of 10^6) I evaluate the finite-size SKR as a function of the sifted-key block length for both the Serfling and Chernoff methods. The resulting curves, shown in Figure 6.3, highlight the performance improvement enabled by the Chernoff bound, particularly in the low-count regime typical of EBQKD, where coincidence rates are inherently limited by the nondeterministic nature of photon-pair generation. As the block size increases, the difference between the two bounds progressively decreases.

Finally, the SKR could be further increased by operating the protocol at a higher clock

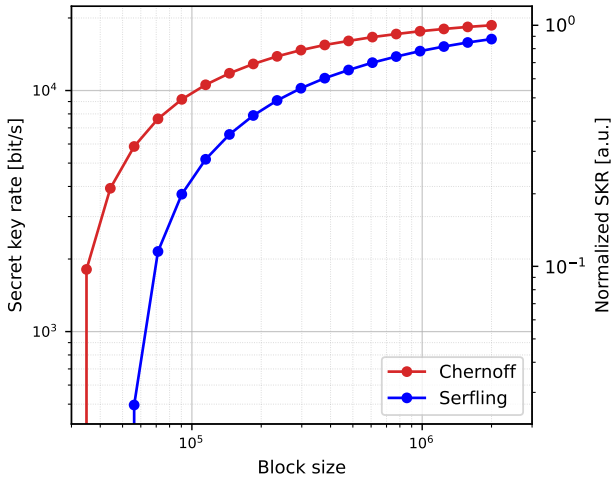

Figure 6.3: **SKR dependence on Block size.** Comparison between the Chernoff and Serfling bounds for the finite-regime computation of the SKR as a function of the block size.

repetition rate. For the design employed in the realized TFLN devices, the upper limit is set by the 100 ps interferometer unbalance, which corresponds to a maximum repetition rate of 5 GHz in order to distinguish successive time-bin states. As will be discussed in Section 6.4, the source generation conditions could also be optimized to increase the pair-generation probability. However, both approaches were not tested in this demonstration, since they would also lead to an increase in the singles detector rates and the available detection system imposed a practical limit of approximately 1.5 MHz single-count rate, consistent with the tested operating point of 1.1 MHz as shown in Figure 6.2.d. The limit is imposed by hardware constraints related to the SNSND dead time, which cause the latching effect at high count rates.

6.1.3 Optimization of time-bin discrimination in the Z basis

As illustrated in the schematic diagram of Figure 6.1, the measurement in the Z basis is performed by directly detecting the arrival time of the entangled photons, which determines whether a photon was detected in the early ($|0\rangle$) or late ($|1\rangle$) time-bin. In our setup, however, the limited temporal resolution of the SNSPDs characterized by a timing jitter of 55 ± 2ps leads to a non-negligible overlap between the detection distributions associated with the two time-bins. This effect is visible in the histogram of coincidence events as a function of the detection arrival time for one user, shown in Figure 6.4a.

To quantify the impact of the limited temporal resolution and to mitigate the resulting ambiguity in time-bin discrimination, I adopted a *discarding window*, indicated by the red shaded region in the figure. This window is centered between the early and late peaks and its width can be tuned. Detection events falling within this region are excluded from the analysis, thereby reducing the QBER by eliminating ambiguous detections that might otherwise be incorrectly assigned to the wrong time-bin. However, this strategy also decreases the total number of valid detection events, as shown in Figure 6.4b.

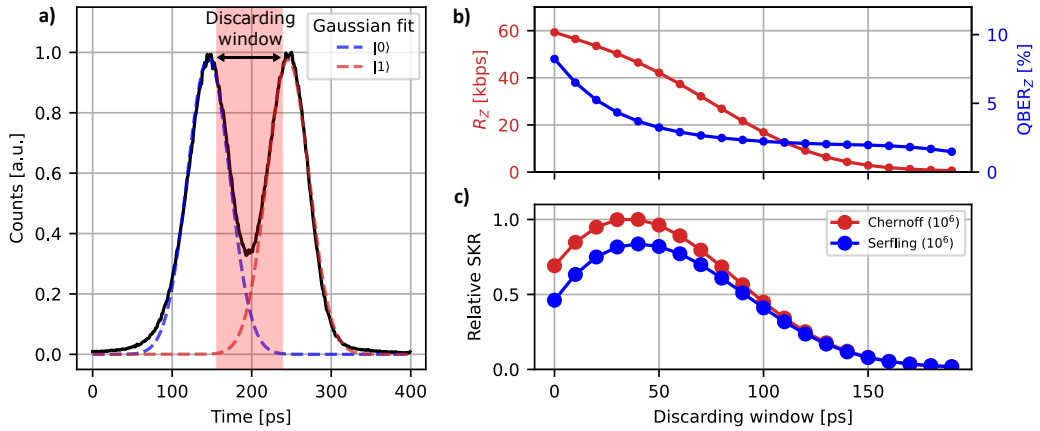

Figure 6.4: **Optimization of detection analysis in the Z basis. a)** Histogram of time-detection events in the Z basis for one QKD user. The detection time is measured relative to the laser pulse emission. **b)** Coincidence rate and QBER between Alice and Bob as a function of the discarding-window width. **c)** SKR as a function of the discarding-window width in the passive basis configuration. The optimal value is 40 ps for both statistical bounds for a block size of 10^6.

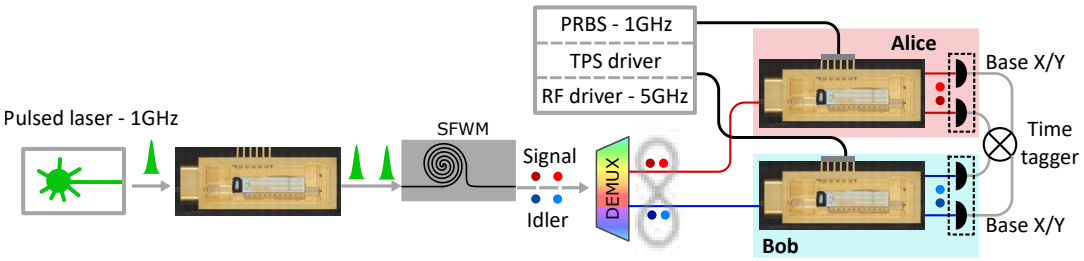

Figure 6.5: **Experimental setup for QKD with active basis selection.** Simplified schematic of the experimental implementation of the active basis selection QKD configuration. Compared to the detailed setup shown in Figure 5.1, the EO modulator integrated in the unbalanced MZI is driven by the pseudo-random bit sequence (PRBS) generator to randomly select the measurement among the X or Y basis.

The resulting trade-off between reduced QBER and decreased detection rate is reflected in the SKR, illustrated in Figure 6.4c. For the data presented in the previous sections, an optimized discarding-window width of 40 ps was used. This value maximizes the SKR for both the Chernoff and Serfling bounds, yielding a resulting QBER of approximately 4.4% while reducing the total coincidence rate from a maximum of about 60 kHz for a zero-width window to approximately 50 kHz with the optimized discarding window of 40 ps.

6.2 Active basis selection

The BBM92 QKD protocol was also implemented using an alternative receiver configuration, whose simplified schematic is shown in Figure 6.5. Compared to the previous setup based on passive basis selection, this configuration removes the beam splitter placed before the two quantum receivers and directs all incoming photons toward the TFLN device. Within the device, projective measurements on two mutually unbiased bases are actively selected by controlling the applied phase of the unbalanced MZI, enabling deterministic basis selection

for each incoming photon. Specifically, the projective measurements are performed in the X and Y bases, both of which exhibit quantum interference for all detection events without temporal post-selection, owing to the time-bin switching (*mode 2*) operated by the first-stage MZM. In particular, each user's receiver implements the PVM defined in Eq. (4.2), corresponding to either $\hat{P}_+(\theta)$ or $\hat{P}_-(\theta)$, depending on the output port of the device. The phase θ determines the measurement basis and is physically implemented by the unbalanced MZI as the sum of two contributions:

$$\theta = \theta_{\mathrm{TPS}} + \theta_{\mathrm{RF}}, \tag{6.10}$$

where θ_{TPS} is a static phase set by the TPS, and θ_{RF} is the dynamic phase modulation applied by the EO modulator.

The basis choice for each user is applied at the repetition rate of the pulsed pump laser (1 GHz) to ensure a random and independent selection for every entangled photon pair. In our setup, the EO modulator within the unbalanced MZI is driven by an arbitrary waveform generator (AWG) (SHF 19120B) programmed to output a pseudo-random bit sequence (PRBS). Alice and Bob use PRBS sequences of lengths $2^7 - 1 = 127$ and $2^9 - 1 = 511$, respectively, both operating at a 1 GHz bit rate. This configuration ensures that the basis choice pattern repeats every $127 \times 511 = 64{,}897$ periods. In practical applications to further improve the security of the protocol, the used PRBS have to be replaced by a QRNG [282]. Such functionality could also be realized through hybrid integration of photonic and electronic circuits [283], ensuring certified randomness of the basis choice. The modulation signals have a peak-to-peak voltage of $V_{\mathrm{pp}} = V_\pi/2 \approx 4\,\mathrm{V}$, according to the V_π value obtained from the device characterization (see Figure 4.16b). To enable switching between the desired X and Y measurement bases, the TPS is statically set to apply a phase offset $\theta_{\mathrm{TPS}} = \pi/4$. In this condition, the total phase θ alternates between 0 and $\pi/2$ at each clock cycle, corresponding respectively to projections onto the X and Y bases.

$$\hat{P}_\pm(\theta) = \begin{cases} \frac{1}{2}\big(|0\rangle \pm |1\rangle\big)\big(\langle 0| \pm \langle 1|\big) = \frac{1}{2}|\pm\rangle\langle\pm| & \text{if } \theta = 0 \\ \frac{1}{2}\big(|0\rangle \pm i|1\rangle\big)\big(\langle 0| \pm i\langle 1|\big) = \frac{1}{2}|R/L\rangle\langle R/L| & \text{if } \theta = \pi/2 \end{cases} \tag{6.11}$$

Thus, the receiver actively toggles the measurement basis every laser pulse, ensuring deterministic and balanced sampling of the two bases. An eye diagram showing the modulation of continuous-wave light through the unbalanced MZI, driven by the PRBS sequence used for the QKD, is shown in Figure 6.6, highlighting the effectiveness to toggling between, in this case maximum and minimum transmission point of the MZI.

6.2.1 Secret key statistical analysis

Following the analysis presented for the passive-basis configuration, an analogous statistical model is applied to the active-basis configuration, with a few differences. In this configuration, measurements are performed in the X and Y bases. Both projective measurements are carried out using the same integrated receiver, which therefore experiences identical optical losses, while the selection of the projection basis is controlled by the PRBS modulation driving the EO modulator. Considering that the PRBS modulation corresponds to a balanced

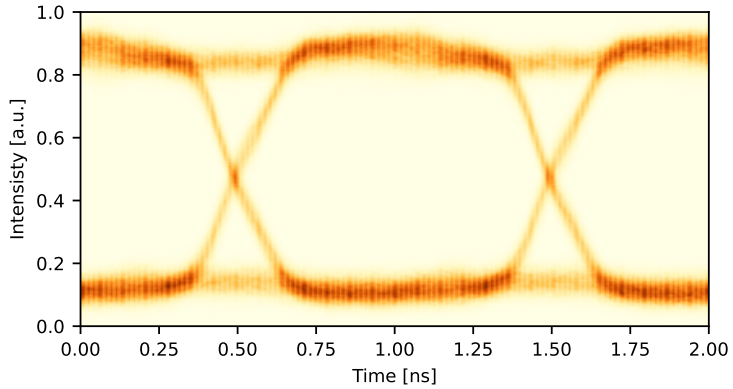

Figure 6.6: **Eye diagram.** Eye diagram obtained by modulating CW laser light through the EO modulator integrated in the unbalanced MZI of the TFLN device, driven with a PRBS at 1 GHz clock rate and a peak-to-peak voltage of V_π.

square-wave pattern applying a logical "0" and "1" each for 50% of the time, the probability of selecting the two bases is equal ($p_X = p_Y = 0.25$), in contrast to the unbalanced basis choice of the passive configuration ($p_X \ll p_Z$). As a consequence, the sifting factor is no longer close to unity; instead, it reduces to $q = p_X + p_Y = 0.5$. The coincidence detection rates for the two mutually unbiased bases similarly to the passive basis selection model are defined as:

$$R_X = \frac{C_{|++\rangle} + C_{|+-\rangle} + C_{|-+\rangle} + C_{|--\rangle}}{\tau},$$
$$R_Y = \frac{C_{|RR\rangle} + C_{|RL\rangle} + C_{|LR\rangle} + C_{|LL\rangle}}{\tau},$$

The corresponding QBERs are given by:

$$Q_X = \frac{C_{|+-\rangle} + C_{|-+\rangle}}{C_{|++\rangle} + C_{|--\rangle} + C_{|+-\rangle} + C_{|-+\rangle}},$$
$$Q_Y = \frac{C_{|RL\rangle} + C_{|LR\rangle}}{C_{|RR\rangle} + C_{|LL\rangle} + C_{|RL\rangle} + C_{|LR\rangle}}.$$

Since both measurement probabilities are equal ($p_X = p_Y = 0.25$), it is not straightforward to define one of the two bases as the key or check basis. I therefore adopt a balanced data allocation strategy: 90% of the detected coincidences in each basis are used to generate the secret key, while the remaining 10% are reserved for parameter estimation in the complementary basis ($B \neq B'$). The overall SKR is expressed as:

$$S = S_X + S_Y, \tag{6.12}$$

where, in the **asymptotic regime**, the contribution of each basis is given by [131]:

$$S_Y = R_Y \left[1 - H(Q_X) - f\, H(Q_Y)\right], \tag{6.13}$$
$$S_X = R_X \left[1 - H(Q_Y) - f\, H(Q_X)\right], \tag{6.14}$$

with the parameters defined as for the passive case.

In the **finite block-size regime**, the contribution of each basis to the SKR is redefined as [131, 272]:

$$S_Y = R_Y \left[1 - H(Q'_X) - f\, H(Q_Y)\right] - \log \frac{2}{\epsilon_{\text{cor}} \epsilon_{\text{sec}}^2}, \tag{6.15}$$

$$S_X = R_X \left[1 - H(Q'_Y) - f\, H(Q_X)\right] - \log \frac{2}{\epsilon_{\text{cor}} \epsilon_{\text{sec}}^2}, \tag{6.16}$$

The QBER upper bounds when using the *Serfling* inequality are given by:

$$Q'_X = Q_X + \sqrt{\frac{(n_Y + 1)\log(1/\epsilon_{\text{sec}})}{2 n_X (n_X + n_Y)}}, \tag{6.17}$$

$$Q'_Y = Q_Y + \sqrt{\frac{(n_X + 1)\log(1/\epsilon_{\text{sec}})}{2 n_Y (n_Y + n_X)}}, \tag{6.18}$$

where n_B represents the total number of coincidence events in basis B, defined as:

$$n_X = C_{|++\rangle} + C_{|--\rangle} + C_{|+-\rangle} + C_{|-+\rangle},$$
$$n_Y = C_{|RR\rangle} + C_{|LL\rangle} + C_{|RL\rangle} + C_{|LR\rangle}.$$

Analogously, when using the *Chernoff* inequality, the adjusted QBERs are defined as:

$$Q'_X = \frac{(n_Y + n_X)\Gamma^+_{n_X, \epsilon_{\text{PE}}}(m_X/n_X) - m_X}{n_Y}, \tag{6.19}$$

$$Q'_Y = \frac{(n_Y + n_X)\Gamma^+_{n_Y, \epsilon_{\text{PE}}}(m_Y/n_Y) - m_Y}{n_X}, \tag{6.20}$$

where ϵ_{PE} is the failure probability associated with the parameter estimation step, and $\Gamma^+_{n,\epsilon}(p)$ is defined as in Section 6.1.1.

6.2.2 Experimental results

As in the passive configuration, a long-duration measurement exceeding 12 hours was carried out continuously, without interruption and without any active stabilization other than maintaining the device package at a constant temperature. The time traces of the SKR in the asymptotic regime and for both the Serfling and Chernoff bounds with a key block size of 4×10^4 are shown in Figure 6.7a. Using the Chernoff bound, a maximum SKR of 1.024 kbit/s was obtained, with an average value of 0.805 kbit/s over the full measurement interval.

The corresponding time traces of the QBER in the X and Y bases are shown in Figure 6.7b. The average QBER over the entire measurement time is 4.2% in the Y basis, while it is higher in the X basis, around 6% with fluctuations between 4.5% and 8%. These variations directly account for the long-term fluctuations observed in the SKR. The slight increase in the Y-basis QBER compared to the passive configuration (where the X-basis QBER was 3.76%) can be attributed to non-ideal AWG modulation, since in this configuration the projection basis is switched every nanosecond. The larger increase observed in the X basis is probably also

caused by a combination of non-ideal initial settings of the applied phase $\theta_{A,B}$ and slow phase drifts occurring during the long experimental run, which gradually degrade the interferometric projection quality. As in the passive case, these QBER fluctuations are not caused by variations in the source-generation rate, as verified by the stability of the coincidence counts in Figure 6.7c and the stable single-photon count rates shown in Figure 6.7d.

Compared with the passive configuration, the SKR is lower in this setup because both measurement bases are implemented through the integrated receiver and therefore experience the full optical loss of the device. The measured losses amount to 12.15 dB for Alice and 10.1 dB for Bob, evaluated from the entangled-photon-pair source to the SNSPD inputs.

Overall, although the SKR is reduced due to the additional insertion loss and the slightly higher QBER associated with fast phase modulation, the active-basis configuration provides two key advantages. First, as in the passive case, it fully removes the temporal PSL. Second, it eliminates the need to resolve the early/late time-bin separation, since no measurements are performed in the Z basis. Indeed, in this configuration only the temporal separation between successive time-bins must be resolved. This greatly relaxes the detection requirements and enables the SKR to be increased simply by raising the pump-laser repetition rate and reducing the time-bin separation.

Given the available electrical bandwidth (Figure 4.20) and the temporal response shown by the eye diagram in Figure 6.6 of the unbalanced MZI EO modulator, the protocol could already be operated at slightly higher repetition rates than the current 1 GHz. For example, given that the switching period remains a multiple of 200 ps to guarantee correct routing inside the device, repetition rates of $1/800$ ps or $1/600$ ps are feasible. The limited EO bandwidth of the unbalanced MZI is primarily due to the packaging and RF routing of the device. With improved RF connections, similar to those used for the optical switch and using the same chip layout, the protocol could operate at repetition rates up to 5 GHz. This upper limit is set by the 100 ps interferometer imbalance, as in the passive configuration. However, while the passive configuration could in principle also operate at 5 GHz, it would additionally require resolving the 100 ps temporal separation between early and late time bins for measurements in the computational (Z) basis.

6.3 QKD performance under variable channel losses

For both the passive and active basis selection, the previously presented SKR data were acquired using a relatively short fiber link within a laboratory setup size. This configuration was intended to demonstrate the stability and operation of the system. Here, I present a more realistic scenario in which the QKD protocol is performed by first varying the optical channel losses through a variable optical attenuator (VOA), which simulates the equivalent loss of a long fiber link, and subsequently by adopting an spooled-fiber connection link up to 25 km for the passive basis selection.

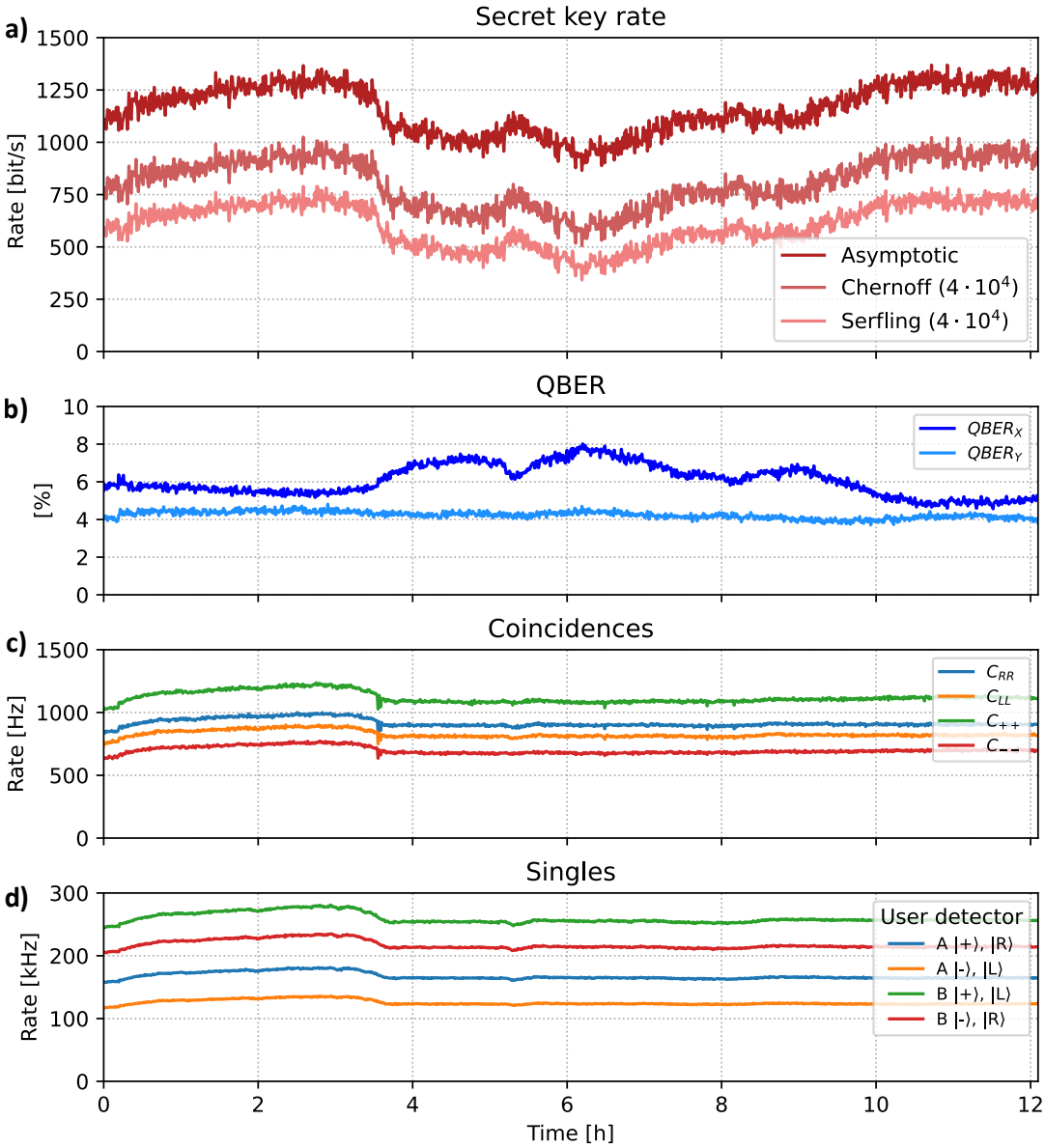

Figure 6.7: **Active basis selection QKD.** Time evolution of the main parameters of the BB92 QKD protocol. **a)** SKR in the asymptotic and finite-key regimes, evaluated using Serfling and Chernoff bounds. **b)** QBER in the X and Y bases. **c)** Coincidence rate in the X and Y interferometric bases, measured without temporal post-selection thanks to the receiver's ability to temporally overlap the time-bin states. **d)** Time trace of the single-photon counts in the X and Y bases.

6.3.1 Variable optical attenuator

Measurements simulating a variable-length fiber link were performed by adjusting the attenuation in Bob's fiber channel using a VOA, as shown in the setup schematic in Figure 6.1. Figure 6.8a reports the measured (dots) and theoretical (dashed lines) SKR values in both the asymptotic regime and for a finite block size of 9×10^4, for both statistical bounds, as a function of the channel loss and the corresponding equivalent fiber length (using a conversion factor of 0.2 dB/km, typical for standard telecom optical fiber [284]). The corresponding QBER values for the two measurement bases are also shown. The attenuation sweep starts from 2 dB, which is the insertion loss of the VOA at its minimum attenuation setting. The reduction of the SKR is mainly caused by two factors, independent of the chosen regime or statistical bound:

- The coincidence rate decreases exponentially with channel attenuation. This produces the linear trend observed in the logarithmic SKR plot.
- As the coincidence rate decreases, the contribution of constant noise sources (such as detector dark counts) becomes increasingly relevant. This degradation of the SNR is particularly critical in the X basis, where the lower coincidence rate results in reduced interference visibility and, consequently, an increased QBER and lower SKR. In contrast, the QBER in the Z basis remains almost unaffected by dark counts throughout the attenuation sweep, owing to its much higher SNR ($R_Z \gg R_X$).

Overall, in the finite-size regime and adopting the Chernoff bound, which provides less conservative statistical estimation than the Serfling bound, QKD operation remains feasible for equivalent fiber lengths exceeding 100 km, whereas the Serfling bound allows secure key estimation only up to approximately 80 km, as shown in Figure 6.8a.

For the **active basis selection** case, no experimental demonstration was performed at variable channel attenuation losses. However, exploiting the agreement observed between the theoretical and measured results for the passive-basis configuration, I estimate the SKR as a function of channel loss also for the active basis configuration. In this case, I account for the SKR reduction arising from both the decrease of the measured coincidence rates (R_X and R_Y) and the increase of the QBER. For the rate reduction, I assume the expected exponential decay of R_X and R_Y as a function of channel loss. For the QBER increase, I extract the constant noise contribution from the QBER measured in the passive basis configuration and include this noise term in both interferometric bases (X and Y) for the active basis case. Figure 6.8b reports the estimated SKR as a function of channel loss for both the asymptotic regime and for a finite block size of 4×10^4. Under these conditions, the use of the Chernoff bound yields a 33.2 % increase in the secret-key generation rate compared to the Serfling-bound estimation. At the measured coincidence rate, one block of key is generated approximately every 25 s. For applications requiring faster key refresh, an average of about 450 bit/s of secret key can be achieved using a shorter block length of 10^4, for which the SKR obtained with the Chernoff bound is 122.3 % higher than that obtained using the Serfling bound. At higher channel losses, the QBER is mainly limited by detector dark counts. In this configuration, compared to the passive one, the onset of QBER degradation in the

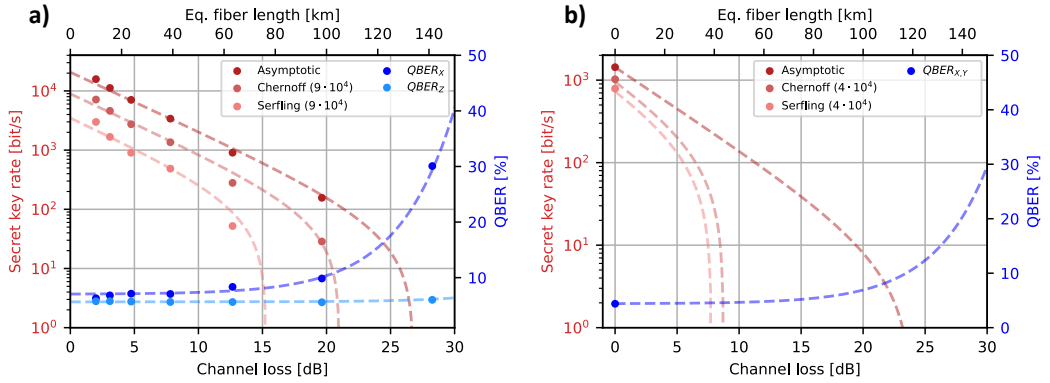

Figure 6.8: **QKD performance under variable channel attenuation.** Measured (dots) and theoretical (dashed lines) SKR values in the asymptotic regime and for a finite block size of 9×10^4, plotted as a function of the channel attenuation for the **(a)** passive-basis and **(b)** active-basis selection configurations. The corresponding QBER values are also reported. In the interferometric X and Y bases, the QBER increases more rapidly with attenuation due to the higher sensitivity to noise and the reduced coincidence rate.

interferometric bases occurs at slightly longer equivalent fiber lengths. This improvement arises because, in the active configuration, the removal of the 50:50 beam splitter increases the coincidence rate at the receiver, avoiding the additional 3 dB loss present in the passive setup.

6.3.2 Spooled fiber

A more realistic proof-of-principle experiment was performed using fiber spools of different lengths, ranging from 2.5 km to 25 km. This experimental test was useful for understanding the system behavior under conditions similar to a metropolitan-area field deployment. The QKD implementation was tested by varying the fiber-channel length using spools of SMF28 optical fiber [41]. The fiber spool was inserted in place of the VOA, thereby affecting only Bob's channel.

For this experiment, I report the detection-event histograms as a function of arrival time for both users, for each tested fiber length. In Figure 6.9, it can be observed that starting from 8 km and above, Bob's temporal distribution of detection events becomes significantly broadened, while Alice's histogram remains unchanged, since her channel length is fixed and serves as a reference. This broadening prevents the correct discrimination of the 100 ps-separated time-bins in the Z basis, leading to greater overlap between the early and late peaks and therefore to an increased QBER, as also reflected in the measured Z-basis error indicated in the Figure panels. For measurements in the interferometric X basis, pulse broadening also affects the correct switching operation inside the integrated receiver.

The broadening originates from chromatic dispersion accumulated during propagation in the optical fiber. In standard single-mode fiber, pulses with an initial FWHM of 9.2 ps and a spectral bandwidth of 0.42 nm experience dispersion of approximately $20\,\mathrm{ps\,nm^{-1}\,km^{-1}}$, resulting in temporal spreading of the time-bin wavepacket. For example, for the longest tested link of 25 km, the induced dispersion is approximately $20 \times 25 \times 0.42 \approx 210$ ps. To mitigate the effects of chromatic dispersion and enable practical deployment of the QKD system

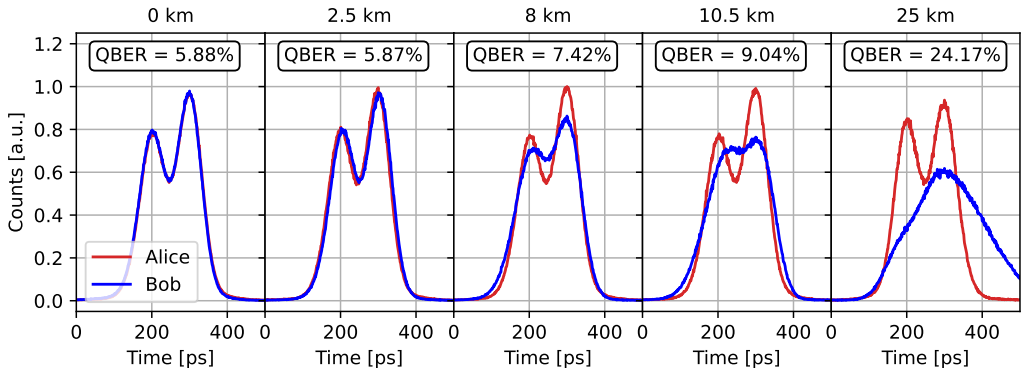

Figure 6.9: **Dispersion effects in optical fiber.** Normalized detection counts in the Z basis for the two QKD users, measured for different fiber-link lengths on Bob's channel. The time reference on the x-axis is defined relative to the pump-pulse emission. As the fiber length increases, chromatic dispersion broadens Bob's pulses, reducing the temporal distinguishability of the time-bin states and thereby compromising the effectiveness of the QKD protocol.

over long fiber links, a dispersion-compensation strategy is required. In standard telecommunication systems, dispersion is commonly compensated using dispersion-compensating fibers or chirped fiber Bragg gratings [285].

6.4 Source optimization

In this section, I discuss the optimization of the entangled photon pair generation conditions in the integrated silicon waveguide based on SFWM that will allow further increase of the SKR.

As described in Section 5.2, due to the probabilistic nature of the nonlinear optical source, the photon-pair generation rate can be enhanced by increasing the pump power. However, this enhancement comes at the cost of reduced quality in the generated entangled state, as quantified by the CAR. A higher pair-generation probability leads to a larger contribution of multi-pair emission events, which increase the accidental coincidence rate and degrade the CAR. In the context of QKD applications, a lower CAR results in a higher QBER, leading to a reduction in the SKR. Consequently, a trade-off exists between the source generation rate and the resulting SKR. In literature theoretical models have been presented [286] which allow for the optimization of the generation probability based on the relevant experimental parameters. Moreover, this trade-off optimization also depends on the link length. Although increasing the generation probability can enhance the SKR at short distances despite a higher QBER, at larger channel attenuations the situation changes. Since the protocol becomes insecure when the QBER exceeds the 11% threshold, this limit may be reached earlier for higher generation probabilities due to the reduced CAR. Consequently, operating at a lower generation probability, resulting in a lower SKR at short distances but a higher CAR and lower QBER, can enable secure key distribution over longer links [287].

In the following paragraph I focus on the experimental characterization to highlight this

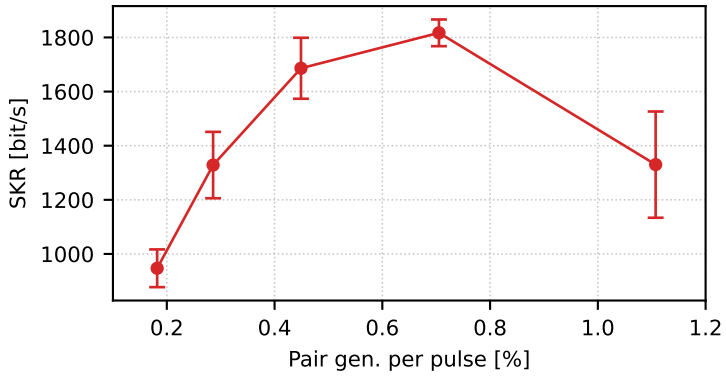

Figure 6.10: **Source optimization for QKD operation.** Normalized secret key rate (SKR) as a function of the internal pair-generation probability for the active-basis configuration. The optimal operating point corresponds to an internal generation probability of approximately 0.7%, in contrast to the value of 0.2% at which the experimental results for the active-basis selection were recorded.

trade-off for the active configuration under minimal channel loss. To identify the optimal operating point that maximizes the SKR, Figure 6.10 reports the experimentally measured SKR for the active basis selection scheme as a function of the internal pair-generation probability, which was obtained by varying the pump power and the source characterization presented in Section 6.4. From the measured experimental results, it is observed that the optimal value occurs for an internal generation probability of approximately 0.7 %. In the active basis QKD configuration, the 12 h stability demonstration was performed at a more conservative mean photon-pair generation probability of approximately 0.2 %. While the optimal operating point identified in Figure 6.10 could further maximize the key rate, the lower generation probability was prioritized for the long-duration implementation to ensure system stability and maintain a high CAR throughout the measurements.

For the passive QKD configuration, a similar optimization characterization could in principle be performed. However, in our experiment, the maximum usable pump power was limited by saturation of the SNSPD detection system, restricting the maximum count rate to approximately 1.5 MHz in the Z basis.

Finally, Table 6.2 summarizes the main experimental parameters and performance metrics for both passive and active basis selection schemes, also comparing the 12 h long demonstrations with the maximum achieved SKR operation point. This comparison provides a view of the generation probability, CAR, QBER, and SKR discussed throughout this section.

Parameters	**Passive** basis selection (12h-long)	**Active** basis selection (12h-long)	**Active** basis selection (max SKR)
Energy per pulse	2.25 pJ	0.9 pJ	1.7 pJ
Pair gen. per pulse	1 %	0.2 %	0.7 %
CAR	52	140	80
Coinc. rate	$R_Z = 57.7$ kHz; $R_X = 852$ Hz	$R_X + R_Y = 3.9$ kHz	$R_X + R_Y = 10.5$ kHz
QBER	Z : 4.3 %; X : 3.76 %	X : 6.1 %; Y : 4.2 %	X : 7.7 %; Y : 7.8 %
SKR	22.4 kHz	805 Hz	1817 Hz

Table 6.2: Comparison of the main experimental parameters and performance metrics for passive and active basis selection QKD configurations. Results are reported for both the 12 h long-term demonstrations and the maximum achieved SKR operating point in the active configuration. All reported rates correspond to average values over the full measurement duration.

Chapter 7

Conclusions and perspectives

In this work, a fully packaged integrated photonic circuit capable of supporting multiple quantum information applications has been designed, fabricated, and experimentally demonstrated. The primary goal of the developed device is to overcome the *temporal PSL* [19], which arises in Franson-like unbalanced interferometers and limits both the security and efficiency of QKD protocols based on time-bin entangled states [235]. I addressed this issue by implementing the active switching solution [121], on a TFLN device developed in collaboration with Advanced Fiber Resources Milan. To the best of my knowledge, this work reports the first realization of such a system on an integrated photonic platform, since a similar implementation was demonstrated only in fiber based systems for entanglement certification [234].

During the initial phase of the project, I identified the required key functionalities and verified their potential realization on integrated photonic circuits based on the TFLN technological platform. This was followed by a development phase, including the design, numerical simulation, and optimization of the essential building blocks, finalized in the fabrication and packaging of a device tailored for quantum communication protocols. Finally, I had the opportunity to demonstrate and benchmark multiple quantum protocols during the experimental phase.

The proposed PSL-free architecture can operate as a reconfigurable time-bin state projector. Thanks to the broadband TFLN EO modulators, the quantum receiver enables fast switching in the gigahertz range of time-bin encoded states. This capability allows the use of closely spaced time-bins, thus supporting high clock rates and increased secret key throughput. Furthermore, due to the combination of integrated TPSs, it enables projective measurements at tunable timescales, from sub-nanosecond switching to stable operation over several hours.

I have demonstrated the versatility of the developed quantum receiver across different tasks: certification of genuine time-bin entanglement (exceeding 38 standard deviations) without the need for temporal post-selection, QST of time-bin encoded states, and a preparation stage by modulating the pump pulses, demonstrating its ability to generate high-fidelity (95%) and high-purity (93%) arbitrary time-bin entangled states when combined, as in this case, with a nonclassical light source. I also demonstrated that the device can effectively implement the BBM92 entanglement-based QKD protocol in both *passive* and *active* basis selection configurations, highlighting its versatility and reconfigurability. To the best of

my knowledge, these represent the first realizations of time-bin QKD without temporal post-selection. The passive-basis configuration, in terms of SKR, yields the highest reported result (exceeding 25 kbit/s) for time-bin entanglement-based systems, even when compared with post-selection-based approaches. In the active-basis configuration, the minimum timing resolution required from the detection system is significantly relaxed. Here, it is sufficient to resolve the time-bin repetition rate, rather than the separation between bins as required in the passive setup for measurement in the Z-computational basis. This is made possible by the device's ability to temporally overlap the two time-bins through switching while applying gigahertz-rate modulation in the Franson-like interferometer. Such fast and precise control of the phase modulation enables high-visibility quantum interference, as confirmed by the low measured QBER values. Both QKD demonstrations were performed over more than 12 hours of continuous operation without interruption and without the need for active feedback stabilization, relying only on temperature control of the packaged devices. This work also reports the first experimental implementation of the BBM92 protocol employing the recently developed Chernoff bound [274] for finite-key SKR estimation. The results confirm its advantage over the previously adopted Serfling bound [272], particularly for small block lengths, which are typical of EBQKD systems.

The presented results demonstrate that the TFLN platform, originally developed for high-speed telecommunication applications [63, 110, 288], can be effectively adapted for quantum technologies using industrial-grade fabrication processes. The compact, integrated quantum receiver developed in this work combines multiple high-quality optical components such as edge couplers, beam splitters, EO modulators, TPSs, and low-loss waveguides. The experimental results confirm the reproducibility and reliability of the technology, with consistent performance across multiple fabricated devices.

The present integrated optical circuit can also be extended to other quantum applications. For instance, recently developed integrated interferometers for multidimensional time-bin states (up to 8 levels) [124] could be combined with our active-switching approach to overcome the PSL. Such an extension would require multi-port interferometers with path delays corresponding to the multiples of the time-bin spacing, as well as multi-port switching implemented through cascaded high-speed modulators. The realized device can also be directly employed for the implementation of entanglement swapping [289]. Furthermore, it could be combined with the processing of other photonic degrees of freedom, such as frequency [290], by exploiting high-speed EO modulators, and polarization by integrated PSR [291].

The following proposed improvements to the developed device primarily aim to increase the achievable SKR. The most straightforward enhancement would be to operate the protocol at higher clock rates, potentially up to 5 GHz, which represents the maximum repetition rate set by the 100 ps delay of the unbalanced MZI for both the passive and active basis selection configurations. In the presented implementation, the active-basis operation was tested only up to 1 GHz due to the limited EO bandwidth of the unbalanced MZI modulation stage, which is constrained by RF connectors and routing not optimized for high-frequency operation. For the passive-basis configuration, the repetition rate was instead limited by the maximum detectable single-photon rate of the available SNSPD system. A second key aspect

affecting the SKR, particularly critical in EBQKD protocols, is the presence of excess optical losses beyond those introduced by the quantum channel link itself. A comprehensive optimization of the entire setup, including the design of the integrated photonic devices, would directly increase the detected coincidence rates and consequently enhance the overall SKR.

The measured quantum interference visibility in the current implementation is approximately 93.5%, which affects the QBER in the interferometric bases X and Y, and limits the maximum achievable QKD distance and SKR. The main limitations arise from the intrinsic accidental detection events generated by the source, as quantified by the CAR; from the non-ideal sinusoidal modulation used for switching the time-bin states, and ultimately, from the finite interference quality caused by residual coupling between the TE and TM modes within the devices. This latter effect can be mitigated by adopting Euler bends [263] and incorporating integrated polarization filters [291] in future designs.

In the perspective of scaling toward large and multi-user optical quantum networks, all experimental demonstrations reported in this work were carried out using the standard ITU 100 GHz bandwidth allocation for each user channel. This choice matches the transform-limited photon bandwidth and optimizes the spectral density of the generated entangled pairs. Moreover, the quantum receiver platform relies on components designed for C+L band operation, ensuring complete compatibility with DWDM systems and paving the way for scalable quantum networking over existing telecom infrastructure [179–182].

In summary, the presented work demonstrates a versatile and high-performance integrated photonic circuit based on the TFLN platform, capable of tailoring pump pulses for the generation of time-bin states, overcoming the PSL limitation, certifying genuine time-bin entanglement, and enabling stable, high-rate EBQKD operation. The demonstrated architecture provides a solid foundation for future scalable, chip-integrated quantum communication networks.

List of publications

Ongoing peer-review papers

- **Bernardi, A.,** Bacchi, M., Clementi, M., Congia, S., Garrisi, F., Martellosio, A., Passoni, M., Wrobel, A., Sabattoli, F. A., Galli, M. & Bajoni, D. Post-selection free time-bin entanglement on a thin-film lithium niobate photonic chip. *arXiv preprint arXiv:2505.04598* (2025).

- **Bernardi, A.,** Clementi, M., Bacchi, M., Bolaños, M., Congia, S., Garrisi, F., Martellosio, A., Passoni, M., Wrobel, A., Agnesi, C., Vallone, G., Villoresi, P., Sabattoli, F. A., Galli, M. & Bajoni, D. Gigahertz-rate thin-film lithium niobate receiver for time-bin quantum communication. *Light: Science & Applications.* Accepted for publication.

Conference proceedings

- Bacchi, M., **Bernardi, A.,** Clementi, M., Congia, S., Garrisi, F., Martellosio, A., Passoni, M., Wrobel, A., Sabattoli, F., Galli, M., *et al. Ultrafast post-selection free time-bin entanglement on a thin film lithium niobate photonic chip* in *European Quantum Electronics Conference* (2025), eb_8_2.

- **Bernardi, A.,** Bacchi, M., Clementi, M., Congia, S., Garrisi, F., Martellosio, A., Passoni, M., Wrobel, A., Sabattoli, F. A., Galli, M., *et al. High switching rate post-selection free time-bin entanglement in thin-film lithium niobate* in *2025 25th Anniversary International Conference on Transparent Optical Networks (ICTON)* (2025), 1–3.

- **Bernardi, A.,** Bacchi, M., Clementi, M., Congia, S., Garrisi, F., Martellosio, A., Passoni, M., Wrobel, A., Sabattoli, F., Galli, M., *et al. Post-selection free time-bin entanglement on a thin-film lithium niobate photonic chip* in *CLEO: Fundamental Science* (2025), FF118_5.

Bibliography

1. Gisin, N. & Thew, R. Quantum communication. *Nature photonics* **1,** 165–171 (2007).
2. Scarani, V. *et al.* The security of practical quantum key distribution. *Reviews of modern physics* **81,** 1301–1350 (2009).
3. Steane, A. Quantum computing. *Reports on Progress in Physics* **61,** 117 (1998).
4. Ladd, T. D. *et al.* Quantum computers. *nature* **464,** 45–53 (2010).
5. Dowling, J. P. & Seshadreesan, K. P. Quantum optical technologies for metrology, sensing, and imaging. *Journal of Lightwave Technology* **33,** 2359–2370 (2015).
6. Hiskett, P. A. *et al.* Long-distance quantum key distribution in optical fibre. *New Journal of Physics* **8,** 193 (2006).
7. Dixon, A. *et al.* Gigahertz decoy quantum key distribution with 1 Mbit/s secure key rate. *Optics express* **16,** 18790–18797 (2008).
8. Hwang, W.-Y. Quantum key distribution with high loss: toward global secure communication. *Physical review letters* **91,** 057901 (2003).
9. Korzh, B. *et al.* Provably secure and practical quantum key distribution over 307 km of optical fibre. *Nature Photonics* **9,** 163–168 (2015).
10. Yin, J. *et al.* Satellite-based entanglement distribution over 1200 kilometers. *Science* **356,** 1140–1144 (2017).
11. Wang, J. *et al.* Integrated photonic quantum technologies. *Nature photonics* **14,** 273–284 (2020).
12. Bonneau, D., Silverstone, J. W. & Thompson, M. G. in *Silicon Photonics III: Systems and Applications* 41–82 (Springer, 2016).
13. Elshaari, A. W. *et al.* Hybrid integrated quantum photonic circuits. *Nature photonics* **14,** 285–298 (2020).
14. Caspani, L. *et al.* Integrated sources of photon quantum states based on nonlinear optics. *Light: Science & Applications* **6,** e17100–e17100 (2017).
15. Uppu, R. *et al.* Scalable integrated single-photon source. *Science advances* **6,** eabc8268 (2020).
16. Flamini, F., Spagnolo, N. & Sciarrino, F. Photonic quantum information processing: a review. *Reports on Progress in Physics* **82,** 016001 (2018).
17. Najafi, F. *et al.* On-chip detection of non-classical light by scalable integration of single-photon detectors. *Nature communications* **6,** 5873 (2015).

18. Ferrari, S., Schuck, C. & Pernice, W. Waveguide-integrated superconducting nanowire single-photon detectors. *Nanophotonics* **7,** 1725–1758 (2018).
19. Aerts, S. *et al.* Two-photon Franson-type experiments and local realism. *Physical review letters* **83,** 2872 (1999).
20. Miller, D. A. Attojoule optoelectronics for low-energy information processing and communications. *Journal of Lightwave Technology* **35,** 346–396 (2017).
21. Asakawa, K., Sugimoto, Y. & Nakamura, S. Silicon photonics for telecom and datacom applications. *Opto-Electronic Advances* **3,** 200011–1 (2020).
22. Vo-Dinh, T. *Biomedical photonics handbook: biomedical diagnostics* (CRC press, 2014).
23. Butt, M. A., Mateos, X. & Piramidowicz, R. Photonics sensors: a perspective on current advancements, emerging challenges, and potential solutions. *Physics Letters A* **516,** 129633 (2024).
24. Pimputkar, S. *et al.* Prospects for LED lighting. *Nature photonics* **3,** 180–182 (2009).
25. Zuo, J. & Lin, X. High-power laser systems. *Laser & Photonics Reviews* **16,** 2100741 (2022).
26. Politi, A. *et al.* Silica-on-silicon waveguide quantum circuits. *Science* **320,** 646–649 (2008).
27. Amiri, I. S. *et al.* Introduction to photonics: Principles and the most recent applications of microstructures. *Micromachines* **9,** 452 (2018).
28. Smit, M., Acket, G. & Van Der Laan, C. Al2O3 films for integrated optics. *Thin solid films* **138,** 171–181 (1986).
29. Soref, R. & Bennett, B. Electrooptical effects in silicon. *IEEE journal of quantum electronics* **23,** 123–129 (1987).
30. Smit, M. K. New focusing and dispersive planar component based on an optical phased array. *Electronics letters* **24,** 385–386 (1988).
31. Sun, C. *et al.* Single-chip microprocessor that communicates directly using light. *Nature* **528,** 534–538 (2015).
32. Borghi, M. *et al.* Nonlinear silicon photonics. *Journal of Optics* **19,** 093002 (2017).
33. Thylén, L. & Wosinski, L. Integrated photonics in the 21st century. *Photonics Research* **2,** 75–81 (2014).
34. Smit, M., Van der Tol, J. & Hill, M. *Moore's law in photonics* 2012.
35. Kaur, P. *et al.* Hybrid and heterogeneous photonic integration. *APL photonics* **6** (2021).
36. Boes, A. *et al.* Status and potential of lithium niobate on insulator (LNOI) for photonic integrated circuits. *Laser & Photonics Reviews* **12,** 1700256 (2018).
37. Butt, M. A., Imran Akca, B. & Mateos, X. Integrated Photonic Biosensors: Enabling Next-Generation Lab-on-a-Chip Platforms. *Nanomaterials* **15,** 731 (2025).
38. Ashtiani, F., Geers, A. J. & Aflatouni, F. An on-chip photonic deep neural network for image classification. *Nature* **606,** 501–506 (2022).

39. Yariv, A., Yeh, P. & Yariv, A. *Photonics: optical electronics in modern communications* (Oxford university press New York, 2007).
40. Ansys (Lumerical). *MODE—Finite Difference Eigenmode (FDE) Solver Introduction* MODE product documentation (2025). `https://optics.ansys.com/hc/en-us/articles/360034917233-MODE-Finite-Difference-Eigenmode-FDE-solver-introduction`.
41. Corning Incorporated. *SMF-28 Ultra Optical Fiber: Product Information* Datasheet. Accessed: 2025-02-17. 2020. `https://www.corning.com/optical-communications/worldwide/en/home/products/fiber/optical-fiber-products/smf-28-contour-fiber.html`.
42. Yamada, J. *et al.* Characteristics of a hemispherical microlens for coupling between a semiconductor laser and single-mode fiber. *IEEE Journal of Quantum Electronics* **16,** 1067–1072 (1980).
43. Wang, X. *et al.* Silicon-nitride-assisted edge coupler interfacing with high numerical aperture fiber. *IEEE Photonics Technology Letters* **31,** 349–352 (2019).
44. He, L. *et al.* Low-loss fiber-to-chip interface for lithium niobate photonic integrated circuits. *Optics letters* **44,** 2314–2317 (2019).
45. Hu, C. *et al.* High-efficient coupler for thin-film lithium niobate waveguide devices. *Optics Express* **29,** 5397–5406 (2021).
46. Jia, D. *et al.* High-efficiency edge couplers enabled by vertically tapering on lithium-niobate photonic chips. *Applied Physics Letters* **123** (2023).
47. Yao, N. *et al.* Efficient light coupling between an ultra-low loss lithium niobate waveguide and an adiabatically tapered single mode optical fiber. *Optics express* **28,** 12416–12423 (2020).
48. Tobing, L. Y. *et al. Compact edge coupler with< 1dB/facet insertion loss in the C-band* in *Integrated Optics: Devices, Materials, and Technologies XXIX* **13369** (2025), 59–64.
49. A manufacturable platform for photonic quantum computing. *Nature* **641,** 876–883 (2025).
50. ANSYS, Inc. *Fiber-to-Chip Edge Coupler with a Microlens* `https://optics.ansys.com/hc/en-us/articles/33444674330131-Fiber-to-Chip-Edge-Coupler-with-a-Microlens`. Accessed: 21 November 2025.
51. Cheng, L. *et al.* Grating couplers on silicon photonics: Design principles, emerging trends and practical issues. *Micromachines* **11,** 666 (2020).
52. Wang, H. *et al.* Ultralow-loss optical interconnect enabled by topological unidirectional guided resonance. *Science Advances* **10,** eadn4372 (2024).
53. Ding, Y. *et al.* Fully etched apodized grating coupler on the SOI platform with- 0.58 dB coupling efficiency. *Optics letters* **39,** 5348–5350 (2014).
54. Zaoui, W. S. *et al.* Bridging the gap between optical fibers and silicon photonic integrated circuits. *Optics express* **22,** 1277–1286 (2014).
55. Bozzola, A. *et al.* Optimising apodized grating couplers in a pure SOI platform to- 0.5 dB coupling efficiency. *Optics express* **23,** 16289–16304 (2015).

56. Marchetti, R. *et al.* High-efficiency grating-couplers: demonstration of a new design strategy. *Scientific reports* **7,** 16670 (2017).

57. Chen, B. *et al.* Low-loss fiber grating coupler on thin film lithium niobate platform. *APL Photonics* **7** (2022).

58. Jacques, M. *et al.* Optimization of thermo-optic phase-shifter design and mitigation of thermal crosstalk on the SOI platform. *Optics express* **27,** 10456–10471 (2019).

59. De, S. *et al.* Design and simulation of thermo-optic phase shifters with low thermal crosstalk for dense photonic integration. *IEEE Access* **8,** 141632–141640 (2020).

60. Frey, B. J., Leviton, D. B. & Madison, T. J. *Temperature-dependent refractive index of silicon and germanium* in *Optomechanical technologies for Astronomy* **6273** (2006), 790–799.

61. Arbabi, A. & Goddard, L. L. Measurements of the refractive indices and thermo-optic coefficients of Si3N4 and SiO x using microring resonances. *Optics letters* **38,** 3878–3881 (2013).

62. Han, H. *et al.* Thermo-optic characterization of thin-film lithium niobate asymmetric Mach–Zehnder interferometer from 290 to 10 K. *Chinese Optics Letters* **23,** 051302 (2025).

63. Wang, C. *et al.* Integrated lithium niobate electro-optic modulators operating at CMOS-compatible voltages. *Nature* **562,** 101–104 (2018).

64. Zhou, G. *et al. Silicon Mach-Zehnder modulator using a highly-efficient L-shape PN junction* in *Tenth International Conference on Information Optics and Photonics* **10964** (2018), 264–267.

65. Yong, Z. *et al.* U-shaped PN junctions for efficient silicon Mach-Zehnder and microring modulators in the O-band. *Optics express* **25,** 8425–8439 (2017).

66. Yuan, Y. *et al.* A 5× 200 Gbps microring modulator silicon chip empowered by two-segment Z-shape junctions. *Nature Communications* **15,** 918 (2024).

67. Siew, S. Y. *et al.* Review of silicon photonics technology and platform development. *Journal of Lightwave Technology* **39,** 4374–4389 (2021).

68. Fang, A. W. *et al.* Electrically pumped hybrid AlGaInAs-silicon evanescent laser. *Optics express* **14,** 9203–9210 (2006).

69. Ding, Y. *et al.* Mode-selective wavelength conversion based on four-wave mixing in a multimode silicon waveguide. *Optics express* **22,** 127–135 (2013).

70. Silverstone, J. W. *et al.* On-chip quantum interference between silicon photon-pair sources. *Nature Photonics* **8,** 104–108 (2014).

71. Barad, Y. *et al.* Nonlinear scanning laser microscopy by third harmonic generation. *Applied Physics Letters* **70,** 922–924 (1997).

72. Zhang, J. *et al.* Optical solitons in a silicon waveguide. *Optics express* **15,** 7682–7688 (2007).

73. Bristow, A. D., Rotenberg, N. & Van Driel, H. M. Two-photon absorption and Kerr coefficients of silicon for 850–2200nm. *Applied physics letters* **90** (2007).

74. Schroder, D. K., Thomas, R. N. & Swartz, J. C. Free carrier absorption in silicon. *IEEE Journal of solid-state circuits* **13,** 180–187 (1978).

75. Xiang, C., Jin, W. & Bowers, J. E. Silicon nitride passive and active photonic integrated circuits: trends and prospects. *Photonics research* **10,** A82–A96 (2022).

76. Ji, X. *et al.* Ultra-Low-Loss Silicon Nitride photonics based on deposited films compatible with foundries. *Laser & Photonics Reviews* **17,** 2200544 (2023).

77. Muellner, P. *et al.* CMOS-compatible Si3N4 waveguides for optical biosensing. *Procedia engineering* **120,** 578–581 (2015).

78. Poulton, C. V. *et al.* Large-scale silicon nitride nanophotonic phased arrays at infrared and visible wavelengths. *Optics letters* **42,** 21–24 (2016).

79. Spencer, D. T. *et al.* An optical-frequency synthesizer using integrated photonics. *Nature* **557,** 81–85 (2018).

80. Frigg, A. *et al.* Optical frequency comb generation with low temperature reactive sputtered silicon nitride waveguides. *APL photonics* **5** (2020).

81. Lüpken, N. M. *et al.* Toward integrated synchronously pumped optical parametric oscillators in silicon nitride. *Optics express* **29,** 39895–39903 (2021).

82. Shih, T.-M. *et al. Indium phosphide based integrated photonic devices for telecommunications and sensing applications* PhD thesis (Massachusetts Institute of Technology, 2012).

83. Schubert, E. F. *Light-emitting diodes (2018)* (E. Fred Schubert, 2018).

84. Coldren, L. A. Diode lasers and photonic integrated circuits. *Optical Engineering* **36,** 616 (1997).

85. Tohmori, Y. *et al.* Wavelength tuning of GaInAsP/InP integrated laser with butt-jointed built-in distributed Bragg reflector. *Electronics Letters* **19,** 656–657 (1983).

86. Tsang, W. *et al.* Semiconductor distributed feedback lasers with quantum well or superlattice gratings for index or gain-coupled optical feedback. *Applied physics letters* **60,** 2580–2582 (1992).

87. Bhardwaj, A. *et al.* Low-loss InGaAsP/InP surface ridge waveguides for photonic integrated circuits. *IEEE Photonics Technology Letters* **28,** 1403–1405 (2016).

88. Coldren, L. A. *et al.* High performance InP-based photonic ICs—A tutorial. *Journal of Lightwave Technology* **29,** 554–570 (2011).

89. Stepanenko, M. *et al.* Multi-parameter optimization of an InP electro-optic modulator. *Symmetry* **12,** 1920 (2020).

90. Gupta, Y. D. *et al.* Implementation, Modelling and Verification of High-Speed Mach-Zehnder Phase Modulators in an Open Access InP Foundry Platform. *Journal of Lightwave Technology* **41,** 3498–3504 (2023).

91. Akin, J. *et al.* InGaP χ (2) integrated photonics platform for broadband, ultra-efficient nonlinear conversion and entangled photon generation. *Light: Science & Applications* **13,** 290 (2024).

92. Flizikowski, G. *et al. Nonlinear Characterization of InGaAsP/InP Platform in the C-band Telecom Range* in *Nonlinear Photonics* (2024), NpM4E–2.
93. Saeidi, S. *et al.* Demonstration of optical nonlinearity in InGaAsP/InP passive waveguides. *Optical Materials* **84,** 524–530 (2018).
94. Billah, M. R. *et al.* Hybrid integration of silicon photonics circuits and InP lasers by photonic wire bonding. *Optica* **5,** 876–883 (2018).
95. Matthias, B. & Remeika, J. Ferroelectricity in the ilmenite structure. *Physical Review* **76,** 1886 (1949).
96. Moss, D. J. *et al.* New CMOS-compatible platforms based on silicon nitride and Hydex for nonlinear optics. *Nature photonics* **7,** 597–607 (2013).
97. Smith, R. Efficient continuous optical second-harmonic generation. *IEEE Journal of Quantum Electronics* **2,** 129–129 (1966).
98. Peterson, G. *et al.* Electro-Optic Properties of LiNbO3. *Applied Physics Letters* **5,** 62–64 (1964).
99. Gnewuch, H. & Pannell, C. N. Monolithic bulk shear-wave acousto-optic tunable filter. *IEEE transactions on ultrasonics, ferroelectrics, and frequency control* **49,** 1635–1640 (2003).
100. Pearsall, T., Chiang, S. & Schmidt, R. Study of titanium diffusion in lithium-niobate low-loss optical waveguides by x-ray photoelectron spectroscopy. *Journal of Applied Physics* **47,** 4794–4797 (1976).
101. Leonberger, F. High-speed operation of LiNbO3 electro-optic interferometric waveguide modulators. *Optics Letters* **5,** 312–314 (1980).
102. Poberaj, G. *et al.* Lithium niobate on insulator (LNOI) for micro-photonic devices. *Laser & photonics reviews* **6,** 488–503 (2012).
103. Della Torre, A. *et al.* Folded electro-optical modulators operating at CMOS voltage level in a thin-film lithium niobate foundry process. *Optics Express* **33,** 6747–6757 (2025).
104. Shams-Ansari, A. *et al.* Reduced material loss in thin-film lithium niobate waveguides. *Apl Photonics* **7** (2022).
105. Mackwitz, P. *et al.* Periodic domain inversion in x-cut single-crystal lithium niobate thin film. *Applied Physics Letters* **108** (2016).
106. Koyaz, Y. *et al.* Ultrabroadband tunable difference frequency generation in a standardized thin-film lithium niobate platform. *Optics Express* **32,** 46776–46787 (2024).
107. Ludwig, M. *et al.* Ultraviolet astronomical spectrograph calibration with laser frequency combs from nanophotonic lithium niobate waveguides. *Nature Communications* **15,** 7614 (2024).
108. Maiman, T. H. Stimulated optical radiation in ruby. *nature* **187,** 493–494 (1960).
109. Weis, R. & Gaylord, T. Lithium niobate: Summary of physical properties and crystal structure. *Applied Physics A* **37,** 191–203 (1985).
110. Zhu, D. *et al.* Integrated photonics on thin-film lithium niobate. *Advances in Optics and Photonics* **13,** 242–352 (2021).

111. Boyd, R. W., Gaeta, A. L. & Giese, E. in *Springer Handbook of Atomic, Molecular, and Optical Physics* 1097–1110 (Springer, 2008).

112. Abel, S. *et al.* Large Pockels effect in micro-and nanostructured barium titanate integrated on silicon. *Nature materials* **18,** 42–47 (2019).

113. Lin, Q., Painter, O. J. & Agrawal, G. P. Nonlinear optical phenomena in silicon waveguides: modeling and applications. *Optics express* **15,** 16604–16644 (2007).

114. Helt, L. G., Liscidini, M. & Sipe, J. E. How does it scale? Comparing quantum and classical nonlinear optical processes in integrated devices. *Journal of the Optical Society of America B* **29,** 2199–2212 (2012).

115. Nielsen, M. A. & Chuang, I. L. *Quantum computation and quantum information* (Cambridge university press, 2010).

116. Einstein, A., Podolsky, B. & Rosen, N. Can quantum-mechanical description of physical reality be considered complete? *Physical review* **47,** 777 (1935).

117. Horodecki, R. *et al.* Quantum entanglement. *Reviews of modern physics* **81,** 865–942 (2009).

118. Dirac, P. A. M. The quantum theory of the emission and absorption of radiation. *Proceedings of the Royal Society of London. Series A, Containing Papers of a Mathematical and Physical Character* **114,** 243–265 (1927).

119. Wayo, D. D. K., Goliatt, L. & Ganji, D. Linear optics to scalable photonic quantum computing. *arXiv preprint arXiv:2501.02513* (2025).

120. Franson, J. D. Bell inequality for position and time. *Physical review letters* **62,** 2205 (1989).

121. Brendel, J. *et al.* Pulsed energy-time entangled twin-photon source for quantum communication. *Physical review letters* **82,** 2594 (1999).

122. Montaut, N. *et al.* Progress in integrated and fiber optics for time-bin based quantum information processing. *Advanced Optical Technologies* **14,** 1560084 (2025).

123. Singh, A. *et al.* Photonic quantum information with time-bins: Principles and applications. *arXiv preprint arXiv:2507.08102* (2025).

124. Yu, H. *et al.* Quantum key distribution implemented with d-level time-bin entangled photons. *Nature Communications* **16,** 171 (2025).

125. Chapman, J. C., Lim, C. C. & Kwiat, P. G. Hyperentangled time-bin and polarization quantum key distribution. *Physical Review Applied* **18,** 044027 (2022).

126. Congia, S. *et al.* Generation of hyperentangled photon pairs in the time and frequency domain on a silicon photonic chip. *Optics Letters* **50,** 5117–5120 (2025).

127. Patel, K. *et al.* Coexistence of high-bit-rate quantum key distribution and data on optical fiber. *Physical Review X* **2,** 041010 (2012).

128. Xavier, G. B. *et al.* Energy-time and time-bin entanglement: past, present and future. *npj Quantum Information* **11,** 129 (2025).

129. Kwiat, P. G. *et al.* New high-intensity source of polarization-entangled photon pairs. *Physical Review Letters* **75,** 4337 (1995).

130. Ursin, R. *et al.* Entanglement-based quantum communication over 144 km. *Nature physics* **3,** 481–486 (2007).

131. Yin, J. *et al.* Entanglement-based secure quantum cryptography over 1,120 kilometres. *Nature* **582,** 501–505 (2020).

132. Xavier, G. *et al.* Full polarization control for fiber optical quantum communication systems using polarization encoding. *Optics express* **16,** 1867–1873 (2008).

133. Erhard, M., Krenn, M. & Zeilinger, A. Advances in high-dimensional quantum entanglement. *Nature Reviews Physics* **2,** 365–381 (2020).

134. Knill, E., Laflamme, R. & Milburn, G. J. A scheme for efficient quantum computation with linear optics. *nature* **409,** 46–52 (2001).

135. Sharma, P., Rao, S. & Kanseri, B. Experimental generation and characterization of partially spatially coherent qubits. *Physica Scripta* **98,** 065115 (2023).

136. Peruzzo, A. *et al.* Quantum walks of correlated photons. *Science* **329,** 1500–1503 (2010).

137. Lu, L. *et al.* Three-dimensional entanglement on a silicon chip. *npj Quantum Information* **6,** 30 (2020).

138. Li, H. *et al.* Reconfigurable controlled two-qubit operation on a quantum photonic chip. *New Journal of Physics* **13,** 115009 (2011).

139. Spring, J. B. *et al.* Boson sampling on a photonic chip. *Science* **339,** 798–801 (2013).

140. Zhong, H.-S. *et al.* Quantum computational advantage using photons. *Science* **370,** 1460–1463 (2020).

141. Chen, M., Menicucci, N. C. & Pfister, O. Experimental realization of multipartite entanglement of 60 modes of a quantum optical frequency comb. *Physical review letters* **112,** 120505 (2014).

142. Kues, M. *et al.* On-chip generation of high-dimensional entangled quantum states and their coherent control. *Nature* **546,** 622–626 (2017).

143. Lu, H.-H. *et al.* Frequency-bin photonic quantum information. *Optica* **10,** 1655–1671 (2023).

144. Pe'Er, A. *et al.* Temporal shaping of entangled photons. *Physical review letters* **94,** 073601 (2005).

145. Lu, H.-H. *et al.* Fully arbitrary control of frequency-bin qubits. *Physical Review Letters* **125,** 120503 (2020).

146. Kolchin, P. *et al.* Electro-optic modulation of single photons. *Physical review letters* **101,** 103601 (2008).

147. Kobayashi, T. *et al.* Frequency-domain hong–ou–mandel interference. *Nature photonics* **10,** 441–444 (2016).

148. Joshi, C. *et al.* Frequency-domain quantum interference with correlated photons from an integrated microresonator. *Physical review letters* **124,** 143601 (2020).

149. Goto, H. *et al.* Observation of an oscillatory correlation function of multimode two-photon pairs. *Physical Review A* **68,** 015803 (2003).

150. Chen, C. *et al.* Efficient generation and characterization of spectrally factorable biphotons. *Optics express* **25,** 7300–7312 (2017).

151. Markidis, S. *What is quantum parallelism, anyhow?* in *ISC High Performance 2024 Research Paper Proceedings (39th International Conference)* (2024), 1–12.

152. Montanaro, A. & Pallister, S. Quantum algorithms and the finite element method. *Physical Review A* **93,** 032324 (2016).

153. Preskill, J. Quantum computing in the NISQ era and beyond. *Quantum* **2,** 79 (2018).

154. Shor, P. W. *Algorithms for quantum computation: discrete logarithms and factoring* in *Proceedings 35th annual symposium on foundations of computer science* (1994), 124–134.

155. Kitaev, A. Y. Quantum measurements and the Abelian stabilizer problem. *arXiv preprint quant-ph/9511026* (1995).

156. Grover, L. K. *A fast quantum mechanical algorithm for database search* in *Proceedings of the twenty-eighth annual ACM symposium on Theory of computing* (1996), 212–219.

157. Simon, D. R. On the power of quantum computation. *SIAM journal on computing* **26,** 1474–1483 (1997).

158. Shor, P. W. Scheme for reducing decoherence in quantum computer memory. *Physical review A* **52,** R2493 (1995).

159. Aghaee Rad, H. *et al.* Scaling and networking a modular photonic quantum computer. *Nature* **638,** 912–919 (2025).

160. Zhong, H.-S. *et al.* Phase-programmable gaussian boson sampling using stimulated squeezed light. *Physical review letters* **127,** 180502 (2021).

161. Madsen, L. S. *et al.* Quantum computational advantage with a programmable photonic processor. *Nature* **606,** 75–81 (2022).

162. Holland, M. J. & Burnett, K. Interferometric detection of optical phase shifts at the Heisenberg limit. *Physical review letters* **71,** 1355 (1993).

163. Aasi, J. *et al.* Enhanced sensitivity of the LIGO gravitational wave detector by using squeezed states of light. *Nature Photonics* **7,** 613–619 (2013).

164. Taylor, M. A. & Bowen, W. P. Quantum metrology and its application in biology. *Physics Reports* **615,** 1–59 (2016).

165. Ludlow, A. D. *et al.* Optical atomic clocks. *Reviews of Modern Physics* **87,** 637–701 (2015).

166. Rivest, R. L., Shamir, A. & Adleman, L. A method for obtaining digital signatures and public-key cryptosystems. *Communications of the ACM* **21,** 120–126 (1978).

167. Wootters, W. K. & Zurek, W. H. A single quantum cannot be cloned. *Nature* **299,** 802–803 (1982).

168. Gisin, N. *et al.* Quantum cryptography. *Reviews of modern physics* **74,** 145 (2002).

169. Bennett, C. H. & Brassard, G. Quantum cryptography: Public key distribution and coin tossing. *Theoretical computer science* **560,** 7–11 (2014).

170. Bennett, C. H. & Brassard, G. Experimental quantum cryptography: the dawn of a new era for quantum cryptography: the experimental prototype is working. *ACM Sigact News* **20,** 78–80 (1989).

171. Bennett, C. H., Brassard, G. & Mermin, N. D. Quantum cryptography without Bell's theorem. *Physical review letters* **68,** 557 (1992).

172. Bennett, C. H., Brassard, G. & Robert, J.-M. Privacy amplification by public discussion. *SIAM journal on Computing* **17,** 210–229 (1988).

173. Berra, F. *et al. High-speed source for satellite quantum key distribution* in *IAC 2023 congress proceedings, 74th International Astronautical Congress (IAC), Baku, Azerbaijan* (2023).

174. Grand View Research. *Quantum Cryptography Market Size and Share Report, 2030* Accessed: 2025-08-29. 2023. `https://www.grandviewresearch.com/industry-analysis/quantum-cryptography-market-report`.

175. Wehner, S., Elkouss, D. & Hanson, R. Quantum internet: A vision for the road ahead. *Science* **362,** eaam9288 (2018).

176. Van Deventer, O. *et al.* Towards European standards for quantum technologies. *EPJ Quantum Technology* **9,** 33 (2022).

177. Kimble, H. J. The quantum internet. *Nature* **453,** 1023–1030 (2008).

178. Azuma, K., Tamaki, K. & Lo, H.-K. All-photonic quantum repeaters. *Nature communications* **6,** 6787 (2015).

179. Mueller, A. *et al.* High-rate multiplexed entanglement source based on time-bin qubits for advanced quantum networks. *Optica Quantum* **2,** 64–71 (2024).

180. Fitzke, E. *et al.* Scalable network for simultaneous pairwise quantum key distribution via entanglement-based time-bin coding. *PRX Quantum* **3,** 020341 (2022).

181. Kim, J.-H. *et al.* Quantum communication with time-bin entanglement over a wavelength-multiplexed fiber network. *APL Photonics* **7** (2022).

182. Huang, Y. *et al.* A sixteen-user time-bin entangled quantum communication network with fully connected topology. *Laser & Photonics Reviews* **19,** 2301026 (2025).

183. Braunstein, S. L. & Van Loock, P. Quantum information with continuous variables. *Reviews of modern physics* **77,** 513–577 (2005).

184. Ralph, T. C. Continuous variable quantum cryptography. *Physical Review A* **61,** 010303 (1999).

185. Grosshans, F. & Grangier, P. Continuous variable quantum cryptography using coherent states. *Physical review letters* **88,** 057902 (2002).

186. Zhang, Y. *et al.* Continuous-variable quantum key distribution system: Past, present, and future. *Applied Physics Reviews* **11** (2024).

187. Wang, H. *et al.* Sub-Gbps key rate four-state continuous-variable quantum key distribution within metropolitan area. *Communications Physics* **5,** 162 (2022).

188. Bell, J. S. On the einstein podolsky rosen paradox. *Physics Physique Fizika* **1,** 195 (1964).

189. Freedman, S. J. & Clauser, J. F. Experimental test of local hidden-variable theories. *Physical review letters* **28,** 938 (1972).

190. Friis, N. *et al.* Entanglement certification from theory to experiment. *Nature Reviews Physics* **1,** 72–87 (2019).

191. Clauser, J. F. *et al.* Proposed experiment to test local hidden-variable theories. *Physical review letters* **23,** 880 (1969).

192. Cirel'son, B. S. Quantum generalizations of Bell's inequality. *Letters in Mathematical Physics* **4,** 93–100 (1980).

193. Terhal, B. M. Bell inequalities and the separability criterion. *Physics Letters A* **271,** 319–326 (2000).

194. Gühne, O. & Tóth, G. Entanglement detection. *Physics Reports* **474,** 1–75 (2009).

195. Olislager, L. *et al.* Frequency-bin entangled photons. *Physical Review A—Atomic, Molecular, and Optical Physics* **82,** 013804 (2010).

196. Seshadri, S. *et al.* Complete frequency-bin Bell basis synthesizer. *Physical Review Letters* **129,** 230505 (2022).

197. Tanzilli, S. *et al.* Highly efficient photon-pair source using periodically poled lithium niobate waveguide. *Electronics Letters* **37,** 26–28 (2001).

198. Thyagarajan, K. *et al.* Generation of polarization-entangled photons using type-II doubly periodically poled lithium niobate waveguides. *Physical Review A—Atomic, Molecular, and Optical Physics* **80,** 052321 (2009).

199. Morrison, C. L. *et al.* Frequency-bin entanglement from domain-engineered down-conversion. *APL Photonics* **7** (2022).

200. Zhao, J. *et al.* High quality entangled photon pair generation in periodically poled thin-film lithium niobate waveguides. *Physical review letters* **124,** 163603 (2020).

201. Maeder, A. *et al.* Programmable Bell State Generation in an Integrated Thin Film Lithium Niobate Circuit. *arXiv preprint arXiv:2506.18079* (2025).

202. Grassani, D. *et al.* Micrometer-scale integrated silicon source of time-energy entangled photons. *Optica* **2,** 88–94 (2015).

203. Azzini, S. *et al.* Ultra-low power generation of twin photons in a compact silicon ring resonator. *Optics express* **20,** 23100–23107 (2012).

204. Clementi, M. *et al.* Programmable frequency-bin quantum states in a nano-engineered silicon device. *Nature Communications* **14,** 176 (2023).

205. Moreno, J. *Spontaneous four-wave mixing in standard birefringent fiber* PhD thesis (University of Delaware, 2012).

206. Loudon, R. *The quantum theory of light* (OUP Oxford, 2000).

207. Gerry, C. C. & Knight, P. L. *Introductory quantum optics* (Cambridge university press, 2023).

208. Thomas, P. *et al.* Efficient generation of entangled multiphoton graph states from a single atom. *Nature* **608,** 677–681 (2022).

209. Meng, Y. *et al.* Deterministic photon source of genuine three-qubit entanglement. *Nature communications* **15,** 7774 (2024).

210. Langer, M. *et al.* An ultra-compact deterministic source of maximally entangled photon pairs. *APL Photonics* **10** (2025).

211. Besse, J.-C. *et al.* Realizing a deterministic source of multipartite-entangled photonic qubits. *Nature communications* **11,** 4877 (2020).

212. Senellart, P., Solomon, G. & White, A. High-performance semiconductor quantum-dot single-photon sources. *Nature nanotechnology* **12,** 1026–1039 (2017).

213. Ekert, A. K. Quantum cryptography based on Bell's theorem. *Physical review letters* **67,** 661 (1991).

214. Bruß, D. Optimal eavesdropping in quantum cryptography with six states. *Physical Review Letters* **81,** 3018 (1998).

215. Lo, H.-K., Ma, X. & Chen, K. Decoy state quantum key distribution. *Physical review letters* **94,** 230504 (2005).

216. Mattle, K. *et al.* Dense coding in experimental quantum communication. *Physical review letters* **76,** 4656 (1996).

217. Bennett, C. H. *et al.* Teleporting an unknown quantum state via dual classical and Einstein-Podolsky-Rosen channels. *Physical review letters* **70,** 1895 (1993).

218. Bouwmeester, D. *et al.* Experimental quantum teleportation. *Nature* **390,** 575–579 (1997).

219. Zukowski, M. *et al.* " Event-ready-detectors" Bell experiment via entanglement swapping. *Physical review letters* **71** (1993).

220. Briegel, H.-J. *et al.* Quantum Repeaters: The Role of Imperfect Local Operations in Quantum Communication. *Phys. Rev. Lett.* **81,** 5932–5935. `https://link.aps.org/doi/10.1103/PhysRevLett.81.5932` (26 Dec. 1998).

221. Duan, L.-M. *et al.* Long-distance quantum communication with atomic ensembles and linear optics. *Nature* **414,** 413–418 (2001).

222. Hu, X.-M. *et al.* Progress in quantum teleportation. *Nature Reviews Physics* **5,** 339–353 (2023).

223. Brendel, J., Mohler, E. & Martienssen, W. Time-resolved dual-beam two-photon interferences with high visibility. *Physical review letters* **66,** 1142 (1991).

224. Marcikic, I. *et al.* Time-bin entangled qubits for quantum communication created by femtosecond pulses. *Physical Review A* **66,** 062308 (2002).

225. Williams, J. *et al. Implementation of quantum key distribution and quantum clock synchronization via time bin encoding* in *Quantum computing, communication, and simulation* **11699** (2021), 16–25.

226. Lima, G. *et al.* Experimental Bell-inequality violation without the postselection loophole. *Physical Review A—Atomic, Molecular, and Optical Physics* **81,** 040101 (2010).

227. Weihs, G. *et al.* Violation of Bell's inequality under strict Einstein locality conditions. *Physical Review Letters* **81,** 5039 (1998).

228. Garg, A. & Mermin, N. D. Detector inefficiencies in the Einstein-Podolsky-Rosen experiment. *Physical Review D* **35,** 3831 (1987).

229. Giustina, M. *et al.* Bell violation using entangled photons without the fair-sampling assumption. *Nature* **497,** 227–230 (2013).

230. Christensen, B. G. *et al.* Detection-loophole-free test of quantum nonlocality, and applications. *Physical review letters* **111,** 130406 (2013).

231. Strekalov, D. *et al.* Postselection-free energy-time entanglement. *Physical Review A* **54,** R1 (1996).

232. Cabello, A. *et al.* Proposed Bell experiment with genuine energy-time entanglement. *Physical Review Letters* **102,** 040401 (2009).

233. Santagiustina, F. B. *et al.* Experimental post-selection loophole-free time-bin and energy-time nonlocality with integrated photonics. *Optica* **11,** 498–511 (2024).

234. Vedovato, F. *et al.* Postselection-loophole-free Bell violation with genuine time-bin entanglement. *Physical review letters* **121,** 190401 (2018).

235. Jogenfors, J. *et al.* Hacking the bell test using classical light in energy-time entanglement–based quantum key distribution. *Science Advances* **1,** e1500793 (2015).

236. Mueller, A. *et al.* Time-walk and jitter correction in SNSPDs at high count rates. *Applied Physics Letters* **122** (2023).

237. Yang, F. *et al.* Monolithic thin film lithium niobate electro-optic modulator with over 110 GHz bandwidth. *Chinese Optics Letters* **20,** 022502 (2022).

238. Fang, X. *et al.* Ultrahigh-speed optical interconnects with thin film lithium niobate modulator. *Journal of Lightwave Technology* **41,** 1207–1215 (2022).

239. Wang, X. *et al.* Achieving beyond-100-GHz large-signal modulation bandwidth in hybrid silicon photonics Mach Zehnder modulators using thin film lithium niobate. *APL Photonics* **4** (2019).

240. Valdez, F. *et al.* 110 GHz, 110 mW hybrid silicon-lithium niobate Mach-Zehnder modulator. *Scientific reports* **12,** 18611 (2022).

241. Xu, M. *et al.* Dual-polarization thin-film lithium niobate in-phase quadrature modulators for terabit-per-second transmission. *Optica* **9,** 61–62 (2022).

242. Liu, X. *et al.* Capacitively-loaded thin-film lithium niobate modulator with ultra-flat frequency response. *IEEE Photonics Technology Letters* **34,** 854–857 (2022).

243. Liu, Y. *et al.* Low Vπ thin-film lithium niobate modulator fabricated with photolithography. *Optics express* **29,** 6320–6329 (2021).

244. Liu, X. *et al.* Wideband thin-film lithium niobate modulator with low half-wave-voltage length product. *Chinese Optics Letters* **19,** 060016 (2021).

245. Zhang, M. *et al.* Monolithic ultra-high-Q lithium niobate microring resonator. *Optica* **4,** 1536–1537 (2017).

246. Wu, R. *et al.* Long low-loss-litium niobate on insulator waveguides with sub-nanometer surface roughness. *Nanomaterials* **8,** 910 (2018).

247. Liu, X. *et al.* Ultra-broadband and low-loss edge coupler for highly efficient second harmonic generation in thin-film lithium niobate. *Advanced Photonics Nexus* **1,** 016001–016001 (2022).

248. Labbé, F. *et al.* Thin-film lithium niobate quantum photonics: review and perspectives. *Advanced Photonics* **7,** 044002–044002 (2025).

249. Webster, J. & Zernike, F. Push- pull thin- film optical modulator. *Applied Physics Letters* **26,** 465–467 (1975).

250. Verstraete, F. & Wolf, M. M. Entanglement versus Bell violations and their behavior under local filtering operations. *Physical review letters* **89,** 170401 (2002).

251. Ibarra Fusté, J. A. Design rules and optimization of electro-optic modulators based on coplanar waveguides (2014).

252. Palik, E. D. *Handbook of optical constants of solids* (Academic press, 1998).

253. Zelmon, D. E., Small, D. L. & Jundt, D. Infrared corrected Sellmeier coefficients for congruently grown lithium niobate and 5 mol.% magnesium oxide–doped lithium niobate. *Journal of the Optical Society of America B* **14,** 3319–3322 (1997).

254. Dassault Systèmes. *CST Studio Suite* 3DS SIMULIA (2025). https://www.3ds.com/products/simulia/cst-studio-suite.

255. Celik, O. T. *et al.* High-bandwidth CMOS-voltage-level electro-optic modulation of 780 nm light in thin-film lithium niobate. *Optics Express* **30,** 23177–23186 (2022).

256. Yang, R.-Y. *et al.* Characteristics of coplanar waveguide on lithium niobate crystals as a microwave substrate. *Journal of Applied Physics* **101,** 014101. ISSN: 0021-8979. eprint: https://pubs.aip.org/aip/jap/article-pdf/doi/10.1063/1.2402978/13341406/014101_1_online.pdf. https://doi.org/10.1063/1.2402978 (Jan. 2007).

257. Hammerstad, E. & Jensen, O. *Accurate models for microstrip computer-aided design* in *1980 IEEE MTT-S International Microwave Symposium Digest* (1980), 407–409.

258. Den Besten, J. H. Integration of multiwavelength lasers with fast electro-optical modulators (2004).

259. Shi, J. *et al.* Reduced material loss caused by electron beam lithography in thin-film lithium niobate through post-process annealing. *Optical Materials* **149,** 115049 (2024).

260. Rabus, D. G. & Sada, C. in *Integrated Ring Resonators: A Compendium* 3–46 (Springer, 2020).

261. Zhao, G. *et al.* Tunable Fano resonances based on microring resonator with feedback coupled waveguide. *Optics express* **24,** 20187–20195 (2016).

262. Wang, M. *et al.* Polarization splitter-rotator on thin film lithium niobate based on multimode interference. *Optics Express* **32,** 28175–28182. https://opg.optica.org/oe/abstract.cfm?URI=oe-32-16-28175 (2024).

263. Jiang, X., Wu, H. & Dai, D. Low-loss and low-crosstalk multimode waveguide bend on silicon. *Optics express* **26,** 17680–17689 (2018).

264. Coherent Corp. *UHNA Fiber: Efficient Coupling to Silicon Waveguides* tech. rep. Application Note (Coherent, 2024). `https://www.coherent.com/resources/application-note/components-and-accessories/specialty-optical-fibers/uhna-fiber-efficient-coupling-to-silicon-waveguides.pdf`.

265. Finco, G. *et al.* Time-bin entangled Bell state generation and tomography on thin-film lithium niobate. *npj Quantum Information* **10,** 135 (2024).

266. Kuzucu, O. *et al.* Joint temporal density measurements for two-photon state characterization. *Physical review letters* **101,** 153602 (2008).

267. Thew, R. T. *et al.* Qudit quantum-state tomography. *Physical Review A* **66,** 012303 (2002).

268. Altepeter, J. B., Jeffrey, E. R. & Kwiat, P. G. Photonic state tomography. *Advances in atomic, molecular, and optical physics* **52,** 105–159 (2005).

269. Shor, P. W. & Preskill, J. Simple proof of security of the BB84 quantum key distribution protocol. *Physical review letters* **85,** 441 (2000).

270. Lo, H.-K., Chau, H. F. & Ardehali, M. Efficient quantum key distribution scheme and a proof of its unconditional security. *Journal of Cryptology* **18,** 133–165 (2005).

271. Serfling, R. J. Probability inequalities for the sum in sampling without replacement. *The Annals of Statistics,* 39–48 (1974).

272. Tomamichel, M. *et al.* Tight finite-key analysis for quantum cryptography. *Nature communications* **3,** 634 (2012).

273. Chernoff, H. A measure of asymptotic efficiency for tests of a hypothesis based on the sum of observations. *The Annals of Mathematical Statistics,* 493–507 (1952).

274. Mannalath, V., Zapatero, V. & Curty, M. Sharp finite statistics for quantum key distribution. *Physical Review Letters* **135,** 020803 (2025).

275. Liao, S.-K. *et al.* Satellite-to-ground quantum key distribution. *Nature* **549,** 43–47 (2017).

276. Bunandar, D. *et al.* Numerical finite-key analysis of quantum key distribution. *npj Quantum Information* **6,** 104 (2020).

277. Khodadad Kashi, A. & Kues, M. Frequency-bin-encoded entanglement-based quantum key distribution in a reconfigurable frequency-multiplexed network. *Light: Science & Applications* **14,** 49 (2025).

278. Honjo, T. *et al.* Long-distance entanglement-based quantum key distribution over optical fiber. *Optics Express* **16,** 19118–19126 (2008).

279. Zhuang, S.-C. *et al.* Ultrabright Entanglement Based Quantum Key Distribution over a 404 km Optical Fiber. *Physical Review Letters* **134,** 230801 (2025).

280. Zhong, Z.-Q. *et al.* Hyperentanglement quantum communication over a 50 km noisy fiber channel. *Optica* **11,** 1056–1061 (2024).

281. Pelet, Y. *et al.* Operational entanglement-based quantum key distribution over 50 km of field-deployed optical fibers. *Physical Review Applied* **20,** 044006 (2023).

282. Bertapelle, T. *et al.* High-speed source-device-independent quantum random number generator on a chip. *Optica Quantum* **3,** 111–118 (2025).

283. Peri, A. *et al.* High-Performance Heterodyne Receiver for Quantum Information Processing in a Laser Written Integrated Photonic Platform. *arXiv preprint arXiv:2506.08924* (2025).

284. *Characteristics of a single-mode optical fibre and cable* ITU-T Recommendation G.652 G.652. Version of August 2024 (International Telecommunication Union, Aug. 2024). `https://www.itu.int/rec/T-REC-G.652-202408-I/en`.

285. Agrawal, G. P. *Fiber-optic communication systems* (John Wiley & Sons, 2012).

286. Ma, X., Fung, C.-H. F. & Lo, H.-K. Quantum key distribution with entangled photon sources. *Physical Review A—Atomic, Molecular, and Optical Physics* **76,** 012307 (2007).

287. Holloway, C. *et al.* Optimal pair-generation rate for entanglement-based quantum key distribution. *Physical Review A—Atomic, Molecular, and Optical Physics* **87,** 022342 (2013).

288. Weigel, P. O. *et al.* Bonded thin film lithium niobate modulator on a silicon photonics platform exceeding 100 GHz 3-dB electrical modulation bandwidth. *Optics express* **26,** 23728–23739 (2018).

289. De Riedmatten, H. *et al.* Long-distance entanglement swapping with photons from separated sources. *Physical Review A—Atomic, Molecular, and Optical Physics* **71,** 050302 (2005).

290. Tagliavacche, N. *et al.* Frequency-bin entanglement-based quantum key distribution. *npj Quantum Information* **11,** 60 (2025).

291. Zhang, J. *et al.* Compact polarization splitter-rotator based on lithium niobate-on-insulator platform. *Journal of Applied Physics* **136** (2024).

292. Bernardi, A. *et al.* Post-selection free time-bin entanglement on a thin-film lithium niobate photonic chip. *arXiv preprint arXiv:2505.04598* (2025).

293. Bernardi, A. *et al.* Gigahertz-rate thin-film lithium niobate receiver for time-bin quantum communication. *Light: Science & Applications.* Accepted for publication.

294. Bacchi, M. *et al. Ultrafast post-selection free time-bin entanglement on a thin film lithium niobate photonic chip* in *European Quantum Electronics Conference* (2025), eb_8_2.

295. Bernardi, A. *et al. High switching rate post-selection free time-bin entanglement in thin-film lithium niobate* in *2025 25th Anniversary International Conference on Transparent Optical Networks (ICTON)* (2025), 1–3.

296. Bernardi, A. *et al. Post-selection free time-bin entanglement on a thin-film lithium niobate photonic chip* in *CLEO: Fundamental Science* (2025), FF118_5.

297. Thomson, D. *et al.* Roadmap on silicon photonics. *Journal of Optics* **18,** 073003 (2016).

298. Xu, Q. *et al.* Micrometre-scale silicon electro-optic modulator. *nature* **435,** 325–327 (2005).

299. Li, X., Yu, S. & Gui, C. Fiber-to-chip three-dimensional silicon-on-insulator edge couplers with high efficiency and tolerance. *Micromachines* **14,** 1500 (2023).

300. Ueno, Y., Ricci, V. & Stegeman, G. I. Second-order susceptibility of Ga0. 5In0. 5P crystals at 1.5 μ m and their feasibility for waveguide quasi-phase matching. *Journal of the Optical Society of America B* **14,** 1428–1436 (1997).

301. Yu, Z. *et al.* Silicon nitride assisted tri-layer edge coupler on lithium niobate-on-insulator platform. *Optics Letters* **48,** 3367–3370 (2023).

302. Blatt, R. & Wineland, D. Entangled states of trapped atomic ions. *Nature* **453,** 1008–1015 (2008).

303. Nakamura, Y., Pashkin, Y. A. & Tsai, J. Coherent control of macroscopic quantum states in a single-Cooper-pair box. *nature* **398,** 786–788 (1999).

304. DiVincenzo, D. P. in *Mesoscopic electron transport* 657–677 (Springer, 1997).

305. Arute, F. *et al.* Quantum supremacy using a programmable superconducting processor. *Nature* **574,** 505–510 (2019).

306. Lo, H.-K., Curty, M. & Qi, B. Measurement-device-independent quantum key distribution. *Physical review letters* **108,** 130503 (2012).

307. Acín, A. *et al.* Device-independent security of quantum cryptography against collective attacks. *Physical Review Letters* **98,** 230501 (2007).

308. Peev, M. *et al.* The SECOQC quantum key distribution network in Vienna. *New journal of physics* **11,** 075001 (2009).

309. Wang, J. *et al.* Multidimensional quantum entanglement with large-scale integrated optics. *Science* **360,** 285–291 (2018).

310. Walls, D. F. Squeezed states of light. *nature* **306,** 141–146 (1983).

311. D'Angelo, M., Chekhova, M. V. & Shih, Y. Two-photon diffraction and quantum lithography. *Physical review letters* **87,** 013602 (2001).

312. Mauerer, W. *et al.* How colors influence numbers: Photon statistics of parametric down-conversion. *Physical Review A—Atomic, Molecular, and Optical Physics* **80,** 053815 (2009).

313. Autebert, C. *et al.* Multi-user quantum key distribution with entangled photons from an AlGaAs chip. *Quantum Science and Technology* **1,** 01LT02 (2016).

314. Bell, J. S. Physics long island city. *NY* **1,** 1 (1964).

315. Aerts, S. *et al.* Two-Photon Franson-Type Experiments and Local Realism. *Phys. Rev. Lett.* **83,** 2872–2875 (15 Oct. 1999).

316. Sabattoli, F. A. Silicon Photonic Integrated Circuits for Quantum Applications (2021).

317. Mercante, A. J. *et al.* 110 GHz CMOS compatible thin film LiNbO3 modulator on silicon. *Optics express* **24,** 15590–15595 (2016).

318. Cuevas, A. *et al.* Long-distance distribution of genuine energy-time entanglement. *Nature Communications* **4,** 2871 (2013).

319. Ekici, Ç. *et al.* Scalable temporal multiplexing of telecom photons via thin-film lithium niobate photonics. *npj Quantum Information* **11,** 21 (2025).

320. Heo, H. *et al.* On-chip quantum key distribution over field-deployed fiber using lithium niobate photonic circuit. *APL Photonics* **10** (2025).

321. Zhang, C. *et al.* Polarization states preparation based on TFLN integrated chip and SOI 2D grating coupler. *Optics & Laser Technology* **188,** 112935 (2025).

322. Yang, H. *et al.* Quantum State Preparation of Time-bin Encoding Based on TFLN Integrated Chips. *Available at SSRN 6056155.*

Ringraziamenti

Il lavoro e i risultati ottenuti in questi tre anni non sarebbero stati possibili senza il sostegno, l'aiuto e i contributi delle persone che mi sono state vicine e hanno collaborato con me, a cui vanno tutti i miei ringraziamenti.

Innanzitutto, vorrei ringraziare i miei supervisori, il prof. Daniele Bajoni e Federico Sabattoli, che hanno contribuito direttamente a tutto il progetto e mi hanno insegnato molto dal punto di vista della formazione che porterò con me nei prossimi anni.

Un ringraziamento va a tutte le persone di AFR che ho conosciuto e che mi hanno aiutato nei due anni in cui ho lavorato con loro, e a cui devo molto di quello che ho imparato, in particolare a tutto il team di R&D: Roberto, Alberto, Giuseppe, Federico (ancora, se lo merita), Francesco, Marco, Alexander, Andrea, Riccardo, Piero, Tania, Monica, Ali, Paolo e Alberto. I also thank the people I met in AFR in China for their hospitality, for giving me the opportunity to learn about different topics, and for allowing me to experience and discover a different culture. This was a unique experience that I will never forget, and I am grateful for it.

Ringrazio tutto il QLab per i bei momenti quotidiani trascorsi assieme e senza il quale non avrei concluso alcuna misura "quantum": i professori Daniele, Matteo e Marco, e poi Massimo, Marco, Marcello, Sara, Emanuele, Noemi, Andrea, Linda e Domenico. Ringrazio anche i relatori di questa tesi che hanno contribuito a migliorare la qualità del lavoro e ai quali sono riconoscente per i loro commenti: il Dott. Davide Grassani e il prof. Enrico Prati.

Ringrazio la mia famiglia: mamma, papà e mio fratello Mattia, che mi hanno sempre sostenuto durante gli anni dell'università e anche negli ultimi tre di dottorato; e i miei nonni, che mi hanno sempre incoraggiato, anche se non sono riuscito a spiegare loro cosa ho fatto durante il dottorato. Alla fine, però, un lavoro l'ho trovato.

Un grazie va anche a tutti i miei amici, compresi quelli che non vivono più a Pavia: Gabri, Tommy e Jack, e a tutto il CUS Pavia Canoa, che mi ha permesso di portare avanti la mia passione per nove anni, regalandomi bellissimi ricordi e soddisfazioni sportive che non dimenticherò.

Infine, il grazie più grande va a Giulia, mia compagna di vita ormai da diversi anni. Grazie per esserci sempre stata nei momenti di difficoltà, ma anche soprattutto per avrer trascorso assieme quelli più belli, per avermi aspettato durante i miei sei mesi in Oriente e per tutti i caffè preparati al mattino, senza i quali non sarei riuscito a completare il dottorato.